JYVÄSKYLÄ STUDIES IN COMPUTING
148

Juha Jeronen

On the Mechanical Stability and Out-of-Plane Dynamics of a Travelling Panel Submerged in Axially Flowing Ideal Fluid

A Study into Paper Production in Mathematical Terms

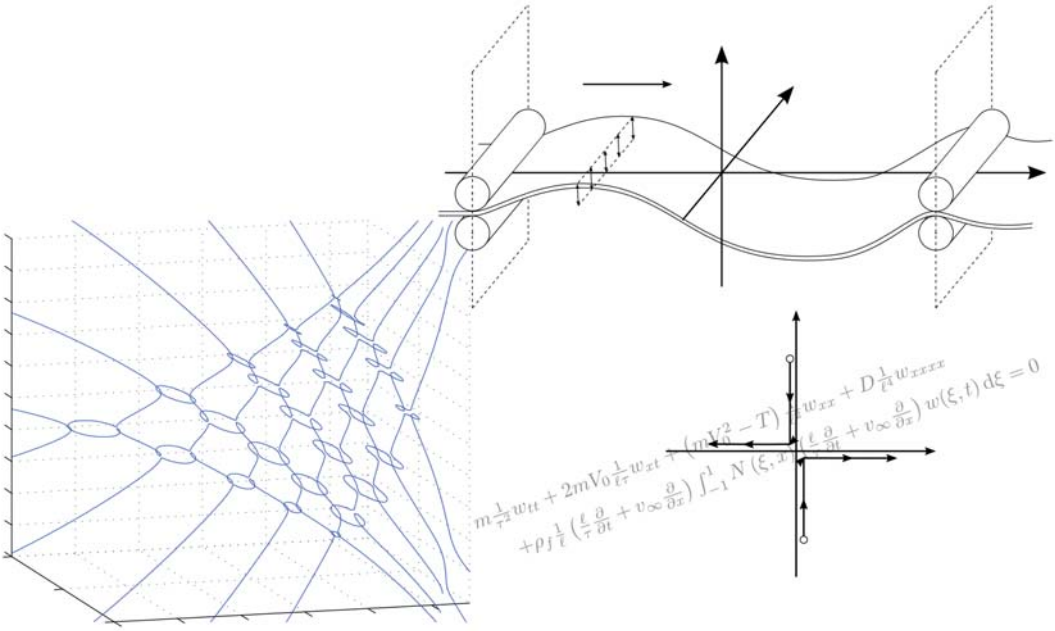

JYVÄSKYLÄN YLIOPISTO

JYVÄSKYLÄ STUDIES IN COMPUTING 148

Juha Jeronen

On the Mechanical Stability and Out-of-Plane Dynamics of a Travelling Panel Submerged in Axially Flowing Ideal Fluid

A Study into Paper Production in Mathematical Terms

Esitetään Jyväskylän yliopiston informaatioteknologian tiedekunnan suostumuksella
julkisesti tarkastettavaksi yliopiston Agora-rakennuksen salissa AgC231
joulukuun 16. päivänä 2011 kello 12.

Academic dissertation to be publicly discussed, by permission of
the Faculty of Information Technology of the University of Jyväskylä,
in building Agora, hall AgC231, on December 16, 2011 at 12 o'clock noon.

UNIVERSITY OF JYVÄSKYLÄ

JYVÄSKYLÄ 2011

On the Mechanical Stability and Out-of-Plane Dynamics of a Travelling Panel Submerged in Axially Flowing Ideal Fluid

A Study into Paper Production
in Mathematical Terms

JYVÄSKYLÄ STUDIES IN COMPUTING 148

Juha Jeronen

On the Mechanical Stability and Out-of-Plane Dynamics of a Travelling Panel Submerged in Axially Flowing Ideal Fluid

A Study into Paper Production in Mathematical Terms

UNIVERSITY OF JYVÄSKYLÄ

JYVÄSKYLÄ 2011

Editors
Timo Männikkö
Department of Mathematical Information Technology, University of Jyväskylä
Pekka Olsbo, Ville Korkiakangas
Publishing Unit, University Library of Jyväskylä

URN:ISBN:978-951-39-4596-1
ISBN 978-951-39-4596-1 (PDF)

ISBN 978-951-39-4595-4 (nid.)
ISSN 1456-5390

Jyväskylä University Printing House, Jyväskylä 2011

ABSTRACT

Jeronen, Juha
On the mechanical stability and out-of-plane dynamics of a travelling panel submerged in axially flowing ideal fluid: a study into paper production in mathematical terms
Jyväskylä: University of Jyväskylä, 2011, 243 p.
(Jyväskylä Studies in Computing
ISSN 1456-5390; 148)
ISBN 978-951-39-4595-4 (nid.)
ISBN 978-951-39-4596-1 (PDF)
Finnish summary
Diss.

In this study, we consider the dynamical behaviour and stability of a moving panel submerged in two-dimensional potential flow in a papermaking context. The steady-state critical velocity of the system is determined in terms of problem parameters. Dynamical response is predicted via direct temporal simulations, and the eigenfrequency spectrum is analyzed, obtaining both the subcritical free vibration behaviour and the initial postbuckling response. By using an analytical functional solution for the reaction force of the surrounding air, the fluid-structure interaction model is reduced to one integro-differential equation. This makes it possible to work with this fluid-structure interaction problem efficiently with modest computational resources, while improving on the accuracy when compared to the classical technique of added-mass approximation. Discretization is performed by the Fourier–Galerkin method, and results from the numerical computations are visualized. The predictions of the model are successfully validated against existing results. It is found that the model works especially well for long, narrow web spans. To accomodate readers from various technical backgrounds, the topics are reported in a detailed, ground-up manner. After a general introduction, the elastic stability properties of the classical moving string and those of the damped moving string are analyzed in detail as an introduction to this class of problems. Finally, to facilitate eigenfrequency spectrum analysis for the main problem, techniques are developed for overcoming the two main practical challenges: producing continuous curves out of randomly ordered eigenvalue data, and classifying physically meaningful solutions versus numerical artifacts.

Keywords: Axially moving, panel, potential flow, fluid-structure interaction (FSI), elastic stability, eigenvalue problem, paper web

Author

M.Sc. Juha Jeronen
juha.jeronen@jyu.fi
Department of Mathematical Information Technology
University of Jyväskylä
Finland

Supervisors

Professor Pekka Neittaanmäki
Department of Mathematical Information Technology
University of Jyväskylä
Finland

Professor Nikolay Banichuk
Institute for Problems in Mechanics
Russian Academy of Sciences
Russia

Professor Raino Mäkinen
Department of Mathematical Information Technology
University of Jyväskylä
Finland

Reviewers

Docent Erkki Laitinen
Department of Mathematical Sciences
University of Oulu
Finland

Professor Boris Epstein
School of Computer Science
The Academic College of Tel Aviv-Yaffo
Israel

Opponent

Dr. Reijo Kouhia
Department of Civil and Structural Engineering
Aalto University School of Engineering
Finland

PREFACE

The motivation of this study comes from paper production, which is an important segment of industry in Finland. In a paper machine, the paper that is being manufactured travels in the machine as a thin sheet. Viewed at the macroscopic scale, this *paper web* appears uniform; hence, continuum models are used for investigating its mechanical behaviour.

Due to inertial effects related to the out-of-plane acceleration, axially moving materials are unstable; in very general terms, running them too fast makes them lose stability. For brittle materials such as paper, loss of stability usually leads to breakage, interrupting the production process. Such interruptions are costly for two reasons. First, keeping the paper machine running requires a constant input of large amounts of energy, regardless of whether paper is being produced. Secondly, the factory remains offline until the web has been properly re-fed through the machine to restart the production process; this takes time.

Thus, avoiding web breaks is a matter of both technological and economical interest. A related technological and economical question is getting the most out of a given kind of paper machine design. Exactly how fast can one expect the paper to move before fundamental physical limits are reached, and what factors should be changed when designing new paper machines, if higher production speeds are desired?

The physical limits of stability for moving materials can be predicted from continuum models. The study of such models thus provides the physical context in which the technological processes must work. This is where the present study comes in.

In such a stability analysis, it is important to account for the fluid-structure interaction of the moving paper web and the surrounding air, because paper is a lightweight material. Only by including this interaction into the model (in some manner) it is possible to make accurate predictions of the mechanical behaviour of the paper web.

These days, supercomputers are often used in scientific computing, to enable the solution of complex high-resolution models with detailed equation systems and a large number of variables (technically speaking, degrees of freedom). But on the other hand, semianalytical methods for simple models are making a return, due to their accuracy and computational efficiency (see e.g. Xing and Liu, 2009b).

It is our view that simple models provide a foundation and reference point for more complex multiphysics studies. Fast solvers, made possible if the model is simple enough, can also be used for applications such as model parameter optimization, fast direct exploration of the parameter space, or statistical analysis and visualization of the effects of uncertain data. Hence, we have approached the problem using the tools of simple models and fast solvers.

Our research team works at the Department of Mathematical Information Technology at the University of Jyväskylä. The team is headed by professor Pekka

Neittaanmäki. Researchers include Ph. Lic. Matti Kurki, M. Sc. Tytti Saksa, M. Sc. Tero Tuovinen and myself. Additionally, and importantly, professor Nikolay V. Banichuk from the Ishlinsky Institute for Problems in Mechanics of the Russian Academy of Sciences, Moscow, is a regularly visiting team member, and many of our studies are based on ideas suggested and projects started by him.

During the last few years, we have performed a number of studies on moving materials with the papermaking application in mind. Fluid-structure interaction of the moving panel with surrounding ideal fluid was investigated in Banichuk et al. (2010b) and Banichuk et al. (2011b). Gravitational loading with an axial component, in inclined moving panels, was studied in Banichuk et al. (2011c).

Semi-analytical steady-state solutions for moving isotropic and orthotropic plates were determined in Banichuk et al. (2010a) and Banichuk et al. (2011a), The effect of linear tension inhomogeneities along the supporting rollers has also been studied, currently reported in the preprint Banichuk et al. (2010c). The last three have been combined, and extended into linear tension inhomogeneities for an orthotropic plate, in the thesis work by Tuovinen (2011).

This thesis concentrates on the problem of the axially moving panel, submerged into ideal fluid for which axial motion of the free stream is allowed. Hence, the study is focused on one-dimensional models of the paper web. These include both the moving string and the moving panel.

As the present work is a thesis, presentation of new, original results is the most important aspect. However, utilizing a monograph format, effort has been made to make the text understandable, so as to accommodate technical readers from various different backgrounds. This has necessitated the inclusion of some preliminary material. The purpose of the additional material is to make the text more self-contained, allowing for clearer presentation and a larger target audience, since axially moving thin materials with fluid-structure interaction are a fairly specific topic. All the preliminary material is fully optional; it is intended that the reader familiar with each topic may skip such sections.

We assume that the technical reader is familiar with at least one of the following:

1. Models of thin continua: strings, beams, panels and plates;
2. Changes to these models required by axial motion (and the difficulties this will introduce compared to classical, stationary continua); or
3. Fluid mechanics: specifically, potential flow,

but familiarity with all three is not assumed.

In the thesis, we analyze the effect of fluid-structure interaction of the moving panel with two-dimensional potential flow, representing the flow of the surrounding air. Using an exact, analytical functional solution for the pressure difference across the web, the fluid-structure interaction model is reduced to a single integro-differential equation.

This approach simplifies the analysis considerably, yet it is closer to solution from first principles than empirical added-mass models. Considering that

added-mass models are classical in this application area, also an added-mass approximation for the present model is derived. However, this is an added bonus; the main analysis is based on the original model, using the exact solution of the pressure difference in terms of the panel displacement.

The main results of the study are as follows.

Using Euler's approach for stability analysis and numerical techniques, the critical velocity of the system is obtained. The critical velocity is analyzed numerically as a function of problem parameters. This makes it possible to account for the fundamental, physical stability limit in paper machine design. The results are validated by a comparison with existing results in literature.

Direct temporal simulations of the system dynamics show the time evolution of the system, starting from a given initial condition. The spacetime behaviour is visualized, and briefly studied with respect to the web (panel) and fluid (free-stream) velocities. This provides some intuitive understanding of the system behaviour.

The complex eigenfrequencies of the system are determined, and studied parametrically as a function of the web and fluid velocities. This shows how the free vibrations of the system behave in different settings. Stability implications are briefly discussed, and it is seen that in the membrane limit, the introduction of the exact analytical aerodynamic reaction qualitatively changes the initial post-buckling behaviour of the model.

Additionally, the complex eigenfrequencies of a moving, damped string are derived analytically. This is a simpler problem in the same problem class, for which a pen-and-paper solution is feasible. The dynamic stability is analyzed. The results from the eigenfrequency analysis are graphed in the same manner as those from the main problem of interest, allowing a direct (qualitative) comparison.

For problems that must be analyzed numerically, two detailed solutions are developed for the practical issue of producing correct piecewise linear curves out of randomly ordered eigenvalue data. The effectiveness of the techniques is demonstrated by applying them to the main problem of interest.

In the present model, independent axial motion of the paper web and the free stream are allowed. The model predicts that in all cases, the surrounding air significantly decreases the natural frequencies of the moving panel; in other words, vibration of the web in air is much slower than in vacuum.

Finally, fast solvers have been implemented for the analysis. Although no formal benchmarking was made, the longest computation times for the figures displayed in this thesis were in the order of minutes on a regular desktop computer; many of the figures were computed within seconds. Especially the steady-state problem was directly solved thousands of times to produce the data for the contour plots of the critical velocity. This demonstrates that the model allows for efficient numerical solution with modest computational resources.

AUTHOR'S CONTRIBUTION

The most important scientific contribution in this study is the material contained in Chapter 6, which discusses the numerical results for the main problems of interest. All the numerics, and the relevant discussion, are by the author.

Of these, the results on the eigenfrequency spectra (subsection 6.3.3) are previously unpublished. Results on direct temporal simulations (Section 6.2) and on the lowest eigenfrequency (subsection 6.3.2) have appeared in Banichuk et al. (2011b). Of the steady-state results (Section 6.1), some have appeared in Banichuk et al. (2010b) and Kurki et al. (2011); some are previously unpublished.

The practical considerations for reliable solution and visualization of higher eigenfrequencies (Chapter 5) are original and previously unpublished. Parker (1999) has previously made some remarks in this area for some models of the same class, but did not consider the tracking problem in visualization. (The solution of complex eigenfrequencies itself is an often recurring theme in the literature; see e.g. Bolotin, 1963; Ulsoy and Mote, 1982; Renshaw and Mote, 1996; Lin, 1997; Parker, 1998; Guo and Païdoussis, 2000; Kim et al., 2003; Païdoussis, 2004; Lee and Oh, 2005; Zhou and Wang, 2007; Vaughan and Raman, 2010.)

The results on the damped moving string, Section 2.2, are previously unpublished.

The material on the moving ideal string, Section 2.1, was developed independently, but the problem has been solved using the same techniques by Swope and Ames (1963).

The steady state solution of the travelling panel in vacuum is based on a preliminaries-type section in Banichuk et al. (2010b). The applicability discussion concerning the panel model is original, by the author.

The general overviews in the Introduction are original and previously unpublished. The literature survey in Section 1.6 is an updated and expanded version of that in the introduction of the article Banichuk et al. (2011b). The original version of the survey was a combined work by the whole research team.

The analytical formula for the aerodynamic reaction, forming the core of the study and providing a starting point, was derived by professor Banichuk. It has appeared in Banichuk et al. (2010b) and Banichuk et al. (2011b) for the steady-state and dynamic cases, respectively. The derivation is reported, with some additional commentary by the author, in Section 3.4. The slip boundary condition, required for the flow problem, was verified in detail by the author.

The detailed properties of the aerodynamic integration kernel (Section 3.5), and the convergence argument (Appendix 1), are by the author. The added mass approximation (Section 3.6) is also original, by the author; it has partly appeared in Banichuk et al. (2011b), but some of the material is previously unpublished.

The problem setup and discretization in Chapter 4 is based on the articles Banichuk et al. (2010b) and Banichuk et al. (2011b), but the presentation has been fully reworked by the author. The original versions were a combined work.

ACKNOWLEDGEMENTS

This research was supported by the MASI Tekes Technology Programme and the Ellen and Artturi Nyyssönen Foundation (EANS).

Picture sources

Figures 1 and 6–76 are original, by the author. Earlier versions of Figures 24–26 have appeared in the articles Banichuk et al. (2010b, 2011b). The dynamical solution and lowest eigenfrequency plots have appeared in Banichuk et al. (2011b).

Figure 2 is a public domain image originally uploaded to Flickr's The Commons. License checked, and picture obtained, from
`http://en.wikipedia.org/wiki/File:Papermaking_machine_at_a_paper_mill_near_Pensacola.jpg`

Figure 3 courtesy of T. Saksa.

Figure 4 is a freely licensed image by Richard Wheeler. The license is Creative Commons Attribution-Share Alike 3.0 Unported. License checked, and picture obtained, from
`http://en.wikipedia.org/wiki/File:PaperAutofluorescence.jpg`

Figure 5 (both images) courtesy of M. Kurki.

Thanks

The author would like to thank the following people, in no particular order:

Pekka Neittaanmäki for organizing an effective team and environment.
Nikolay Banichuk for starting the research, and for lending his expertise.
Tero Tuovinen for extensive literature searches over the last few years.
Matti Kurki for engineering knowledge and an industry viewpoint.
Raino Mäkinen for lecturing very informative courses.
Sergey Repin for asking the right difficult questions.
Matti Nurmia for checking the English.
Tuomo Ojala for discussions related to the free-vibration solutions.

Antti Huhtala at Aalto University for the initial suggestion to try a MAC based approach to eigenfrequency tracking.

Olli Mali for mathematical assistance, and for numerous discussions over the last few years that have been both enlightening and fun.

Tytti Saksa for keen analytical insight, making a few pinpoint observations that have improved the work, and for finding some very useful literature.

And of course,

my fiancée Anne Kainulainen for her patience and support during the writing process, and

my parents Eila and Seppo for support in matters both scientific and personal.

NOMENCLATURE

The traditional, hopefully reasonably complete listing of symbols used follows. Symbols are listed alphabetically, Latin first, then Greek. The ordering is case insensitive, but symbols with subscripts appear after symbols with no subscripts.

In case of symbols that are defined with reference to other symbols, the note *(p. xx)* shows on which page the definition can be found. For physical quantities, the dimensions are given in standard SI units, like [unit: m]; the special label [dimensionless] denotes dimensionless physical quantities.

There has been an effort to avoid using the same symbol for more than one purpose, but in a text of this length some degree of namespace conflict is unfortunately unavoidable.

In addition to the symbols listed here, some symbols are used with a very short scope of definition. Since these are only needed very near to where they are defined in the text, they have been left out of this list.

For meta-conventions used, see the separate section on notation, included at the end of this list.

Latin symbols

a, b, c: coefficients (see context); in discussion of free-vibration solutions, coefficients of original second-order terms in corresponding PDE (p. 58)

$a(\xi, x)$: integrand in aerodynamic matrix a_{jn} (in discussion on aerodynamic matrices, p. 238)

A_1, A_2, B: in discussion on damped string, coefficients in original PDE (p. 68)

$A_{jn}, B_{jn}, C_{jn}, D_{jn}$: in discrete form, matrices related to vacuum terms (p. 133)

a_{jn}, b_{jn}, c_{jn}: in discrete form, matrices related to fluid terms (p. 133)

C: in discussion on axially moving string, critical velocity $C \equiv \sqrt{T/m}$

D: bending rigidity of panel (p. 92). Also known as *cylindrical rigidity*.

E: Young modulus (stretching/compression resistance) of an elastic object. Used in the definition of bending rigidity (p. 92). [unit: Pa $\equiv$ N/m^2]

$f(x), g(x), h(x)$: functions (see context)

g: external or gravitational loading experienced by the panel, $g = g(x,t)$. [unit: Pa $\equiv$ N/m^2]

g': external loading as function of nondimensional coordinates, $g' = g'(x',t')$. The function g' is defined by the relation $g'(x',t') \equiv g(x,t)$, where the nondimensional point (x',t') corresponds to the dimensional point (x,t). As the only exception to the prime notation, this is not a nondimensional quantity; g' has the dimension of the original g. (p. 129) [unit: Pa $\equiv$ N/m^2]

g'': dimensionless external loading (p. 129). The double-prime is used to distinguish this quantity from g'.

$\mathcal{G}$: abstract external load function (eq. (143), p. 127; compare the form of (143) to eqs. (146), (150) and (154))

h: thickness of the panel [unit: m]

k, j, n: indices (see context; note: i is avoided in indices when possible)

ℓ: span length or half-length (see from relevant boundary conditions in each context) [unit: m]

m: area mass (*grammage*) of panel [unit: $\mathrm{kg/m^2}$]

$\mathbf{n}$: local unit normal vector of panel surface, $\mathbf{n} = (n_x, n_z)$

$N(\xi, x)$: aerodynamic kernel (Green's function of airflow problem; p. 113)

p: in discussion on stability, any problem parameter of interest; in airflow problem, fluid pressure

p_2: in discussion on damped string, second-degree polynomial

p_4: in discussion on damped string, fourth-degree polynomial

q_f: aerodynamic reaction pressure experienced by the panel [unit: $\mathrm{Pa} \equiv \mathrm{N/m^2}$]

s: in discussion of free-vibration solutions, stability exponent (*complex eigenfrequency*, defined in discussion p. 47 ff.); in discrete problem, arbitrary scaling factor (p. 131)

s_*: in discussion of free-vibration solutions, stability exponent, as expressed specifically in the (x, t) coordinate system (in contrast to the transformed (ξ, η) coordinate system). This symbol is used only when both coordinate systems are referred to in the same discussion.

S: in airflow problem, the surface of the panel or other object placed in the flow (p. 108 ff.). Refer to Figure 28, p. 109. In discussion on convergence of aerodynamic integrals, line segment (p. 233 ff.). Refer to Figure 75, p. 234.

t: time coordinate [unit: s]

t': nondimensional t. Usually the prime is omitted. (p. 58)

T: axial tension of panel, $T \equiv \sigma h$ (p. 55) [unit: N/m]

u: in discussion on damped string, auxiliary function for w (eq. (44), p. 70); elsewhere, longitudinal (axial) displacement of the panel [unit: m]

$\mathbf{U}$: panel displacement field, $\mathbf{U} \equiv (u, w)$. (p. 104 ff.)

V_0: axial velocity of panel [unit: m/s]

v_∞: free-stream axial velocity of surrounding air [unit: m/s]

$\mathbf{v}_f$: fluid velocity field (p. 103 ff.)

w: transverse (out-of-plane) displacement of the panel or string [unit: m]. Refer to Figures 25 (panel, dynamic case, p. 101), 26 (panel, steady state, p. 102), 22 (panel, in vacuum, p. 93) and 8 (string, p. 56). See also w'.

w': nondimensional transverse displacement of the panel. Note: usually the prime is omitted. (p. 58)

W: in the time-harmonic trial, complex-valued space component of solution. The relation is $w(x, t) = \exp(st)W(x)$ (p. 47). In aerodynamic problem, auxiliary function $W(\eta)$ (complex velocity potential; p. 111).

x: axial space coordinate in Euler or *laboratory* system [unit: m]

x': nondimensional x. Usually the prime is omitted. (p. 58)

z: transverse space coordinate (unless otherwise noted) [unit: m]

Greek symbols

α: nondimensional dynamic time scale parameter in dynamic problem (p. 126); in other contexts, angle as indicated in the relevant figure (p. 62, 94, 104, 150)

β: nondimensional bending rigidity (p. 126); in discussion of moving ideal string, amplitude coefficient (p. 63); in discussion on moving damped string, helper coefficient for shorter notation (p. 69); in other contexts, angle (when two are needed in the same discussion; p. 150)

γ: nondimensional fluid density (p. 126); in discussion on moving damped string, helper coefficient for shorter notation (p. 70)

α, β, γ: in other contexts, coefficients (see context)

ε: small positive real number; $\varepsilon > 0$

ζ: auxiliary coordinate (see context)

η: in airflow problem, complex number $\eta = x + zi$ (p. 108); in discussion of free vibrations of moving string, generalized time coordinate (p. 61); otherwise, auxiliary coordinate (see context)

θ: nondimensional axial free-stream velocity of fluid (p. 126). In some of the steady-state problems (Section 6.1), the fluid velocity is an eigenvalue (eqs. (184) and (186), p. 157 ff.). In temporal simulations (Section 6.2) and in eigenfrequency considerations (Section 6.3), it is a parameter.

$\varkappa$: in discussion on moving damped string, helper coefficient for shorter notation (p. 69); in the abstract generalized eigenvalue problem, scalar eigenvalue (p. 158)

λ: in all main problems, nondimensional axial velocity of panel (p. 126). In the steady-state problems (Section 6.1), for cases where the panel moves, the velocity is an eigenvalue (eqs. (181) and (182), p. 156 ff.). In temporal simulations (Section 6.2) and in eigenfrequency considerations (Section 6.3), it is a parameter. In discussion of vacuum solution of moving panel, λ denotes the eigenvalue of the auxiliary problem (p. 95).

$\Lambda(\xi, x)$: helper function for definition of aerodynamic kernel (p. 113)

ν: Poisson's ratio (i.e., coefficient for how much an isotropic elastic object shrinks in the transverse direction when it is stretched by a given amount in the axial direction). Used in the definition of bending rigidity (p. 92). [dimensionless]

ξ: axial space coordinate in Lagrange or *co-moving* system (p. 55 ff.; pp. 105–107) [unit: m]; in airflow problem, dummy variable for integration (p. 111 ff.) [dimensionless]; in discussion of free vibrations of moving string, generalized space coordinate (p. 61) [dimensionless]

ρ_f: density of surrounding fluid (air) [unit: $\mathrm{kg/m^3}$]

σ: axial stress [unit: $\mathrm{Pa} \equiv \mathrm{N/m^2}$]

τ: characteristic time (arbitrary normalization constant; p. 58) [unit: s]

ϕ_k: Galerkin basis function k, piecewise linear basis (p. 137); in least-squares fitting, basis function k (p. 122, 185)

Φ: in aerodynamic problem, fluid velocity potential (p. 102)

φ: in aerodynamic problem, fluid velocity disturbance potential (p. 102)
ψ: in discussion of steady state of travelling panel, auxiliary function (p. 95)
Ψ: in aerodynamic problem, stream function (p. 111)
Ψ_k: Galerkin basis function k, sine basis (p. 131)
χ: in aerodynamic problem, auxiliary function (p. 111)
ω: in discussion of free-vibration solutions, wavenumber-like parameter for boundary condition fitting (p. 63, eq. (29) for both the string and the damped string)
Ω: space domain (see context; for our problems, it is either the interval $[0, 1]$, or the interval $[-1, 1]$)

Notation

$\partial/\partial\cdot$: partial (local) derivative with respect to variable $\cdot$
$\mathrm{d}/\mathrm{d}t$: material (*convective*, *total*, *Lagrange*) derivative; only used w.r.t. time t.
w_x, w_ξ, w_t: notation for derivatives; $w_x \equiv \partial w/\partial x$, $w_\xi \equiv \partial w/\partial \xi$, $w_t \equiv \partial w/\partial t$
$\mathcal{L}$: linear differential operator; linear integro-differential operator
$\mathcal{K}$: linear integro-differential operator (when more than one is needed in the same discussion)
i: imaginary unit, $i \equiv \sqrt{-1}$ (note: i is avoided in indices when possible)
$\overline{z}$: complex conjugate of z. For $z = a + bi$ (where $a, b \in \mathbb{R}$), $\overline{z} = a - bi$. (Mainly used in Chapter 5.)
$\mathrm{Re}\,\cdot$: real part of complex-valued quantity $\cdot$
$\mathrm{Im}\,\cdot$: imaginary part of complex-valued quantity $\cdot$
$\|\cdot\|$: norm of $\cdot$ (which norm, see from context)
$\|\cdot\|_{L^\infty}$: the L^∞ norm of $\cdot$ (and similarly for other explicitly designated norms)
$|\cdot|$: absolute value of $\cdot$
$f^\pm$: limit for any function $f(x, z, t)$ at $z \to 0^\pm$. Defined as $f^\pm(x, t) \equiv \lim_{z \to 0^\pm} f(x, z, t)$. (Not to be confused with the functions named $f^\pm$ in subsection 2.2.4, only used within that subsection.)
$f(x, z; \alpha, \beta)$: function of *variables* x and z, with *parameters* α and β. (Note the semicolon.)
$x \mapsto y$: "x maps to y"; used for function definitions having a short scope.
a': nondimensional version of quantity a. Note: usually the prime is omitted, since most algebraic manipulation in the present work is performed in the nondimensional form.
$()^T$: transpose of a matrix
$()^H$: Hermitian conjugate of a matrix

LIST OF FIGURES

LIST OF TABLES

LIST OF ALGORITHMS

CONTENTS

1 INTRODUCTION

This work draws elements from the branch of physics known as continuum mechanics, often nowadays seen as belonging to the engineering sciences, and from the field of scientific computing, which contains areas such as mathematical modelling of physical phenomena, numerical solution of partial differential equations (PDEs), simulation, mathematical optimization and uncertainty analysis.

The structure and context of the study, for readers familiar with solid and fluid mechanics, is depicted in Figure 1. For readers wishing to know more, the concepts in the Figure will be explained during the Introduction.

We will first motivate the study and mention the main results in Section 1.1. In Sections 1.2–1.4, we will give a short general introduction into models of thin continua, axial motion, and fluid models (and fluid-structure interaction). Section 1.5 briefly discusses elastic stability on a general level, and explains how it will be investigated in the present study (we will use the time-harmonic trial function approach).

The reader comfortable with all the required background may skip directly to the end of the Introduction, Section 1.6, where we provide a look at the literature of axially moving materials in connection with fluid-structure interaction.

1.1 Motivation and main results

The motivation of the present study comes from paper production, which is an important segment of industry in Finland. In a paper machine, the paper that is being manufactured travels in the machine as a thin sheet (see Figure 2, and the schematic side view in Figure 3). Viewed close up, this *paper web* (as it is called) is made of a web of fibers (see Figure 4), but at the macroscopic scale it appears as a uniform sheet; hence, continuum models are used. The sheet is very thin (see Figure 5); typical thicknesses vary from 0.1 mm (office paper) to 1 mm (cardboard).

All paper machines contain *open draws*, where the paper web momentar-

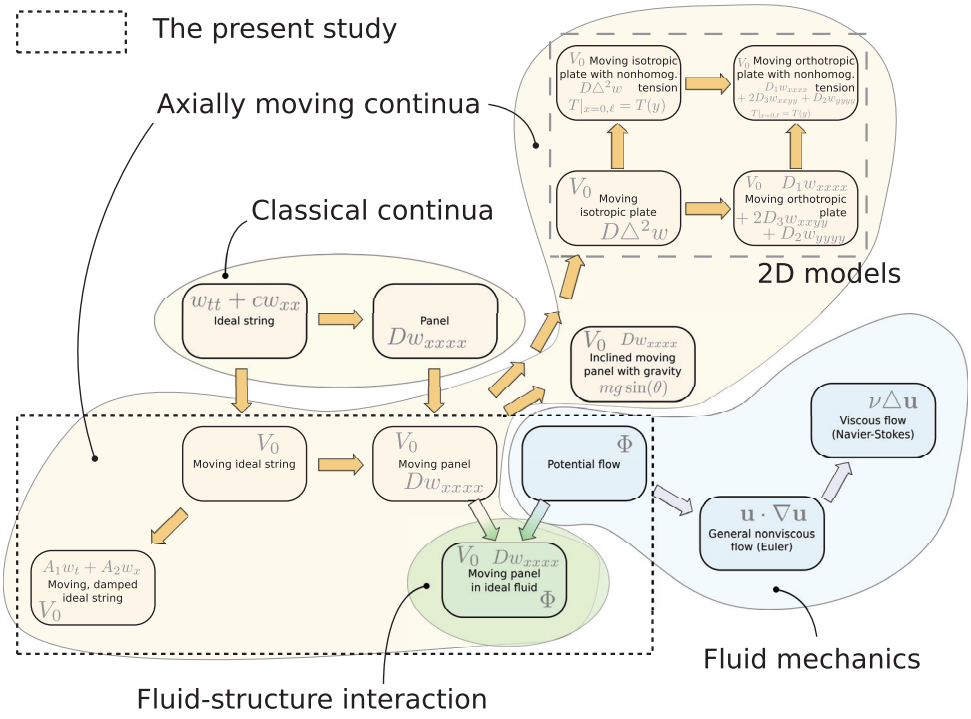

FIGURE 1 Structure and context of the present study.

ily travels without mechanical support, while it is moving from one supporting roller to another. In any practical paper machine there is always at least one open draw, in the transfer from the press nip (which squeezes out most of the water) to the dryer section. Also, if the dryer section is of the classical heated cylinder type, which has been used for over a century (see Figure 2), an open draw exists between each successive pair of cylinders (Karlsson, 2000).

When a thin sheet of material travels without mechanical support, it is subject to destabilizing effects such as the centrifugal effect (due to inertia of the axially moving material particles), and aerodynamic reaction forces (due to the surrounding air). *Aerodynamic reaction*[1] is a technical term that refers to how the surrounding fluid "pushes back", as its motion is disturbed by the vibration of the material sheet.

The interaction between the travelling material and the surrounding air is found to be especially important for applications in paper production, where the material itself is lightweight. Including this *fluid-structure interaction* (FSI) into the

[1] Originally, the term *aerodynamic* has referred specifically to interaction with air, and *hydrodynamic* specifically with water. However, flows of fluids of both kinds – gases and liquids – share many similarities, and as a result the same theories can often be used for both. Hence, the terms *aerodynamic* and *hydrodynamic* are sometimes used interchangeably, with some researchers preferring the other and some the other. In this work, we will use the term *aerodynamic*.

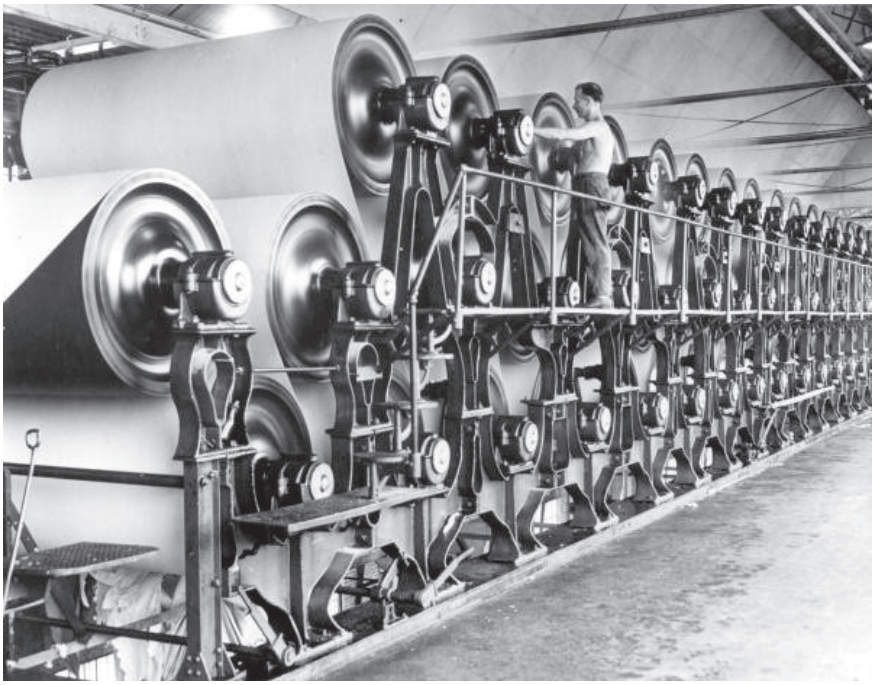

FIGURE 2 Dryer section of a paper machine. This is an old photo, in which the open draws can be seen. In modern machines, the dryer section is covered by a metallic hood.

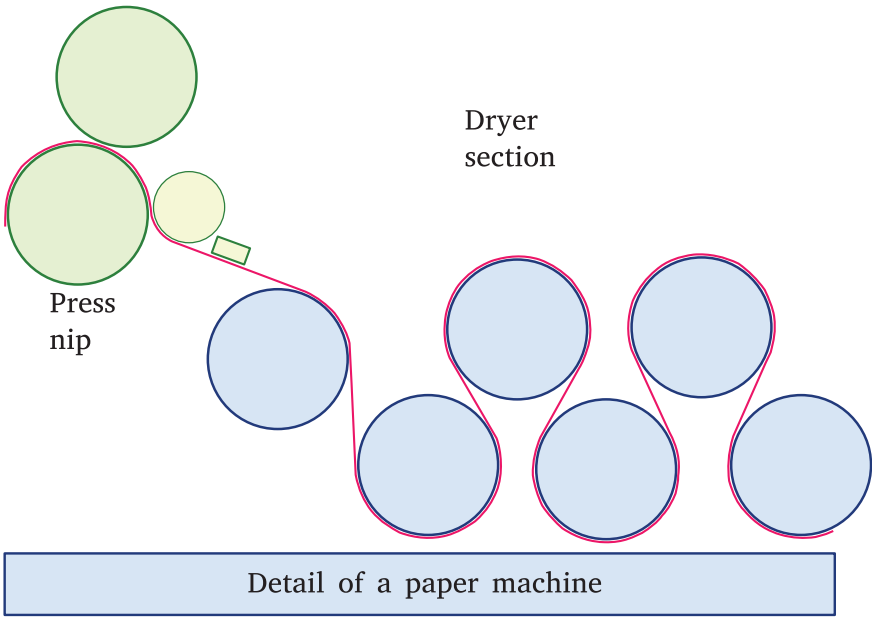

FIGURE 3 Start of the dryer section of a paper machine. Schematic diagram.

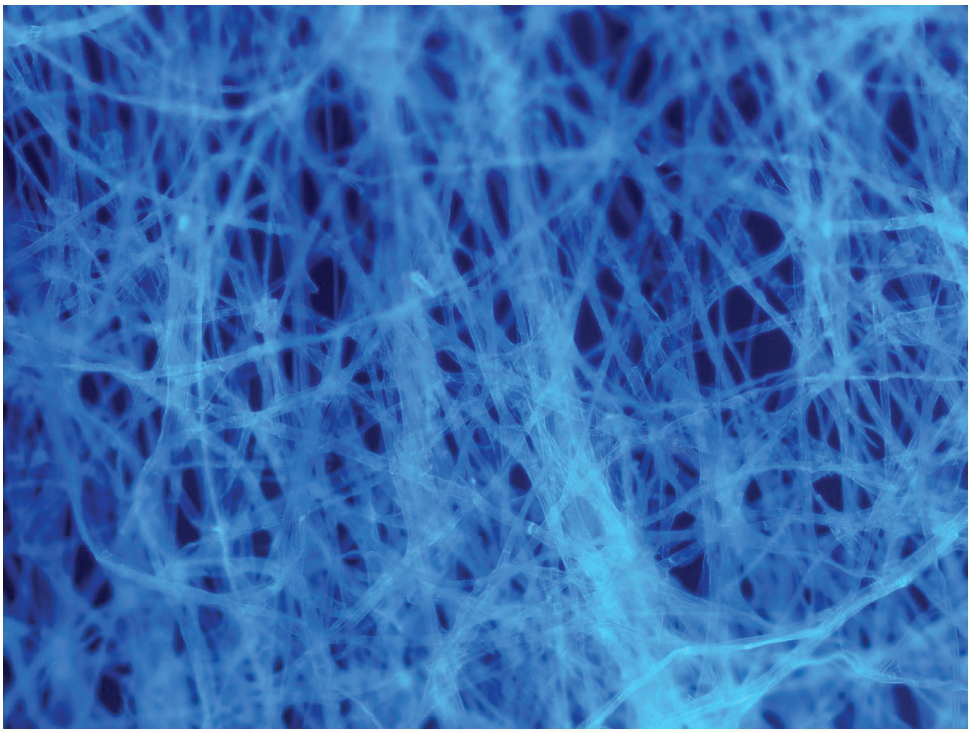

FIGURE 4 Microscopic structure of paper. The individual fibers are 10 μm in diameter.

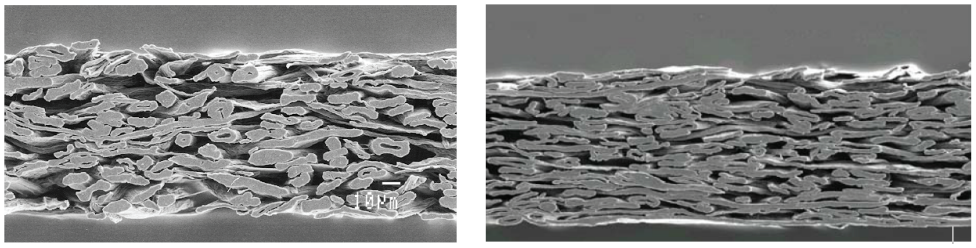

FIGURE 5 Microscopic structure of paper, viewed across the web thickness. Electron microscope images of copy paper made of eucalyptus. *Left*: result of light wet pressing. *Right*: result of heavy wet pressing. On the left, the total thickness of the web is about 100 μm (= 0.1 mm).

model forms a coupled, *multiphysical*[2] model: it is not sufficient to consider only the dynamics of the travelling material, but the behaviour of the surrounding airflow must be analyzed, too, and its effects on the material fed back into the first part of the model. This coupling changes the dynamics, which, in turn, affects the surrounding flow.

Now, if the moving material loses stability, the most likely result (in the case of brittle materials such as paper) is that it will break apart, interrupting the production process. Such interruptions in paper factories are costly; hence, avoiding web breaks becomes an important practical question in the design of paper machines. This design, in turn, must take into account the limits created by the fundamental physics of the situation. Thus, fundamental stability limits must be analyzed.

This is where the present study comes in. It is a basic research type study, concerning the effect of surrounding ideal fluid on the stability and dynamics of an axially travelling panel. These theoretical models are used to represent the surrounding air and the moving paper web, respectively. We will clarify in subsection 1.4.1 what we mean by *ideal fluid*; for readers already familiar with modelling of fluid flows, *potential flow* is the appropriate short label (as shown in Figure 1).

In this context, the term *panel* refers to a thin sheet, for which it is assumed that there is no variation in the displacement profile in the width direction (see, e.g., Bisplinghoff and Ashley, 1962, keyword *flat panel*). It shares mathematical similarities with the classical Euler–Bernoulli beam model, although the physical interpretations are different (see the comparison at end of subsection 1.2.1).

Typical applications for the family of models of axially travelling continua are band saws, tape drives (Ulsoy and Mote, 1980), computer hard drives and optical drives (Hosaka and Crandall, 1992; reviewed in Païdoussis, 2004), and indeed the production of thin sheets of continuous material such as steel, paper or textiles (Vaughan and Raman, 2010). Sometimes more exotic applications for moving materials are suggested; for example, in 1914, D. P. Riabouchinsky investigated the use of an axially moving surface in an airfoil to delay flow separation, thereby achieving higher lift (Tokaty, 1994, p. 176, and plate 16).

Stability analysis comes with a long tradition. The steady-state stability of parabolic shapes partially immersed in a homogeneous medium was analyzed in the two-part book *On Floating Bodies* by Archimedes of Syracuse. This book, originally dating from the 3rd century BCE, can be thought of as the oldest surviving work on stability analysis; its probable application was shipbuilding (Russo, 2004). A fluid-structure interaction problem!

The present form of static stability analysis that will be applied in this work, originally developed for a differential equation describing the bending of a beam, was introduced by Euler (1766). The dynamic stability analysis for linear elastic systems, which extends Euler's method, is due to Bolotin (1963). According to

[2] The term *multiphysical* refers to any situation where models from different branches of physics must be combined or connected together for a full analysis. *Fluid-structure interaction* (FSI) is a multiphysical discipline.

Mote and Wickert (1991), the instability behaviour of some axially moving materials is mathematically analogous to the buckling of a compressed column, enabling the use of these techniques.

To sum up, the main topic of interest in this work is the fluid-structure interaction of a moving web with two-dimensional potential flow, representing the flow of the surrounding air.

Using an exact, analytical functional solution for the pressure difference across the web, the fluid-structure interaction model is reduced to a single integro-differential equation. This approach simplifies the analysis considerably, yet is closer to solution from first principles than empirical added-mass models. Considering that added-mass models are classical in this application area, also an added-mass approximation for the present model is derived. However, this is an added bonus; the main analysis is based on the original model, using the exact solution of the pressure difference with no added-mass approximation.

The main results of the study are as follows.

Using Euler's approach for stability analysis and numerical techniques, the critical velocity of the system is obtained. The critical velocity is analyzed numerically as a function of problem parameters. This makes it possible to account for the fundamental, physical stability limit in paper machine design. The results are validated by a comparison with existing results in literature.

Direct temporal simulations of the system dynamics show the time evolution of the system, starting from a given initial condition. The spacetime behaviour is visualized, and briefly studied with respect to the web (panel) and fluid (free-stream) velocities. This provides some intuitive understanding of the system behaviour.

The complex eigenfrequencies of the system are determined, and studied parametrically as a function of the web and fluid velocities. This shows how the free vibrations of the system behave in different settings. Stability implications are briefly discussed, and it is seen that in the membrane limit, the introduction of the exact analytical aerodynamic reaction qualitatively changes the initial post-buckling behaviour of the model.

Additionally, the complex eigenfrequencies of a moving, damped string are derived analytically. This is a simpler problem in the same problem class[3], for which a short, closed-form solution is possible. The dynamic stability is analyzed. The results from the eigenfrequency analysis are graphed (subsection 2.2.5) in the same manner as those from the main problem of interest (subsection 6.3.3), allowing a direct (qualitative) comparison.

For problems that must be analyzed numerically, two detailed solutions are developed for the practical issue of producing correct piecewise linear curves out of randomly ordered eigenvalue data (Chapter 5). The effectiveness of the techniques is demonstrated by applying them to the main problem of interest.

In the present model, independent axial motion of the paper web and the free stream are allowed. The model predicts in all cases that the surrounding air

[3] Albeit with an important difference that should be mentioned. The damped problem does not conserve energy, while the main problem of interest does.

significantly decreases the natural frequencies of the moving panel (subsection 6.3.2). This agrees with existing literature, such as Pramila (1986), Frondelius et al. (2006) and Kulachenko et al. (2007b).

Finally, the model and the chosen numerical methods allow for fast solvers, which have been implemented. Although no formal benchmarking was made, the longest computation times for the figures displayed in this thesis were in the order of minutes on a regular desktop computer; many of the figures were computed within seconds. Especially the steady-state problem was directly solved thousands of times to produce the data for the contour plots of the critical velocity. This demonstrates that the model allows for efficient numerical solution with modest computational resources.

Now, it is time to go into a more detailed introduction. In the following sections, we will give a short general introduction into models of thin continua, axial motion, fluid models (with fluid-structure interaction), and elastic stability. Readers familiar with the background may want to skip forward to the literature survey in Section 1.6 (p. 50).

1.2 Material models

Material modelling can be roughly divided into three categories, depending on the physical scale of the problem. Microscale models are concerned with the detailed behaviour of the microstructure. Macroscale models consider the large-scale behaviour. Mesoscale models fall between these two extremes. Multiscale models combine several of these.

The present thesis is a classical macroscale study. It is well-known that materials with different microstructures behave very differently on a macroscopic level. The usual way, also followed here, of taking the microstructure into account in macroscale models is homogenization. That is, the material is assumed homogeneous when viewed at a sufficiently large scale. A well-known example comes from the physics of viscous flow through porous media, where this approach was pioneered by Darcy (1856) and later Whitaker (1969).

Homogenization leads to effective material constants for each particular material in the considered class. These are usually measured (e.g. Bonnin et al., 2000; Seo, 1999; and Mann et al., 1980), or derived mathematically. The latter can be done either by analytical considerations, or numerically by simulation. For some examples of the analytical approach, see e.g. Yokoyama and Nakai (2007) for elastic constants, and Whitaker (1969, 1986a,b) for flow in porous media. Quintard and Whitaker (1994a,b,c,d,e) provide an example of simulation of flow in porous media using computer-generated microstructures for validation.

1.2.1 Models of thin sheets of stationary continua

Before discussing moving materials, let us first review the common macroscale models for thin sheets of classical, stationary materials. The changes needed to account for global axial motion will be explained in Section 1.3.

On a macroscopic scale, there are two main kinds of variation in material properties: location-dependent and orientation-dependent. If there is location-dependent variation, the material is said to be *nonhomogeneous*. If there is no such variation, the material is *homogeneous*. This is what homogenization aims at: the material is assumed to be same everywhere on average, when viewed at a sufficiently large scale.

The second kind of variation depends on the orientation of a coordinate system with the origin placed at a fixed point inside the material. If there is no variation regardless of which directions the axes point to, the material is said to be *isotropic*. If there is directional variation, the general term used to describe such materials is *anisotropic.* Like the term "nonlinear", this tells very little of the specific properties.

Concerning paper materials, a particularly relevant specific class of anisotropicity is *orthotropicity*, which is briefly introduced below. Also, from a paper science viewpoint, it makes sense to concentrate on the family of models for thin sheets of continuous material. Before concentrating on the particular, simple model that will be used in this study, let us have a qualitative look into the general class of models.

A very useful, general constant-coefficient model is the *orthotropic* thin plate. In this model, the material is *orthogonally anisotropic* (Huber, 1926). This model was pioneered by M. T. Huber for steel-reinforced concrete (Huber, 1914, 1923, 1926), but it works well also for paper materials. This is because paper has a fiber structure with the fibers mostly aligned in one direction (see, e.g., the comprehensive review Alava and Niskanen, 2006), which is geometrically similar to steel-reinforced concrete. The alignment of the fibers causes the mechanical properties to differ in the along-fiber and cross-fiber directions.

In the basic form of this model, the material axes are aligned with the problem axes. This is not an intrinsic limitation, however; it is possible to derive a transformation to obtain the effective material constants at an arbitrary angle of orientation between the material and problem axes. (See e.g. Reddy, 2009, or books by the same author.)

A further generalization of the orthotropic model is *laminate theory*, in which a stack of arbitrarily oriented layers of thin orthotropic material, together making up a thin *laminate*, is modelled as a single entity (Reddy, 2009). For a history of and references on laminate theory, a good starting point is the extensive review article Piskunov and Rasskazov (2002), which discusses about 180 sources on the topic.

A simpler model is that of the *isotropic* plate, in which the material parameters are independent of coordinate system orientation. It is more appropriate for simple materials such as steel, than for paper, but it is occasionally used as a

simplified model also in the paper context.

Note that in the orthotropic model, by taking the in-plane shear modulus G_{12} as a geometric average based on the properties in the material directions 1 and 2, the orthotropic, linear out-of-plane bending theory can be reduced to the isotropic one. For details, see the classic book Timoshenko and Woinowsky-Krieger (1959, p. 365 onward). The same transformation works also for moving materials (see note in Banichuk et al., 2011a). The geometric average for G_{12} is sometimes called the *Huber value*, after M. T. Huber. If this assumption is not made, then we have the general orthotropic theory.

Another classification in this category of models is that of membranes versus plates. A *membrane* has no bending rigidity; it can only support tensile loads tangent to the membrane edge.[4] It is the two-dimensional analog of an ideal string. The partial differential equation describing the out-of-plane dynamics of a membrane is of the second order both in space and in time.

Plates are defined as having bending ridigity; they resist bending out of the rest plane. A *thin plate* is one where the thickness is much smaller than the other two dimensions. Its dynamical equation is of the fourth order in space and second in time, the bending resistance adding the fourth-order term. A *thick plate* has no restriction on the thickness.

Thin plates and membranes allow reducing the three-dimensional elastic problem into two dimensions. Many studies concentrate on these two classes only.

As plates and membranes are not the topic of the present thesis, we will not go into the details. For a classic introduction into and reference about plates (and shells), see the book by Timoshenko and Woinowsky-Krieger (1959). For membrane theory, see e.g. the books by Weinstock (2008) or Sagan (1961). For the history of plates and membranes, see the book by Ventsel and Krauthammer (2001) or the historical summary in the Ph. D. thesis by Ruggiero (2005, ch. 4). For studies by our group into the isotropic and orthotropic cases (neglecting fluid-structure interaction), see Banichuk et al. (2010a, 2011a).

If the displacement is *cylindrical*, i.e., effectively one-dimensional with no variation across the width of the material sheet (Timoshenko and Woinowsky-Krieger, 1959), the models of the thin plate and the membrane simplify to the *panel* (Bisplinghoff and Ashley, 1962, keyword *flat panel*) and the *string*, respectively. (The corresponding axially moving cases are illustrated in our Figures 24 (p. 101), 25 and 8 (p. 56).) The panel model is most commonly encountered in aerodynamics, where it is used to model *aerofoils*, i.e. cross sections of an aeroplane wing. See e.g. the books by Bisplinghoff and Ashley (1962), Ashley and Landahl (1985), and Anderson (1985).

In other contexts, the *beam model* is more common. The classical Euler–Bernoulli beam model shares most of its mathematical form with the panel model, but it should be kept in mind that their interpretations are wholly different. As was explained above, the panel is a thin sheet that is undergoing cylindrical deformation. The beam model describes a stringlike object with bending resistance

[4] In other words, a membrane resists stretching, but not bending.

rather than a thin, wide sheet. A beam may bend three-dimensionally, while a panel cannot. The displacement of a panel may be divided into in-plane and out-of-plane, while a beam has two independent axes which allow for bending behaviour that is similar to the out-of-plane bending of a panel. (This is in addition to the longitudinal displacement, which is common to both models.) Furthermore, it makes sense to study torsional bending for beams, while for panels any torsion would break the cylindrical displacement assumption. For thin sheets, plate models are the usual way for analyzing width-dependent bending behaviour.

1.2.2 Viscoelasticity

All the models discussed above are designed for a purely *elastic* material. The deformation of an elastic material depends only on the applied forces; it has no explicit time dependence. The simplest example is a one-dimensional spring, where the restoring force depends only on the distance from the rest length. Elastic deformation is fully reversible. The material reassumes its original shape perfectly if the external load is removed sufficiently slowly (technically speaking, *quasistatically*). Note, however, that if the load is removed suddenly, linear elastic systems will vibrate in a time-harmonic manner.[5]

Paper, however, is more complicated as a material. It is *viscoelastic*. This means that in addition to elastic properties, it has also viscous properties, which cause the phenomena of creep and relaxation (see, e.g., Alava and Niskanen, 2006). As examples of familiar materials where these phenomena can be readily observed are chewing gum and jello. The simplest model for viscoelastic material is the Kelvin–Voigt model, which consists of a linear spring and a dashpot (damper) connected in parallel.

Creep refers to the phenomenon of time-dependent, growing deformation even for a constant external force, and *relaxation* to the phenomenon where the internal stress decreases in a time-dependent way if the deformation is kept constant. In a viscoelastic material, there is thus an explicitly time-dependent component in the internal reaction forces. As far as paper production is concerned, this effect is most significant in the so-called wet end of the paper machine. As the web dries, the material becomes more purely elastic.

In this thesis, we concentrate on the dry end of the production process, and consider paper as a purely elastic material only. As the viscoelasticity, which introduces damping into the system, is ignored, the real system is approximated with a conservative one. This is not expected to change e.g. the critical velocity, but it does modify the postdivergence behaviour (Ulsoy and Mote, 1982), and the dynamic response.

---

[5] For example, consider the transverse deflection of a beam, which is initially under a transverse load, which is then suddenly removed. A correct mathematical setup for describing the resulting dynamic behaviour is an *unloaded* initial-boundary value problem, with the initial conditions set to the position and transverse velocity that the beam had at the instant of time when the load ceased to affect it. This leads to time-harmonic vibrations.

1.3 Axial motion

The field of study of axially moving materials differs from classical continuum mechanics due to the axial motion. Although the coordinate transformation for constant-velocity axial motion is one of the simplest possible, it nevertheless reflects an important qualitative change in the physics of the situation, and has important consequences for the mathematical behaviour of the models. Mathematically, it even changes the inner-product space that is the natural choice for the problem (for a Hamiltonian mechanics viewpoint related to this, see Wang et al., 2005).

One must account for the motion of the material, either by the introduction of moving boundaries in the local (Lagrange) coordinate system, or by viewing the situation in the laboratory (Euler) coordinate system in which the material itself is in axial motion. See, e.g., Archibald and Emslie (1958); Chang et al. (1991) for articles utilizing both approaches. Also worth a mention are Mujumdar and Douglas (1976), which starts in the Lagrange system, and then immediately transforms to the Euler system; and Miranker (1960), which starts in the Euler system, and transforms into the Lagrange system.

Note, especially, that due to the motion of the material with respect to the boundaries, the physical situation with moving materials is different from that of e.g. an airfoil, where it is possible to fix the coordinate system to the moving object and perform the analysis there.

The Euler approach, like in flow physics, is the standard one for handling moving materials. We will follow it also in this thesis. Any local (Lagrange) acceleration experienced by a material point thus leads — via the material derivative — to Coriolis and centrifugal effects in the laboratory coordinates. This makes the system gyroscopic, and e.g. the eigenforms of a travelling string acquire a space- and velocity-dependent phase shift, unlike those of the stationary string (see e.g. Wickert and Mote, 1990). In general, this makes the equations difficult to solve, and except for very particular special cases (e.g., Simpson, 1973 for the moving, non-tensioned string), no analytical solutions are known (or probably even possible) for the fourth-order PDE models describing systems that have nonzero bending rigidity.

In the present work, we study the case with the moving web modelled as an axially moving panel, surrounded by two-dimensional fluid flow. The applicability of this model to physical situations will be discussed later, in subsection 2.3.4.

The ideal string model will be introduced as a classical reference case. Its free vibrations can be solved analytically, so it provides a good reference point for eigenfrequency studies. For a panel with a small bending rigidity, it is possible to use singular perturbation theory to solve the approximate eigenfrequencies. Kong and Parker (2004) have done this; their solution is provided in subsection 2.3.3. (Note here the mathematical identity between the relevant parts of the panel and beam models.)

Finally, before we move on to fluid models, it should be noted that all of the models discussed above are often used with constant coefficients only. It is possible to consider more complex situations with variable coefficients. For example, the axial tension at the rollers supporting the paper varies in the machine width direction, and this is often neglected. For a preliminary study, see the report Banichuk et al. (2010c). In this study, we will limit our considerations to a constant-coefficient model.

1.4 Fluid models and FSI

On the macroscale, fluids are modelled by continuum models. In this section we will review the most important fundamental fluid models, including some of their properties and history, and mention some methods used for solving them.

We will then look into how the fluid models are coupled into material models for fluid-structure interaction (FSI).

1.4.1 Fluid models

Theoretical fluid statics dates back to Archimedes (recall his work *On Floating Bodies*), but fluid mechanics in its modern form, described by differential equations, was founded by Leonhard Euler in the 18th century, with his introduction of the concept of the fluid particle. The particle was assumed to be small enough to be described mathematically by a continuum model, but large enough to possess physical quantities such as volume, mass, density and inertia. (Tokaty, 1994, pp. 73–74; see also Lighthill, 1986, p. 15)

Euler's results are nowadays commonly called the *Euler model* of fluid mechanics: a set of nonlinear differential equations describing the motion of incompressible, nonviscous (i.e. frictionless) fluids. The book Lighthill (1986) is a clearly written technical, but informal, introduction into the topic.

Compressibility refers to the physical phenomenon where changes in the pressure field within the fluid cause changes in local fluid density. Water can be considered incompressible (e.g. Lighthill, 1986). The degree of compressibility of air depends on the mach number of the flow. Up to 0.1 . . . 0.3M (recommendations differ in different sources), air can be considered incompressible. See e.g. Ashley and Landahl, 1985; and Lighthill, 1986, p. 15. The book by Anderson, 1985, p. 328–329, provides a formula and a graph of isentropic changes in fluid density versus mach number, and notes that up to $M = 0.32$, density changes are predicted as below 5%. Hence, "many aerodynamicists have adopted the rule of thumb that the density variation should be accounted for at Mach numbers above 0.3; i.e. the flow should be treated as compressible." (Anderson, 1985, p. 328)

Returning to the history of fluid mechanics, Louis de Lagrange was the first to integrate Euler's equations. He published his book, called *Mechanique Analytique*, in 1788. The Cauchy–Lagrange integral, which we will encounter

in Chapter 3, was originally derived by him. According to Tokaty: "Aristotle, Archimedes, Galileo, Torricelli, Stevinus, Pascal, Huyghens, Bernoulli, Clairaut, Descartes, d'Alembert, and many others contributed to the formation of the discipline [of fluid mechanics]; but Newton was the first to cement the foundation of the edifice, Euler to erect its walls and floor, and Lagrange to add all, or almost all, those other major parts which make an edifice a safe and rather enjoyable house." (Tokaty, 1994, p. 78)

One major theoretical problem still remained, discovered in 1744 by Jean le Rond d'Alembert.[6] When one attempted to calculate the amount of resistance experienced by an object immersed in a fluid stream (called the *drag*), the theoretical fluid mechanics of Euler led to the answer that the resistance should be zero. Obviously, experimentally it had been long known that this was not the case. The problem became known as d'Alembert's paradox (Lighthill, 1986, pp. 110–114), which he, after many attempts at its resolution, famously left "for future geometers to elucidate" (Tokaty, 1994; but see footnote[7]).

Theoretical fluid mechanics, and the experimental science of hydraulics, went separate ways until this paradox was resolved (Schlichting, 1960, introduction; White, 1994, p. 39; for original sources, see footnote[8]). The crucial contribution to understanding the phenomenon of drag came over a century later, from Ludwig Prandtl in 1904, when he solved the problem of motion of fluids with very small viscosity[9], such as air and water. Others, such as Stokes, Hagen and Poiseuille, had already worked on viscous flows, but Prandtl's approach was different and original (Tokaty, 1994, p. 172). Building upon a suggestion by Osborne Reynolds (Tokaty, 1994, p. 119), Prandtl assumed that effect of the friction of the fluid was concentrated in a thin layer near the surface of the obstacle, and developed what became known as *boundary layer theory*.

For a technical introduction into the theory, see e.g. the standard monograph Schlichting (1960). Boundary layer theory has been widely successful; this is reflected by the fact that Schlichting's monograph is still current with its

---

6 The 1744 date is according to Anderson, 1985, p. 150. Cf. Hoffman and Johnson (2008), who report that d'Alembert formulated the paradox when working on a 1749 Prize Problem of the Berlin Academy on flow drag.

7 One sees slightly different versions of the quote in different sources. Cf. Anderson, 1985, p. 488, which ends with "[...] a singular paradox which I leave to geometricians to explain." The source of Anderson's version is given on p. 180 as Jean le Rond d'Alembert, 1768: *Opuscules mathematiques*.

8 On p. 41, White gives the following citations:
H. Rouse & S. Ince. *History of Hydraulics*. Iowa Institute of Hydraulic Research, University of Iowa, Iowa City, 1957; reprinted by Dover, New York. 1963.
H. Rouse. *Hydraulics in the United States 1776-1976*. Iowa Institute of Hydraulic Research, University of Iowa, Iowa City, 1976.
G. Garbrecht. *Hydraulics and Hydraulic Research: An Historical Review*. Gower Pub., Aldershot, UK, 1987.

9 The original paper is L. Prandtl: *Über Flüssigkeitsbewegung bei sehr kleiner Reibung*. Proceedings of the Third Intern. Math. Kongr. Heidelberg 1904. Reprinted in *Vier Abhdl. zur Hydro- u. Aerodynamik*, Göttingen 1927; and as NACA Tech. Memo. 452 (1928). Referenced in Schlichting, 1960, chap. VII, references. The NACA technical memo, Prandtl (1928), is nowadays available online.

8th edition, Schlichting and Gersten (1999). White (1994, p. 40), calls Prandtl's study "perhaps the most important paper ever written on fluid mechanics." Put in modern-day terms, it can be seen as a singular perturbation analysis of the Navier–Stokes equations in the small viscosity regime (Schlichting and Gersten, 1999, p. XXII).

Lighthill (1986, pp. 113–114) remarks that, in light of modern knowledge about boundary layers, "[...] [d'Alembert's paradox] should perhaps be more positively designated as d'Alembert's theorem: the first clear indication that if 'streamlined' shapes could be designed so as to meet the stringent conditions required to avoid boundary layer separation, then resistances of a very much smaller order of magnitude could be achieved."

Indeed, Ashley and Landahl (1985, p. 58) report that "The theoretical value of zero for drag in two dimensions is the most prominent failure of inviscid flow methods. It represents a nearly achievable ideal, however, as evidenced by the lift-to-drag ratio of almost 300 from a carefully arranged experiment, which is reported on page 8 of Jones and Cohen (1960)."[10]

Although boundary layer theory is well-established, also experimentally (according to e.g. the comment in Lighthill, 1986, p. 36–37), it has recently been suggested that the chief mechanism of drag generation in fluids with small viscosity, such as air and water, could rather be turbulence than a viscous boundary layer (Hoffman and Johnson, 2008). According to the cited study, an Euler flow computationally initiated as a potential flow, even in the absence of any viscosity, has a tendency to develop into a turbulent Euler solution, which is well-posed with respect to drag and lift.

The term *turbulence* refers to the phenomenon where flow patterns of widely different sizes (length scales) simultaneously exist in the flow. It makes the overall flow pattern very irregular, and is known to increase drag (Schlichting, 1960). Some approaches to take turbulence into account are the $k - \varepsilon$ model (see e.g. Launder and Spalding, 1972), large eddy simulation (LES), and direct numerical simulation (DNS). With the exception of direct numerical simulation (resolving directly the smallest flow patterns, but requiring an enormous amount of computing power), approaches for modelling turbulence are usually based on splitting the quantities of interest into time-average and rapidly fluctuating (turbulent) parts. (Schlichting, 1960; Rodi, 1984; see the updated Schlichting and Gersten, 1999 for an extensive review on turbulence models.)

Today, computational fluid mechanics, especially in engineering practice, mainly concentrates on the numerical solution of the Navier–Stokes equations, which describe the motion of fluids including the effect of internal friction (viscosity). Fluid mechanics remains, due to the nature of the equations, computationally heavy and mathematically challenging (Gresho and Sani, 1999), but it is possible to determine the flow around objects of arbitrary shapes numerically with the help of modern computers.

For the numerical solution of many different kinds of partial differential

[10] The citation in the quote refers to Jones, R. T. and Cohen, D., 1960. *High Speed Wing Theory*, Princeton Aeronautical Paperback No. 6, Princeton University Press.

equations, the *finite element method* (FEM) is well-understood mathematically, and commonly used in practice. The theory was developed in the late 1960s. Classic books include Strang and Fix (1973) and Ciarlet (1978). Summarized in one sentence, FEM is based on weak (variational) forms, appropriately defined Sobolev spaces, and discretization of the function space where the solutions reside (as opposed to discretizing the differential operator). The method is often applied also to the Navier–Stokes equations, but this application is mainly heuristic.

See also Johnson (1987); Krizek and Neittaanmäki (1990); Hughes (2000). For the application of FEM specifically to problems of incompressible flow, see Gresho and Sani (1999); and for guides for implementing FEM as a numerical computer code, Haataja et al. (2002); Hämäläinen and Järvinen (2006).[11]

In the case of Navier–Stokes equations, often a stabilization method is used in FEM to make the equations numerically easier, but Gresho and Sani (1999) argument for the use of standard Galerkin FEM on carefully designed meshes. One well-known stabilization method is SUPG (Streamline Upwinding Petrov–Galerkin); see Johnson (1987), keywords *streamline diffusion* and *Petrov–Galerkin method*; see also Hämäläinen and Järvinen (2006).

Another, different numerical approach widely used specifically in computational fluid dynamics is the *finite volume method* (FVM; also *control volume method*). From a physics viewpoint, it is based on balancing in- and outflow across small, non-overlapping control volumes, which are often tetrahedra, polygonal prisms, or hexahedra. FVM is used in many commercial flow computation software (such as Fluent), and also in the open-source flow solver OpenFOAM. Mathematically, it is interesting to note that in their FEM book, Gresho and Sani (1999) view FVM as a special case of an integral-based weighted residual method.

Despite the field's focus on Navier–Stokes, the simpler Euler and potential flow models are not outdated. As will be reviewed in Section 1.6, these models are used especially in conjunction with (geometrically) linear structure models, such as small-displacement theory of beams and panels.

In the present work, we will use the potential flow model. It is a linear model for inviscid, irrotational, incompressible flow of constant-density fluid. *Irrotational* is mathematically defined as having zero vorticity, $\omega = \nabla \times \mathbf{v} = 0$ everywhere. In physical terms, the fluid particles are allowed to move by translation, but they do not rotate (Anderson, 1985, p. 95). In this model, the boundary layer is neglected. Due to the incompressibility, the speed of sound is infinite; any disturbance in the fluid instantly spreads throughout the whole fluid domain (Lighthill, 1986, p. 82; Ashley and Landahl, 1985, p. 21). This is a reasonable approximation for sufficiently small domains.

Mathematically, potential flows have a *velocity potential*, which is a scalar

[11] These last two are in Finnish. The first book is a practical guide to numerical methods in general. It includes a chapter on FEM, walking through elementary topics such as Lagrange interpolation polynomials, reference elements, and the required coordinate transforms. Linear FEM for parabolic problems is demonstrated in detail. The second book concentrates on applying FEM specifically to flow problems. Discussed are the advection-diffusion equation, Navier–Stokes, some stabilization schemes, and finally some elementary material on turbulence models and free-surface problems.

function that satisfies the Laplace equation. For an extensive account from a fairly mathematical aerodynamics viewpoint, see Ashley and Landahl (1985). For an engineering overview, see Anderson (1985). For a rigorous, clearly written mathematical treatment of the Laplace equation, see the textbook by Evans (1998).

1.4.2 Fluid-structure interaction

When structures or materials are subjected to a surrounding flow, it is always the case that the structure will deform, which in turn induces changes in the flow field. The two domains are coupled; each component of the multiphysical situation causes changes in the other, forming a feedback loop. This is known as *fluid-structure interaction*, and it is especially important for lightweight structures and materials, as they will be displaced more strongly by the flow.

Aerodynamics, which was touched upon above, investigates the behaviour of a rigid body immersed in a fluid stream. It does not take into account the deformation of the solid object. The coupling is one-way: the obstacle disturbs the fluid stream. The analysis typically concentrates on quantities such as lift and drag (e.g. for airplane wing sections). The interesting quantities are related to the obstacle, but determining them requires only fluid flow calculation. Books such as the aforementioned Anderson (1985); Ashley and Landahl (1985) concentrate on this topic.

When elastic deformation of the solid object is added to the model, one speaks of *aeroelastics*. A standard reference book is Bisplinghoff and Ashley (1962). A related area of research is that of axial flows, e.g. in elastic pipes conveying fluid; see the extensive two-volume book by Païdoussis (1998, 2004).

In aeroelastics, the coupling between the fluid and the structure is two-way: the obstacle disturbs the flow, which causes the obstacle to deform. The elastic deformation of the obstacle changes its effects on the fluid stream, which causes changes in the deformation. At this point, we see that a feedback loop has formed.

In modelling, it is possible to use either *strong* or *weak* coupling. These fairly standard terms refer to arrangements, where the multiphysical situation is described using one equation only (strong coupling), or using several partial differential equations, which are typically coupled numerically through boundary conditions on the surface delimiting the two domains (weak coupling). When large deformations of the structure are allowed, also the motion of the delimiting surface is accounted for.

In most contexts, the standard approach to dynamic fluid-structure interaction problems during the last two decades has been numerical simulation of the fluid with the Navier–Stokes equations, numerically coupled with an elasticity model for the structure. The elasticity model may be nonlinear and allow large deformations. For example, Stein et al. (2000, 2001) and Sathe et al. (2007) have studied complex fluid-structure interaction in parachutes.

In the present work, we combine aeroelastics with axially moving materials. See e.g. the book by Marynowski (2008) about modelling orthotropic moving webs in the papermaking context. A proper literature review of moving materials

will follow below, in Section 1.6.

We utilize a strong, two-way coupling: vibrations of the moving panel cause a reaction force in the fluid, which then feeds back into the vibrations. However, as is well-known, because potential flow possesses an infinite speed of sound (as was noted above) and ignores inertial effects (being linear), it is memory-free. That is, at each moment of time t, only the current shape of the vibrating surface affects the flow; its history has no effect. Thus, the coupling that is in a physical sense two-way, is mathematically one-way only, and the model remains linear.

1.5 Elastic stability

Because it is well-known that the normal vibrations of an elastic linear system are time-harmonic (Xing and Liu, 2009a), for the stability analysis of all such systems it is standard to use the trial function

$$w(x,t) = \exp(st)\, W(x)\ , \tag{1}$$

where s is complex and $W(x)$ is an unknown eigenmode, to be determined.[12] This removes the time dependence from the PDE, making it sufficient to solve a (pseudo-)steady-state problem including the unknown scalar s, the allowed values of which are determined implicitly by the boundary conditions and problem parameters. The resulting equation will be a differential equation in x, but polynomial with respect to s.

The trial function (1) produces a complex-valued solution $w(x,t)$. The space component $W(x)$ is typically real-valued for stationary materials, and complex-valued for moving materials. Under certain conditions for the form of the original PDE, the real and imaginary components of $w(x,t)$ will also be solutions of the original problem.

It is easy to see that the required condition is linearity with real-valued coefficients. Consider applying a linear differential operator $\mathcal{L}$ to a complex-valued function w. For the real part of the result, we have

$$\begin{aligned} \mathrm{Re}\,(\mathcal{L}(w)) &= \mathrm{Re}\,[\ \mathcal{L}(\ \mathrm{Re}\,(w) + i\,\mathrm{Im}\,(w)\ )\ ] \\ &= \mathrm{Re}\,[\ \mathcal{L}(\mathrm{Re}\ (w))\ +\ i\,\mathcal{L}(\mathrm{Im}\ (w))\ ] = \mathcal{L}(\mathrm{Re}\ (w))\ , \end{aligned} \tag{2}$$

where the last equality holds only if the coefficients contained in $\mathcal{L}$ are real. A similar equality obviously holds for the imaginary part. Thus, either Re $w(x,t)$ or Im $w(x,t)$ may be taken as the real-valued solution that was sought.

However, for moving materials, the real and imaginary components of $W(x)$ are typically not solutions of the auxiliary steady-state problem; using the trial function (1), only the full complex-valued solution $W(x)$ is valid for the auxiliary problem. It is only the complete solution $w(x,t)$ whose real and imaginary

[12] The trial function itself probably dates back to Euler. In the paper Xing and Liu (2009a), the authors give the above-cited reason for why this trial is standard.

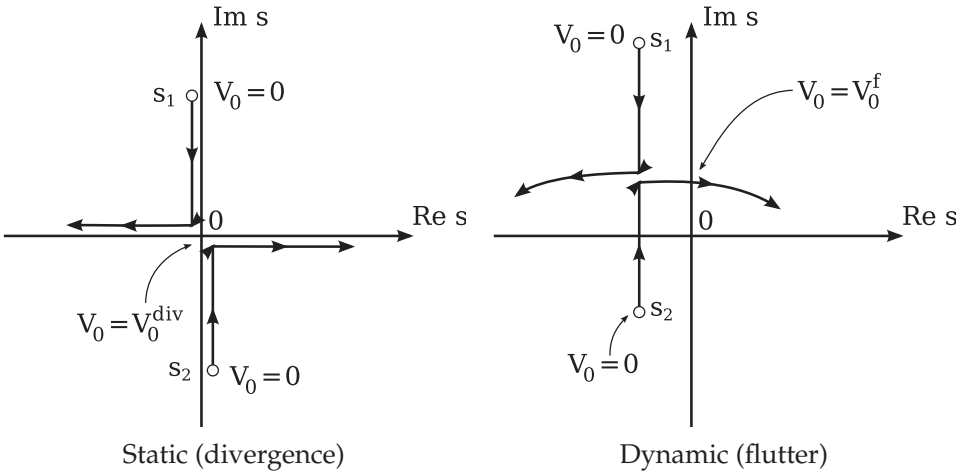

FIGURE 6 Behaviour of the stability exponent s for the two different instability types. The arrows show the motion of the eigenvalues s_j as V_0 is increased quasistatically. In the left picture, the symbols are drawn off the axes for legibility reasons only; $s^2 \in \mathbb{R}$ for all V_0. In the right picture, the real part is initially negative. In both cases, the eigenvalues merge at the collision point, and then immediately separate. After Bolotin (1963).

components satisfy the original problem separately. The reason is, of course, that the stability exponent s, which enters the coefficients of the auxiliary problem, is complex.

The allowed values of the *stability exponent* s completely characterize the free vibrations of the elastic linear system under consideration. Consider the problem parameters fixed. If Re $s \leq 0$ for all solutions (s, W), the system is *stable* and undergoes time-harmonic vibration. If Re $s < 0$ for one or more solutions (s, W), these solutions also contain a damping component. If Re $s > 0$ for at least one solution (s, W), the vibrations will grow without bound, and the system is *unstable*. (Bolotin, 1963)

There are several ways to classify mechanical instabilities. From (1) we can make the standard distinction of *static* versus *dynamic* instability, depending on whether Im $s = 0$ in the critical state (Bolotin, 1963). The related concepts are illustrated in Figure 6.

Roughly speaking, the *critical state* is defined as follows. We begin in some initially stable state of the system. For axially travelling materials, the initial state is usually taken as zero axial velocity, $V_0 = 0$. We then start increasing the problem parameter of interest, call it p, quasistatically. After a while, the parameter p has reached a value p_0. If there exists at least one solution (s, W) such that Re $s > 0$ for all $p = p_0 + \varepsilon$ with arbitrarily small $\varepsilon > 0$, but Re $s \leq 0$ for all solutions s for $p = p_0 - \varepsilon$, the value p_0 is called the *critical* parameter value. It is the point of transition from stable to unstable behaviour.

Assume we have found a critical parameter value $p = p_0$, above which the system is unstable. If Im $s = 0$ just above the critical value, $p = p_0 + \varepsilon$, the

complex-valued exp in (1) simplifies to a real-valued exp, and the displacement will grow exponentially with time. This is called *static instability* or *divergence* (Figure 6, left). This corresponds to s passing through the origin of the complex plane, and thus the critical states for this kind of instability can be caught by a steady-state analysis (Bolotin, 1963; to see this, consider (1) for $s = 0$).

Often the existence of a nontrivial steady-state solution is taken as indication of an instability, and e.g. the buckling analysis of travelling panels and plates is (correctly) based on this idea. However, as we can see from the remark in Wang et al. (2005), steady-state solutions may exist for some systems without indicating an instability, if the eigenfunctions remain linearly independent at the critical parameter value. Thus, we may conclude that a static instability can only arise from a steady state, but in a rigorous analysis, the existence of a steady state should be taken only as a necessary condition, not a sufficient one.

If Im $s \neq 0$ for $p = p_0 + \varepsilon$, the complex-valued exp in (1) becomes a product of a real-valued exp and a harmonic component (sin, cos or a linear combination of these). In this case, the displacement will exhibit exponentially growing vibrations with time (Figure 6, right). In the standard classification, this is called *dynamic instability* or *flutter*. This should not be confused with the engineering use of the term *flutter* to describe also stable vibrations (sometimes seen in papermaking sources).

Linear perturbation analysis around the critical parameter value is one approach that can be used to confirm that the critical state indicates an instability for $p = p_0 + \varepsilon$ (see e.g. the analysis in Parker, 1998, for the moving beam). Another method, used in the present work, is to compute the complex eigenfrequencies of the system (based on the trial (1)) for a range of parameter values $[p_0 - \varepsilon,\ p_0 + \varepsilon]$. This can be seen as a type of numerical initial postbuckling analysis.

Note that there are at least three different mathematical mechanisms through which instability may occur. Consider the small transverse vibrations of a panel (or beam) as an example. A common feature to all three is that the system obtains vanishing stiffness in the direction of at least one nontrivial eigenfunction $w(x)$. This is classical in buckling analysis (see e.g. Kouhia, 2009).

The first mechanism is the action of an external, in our case transversal, load. Depending on the properties of the load function, the load may be able to feed an indefinite amount of energy into the system (viewed as a time-dependent problem) for any given value of the problem parameter p (even if $p < p_0$). The exact conditions under which this kind of instability can occur are beyond the scope of the present work. Roughly speaking, the differential operator for a vibration problem usually has a nontrivial kernel (the free vibrations); this suggests that there exist right-hand sides (load functions) for which no unique solution for the displacement exists. These load functions are candidates for inducing this kind of instability. In physical terms, it may be expected that these load functions excite the system at one or more of its eigenfrequencies, leading to resonance.

A second possibility is that there exists at least one solution $w(x,t)$ of the homogeneous PDE describing the dynamical behaviour of the unloaded[13] sys-

[13] We call the system *unloaded*, if there appears no *load function* on the right-hand side of the

tem, such that $\limsup_{t\to\infty} \|w(x,t)\|_{L^\infty} = \infty$. Commonly, the situation where this kind of instability is encountered is $p = p_0 + \varepsilon$ for any (small) $\varepsilon > 0$, with zero right-hand side.

Finally, the third kind occurs when the coefficient in front of the eigenfunction approaches infinity as the problem parameter p approaches its critical value p_0. Predicting this kind of instability requires techniques beyond eigenvalue analysis. This is the kind Wickert and Mote (1990) refer to (for moving strings and beams), and which Wang et al. (2005) handle through Hamiltonian mechanics.

In this classification, dynamic stability analysis using the standard time-harmonic trial function picks up the second kind of instability. This is the kind we will concentrate on in the present work.

Classical buckling analysis can be thought of belonging either to the first kind (with $p = p_0$ and all eigenfrequencies zero) or to the second kind. By tracking down the steady states, it suggests possible parameter values that may act as thresholds for instabilities of the second kind. On the other hand, the exact critical parameter value, obtained from the static analysis, may be sufficient for the system to lose stability under an external load, if the critical point is unstable. Koiter's initial postbuckling analysis can be used to determine the type of the point (see e.g. Kouhia, 2009).

In the case of stability analysis of linear PDEs, it is evident from the linear superposition property that solution components which obviously always stay bounded may be discarded without further consideration. Thus, linear stability analysis can be focused on the components for which the boundedness of the long-term behaviour (under various different values for the problem parameters) is nontrivial.

Finally, it should be noted that for the investigation of small vibrations of elastic systems, linearized models are often used. If the system enters an unstable state, the small displacement assumption eventually breaks (possibly very quickly), and from that point on, the model no longer describes the physics of the situation being analyzed. It is generally agreed that linearized small-displacement models are sufficient up to the first instability (e.g. Païdoussis, 2005).

1.6 Existing research on axially moving continua

Now, let us take a closer look at the research more immediately related to the present problem. Since the seminal paper by Skutch (1897), an extensive amount of research has been conducted on travelling flexible strings, membranes, beams and plates. Classical papers in this area are e.g. Sack (1954), Archibald and Emslie (1958), Miranker (1960), Swope and Ames (1963), Ames et al. (1968), Mote (1968a,b, 1972, 1975), Simpson (1973), Mujumdar and Douglas (1976), Ulsoy and Mote (1980, 1982), Chonan (1986), Pramila (1986, 1987), Wickert and Mote (1989), Wickert and Mote (1990), and Lin and Mote (1995, 1996); Lin (1997).

equation. This is a purely mathematical property.

Recent research includes e.g. Shen et al. (1995), Parker (1998), Marynowski (2002), Wang (2003), Shin et al. (2005), Wang et al. (2005), Sygulski (2007), Kulachenko et al. (2007a,b), and Vaughan and Raman (2010). The monograph by Marynowski (2008) discusses orthotropic moving webs specifically.

There are of course much more papers in the field than can be mentioned here. For example, for a recent review focusing on the topic of moving strings only, see Chen (2005), which alone cites 242 references.

In the mentioned studies, models described by second- and fourth-order differential equations have been used, focused on various aspects of free vibrations and forced vibrations. The effects of axial motion on the frequency spectrum and eigenfunctions were investigated in Sack (1954), Archibald and Emslie (1958), Swope and Ames (1963) and Simpson (1973). Stability considerations were reviewed in Mote (1972).

The set of papers from the group of C. D. Mote has been particularly numerous. In addition to the ones already mentioned above, see e.g. Thurman and Mote (1969), Ulsoy et al. (1978), Mote and Wu (1985), Yang and Mote (1991), Renshaw and Mote (1996), and Lee and Mote (1996). There are also the reviews Wickert and Mote (1988) and Mote and Wickert (1991) summing up the knowledge up to those points.

After Skutch's paper, the extremely compact Archibald and Emslie (1958) was one of the first studies of axially moving materials. In the study, the threadline equation was briefly derived in two different ways: using Hamiltonian mechanics, and by coordinate transformation of the standard wave equation. It was also shown that the natural frequency of each mode decreases when transport speed increases, and that the travelling string and beam both experience divergence instability at a sufficiently high speed.

Note however, that according to Wang et al. (2005), in the case of the string this classical result of the existence of a divergence instability at the critical speed is incorrect. It was shown using Hamiltonian mechanics, that due to weak interaction of eigenvalue pairs, there is no instability in the string case. The well-known divergence of the eigenmode coefficients (see e.g. Wickert and Mote, 1990, for an explicit expression), as the velocity approaches critical, was shown to be a mathematical artifact, which can be eliminated by using the Hamiltonian approach (effectively looking for solutions in a different mathematical space).

The paper Swope and Ames (1963) concentrated on constructing analytical solutions for the free vibrations of a travelling string. The threadline equation was derived in a detailed manner, based on a differential force balance. The equation obtained was the same as in the above-mentioned Archibald and Emslie (1958), as expected. The free-space behaviour of the moving string was analyzed using the travelling-wave approach of d'Alembert. For the finite string, a coordinate transformation was used (based on the method of characteristics) to transform the second-order hyperbolic constant-coefficient problem into a form from which the solution is apparent.

Simpson (1973) derived an analytical solution for the free harmonic vibrations of an axially travelling beam without tension applied at the ends, by fac-

toring the fourth-order characteristic equation. The limitation of this approach is that it is not generalizable to the tensioned case.

Response prediction has been given for particular cases when excitation assumes special forms, such as a constant transverse point force (Chonan, 1986) or harmonic transverse motion of the supports (Miranker, 1960). Arbitrary excitation and initial conditions have been analysed with the help of modal analysis and a Green function method in Wickert and Mote (1990). As a result, the associated critical speeds have been determined explicitly.

Both two- and three-dimensional approaches, as also various different approaches to taking into account the effect of the surrounding fluid, have been used for modelling paper production. Because paper has a relatively low density, the effect of the surrounding air is important (Pramila, 1986; Kulachenko et al., 2007a,b). As we can see from Chang et al. (1991); Chang and Moretti (1991, 2002) and Watanabe et al. (2002), potential flow type models play an important part in the investigation of dynamic fluid-structure interaction in paper production. Because the paper web is fragile, linear theory is sufficient to cover the physically meaningful range of deformations up to the first instability.

The first attempt to take into account the interaction between a travelling paper web and the external medium, using at first analytical added-mass approximations and then the finite element method, was made in the series of papers Niemi and Pramila (1986); Pramila and Niemi (1987); Pramila (1986, 1987). In all of these studies, it was found that the surrounding air significantly reduces the eigenfrequencies and critical velocities of the web when compared to the vacuum case. According to Pramila (1986), the presence of air may reduce both to about 25% of the vacuum case.

However, in a recent paper, Frondelius et al. (2006) contrasted these classical results by using an added-mass model for the fluid, with non-constant (space coordinate dependent) added masses computed from boundary layer theory. They reported that while the eigenfrequency predictions agree with those from potential flow theory, the divergence velocities are found to be significantly higher. The boundary layer used in the mentioned study was of the Sakiadis type. To our knowledge, at the present time it remains an open question how the system would behave with other types of boundary layers.

The use of boundary layer theory in Frondelius et al. (2006) can be contrasted with the remarks of its use for moving materials in Chang et al. (1991). In the latter, the authors note that since the moving band does not have a leading edge, the usual boundary layer which grows in thickness as the distance increases from the leading edge, is not applicable to this physical situation. According to them, the boundary layer should grow in time, forever or until the momentum transfer is balanced by fluid friction on the outer boundaries. The authors continue, that a more nearly correct analogy from classical fluid physics, for the boundary layer growth, is the flow field around a rotating cylinder or sphere. In this case, finding the equilibrium flow field requires considering also the outer boundaries of the flow.

However, it is also possible to use a model which does include a leading

edge; for such models, the remark of Chang et al. (1991) does not apply. This is what Frondelius et al. did, so both papers are in a sense correct; which approach leads to a better model is a nontrivial question.

Other used approaches include the following. In Chang and Moretti (1991), the web was modelled as a linear membrane, while the surrounding air was treated using potential flow theory. A nonlinear membrane element was used in Koivurova and Pramila (1997) to model a narrow axially moving band surrounded by air. The influence of air was accounted for with acoustic elements placed on one side of the band only. In Kulachenko et al. (2007a), the influence of air was accounted for by utilising fluid-solid interaction analysis based on acoustic theory. Results in this paper also show that air reduces the eigenfrequencies of the web.

In Watanabe et al. (2002), two different methods of analysis were developed in order to clarify the phenomenon of paper flutter. One of these was a flutter simulation using a Navier–Stokes code, and the other method was based on a potential flow analysis of an oscillating thin airfoil. In Wu and Kaneko (2005), both linear and nonlinear analyses of sheet flutter caused by fluid-structure interaction in a narrow passage were developed. The sheet was considered as a combination of massless beam elements, springs, and discrete mass particles, in which the mass of each particle and the spring coefficients were calculated based on the beam model.

From an academic research viewpoint, the potential flow problem is a standard reference case. It has been studied both for axially moving materials in stationary air (e.g. the aforementioned Pramila, 1986), and for stationary structures in axial flow (e.g., Eloy et al., 2007).

The form of the axially travelling panel problem shares some similarities with the problems of pipes conveying fluid, and stationary structures subjected to axial flow. These similarities have been discussed in the review by Païdoussis (2008). See also Dugundji et al. (1963) and Guo and Païdoussis (2000), and, for a summary comparing the different results, the book by Païdoussis (2004).

A model similar to the one in the present work, but in three dimensions, was analyzed in Vaughan and Raman (2010). The finite element method was used for solving the ideal fluid velocity potential numerically.

A functional analytical solution for the aerodynamic reaction of the two-dimensional surrounding fluid, using a Green's function method, has been found for a stationary plate in axial flow by Kornecki et al. (1976). The panel model was used. It was assumed that the panel is infinite in extent, being elastic in a finite interval and rigid elsewhere. Flow was assumed on one side of the panel only. The solution of Kornecki et al. is similar in methodology to the present solution of the flow problem, but the flow geometry and importantly also the topology are different.

2 AXIALLY MOVING STRINGS AND PANELS

In this chapter, we will analyze some simplified models. Specifically, our topics are the axially moving string, the damped axially moving string on an (optional) elastic foundation of the classical Winkler type, and the axially moving panel. These topics provide a qualitative overview of this class of systems, which will be useful for the eigenfrequency analysis of Chapter 5.

The material on the classical moving ideal string, Section 2.1, consists mostly of known results and is intended as introductory. We will give a detailed derivation for the free vibrations, and extract the eigenfrequencies. We follow the approach of Archibald and Emslie (1958) for problem setup, and that of Swope and Ames (1963) for the solution of the free vibration problem.

We will then extend the analysis to the moving damped string on an elastic foundation, in Section 2.2. Although the general behaviour of the eigenvalues of damped systems is well-known (see e.g. Bolotin, 1963), this analysis is original, giving an explicit solution of the eigenfrequencies and eigenfunctions in terms of the problem parameters for this particular system. The solution is derived by applying the technique of Swope and Ames (1963). The obtained analytical, explicit solution for the eigenfrequencies is visualized in subsection 2.2.5. The results are summarized in subsection 2.2.6.

The chapter ends with some optional, introductory material on the axially moving panel. The governing equation and typical boundary conditions are introduced. The steady-state behaviour is determined, and the approximate free-vibration solution of Kong and Parker (2004) for small bending rigidities is reviewed for convenience. Finally, the applicability of the panel model is discussed.

2.1 Classical ideal string

Let us first review the ideal string model. As is well-known, this is a linear model describing the small vibrations of a thin string, which has no bending resistance, but which can support tensile loads (i.e. resists stretching) along its length.

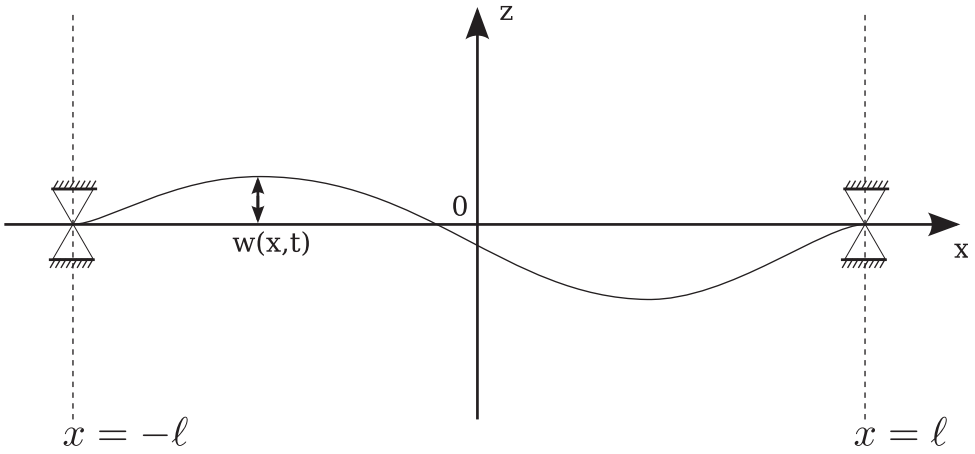

FIGURE 7 Stationary (non-travelling) ideal string, held fixed at ends. At the boundaries, the displacement $w = 0$.

2.1.1 Stationary (non-travelling) ideal string

The dynamics of free transverse small-amplitude vibrations of a classical, stationary (non-travelling) ideal string (see Figure 7) is governed by the partial differential equation

$$mw_{tt} - Tw_{xx} = 0 \, . \tag{3}$$

Equation (3) follows from Newton's second law written for a differential element of the string. For tensile loads, $T > 0$. Thus, (3) is the standard wave equation in one dimension. The tension in the string balances the out-of-plane acceleration, making the string vibrate.

For beams and strings, it is customary to define m as the mass per unit length. Then the tension T has the unit of force.

When (3) is seen as an approximation of a panel in the limit of vanishingly small bending rigidity, m is usually taken as the mass per unit area. For the panel, equation (3) represents pressures. The tension in a panel is defined as

$$T = \sigma h \, , \tag{4}$$

where σ is the in-plane stress and h the panel thickness. The dimension of T (for a panel) is force per unit length.

2.1.2 Travelling string: problem setup

We will set up the problem for the moving string by following the second approach of Archibald and Emslie (1958). Consider an ideal string travelling axially at a constant velocity V_0 (Figure 8).

We set up two coordinate systems, the *Lagrange* (local, material, co-moving) system (ξ, z, t) which moves axially at velocity V_0, and the *Euler* (global, laboratory, stationary) coordinate system (x, z, t). In the Lagrange system, the string

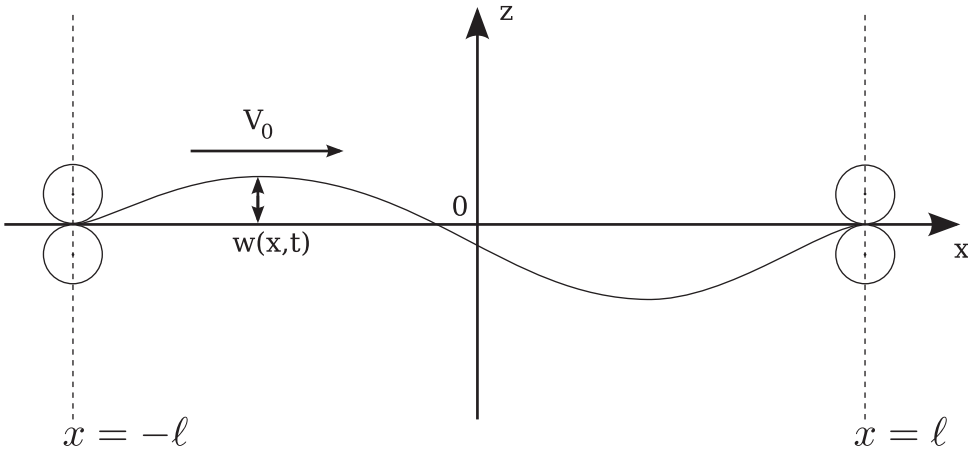

FIGURE 8 Axially moving ideal string, travelling through two pinholes. The pinholes restrict the displacement at the boundaries to $w = 0$. The roller symbols indicate the presence of axial motion.

is axially stationary, while in the Euler system, the moving string flows past at velocity V_0.

Regardless of the chosen coordinate system, the described physical situation is the same, i.e.

$$w(x(\xi, t), t) \equiv \tilde{w}(\xi(x, t), t) \ , \tag{5}$$

where w is the transverse displacement function defined in terms of the Euler coordinates, and $\tilde{w}$ is the corresponding function defined in terms of the Lagrange coordinates.

We write the physics of the moving string, from a differential force balance viewpoint, initially in the co-moving (ξ, z, t) coordinates, and then transform the equation to (x, z, t) coordinates. In the co-moving coordinates, we have a stationary string, and thus the governing equation is simply (3):

$$m\tilde{w}_{tt}|_{\xi=\text{const.}} - T\tilde{w}_{\xi\xi} = 0 \ . \tag{6}$$

The relation between our two coordinate systems is given by

$$\xi \equiv \xi(x, t) = x - V_0 t \ , \qquad \Leftrightarrow \qquad x \equiv x(\xi, t) = \xi + V_0 t \ , \tag{7}$$

where we can pick either form depending on which system — the local (ξ, z, t) or the laboratory (x, z, t) — we wish to use as independent variables. Either the pair (x, t) is independent, or the pair (ξ, t) is independent. In the first (respectively second) case, ξ (respectively x) is a dependent variable defined in terms of the independent variables by the relation (7).

Strictly speaking, (7) is a linearized relation, because we have used only V_0, and not accounted for changes in the axial velocity due to time-dependent axial displacement, nor have we accounted for any vertical motion. However, (7) is the relation that is generally used in the literature, being accurate enough in the small-displacement regime.

Consider transforming a local time derivative from the Lagrange (ξ, t) to the Euler (x, t) coordinate system. By (5), the chain rule and the expression of $x = x(\xi, t)$ from (7), we have

$$\begin{aligned}\frac{\partial \tilde{w}(\xi,t)}{\partial t}|_{\xi=\text{const.}} &= \frac{\partial w(x(\xi,t),t)}{\partial t}|_{\xi=\text{const.}} \\ &= \frac{\partial w}{\partial x}\frac{\partial x}{\partial t} + \frac{\partial w}{\partial t}|_{x=\text{const.}} = \frac{\partial w}{\partial x}\cdot V_0 + \frac{\partial w}{\partial t}|_{x=\text{const.}} . \end{aligned} \tag{8}$$

Motivated by (8), the *material derivative* (also known as the *Lagrange derivative* and as the *total derivative*) is defined as

$$\frac{\mathrm{d}w}{\mathrm{d}t} \equiv \frac{\partial w}{\partial t}|_{x=\text{const.}} + V_0\frac{\partial w}{\partial x} \tag{9}$$

for any function $w = w(x, t)$. Applying (9) to itself gives the *second material derivative*,

$$\frac{\mathrm{d}^2 w}{\mathrm{d}t^2} \equiv \left(\frac{\partial}{\partial t} + V_0\frac{\partial}{\partial x}\right)\left(\frac{\partial w}{\partial t} + V_0\frac{\partial w}{\partial x}\right) = w_{tt} + 2V_0 w_{xt} + V_0^2 w_{xx} , \tag{10}$$

where in the right-hand side we have assumed $V_0 = \text{constant}$.[1] The expression (10) represents the local acceleration in co-moving (Lagrange) coordinates, as it appears when viewed in the laboratory (Euler) coordinates. The three terms on the right-hand side physically represent the accelerations of (respectively) local inertia, the Coriolis effect[2], and the centrifugal effect[3].

The next task is to transform the $\tilde{w}_{\xi\xi}$ term. In the same manner as above, it is easy to construct the transformation:

$$\frac{\partial \tilde{w}(\xi,t)}{\partial \xi} = \frac{\partial w(x(\xi,t),t)}{\partial \xi} = \frac{\partial w}{\partial x}\frac{\partial x}{\partial \xi} = \frac{\partial w}{\partial x} . \tag{11}$$

Note that t does not depend on ξ (regardless of coordinate system, t is the other independent variable), so the chain rule produces only one term. By (7), we have $\partial x/\partial\xi = 1$. We see that the appropriate transformation for the space derivative is the identity function, i.e., $\tilde{w}_\xi = w_x$. Thus also $\tilde{w}_{\xi\xi} = w_{xx}$.

Applying the transformations (10) and (11) to (6), we obtain the well-known equation for small displacements of an axially travelling string (Skutch, 1897; Archibald and Emslie, 1958; Swope and Ames, 1963; also known as the *threadline equation*)

$$m w_{tt} + 2mV_0 w_{xt} + \left(mV_0^2 - T\right) w_{xx} = 0 . \tag{12}$$

---

1 If the velocity is not constant, there will be additional terms, depending on the coordinate transformation that plays the role of (7) in the modified situation.

2 Note that $w_{xt} = (\partial/\partial t)(w_x) = (\partial/\partial t)(\tan\alpha) \approx (\partial/\partial t)\alpha$ for small α. Here α is the angle between the local positive-x tangent vector of the string and the x axis. Thus, w_{xt} is a linear approximation of local rotation speed. The presence of time-dependent rotation leads to the Coriolis effect.

3 For the local radius of curvature R, we have the well-known formula $1/R = w_{xx}/(1 + (w_x)^2)^{3/2}$. In the small displacement regime, w_x is assumed small, and thus $1/R \approx w_{xx}$. Therefore, we have an acceleration that is inversely proportional to the local radius of curvature. Hence, centrifugal effect.

The first three terms come from the second material derivative, and as before, the Tw_{xx} term represents the restoring force of the tension. The same remarks apply about the units of m and T as for the stationary string.

Typically, dimensionless coordinates are used. Let us set

$$x' := x/\ell \,, \qquad t' := t/\tau \,, \qquad w'(x',t') := w(\ell x', \tau t')/h \,, \tag{13}$$

where the prime indicates a dimensionless quantity. The symbol ℓ indicates a characteristic length, τ a characteristic time, and h a characteristic displacement (the string or panel thickness can be used for this; hence the symbol h). By convention, these are positive constants. The values of the scalings are arbitrary, and are usually chosen as whatever is the most convenient choice for the problem under discussion.

In the following, we will omit the primes from the notation for brevity. We insert $w = hw'$, cancel h (since the equation is linear in w and the right-hand side is zero), perform the differentiations using (13) and the chain rule, and multiply the resulting equation by τ^2. We have

$$w_{tt} + 2V_0 \frac{\tau}{\ell} w_{xt} + \left(V_0^2 - \frac{T}{m} \right) \frac{\tau^2}{\ell^2} w_{xx} = 0 \,, \tag{14}$$

which is now in dimensionless coordinates.

With the obvious identifications, (14) is a second-order constant-coefficient PDE of the form

$$aw_{tt} + 2bw_{xt} + cw_{xx} = 0 \,. \tag{15}$$

Second-order PDEs are either elliptic, parabolic or hyperbolic. Because the coefficients are constants, the same type holds globally regardless of x and t. The discriminant of (14) is (see e.g. Polyanin et al., 2008)

$$b^2 - ac = V_0^2 \frac{\tau^2}{\ell^2} - 1 \cdot \left(V_0^2 - \frac{T}{m} \right) \frac{\tau^2}{\ell^2} = \frac{T}{m} \frac{\tau^2}{\ell^2} > 0 \,.$$

Thus the equation is always hyperbolic regardless of the axial velocity V_0. This matches physical intuition: the inclusion of the axial velocity should not change the basic nature of the vibrating behaviour. Indeed, in the local (Lagrange) coordinate system the physics is identical to that of the stationary string; from that viewpoint, it is only the boundaries that are moving.

Equation (12) requires two initial and two boundary conditions. For free vibration analysis, we set only the boundary conditions, and the solution will have undetermined coefficients. This is fine, because free vibration analysis is only concerned with determining possible motions of the unloaded system (mathematically, nontrivial solutions of the homogeneous PDE).

The customary boundary conditions for the moving string are zero Dirichlet, describing a string travelling through two pinholes, which are fixed to zero height:

$$w(0,t) = w(1,t) = 0 \,, \tag{16}$$

where $w = w(x,t)$. (See Figure 8 above.)

2.1.3 Special case: critical velocity

Let us begin with a special case. If $V_0 = \sqrt{T/m} \equiv C$, then the parenthetical term in (14) vanishes, and the equation simplifies into

$$w_{tt} + 2C\frac{\tau}{\ell}w_{xt} = 0 \ . \tag{17}$$

The equation is still globally hyperbolic, since $b^2 > 0$.

This special value for the axial velocity is known as the *critical velocity*. For historical reasons[4], it is also called the *divergence velocity*. In this special case we no longer have the original equation. Instead, (17) says

$$\frac{\partial}{\partial t}\left(w_t + 2bw_x\right) = 0 \ , \tag{18}$$

which can be reworded as

$$v_t + 2bv_x = 0 \ , \tag{19}$$

where $v := w_t$ is the transverse (out-of-plane) velocity field. We see that the transverse velocity obeys the first-order transport equation (along the string length) with constant velocity $2b$. Thus, $v(x,t) = g(x - 2bt)$ for some differentiable function g. The displacement w consists of this moving component, and by (18), a second component $f(x)$ which does not depend on t:

$$w(x,t) = f(x) + g(x - 2bt) \ .$$

The boundary conditions (16) imply also $v = 0$ at the boundary points. The only solution of (19) satisfying the boundary conditions is the trivial solution $v = 0$. Thus, the transverse velocity in this degenerate case must be zero everywhere, i.e. the string stays in a steady-state configuration. This very compact way to solve the special case was reported by Wang et al. (2005).

We can find the function $f(x)$ explicitly using a more direct approach. Equation (18) can be integrated with respect to t, producing

$$w_t + 2bw_x = h(x) \ ,$$

which is the nonhomogeneous transport equation. Its solution is (Polyanin, 2004a)

$$w(x,t) = \frac{1}{2b}\int h(x)\ \mathrm{d}x + g(x - 2bt) \ , \tag{20}$$

As above, this is a linear superposition of two components: a steady-state one, and one moving toward the right at velocity $2b$. This agrees with the first solution. By the boundary condition argument, again $g(s) \equiv 0$. By differentiating (20) with

[4] For the conventional wisdom, see e.g. Wickert and Mote (1990). For a new result contradicting this, see Wang et al. (2005). According to the latter study, by Hamiltonian mechanics it can be shown that due to weak interaction of eigenvalue pairs (linear independence of eigenmodes at the critical velocity), no divergence instability exists for the travelling ideal string.

respect to x, and then restricting to $t = 0$, we can determine $h(x) = 2b\, w_x(x,0)$, and by substituting this back into (20), $w(x,t) = w(x,0)$ for all t.

Thus, the initial condition for the position (which must satisfy the boundary conditions!) completely determines the solution. The other initial condition must be $w_t(x,0) \equiv 0$ for compatibility. We conclude that, if this compatibility condition holds for our initial conditions, upon a quasi-static transition to the limit state $V_0 = C$ the displacement profile of a freely vibrating axially travelling string will "freeze" into the shape it had when the limit state was reached.

In practice, the compatibility condition $w_t(x,0) \equiv 0$ is a fairly good approximation for any physically reasonable situation for this model near $V_0 = C$, because as we will see in subsection 2.1.4, all eigenfrequencies of the travelling string tend to zero in the limit $V_0 \to C$.

Nevertheless, the quasi-static analysis has its limitations. It is easy to construct a situation to which it is not applicable. For example, consider a case where we initially set $V_0 = C - \varepsilon$ (with $\varepsilon > 0$ small), $w(x,0) \equiv 0$, $w_t(x,0) = f(x) \not\equiv 0$, and then perform a transition to $V_0 \to C$. The quasi-static analysis cannot be used, because the given initial condition for w_t contradicts the compatibility condition. A more general treatment including the effects of accelerating motion (where $V_0 = V_0(x,t)$) for the dynamics is required if we wish to analyze such a case. The problem of accelerating strings and beams has been studied in the literature; see e.g. the classic paper by Mote (1975).

In conclusion for this section, the existence of a steady-state solution for the travelling string is interesting. As we will see later (subsection 2.3.2), a steady-state solution exists also for the panel, but the mathematical mechanism generating it is different.

For the rest of the discussion on the travelling string model, it is assumed that $V_0 \neq C$.

2.1.4 Free vibration analysis

Let us briefly go through the derivation for an analytical solution for the free vibrations of the axially travelling string. We will proceed in a manner similar to Swope and Ames (1963).

Consider equation (15). A systematic way to derive the solution is the standard approach of diagonalizing the principal part of the operator (see e.g. Polyanin et al., 2008 or references therein). Because (15) contains only second-order derivatives, we have only the principal part to consider.

It is known that the second-order PDE in two variables can always be transformed into one of the canonical forms, depending on its type. We start with the characteristic equation of (15), namely

$$a(\mathrm{d}x)^2 - 2b\mathrm{d}x\mathrm{d}t + c(\mathrm{d}t)^2 = 0\,. \tag{21}$$

Note that the coefficients a, b and c are constants. Because the discriminant $b^2 - ac > 0$ (as was shown above) and $c \neq 0$ (i.e. $V_0 \neq C$), this can be thought of as a

second-order algebraic equation in $\mathrm{d}t/\mathrm{d}x$, with the real-valued solutions

$$\frac{\mathrm{d}t}{\mathrm{d}x} = \frac{1}{c}(b \pm \sqrt{b^2 - ac}) \; . \tag{22}$$

The characteristics are curves $u(x,t)$ such that

$$\mathrm{d}u \equiv A\mathrm{d}t + B\mathrm{d}x = 0 \; .$$

From (22), we obtain

$$c\,\mathrm{d}t - (b \pm \sqrt{b^2 - ac})\,\mathrm{d}x = 0 \; ,$$

and by integrating both sides,

$$u_\pm(x,t) \equiv ct - (b \pm \sqrt{b^2 - ac})x = C_\pm \tag{23}$$

for the "+" and "−" terms, respectively. Assigning a value to the constants $C_\pm$ (which have no relation to C!) picks one specific curve from the family of characteristics; equation (23) represents the whole family. We see that the characteristics $u_\pm$ for this equation are straight lines, as expected. Performing the change of variables (leaving $C_\pm$ free, taking only the left-hand side)

$$y = u_+(x,t) \; , \qquad z = u_-(x,t) \; ,$$

the original equation (15) transforms into the *first canonical form* of the wave equation,

$$w_{yz} = 0 \; .$$

Note that here y and z are just arbitrary labels for the transformed (x,t) coordinates, and have nothing to do with the y and z axes of the laboratory coordinate system. We change variables again, now to ξ and η such that

$$y = \xi - \eta \; , \quad z = \xi + \eta \; , \qquad \Leftrightarrow \qquad \xi = (y-z)/2 \; , \quad \eta = (y+z)/2 \; .$$

We now have the *second canonical form* of the wave equation,

$$w_{\eta\eta} - w_{\xi\xi} = 0 \; . \tag{24}$$

Performing both steps at once and letting $a = 1$, we have in terms of the original coordinates the final coordinate transforms[5]

$$\xi = -\sqrt{b^2 - c} \cdot x \; , \tag{25}$$

$$\eta = ct - bx \; , \tag{26}$$

which can be used to transform (15) into (24) directly (for $a = 1$).

Lines of constant x have been transformed into lines of constant ξ, so a suitable separable solution in (ξ,η) of (24) will satisfy boundary conditions at constant x. This solution approach is only useful for free vibration analysis, because

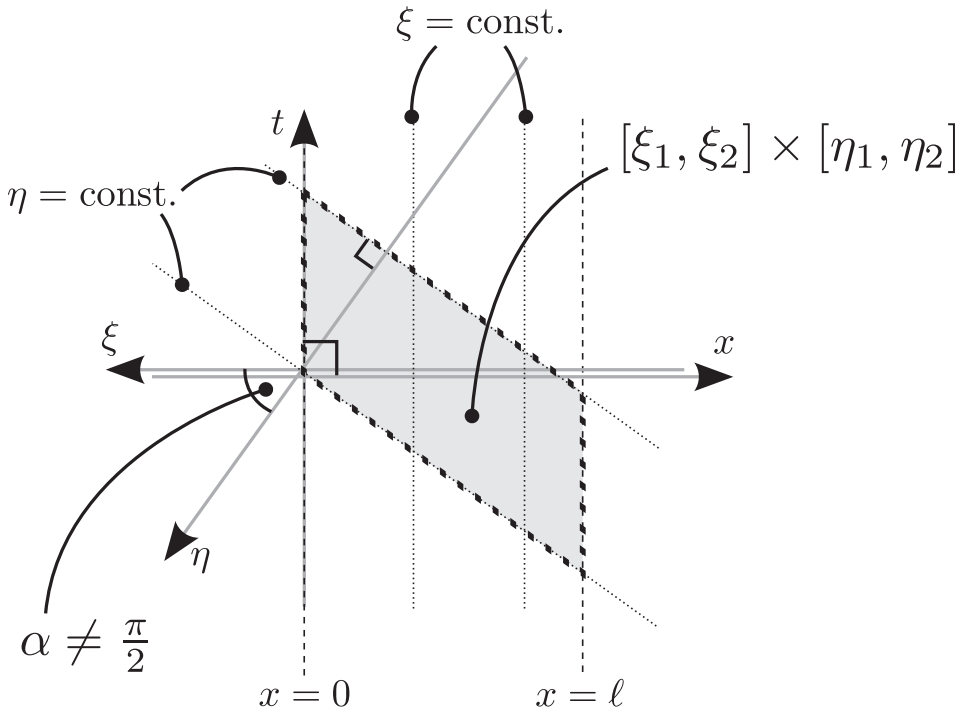

FIGURE 9 The (x, t) and (ξ, η) coordinate systems in the plane. The systems share the origin; in the diagram, the horizontal axes are shifted vertically for legibility only. The shaded parallelogram indicates an area delimited by constant values for the (ξ, η) coordinates; on the edges of such shapes, boundary conditions can be easily enforced by a solution separable in (ξ, η). Additionally, some constant values of ξ are indicated; note that these are parallel to constant x. Also note that if $b \neq 0$ i.e. $V_0 \neq 0$, the (ξ, η) axes are not orthogonal (see equations (25) and (26)).

initial conditions cannot be (easily) enforced for such a separable solution, due to the fact that η is a linear combination of x and t. See Figure 9.

Now that there is no mixed derivative, a compact way to find the free vibrations of (24) in the transformed coordinates (ξ, η), is to use the standard time-harmonic trial function

$$w(\xi, \eta) = \exp(s\eta)\, W(\xi) \,. \tag{27}$$

Substituting (27) into (24) gives

$$s^2 W - W'' = 0 \,, \qquad \text{i.e.,} \qquad W'' = s^2 W \,. \tag{28}$$

This is a linear eigenvalue problem for (s^2, W). Considering (28) and the boundary conditions (16), we see that the eigenfunction must be

$$W(\xi) = \sin(\omega\xi) \,,$$

and for the kth mode we have

$$\omega = -\frac{k\pi}{\sqrt{b^2 - c}} = -\frac{k\pi\ell}{C\tau} \,, \quad k \in \mathbb{Z}^+ \,. \tag{29}$$

In order to satisfy the PDE (24), we must have

$$s^2 = -\omega^2 \,, \qquad \text{i.e.,} \qquad s = \pm i\omega \,. \tag{30}$$

Thus the solution in (ξ, η) coordinates is

$$w(\xi, \eta) = \exp(s\eta)\, \sin(\omega\xi) \,. \tag{31}$$

By transforming back using (30), (29), (26), (25), and the values for the coefficients a, b and c from (15) and (14), we obtain the solution in (x, t) coordinates.

Explicitly, the complex-valued free vibration solution of (14), with zero Dirichlet boundary conditions (16), for the kth vibration mode is

$$w(x, t) = \beta \exp\left(\mp i \frac{k\pi\ell}{C\tau} \left[(V_0^2 - C^2) \frac{\tau^2}{\ell^2} t - V_0 \frac{\tau}{\ell} x \right] \right) \sin(k\pi x) \,, \tag{32}$$

where the $\mp$ corresponds to the $\pm$ in (30), $C \equiv \sqrt{T/m}$, and β is free. Note that the x and t in (32) are the dimensionless variables (13); the primes have been omitted for brevity. The pinholes are placed at $x' = 0$ and $x' = 1$. Compare Wickert and Mote (1990), and Swope and Ames (1963).

We observe that there is an exp factor in the complex-valued solution (32), and it admits separation in x and t. That is, $w(x, t) = f(x)\, g(t)$ for some f and g.

---

[5] Warning: if we had the nonhomogeneous case, with a load function on the right-hand side, a scale factor would need to appear in front of the load function. The factor can be determined by making the change of variables $\xi = \beta x$, $\eta = \alpha_1 x + \alpha_2 t$, and working out the coefficients α_1, α_2 and β by the chain rule for partial derivatives, working backward from $w_{\eta\eta} - w_{\xi\xi} = f(x, t)$ and requiring that the resulting terms match equation (15) with $a = 1$.

Specifically, $g = \exp$. Thus, (32) represents time-harmonic behaviour, and we can apply Bolotin's approach for determining the dynamic stability. The stability exponent of the kth mode is the coefficient of t in the exp. From (32), we have

$$s_* = \mp \frac{1}{C\ell} ik\pi\tau(V_0^2 - C^2) \; . \tag{33}$$

The symbol s_* means that (33) is expressed in the original (x, t) coordinates, as contrasted with the transformed (ξ, η) coordinates used in (30). Because $\eta = ct - bx$, and no additional transformations[6] were needed to produce w, the relation between the stability exponents in the two coordinate systems is simply $s_* = cs$. The exponent s_* is the one that determines the elastic stability behaviour.

A plot of the eigenfrequency spectrum described by equation (33), as a function of V_0, is provided in Figure 10 up to mode number $k = 10$. The parameter values used for T, m and ℓ in the plot are given in Table 1 on page 155. For convenience, we repeat them here: $T = 500$ N/m, $m = 0.08$ kg/m^2 (model seen as a panel in the membrane limit), and $\ell = 1$. The timescale parameter was chosen as $\tau = \ell/\sqrt{T/m}$, which leads to $\sqrt{b^2 - c} = 1$.

We see that the eigenvalues (33) come in pairs. This is a common feature of undamped gyroscopic systems, and is due to the structure of the characteristic equation. If s is an eigenvalue of such a system, then $-s$ is, too. See e.g. the paper Huseyin and Plaut (1974–1975, p. 166). (For the relation of axially moving materials to classical gyroscopic systems, see Mote and Wickert, 1991.)

For all $V_0 \neq C$, the stability exponent s_* is always pure imaginary. Thus, the string will undergo undamped harmonic vibrations, as expected.[7]

We have obtained the following result: after a quasistatic transition from an initial stable state ($V_0 = 0$) to the present state (V_0 nonzero), if the assumptions of linear theory have not been violated anywhere up to that point, the stability exponent (33) determines the behaviour of free vibrations in the present state.

Especially, the system is stable at $V_0 = 0$. Hence, the governing PDE, (14), is valid at least for all $|V_0| < C$ (as is indeed well-known). Whether the equation is valid at supercritical velocities, $|V_0| > C$, is therefore a question of whether there exists an instability at the critical velocity, where s_* vanishes.

Now, consider the problem as an initial boundary value problem with some initial conditions matching a free vibration solution. Because a purely time-harmonic vibration never exceeds its original maximum amplitude (defined as $M \equiv \|w\|_{L^\infty}$ taken over one period), we conclude that if the original maximum amplitude at $V_0 = 0$ was "small" ($M = \varepsilon$, $\varepsilon > 0$), so is the maximum amplitude at every V_0 (as V_0 is increased quasi-statically). This holds especially in the limit of the dynamic free vibration solution as $V_0 \to C$ (and respectively, as $V_0 \to -C$). On the other hand, from subsection 2.1.3 we know that the limit solution is a

---

6 I.e. out of some auxiliary function defined during the solution process. We will need to do this in the damped case, subsection 2.2.2.

7 We see that for this particular problem, since $c \in \mathbb{R}$ and s is pure imaginary, the inclusion of the c factor does not affect how s_* behaves when compared to the original s. The fact that in the subcritical regime $c < 0$ does not affect anything, either, because of the sign ambiguity in s. The pair of solutions simply switches roles.

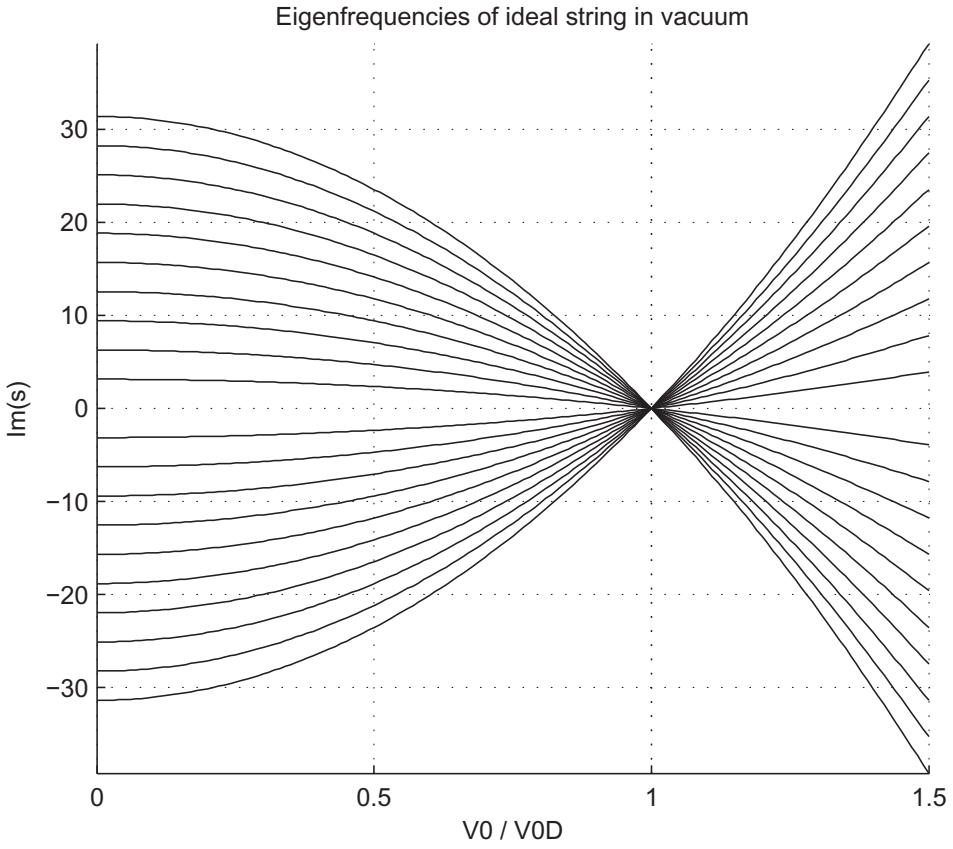

FIGURE 10 Eigenvalues of the moving ideal string, up to mode number $k = 10$. Analytical result, equation (33). $\mathrm{Re}\, s \equiv 0$.

steady state, i.e. it does not depend on time (and thus cannot blow up as $t \to \infty$). Gathering these facts together, the conclusion is that at least by this elementary quasi-static analysis, there exists no instability for the axially travelling string at $V_0 = \pm C$.

However, the argument just developed leaves open two possibilities for instability. First, as was commented further above, it is easy to construct dynamic free vibration solutions, which are not compatible with the quasi-static transition into the steady state at $V_0 = \pm C$. An analysis accounting for axial acceleration may be needed to remove this limitation. The second possibility is that the coefficient in front of the eigenfunction may blow up (if we use a suitably chosen nonzero load) as $t \to \infty$. Deciding this question requires techniques beyond eigenvalue analysis. Wang et al. (2005) have considered this problem using Hamiltonian mechanics, and report that there indeed is no instability at $V_0 = \pm C$.

From (32), the real and imaginary parts of the solution follow trivially using Euler's identity:

$$\begin{aligned}
\text{Re } w(x,t) &= \beta \cos\left(\mp \frac{k\pi\ell}{C\tau} \left[(V_0^2 - C^2)\frac{\tau^2}{\ell^2} t - V_0 \frac{\tau}{\ell} x \right] \right) \sin(k\pi x) \,, \\
\text{Im } w(x,t) &= \beta \sin\left(\mp \frac{k\pi\ell}{C\tau} \left[(V_0^2 - C^2)\frac{\tau^2}{\ell^2} t - V_0 \frac{\tau}{\ell} x \right] \right) \sin(k\pi x) \,.
\end{aligned}$$

By comparing these equations, it is obvious that the only difference between them is a phase shift with regard to $\eta = ct - bx$, because $\cos(\alpha) = \sin(\alpha + \pi/2)$ for all $\alpha \in \mathbb{R}$. By substituting these into (14), one at a time, a lengthy but trivial calculation verifies that both are real-valued solutions of the original equation. The undetermined phase and amplitude are fine, because we did not specify any initial conditions. These solutions just determine possible free vibration behaviour.

Note that the complex-valued solution (32) is separable as a product of functions of x and t, but its real and imaginary parts are not.

To finish this section, we list some alternative representations for the solution, and observe certain properties from them. A classical and very compact way to solve the problem is to directly substitute (1) into (14), assume a complex exponential space component, and solve the characteristic polynomial of $W(x)$. This way we obtain the complex-valued space component as

$$W(x) = \beta \left[e^{-ik\pi x(1+\lambda)} - e^{+ik\pi x(1-\lambda)} \right] \,, \tag{34}$$

where $\lambda \equiv V_0/C$, $C \equiv \sqrt{T/m}$, β is free, and x is the dimensionless space coordinate. From this form, it is apparent that if $V_0 = 0$, the space component reduces to $\sin(k\pi x)$, by choosing $\beta = -1/2i$ and applying de Moivre's formula. A nonzero velocity causes a shift into both terms, and the space component becomes complex-valued.

For general V_0, the solution (34) can be represented in the following alternative way after applying some trigonometric identities:

$$W(x) = \gamma \sin(k\pi x) e^{-\lambda k\pi x i} \,, \tag{35}$$

where $\gamma = -2i\beta$. From this representation, a velocity-dependent phase shift along the string is apparent, as reported by Wickert and Mote (1990); Mote and Wickert (1991).

Using the same notation as above, when the time component is included, the full solution (picking the $-$ sign for s to get rid of the $\mp$) can be written in the form

$$\begin{aligned} w &= \beta e^{iC\frac{\tau}{\ell}[\lambda^2-1]k\pi t}\left[e^{-ik\pi x(1+\lambda)} - e^{+ik\pi x(1-\lambda)}\right] , \quad k \in \mathbb{Z} \\ &\equiv \beta e^{i\tilde{c}t}\left[e^{i\tilde{a}x} - e^{i\tilde{b}x}\right] = \beta\left[e^{i(\tilde{a}x+\tilde{c}t)} - e^{i(\tilde{b}x+\tilde{c}t)}\right] , \\ &= \beta\left[e^{i<(x,t),(\tilde{a},\tilde{c})>} - e^{i<(x,t),(\tilde{b},\tilde{c})>}\right] , \end{aligned} \tag{36}$$

where $\tilde{a}$, $\tilde{b}$ and $\tilde{c}$ are defined by the obvious identifications. The symbol $< \cdot,\cdot >$ denotes the usual scalar product. From (36) it can be seen that the solution, when considered in the space-time plane, is a superposition of two plane waves with different directions of propagation.

From (36), it is also directly obvious why the real and imaginary parts of the solution can satisfy the equation (15) separately. The differentiation in the Coriolis term is of the second order when considered in the (x, t) plane, and this conveniently eliminates the imaginary unit that would result from first-order differentiation of (36) with respect to only either x or t. Indeed, we have by equation (2) (page 47) that this separation property must hold for the original, full equation (15), but — because s_*, by equation (33), is imaginary — it cannot hold for the space-component equation (28).

2.1.5 Summary and conclusion

We considered the classical axially moving ideal string with zero Dirichlet (pinhole) boundary conditions. The problem was set up following Archibald and Emslie (1958), by transforming the classical ideal string equation from the comoving coordinates to the laboratory coordinates. The classical moving string equation was thus obtained.

At the critical velocity $|V_0| = C$, one of the terms in the PDE is eliminated, requiring a separate analysis. This analysis was performed, and it was shown that at the critical velocity, a steady state occurs, for which any function $w(x)$ satisfying the boundary conditions is a solution.

The free vibrations of the moving string for $|V_0| \neq C$ were solved following the approach of Swope and Ames (1963). The eigenfrequencies and eigenfunctions were found explicitly. The result agrees with Swope and Ames (1963), as expected. It was seen that the eigenvalues come in pairs $\pm s$, which is also as expected (Huseyin and Plaut, 1974–1975, p. 166; Mote and Wickert, 1991).

An elementary argument was developed, based on quasistatic transition and the maximum-amplitude preserving property of time-harmonic vibration, suggesting that the ideal string experiences no instability at the critical velocity. A definite answer to the question requires techniques beyond eigenvalue analysis; the question has been investigated by Wang et al. (2005), who found that there indeed is no instability.

2.2 String with damping and an elastic foundation of the Winkler type

In this section, we extend the above analysis into the case, where also first-order derivatives and a reaction term are present in the PDE.

As was noted in the literature review, added-mass models are often used to approximate fluid-structure interaction with surrounding air. Furthermore, the viscosity of air is sometimes approximated by adding first-order terms to the dynamic equation (see e.g. Vaughan and Raman, 2010, for the case of a travelling plate), using the idea that first-order terms in an elastic equation cause damping. The values of the viscosity coefficients are then chosen empirically.

It is fairly simple to extend the above free vibration analysis (subsection 2.1.4) to account for this situation. Since the required transformations will generate a linear reaction term regardless of whether one is present in the original equation, we will include one right from the start for generality. The reaction term, in this context, is also known as a *Winkler foundation* or *elastic foundation*.[8] Roughly speaking, this term behaves like a grid of uniformly spaced, independent linear springs, which have their rest levels at $w(x) = 0$ for each fixed x. It is assumed that the vibrating string never breaks contact with the elastic foundation.

2.2.1 Problem setup

Consider the PDE

$$w_{tt} + 2bw_{xt} + cw_{xx} + A_1 w_t + A_2 w_x + Bw = 0 \,. \tag{37}$$

Compare (15). We have fixed $a = 1$, and added the first-order and reaction terms. Equation (37) is the general, constant-coefficient, second-order, autonomous (does not explicitly contain the independent variables), homogeneous partial differential equation in two variables.

Again, we take the classical zero Dirichlet boundary conditions describing a string travelling through two pinholes, (16). For convenience, we repeat them here:

$$w(0,t) = w(1,t) = 0 \,,$$

[8] Originally investigated by Winkler (1867).

where $w = w(x,t)$. If there is no elastic foundation ($B = 0$), the setup looks the same as for the ideal string, Figure 8 (p. 56).

2.2.2 Free vibration analysis

We will derive an analytical free vibration solution for (37) by reducing it to the Klein–Gordon equation, for which solutions are known. We first eliminate the Coriolis term w_{xt}, as was done for (15) earlier. Then, standard substitutions (see e.g. Polyanin (2004b), or the corresponding handbook from the same author) can be used to get rid of the first-order terms.

By the same discriminant check as earlier, we know that with our definitions for b and c, (37) is (globally) hyperbolic. We use the same coordinate transformation as above, (25) and (26), now applying it to (37). The second-order terms were handled above, so we only need to determine the lower-order ones. The x and t derivatives become, by the chain rule,

$$\frac{\partial w}{\partial t} = \frac{\partial w}{\partial \eta}\frac{\partial \eta}{\partial t} + \frac{\partial w}{\partial \xi}\frac{\partial \xi}{\partial t} = c\frac{\partial w}{\partial \eta} \tag{38}$$

$$\frac{\partial w}{\partial x} = \frac{\partial w}{\partial \eta}\frac{\partial \eta}{\partial x} + \frac{\partial w}{\partial \xi}\frac{\partial \xi}{\partial x} = -b\frac{\partial w}{\partial \eta} - \sqrt{b^2 - c}\,\frac{\partial w}{\partial \xi}\,. \tag{39}$$

Note that the w_x term has transformed into a linear combination in the new coordinates. Thus, if we have a w_x term in our equation, we need to consider the form with the first-order terms both in ξ and η, regardless of whether the original equation had a w_t term.

Inserting (38)–(39) into (37), we have

$$w_{\eta\eta} - w_{\xi\xi} + (A_1 c - A_2 b) w_\eta - A_2\sqrt{b^2 - c}\, w_\xi + Bw = 0\,. \tag{40}$$

Let us compact the notation by defining

$$\beta = A_1 c - A_2 b \tag{41}$$

$$\varkappa = A_2\sqrt{b^2 - c}\,, \tag{42}$$

so that (40) becomes

$$w_{\eta\eta} - w_{\xi\xi} + \beta w_\eta - \varkappa w_\xi + Bw = 0\,. \tag{43}$$

The signs of β and $\varkappa$ have been chosen so that the signs of the first-order terms match the second-order ones.

Next, we will get rid of the first-order terms. We substitute

$$w(\xi,\eta) := \exp(\alpha\eta)\, v(\xi,\eta)\,.$$

The new unknown function v is still a function of both ξ and η, so no new assumptions are made about the solution. By choosing α suitably, the w_η term can be eliminated and only zeroth- and second-order derivatives in η will remain. The resulting factor $\exp(\alpha\eta)$ that is common to all terms is obviously irrelevant. This

is the technique that transforms the telegraph equation into the Klein–Gordon equation, and it can be found in standard references (e.g. Polyanin, 2004b and references therein). Then, a similar substitution can be made to get rid of the w_ξ term.

Performing both steps simultaneously, the substitution that eliminates both w_ξ and w_η is

$$w(\xi,\eta) = \exp\left(-\frac{\beta}{2}\eta - \frac{\varkappa}{2}\xi\right) u(\xi,\eta) \,, \tag{44}$$

where $u(\xi,\eta)$ is a new unknown function. Note that the asymptotic behaviour of the solution will depend on the sign of β, i.e. the signs and relative magnitudes of A_1 and A_2. Also note that because $c < 0$, the sign of the time term has switched: thus $\eta \propto -t$. If both A_1 and A_2 are positive, then β is negative. Thus $(-\beta)(-t)$ is negative and the damping introduces a time-decaying factor, as expected.

It is slightly more difficult to see toward which end of the domain the solution will be skewed due to the $-(\varkappa/2)\xi$ term, but a similar argument can be developed. By physical intuition, one would expect the viscosity to cause the solution to decay toward the direction of axial motion. However, this depends on the relative magnitudes of b and A_2, as both $\xi \propto -x$ and $\eta \propto -x$, and the signs of these terms in (44) are different (assuming positive A_2).

With the substitution (44), and neglecting the common exp factor, equation (43) becomes

$$u_{\eta\eta} - u_{\xi\xi} + \frac{1}{4}\left(\varkappa^2 - \beta^2 + 4B\right) u = 0 \,.$$

Defining the new constant

$$\gamma = \frac{1}{4}\left(\beta^2 - \varkappa^2 - 4B\right) \,, \tag{45}$$

we can write

$$u_{\eta\eta} - u_{\xi\xi} = \gamma u \,, \tag{46}$$

which is the Klein–Gordon equation.

We see immediately that the special case $\gamma = 0$ has the same form as a classical travelling string with no damping or reaction terms, which was already handled above. Thus the solution in the special case is (44), where $u(\xi,\eta)$ is given by the w in equation (31), for which s and ω are determined by (30) and (29) respectively. Below, we assume $\gamma \neq 0$.

The final task is to find a free vibration type solution for (46). In the transformed coordinates, let us use the classical trial function:

$$u(\xi,\eta) = \exp(s\eta)\, U(\xi) \,, \tag{47}$$

where s is the complex eigenfrequency on the η axis. Inserting (47) into (46) and neglecting the common exp factor gives

$$s^2 U - U'' = \gamma U \,, \qquad \text{i.e.} \qquad U'' = (s^2 - \gamma) U \,. \tag{48}$$

Equation (48) is an eigenvalue problem for (s, U). It differs from the previous case in only that the eigenvalue has shifted from s^2 to $s^2 - \gamma$. Thus, by (48) and the boundary conditions (16), we again have

$$U = \sin(\omega\xi) \,, \tag{49}$$

where ω is to be determined from (16). Again, a quick inspection of the boundary conditions (16) suggests that

$$\omega = -\frac{k\pi}{\sqrt{b^2 - c}} = -\frac{k\pi\ell}{C\tau} \,, \quad k \in \mathbb{Z}^+ \,,$$

i.e. we have the same solution for ω, equation (29), as in the original undamped case. Same remark about applying the boundary conditions via a separable solution applies as in the original case: lines of constant x have been transformed into lines of constant ξ (refer to Figure 9, p. 62).

Substituting (49) into (48), we obtain

$$-\omega^2 U = (s^2 - \gamma)U \,,$$

and thus

$$s^2 = \gamma - \omega^2 \qquad \Leftrightarrow \qquad s = \pm\sqrt{\gamma - \omega^2} \,. \tag{50}$$

We see that the quantity s^2 is always real; thus s is always either pure imaginary or pure real. However, before we make any elastic stability conclusions from this, we must apply the backtransformation (44). The transformation has made the problem easier to solve, but in the transformed space, the stability behaviour differs from the original. This is because the transformed problem is missing the damping terms.

The kth complex eigenfrequency s in (ξ, η) coordinates is found from (50) and (29) as

$$s^2 = \gamma - \frac{k^2\pi^2}{b^2 - c} = \gamma - \frac{k^2\pi^2\ell^2}{\tau^2 C^2} \,. \tag{51}$$

The transformed solution in the transformed coordinates is then

$$u(\xi, \eta) = \exp(s\eta)\, \sin(\omega\xi) \,, \tag{52}$$

which is of the same form as (31) in the previous problem, but now with s given by (51).

By applying the backtransformations (51), (45), (44), (42), (41), (29), (26), and (25), the solution (52) can be converted to the original (x, t) coordinate system.

2.2.3 Explicit expression for eigenfrequencies

Let us perform the backsubstitution part of the way. This will serve as a simple example for the analysis of complex-valued eigenfrequencies that will be done numerically to our main system of interest, beginning in Section 6.3.

For dynamic stability analysis via Bolotin's approach, we need the coefficient of t in the resulting exp. Using (52) and (44), the full solution in (ξ, η) coordinates, including the damping terms, is

$$w(\xi, \eta) = \exp\left(-\frac{\beta}{2}\eta - \frac{\varkappa}{2}\xi\right) \exp(s\eta) \sin(\omega\xi) \ .$$

This separates as

$$w(\xi, \eta) = \exp\left(\left[s - \frac{\beta}{2}\right]\eta\right) \cdot \exp(-\frac{\varkappa}{2}\xi) \sin(\omega\xi) \ .$$

Note that ξ does not contribute to the component that will eventually involve t. This is important, so that we can extract $\exp(\hat{c}t)$ as an independent factor (where $\hat{c}$ is some constant coefficient). Because again by (26) we have $\eta = ct - bx$, we see that for this problem, the coefficient of t in the exp in the final complex-valued (x, t) solution is

$$s_* = c[s - \beta/2] = c\left[\pm\sqrt{\gamma - \omega^2} - \beta/2\right] \ , \tag{53}$$

where the last form follows from (50), γ is given by (45), β by (41), and ω by (29). Again, the symbol s_* means that (53) is expressed in (x, t) coordinates (as opposed to (ξ, η) coordinates). We will plot (53) for some choices of parameter values in subsection 2.2.5; see Figures 11–21.

The value (53) determines the stability of the modified system. Due to the $\beta/2$ term, we see a global (but V_0-dependent) shift along the real axis for all eigenvalues. This is typical for damped systems (Bolotin, 1963).

The contribution of the damping term is always purely real. It is likely that if we take physically meaningful values for all coefficients, $-c\beta < 0$ and the square root is imaginary. In such a case, (53) represents exponentially decaying time-harmonic vibrations. We can be a bit more exact. In the subcritical regime, $c < 0$, and if $A_1 > 0$ and $A_2 \geq 0$, then $\beta < 0$ for positive V_0 (see equations (41), (14) and (15)). If $A_2 = 0$, this holds also for negative V_0. If $A_2 > 0$, negative V_0 will reduce the magnitude of β, but for sufficiently small V_0, β will remain negative. Hence $c\beta > 0$, and $-c\beta < 0$, at least near $V_0 = 0$.

In the limit $V_0 \to C$ (or $V_0 \to -C$), we have $s_* \to 0$ just like for the undamped system. This suggests the existence of a steady state there. However, keep in mind that our solution is only applicable if $c \neq 0$ (i.e., $V_0 \neq C$), because at this one point the w_{xx} term disappears from (37) and our coordinate transformation is no longer valid. To determine the situation at $V_0 = C$, we would need to solve the special case $c = 0$ separately, as was done for the undamped system in subsection 2.1.3.

Note the dependence of the quantities in (53) on the axial velocity: $c = c(V_0)$, $\beta = \beta(b, c) = \beta(V_0)$ and $\gamma = \gamma(\beta) = \gamma(V_0)$. The quantity $\omega = \omega(k)$ does not depend on the velocity (see (29); the solution is required to fulfill the boundary conditions, which do not depend on the velocity), but depends on the

number of the vibration mode; thus each mode has a different base frequency (at $V_0 = 0$), as expected. These frequencies also differ from the ones of the undamped system; if $\gamma > 0$, the frequencies of the modified system are lower than those of the original, and if $\gamma < 0$, higher.

If $\gamma < \omega^2$, the quantity under the square root is negative, and the contribution of this term is purely imaginary (it represents time-harmonic vibrations). From (29), we see that $|\omega(k)|$ increases as the mode number k increases. Thus at $V_0 = 0$, the negativity criterion breaks most easily at the low end. If $\exists k_0 : \omega(k)^2 < \gamma \; \forall \; 1 \leq k \leq k_0$ (first few modes), these modes cannot vibrate, but either just decay or grow exponentially, depending on the sign of the resulting s_*. Note that this also depends on the sign and relative magnitude of β. Because $\gamma = \gamma(V_0)$, the other way the criterion can break is when $|V_0|$ is "large enough", due to the β^2 term in γ, which leads to a fourth-degree polynomial with a positive leading coefficient. This suggests that asymptotically, we always have $\operatorname{Im} s_* = 0$. We will observe both phenomena in the plots in subsection 2.2.5, but first we will do a proper stability analysis.

2.2.4 Instability thresholds

In this section we will analyze the real and imaginary parts of (53), and extract an important asymptotic property.

Steady-state solutions Let us concentrate on the whole expression first. Upon backsubstituting in terms of $b = V_0\tau/\ell$, $c = (V_0^2 - C^2)\tau^2/\ell^2$ and $C = \sqrt{T/m}$ (note that these are connected by the relation $c = b^2 - C^2\tau^2/\ell^2$), for the kth mode equation (53) becomes

$$s_* = c\left[\pm\sqrt{\frac{1}{4}\left[(A_1c - A_2b)^2 - (A_2C\frac{\tau}{\ell})^2 - 4B\right] - \frac{k^2\pi^2\ell^2}{\tau^2C^2}} - \frac{1}{2}(A_1c - A_2b)\right] . \tag{54}$$

This may be zero if $c = 0$, or if the parenthetical expression is zero. The former case was already analyzed, leading to the solutions $V_0 = \pm C$. In the latter case, for a fixed k,

$$f^{\pm}(V_0;k) \equiv \pm\sqrt{\frac{1}{4}\left[(A_1c - A_2b)^2 - (A_2C\frac{\tau}{\ell})^2 - 4B\right] - \frac{k^2\pi^2\ell^2}{\tau^2C^2}} - \frac{1}{2}(A_1c - A_2b) = 0 . \tag{55}$$

This is a set of two functions, each corresponding to a different eigenvalue s_*.

Because the second term is always real-valued for real V_0, we see that (55) can hold only if the first term is real. Thus, if a solution exists, the quantity under the square root must be nonnegative, i.e. $\gamma(V_0) - \omega(k)^2 \geq 0$. The conditions for this were analyzed above.

We see that the sign of the first term of (55) depends only on the sign chosen

in the $\pm$. We observe that (55) is of the form

$$f^{\pm}(a_1, a_2) = \pm\sqrt{a_1^2 + a_2} - a_1 \,, \tag{56}$$

where $a_1 \equiv \beta/2 = (A_1 c - A_2 b)/2$, and we have collected the rest of the terms under the square root into a_2. If $a_1 > 0$, only the function f^+ can be zero, and additionally it must hold that $a_2 = 0$. Similarly, if $a_1 < 0$, only f^- can be zero, and again we must have $a_2 = 0$. However, a_2 does not depend on V_0; only a_1 does. Thus, in either case, (55) has no solution in terms of V_0. Finally, since it has no solution in the case $\gamma(V_0) - \omega(k)^2 < 0$, either, we conclude that equation (55) has no (real) solutions at all (in terms of V_0).

Finally, note that for certain very special parameter combinations, a_2 may vanish for a single mode number k. Because all other quantities in a_2 are squared, this can only occur if $B < 0$, i.e. the reaction coefficient (elastic foundation modulus) is negative. This is unrealistic, but for completeness of mathematical treatment we will make some remarks. In this case, $f^+ = 0$ for all V_0 for which $a_1 > 0$, and $f^- = 0$ for all V_0 for which $a_1 < 0$. Assuming positive A_1, A_2 and b, we have that c, and hence a_1, is negative for all $|V_0| < C$, and positive for all $|V_0| > C$. Thus, for this very special case, the eigenvalue corresponding to the $+$ sign in (55) vanishes for all $|V_0| > C$, and the one corresponding to the $-$ sign vanishes for all $|V_0| < C$. We conclude that under the purely theoretical condition of a negative, specially chosen value for foundation modulus B, a steady-state solution may develop for this equation at any V_0.

Excluding the special case, s_* can pass through the origin only at $V_0 = \pm C$. If there are other instability thresholds, they must be of the dynamic type (Re $s_* = 0$ with Im $s_* \neq 0$).

We have fully analyzed the case $\gamma(V_0) - \omega(k)^2 \geq 0$. Next we will investigate what happens when $\gamma(V_0) - \omega(k)^2 < 0$, making the square root in (54) imaginary.

Real part Let us look for the dynamic instability thresholds. We will attempt to find the remaining zeroes of the real part of s_*, if any exist. For the sake of simplicity, let us assume that A_1 and A_2 do not depend on V_0. (We will remark upon introducing this dependence in A_2 at the end.) When $\gamma(V_0) - \omega(k)^2 < 0$, we have

$$\begin{aligned}
\text{Re } s_* &= -\frac{c}{2}(A_1 c - A_2 b) \\
&= -\frac{c}{2}\left[A_1(V_0^2 - C^2)\frac{\tau^2}{\ell^2} - A_2 V_0 \frac{\tau}{\ell}\right] \\
&= -\frac{c}{2}\left[\left(A_1\frac{\tau^2}{\ell^2}\right)V_0^2 + \left(-A_2\frac{\tau}{\ell}\right)V_0 + \left(-A_1 C^2\frac{\tau^2}{\ell^2}\right)\right] \,,
\end{aligned} \tag{57}$$

where the parenthetical expression is a second-order polynomial in V_0. With the c in the front, Re s_* is a fourth-order polynomial in V_0. Two of its zeros are, of course, the aforementioned $V_0 = \pm C$. The other two zeros are those of the

parenthetical term. A simple calculation finds that

$$\begin{aligned} V_0^{\text{crit}} &= \frac{1}{2A_1\frac{\tau^2}{\ell^2}}\left(A_2\frac{\tau}{\ell} \pm \sqrt{A_2^2\frac{\tau^2}{\ell^2} + 4A_1^2C^2\frac{\tau^4}{\ell^4}}\right) \\ &= \frac{1}{2}\frac{A_2}{A_1}\frac{\ell}{\tau} \pm \sqrt{\frac{1}{4}\frac{A_2^2}{A_1^2}\frac{\ell^2}{\tau^2} + C^2} \\ &= M \pm \sqrt{M^2 + C^2} \end{aligned} \tag{58}$$

where we have defined

$$M \equiv \frac{1}{2}\frac{A_2}{A_1}\frac{\ell}{\tau}\,. \tag{59}$$

The points (58) are the flutter instability thresholds. We can see that they depend on the relative magnitude of the viscosity terms, and on T and m (via C). They do not depend on k, because (57) now does not involve the $\gamma(V_0) - \omega(k)^2$ term.

Because the quantity under the square root in (58) is always positive, V_0^{crit} is always real. Thus, these thresholds exist, if and only if (57) is a valid representation for Re s_* at that value of V_0. That is, if we compute V_0^{crit} from (58)–(59), and find for a given mode number k that $\gamma(V_0^{\text{crit}}) - \omega(k)^2 < 0$, then the threshold exists for that mode k.

If we find that $\gamma(V_0^{\text{crit}}) - \omega(k)^2 > 0$, the threshold does not exist for the mode k. This is because if $\gamma(V_0^{\text{crit}}) - \omega(k)^2 > 0$, then (57) is not applicable at that value of V_0^{crit}. In principle, the threshold should then be solved from the full expression (54), since all terms contribute to the real part. However, as we saw above, in that case there is no solution in terms of V_0.

Doing all the backsubstitutions, we obtain the function $\gamma(V_0)$ from (45) as

$$\begin{aligned} \gamma(V_0) &= \frac{1}{4}\left(\beta^2 - \cancel{\alpha}^2 - 4B\right) \\ &= \frac{1}{4}\left((A_1c - A_2b)^2 - A_2^2(b^2 - c) - 4B\right) \\ &= \frac{1}{4}\left(A_1^2c^2 - 2A_1A_2cb + A_2^2b^2 - A_2^2b^2 + A_2^2c\right) - B \\ &= \frac{1}{4}\left(A_1^2c^2 - 2A_1A_2cb + A_2^2c\right) - B \\ &= \frac{1}{4}c\left(A_1^2c - 2A_1A_2b + A_2^2\right) - B \\ &= \frac{1}{4}\left[V_0^2 - C^2\right]\frac{\tau^2}{\ell^2}\left(A_1^2\left[V_0^2 - C^2\right]\frac{\tau^2}{\ell^2} - 2A_1A_2V_0\frac{\tau}{\ell} + A_2^2\right) - B\,. \end{aligned} \tag{60}$$

It was noted above that V_0^{crit} does not depend on k. Recall that $\omega(k) = k\pi\ell/(\tau C)$; hence ω grows with increasing k. Thus, when the mode number k becomes large enough, it will always be the case that $\gamma(V_0^{\text{crit}}) - \omega(k)^2 < 0$, and the flutter threshold (58)–(59) exists (i.e. there will be a point such that Re $s_* = 0$).

Now, let us consider the asymptotic behaviour of (57) in terms of V_0. For completeness of analysis, let us handle the unrealistic case $A_1 < 0$ (negative

damping, i.e. amplification) first. In this case, the coefficient of the highest-order term in (57) is positive (if we expand the c in front, too); thus the expression is positive for any V_0 that is smaller than the smallest real root, or larger than the largest real root of the fourth-degree polynomial. This corresponds to an instability as $|V_0|$ increases (quasistatically) without bound.

The case $A_1 > 0$ is more problematic. Now the coefficient of the highest-order term in (57) is negative. As $|V_0|$ increases without bound, the expression eventually becomes negative and its magnitude grows indefinitely. This seems to imply that the strength of damping increases without bound as $V_0 \to \pm\infty$. For some parameter values, we will see numerically that this indeed happens.

However, here we must be careful. Recall that equation (58) is valid only if $\gamma(V_0^{\text{crit}}) - \omega(k)^2 < 0$. For some parameter values, this criterion may fail as $|V_0|$ increases without bound. As was mentioned, in these cases, the full expression (54) must be used for the real part instead of (57).

The conclusion from the analysis of the real part is that up to two additional values of V_0 may exist at which the damping vanishes (Re $s_* = 0$), and these values are the same for each mode k.

The coefficient A_1 controls the amount of damping in the $\partial/\partial t$ term in (37). From (59) we see that in the limit of vanishing A_1, $|M|$ increases without bound, and the thresholds approach 0 and $\pm\infty$ (the $\pm$ depending on the sign of A_1). Trivially, the threshold that approaches 0 corresponds to no damping at $V_0 = 0$ in the limiting case of vanishing fluid viscosity.

The coefficient A_2 controls the damping in the $\partial/\partial x$ term. If it is zero, the flutter thresholds are placed symmetrically around the origin. If it is nonzero, there is a shift. This is as expected: considering the physics of the situation, the value of A_2 depends linearly on the axial velocity (in the Euler coordinates) of the surrounding fluid, and possibly that of the moving string (or panel). We will finalize the handling of this issue at the end of Section 3.2. For now, it is sufficient to know that if the whole fluid mass is assumed to move along with the travelling panel, instead of having an independent axial velocity, there will be a linear dependence on V_0; otherwise not. If there is a linear dependence on V_0 in A_2, this changes the coefficient of V_0^2 in (57).

Imaginary part Now, let us investigate the imaginary part. The thresholds for its zeroes indicate the start and end of ranges where a given mode may either vibrate (depending on the real part, in a stable manner, or in an exponentially growing or decaying manner), or only grow or decay exponentially.

The imaginary part of s_{xt} is nonzero only if $\gamma(V_0) - \omega(k)^2 < 0$. When this occurs, we have from (54) that

$$i \operatorname{Im} s_* = \pm c \sqrt{\frac{1}{4}\left[(A_1 c - A_2 b)^2 - (A_2 C \frac{\tau}{\ell})^2 - 4B\right] - \frac{k^2\pi^2\ell^2}{\tau^2 C^2}} \,. \tag{61}$$

The zeroes of this expression occur at $c = 0$ (i.e. $V_0 = \pm C$), and at where the quantity under the square root is zero. For the latter, we have a fourth-degree

polynomial equation in V_0,

$$4 \cdot p_4(V_0;k) \equiv (A_1 c - A_2 b)^2 - \left[(A_2 C \frac{\tau}{\ell})^2 + 4B + 4\frac{k^2\pi^2\ell^2}{\tau^2 C^2} \right] = 0 \qquad (62)$$

$$\begin{aligned} &\Leftrightarrow \quad (A_1 c - A_2 b)^2 = \left[(A_2 C \frac{\tau}{\ell})^2 + 4B + 4\frac{k^2\pi^2\ell^2}{\tau^2 C^2} \right] \\ &\Rightarrow \quad A_1 c - A_2 b \;\; = \pm\sqrt{(A_2 C \frac{\tau}{\ell})^2 + 4B + 4\frac{k^2\pi^2\ell^2}{\tau^2 C^2}} \\ \Leftrightarrow \;\; &\left(A_1 \frac{\tau^2}{\ell^2} \right) V_0^2 + \left(-A_2 \frac{\tau}{\ell} \right) V_0 + \left(-A_1 C^2 \frac{\tau^2}{\ell^2} \right) = \pm\sqrt{(A_2 C \frac{\tau}{\ell})^2 + 4B + 4\frac{k^2\pi^2\ell^2}{\tau^2 C^2}} \,, \end{aligned} \qquad (63)$$

which, if A_1 and A_2 are independent of V_0, is a set of two second-degree polynomials in V_0 (one for each choice of sign in $\pm$). Let us call them $p_2^+(V_0;k)$ and $p_2^-(V_0;k)$. In (63), we have factored the original equation (62) as $p_4(V_0;k) = p_2^+(V_0;k) \cdot p_2^-(V_0;k) = 0$. Note that both signs in (63) correspond to the same eigenvalue s_*. This $\pm$ is independent of the $\pm$ in (61), which corresponds to different eigenvalues.

If A_2 depends on V_0, we cannot take the square root, but must solve the original fourth-degree problem directly instead.

In either case, because we have a fourth-degree polynomial, we see that for each mode k, there may be up to four additional values of V_0, where Im $s_* = 0$. These are different for each mode k, due to the right-hand side of (63), which contains $\omega(k)$. Thus these thresholds (if they exist) are spread out on the V_0 axis, in terms of mode number k.

We also see that regardless of the sign of A_1, the coefficient of the leading term (V_0^4) is positive. Thus, for any V_0 smaller than the smallest real root of p_4, and for any V_0 larger than the largest real root of p_4, we have $p_4(V_0;k) > 0$. On the other hand, $p_4(V_0;k) = \gamma(V_0) - \omega(k)^2$; it is the quantity under the square root in (54). In regions where it is positive, Im $s_* = 0$ as was noted above, and the square root contributes to Re s_* instead.

We have obtained an asymptotic result. For this system, eventually the imaginary part of each mode will reach zero, as $|V_0|$ increases without bound. We conclude that if any *flutter type* instabilities exist for this system, they must occur within such limits for $|V_0|$ that $|\text{Im } s_*| \neq 0$ is possible.

Outside the range of real roots of $p_4(V_0;k)$ in terms of V_0, any instabilities must be of the *divergence type*. However, for such values of V_0, all terms in (54) contribute to the real part. As was shown above, the only zeroes of the full expression are located at $V_0 = \pm C$. Hence, outside the real root range of $p_4(V_0;k)$, the real part (being continuous in V_0) cannot change sign. The conclusion is that the only possible divergence instabilities of this system are at $V_0 = \pm C$.

2.2.5 Graphical representations

This problem is already complicated enough that in addition to the solution in equation form, it is useful to have a visualization. Some eigenfrequency spectra described by equation (53) are plotted in Figures 11–21 for various values of the damping parameters A_1 and A_2. We have plotted up to mode number $k = 10$. The properties that were analytically shown above can be observed in the pictures.

Two kinds of plots are presented. Let $\lambda = V_0/C = V_0/\sqrt{T/m}$. The first kind of plot is a full 3D visualization in (λ, Re s, Im s) space, tracing out the eigenvalues as functions of λ. The second kind is the projection of the first onto the (λ, Re s) and (λ, Im s) planes. Both projections are plotted into the same image, with red (dark) lines denoting the real parts and blue (light) lines the imaginary parts. In the projection, the values $\lambda = \pm 1$ are indicated with a dashed line if they fall inside the plot range. Note that in the projection, several eigenvalues may fall onto the same point in the image; the 3D plots can be used to ease interpretation.

The values of the other parameters used in the plots are given in Table 1 on page 155. For convenience, we repeat them here: $T = 500$ N/m, $m = 0.08$ kg/m^2 (model seen as a panel in the membrane limit), and $\ell = 1$. The timescale parameter was chosen as $\tau = \ell/\sqrt{T/m}$, which leads to $\sqrt{b^2 - c} = 1$. Additionally for this model, there was no elastic foundation; $B = 0$.

The effect of the elastic foundation is not shown in the pictures, because to illustrate the effect of damping already requires quite a few examples, and there was not much difference in the results. It was found that if $B > 0$, the imaginary parts of the modes pack closer together, and there is more space between the lowest mode and the real axis. Otherwise the results were found to be very similar to the ones shown. Qualitative similarity is of course to be expected, because as was mentioned at the beginning, the solution process generates the linear reaction term, regardless of whether such a term is present in the original problem.

Four major cases are illustrated. First, in Figures 11–14 is the case of purely time-dependent, light damping. For this first case, four different zoom levels are shown, illustrating respectively the asymptotic behaviour for large λ, the point where the imaginary part of the first mode vanishes, the subcritical regime, and the critical region. We observe that Re $s_* \leq 0$ for all V_0. We see that, as was analyzed, the imaginary part vanishes for different modes at different values of V_0. It is also seen that asymptotically, the imaginary part vanishes for all modes, and each eigenvalue pair settles onto purely real values diverging from each other.

In Figures 15–16, the case with purely time-dependent heavy damping is shown. Here we show two zoom levels, illustrating the asymptotic behaviour and the subcritical regime. The local behaviour near the critical point looks very similar to the first case, and is not shown. Here also Re $s_* \leq 0$ for all V_0. We see that if the damping is strong enough, some modes start out as real-valued at $V_0 = 0$. This illustrates the remark about the case where $\gamma(V_0 = 0) < \omega(k)^2$ at the end of subsection 2.2.3.

The asymmetric case, with nonzero A_2 introducing a space-dependent com-

ponent in the damping, is illustrated in Figure 17. Only the asymptotic behaviour is shown. We observe that the behaviour is otherwise similar to the first case, but now the "handles" (onion-shaped regions of nonzero Im s_*) have become asymmetric with respect to V_0. Compare Figure 11, where one "handle" of the symmetric case can be seen. The subcritical regime and the local behaviour near the critical point look very similar to the symmetric case, so they are not presented separately.

In the final Figures 18–21, we illustrate what happens when $A_2 = V_0 A_1$, i.e. when the damping coefficients assume the form that is generated by a Lagrange (convective, material) derivative. The four different zoom levels show the asymptotic behaviour, the subcritical regime, the critical region, and the type of the instability, respectively. The behaviour is again symmetric with respect to V_0.

In this last case, we observe an interesting phenomenon. Figure 20 indicates that the damping has introduced an instability, which did not exist in the undamped system! This general effect of dissipation-induced destabilization, known as Ziegler's paradox, was discovered in 1952 (Kirillov and Verhulst, 2010). For some more examples of the topic, see also e.g. Datko and You (1991); Freitas et al. (1997); Krechetnikov and Marsden (2006).

Zooming further in, Figure 21 shows that the instability at $\lambda = \pm 1$ is of a special flutter type. The eigenvalues pass through the origin, but on the supercritical side of the critical point, $|\text{Im } s_*| > 0$ for all modes at $\lambda = 1 + \varepsilon$ with $\varepsilon > 0$ "small enough". From the Figure, with the parameter values used the upper limit for ε is slightly under $\varepsilon_{\max} \approx 0.004$. The imaginary part of the lowest mode vanishes first, and modes with different k do not interact (in this problem), so we can be sure that this same behaviour occurs even if we account for higher values of mode number k.

2.2.6 Summary and conclusion

Using the method of Swope and Ames (1963), the free vibrations were solved analytically for a moving string including damping and an optional elastic foundation term. The eigenfrequencies and the eigenfunctions were both obtained. The eigenfrequencies were illustrated graphically for various choices of damping parameter values. The derived analytical results provide a general qualitative description of the stability behaviour of the damped moving string. What remains is to provide such a description, which we will do now.

In realistic cases, all modes start as stable and damped at $V_0 = 0$. Excessive amounts of damping may cause some eigenvalues to become purely real at $V_0 = 0$, leading to modes that cannot vibrate, but only decay exponentially. Although it was not rigorously verified, the dynamic analysis suggests that some sort of steady state exists at $V_0 = \pm C$.

If the model is studied as a purely mathematical object, the modes eventually settle, one pair at a time, into a state with Im $s_* = 0$ as $|V_0|$ grows without bound. The eventual sign of the real part may depend on the problem parameters, but (for each mode separately) the sign cannot change after the point where

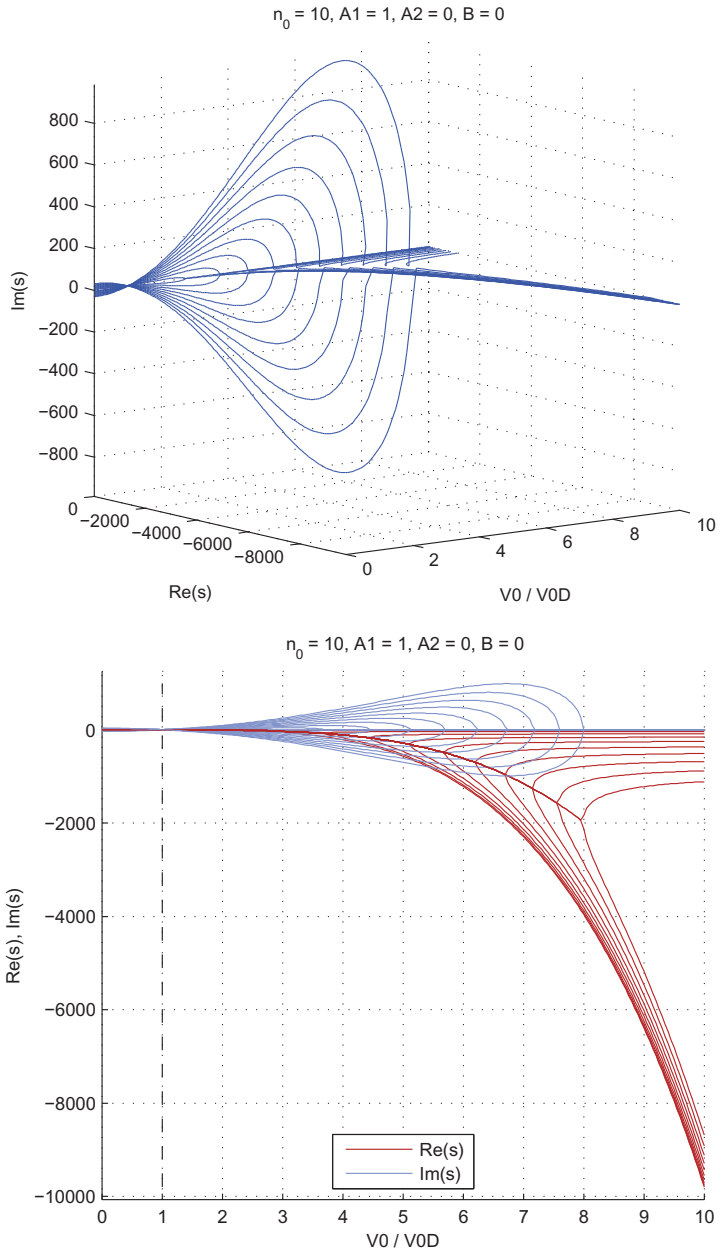

FIGURE 11 Eigenvalues of the damped moving string. Damping parameters $A_1 = 1$, $A_2 = 0$. Dimensionless velocity $\lambda = [0, 10]$, showing asymptotic behaviour for large λ. The solution is symmetric with respect to $\lambda = 0$, hence only the positive half is shown. *Top*: 3D plot in (λ, Re s, Im s) space. *Bottom*: projections onto the (λ, Re s) and (λ, Im s) planes. In the projection, blue (light) line denotes imaginary part, red (dark) line real part.

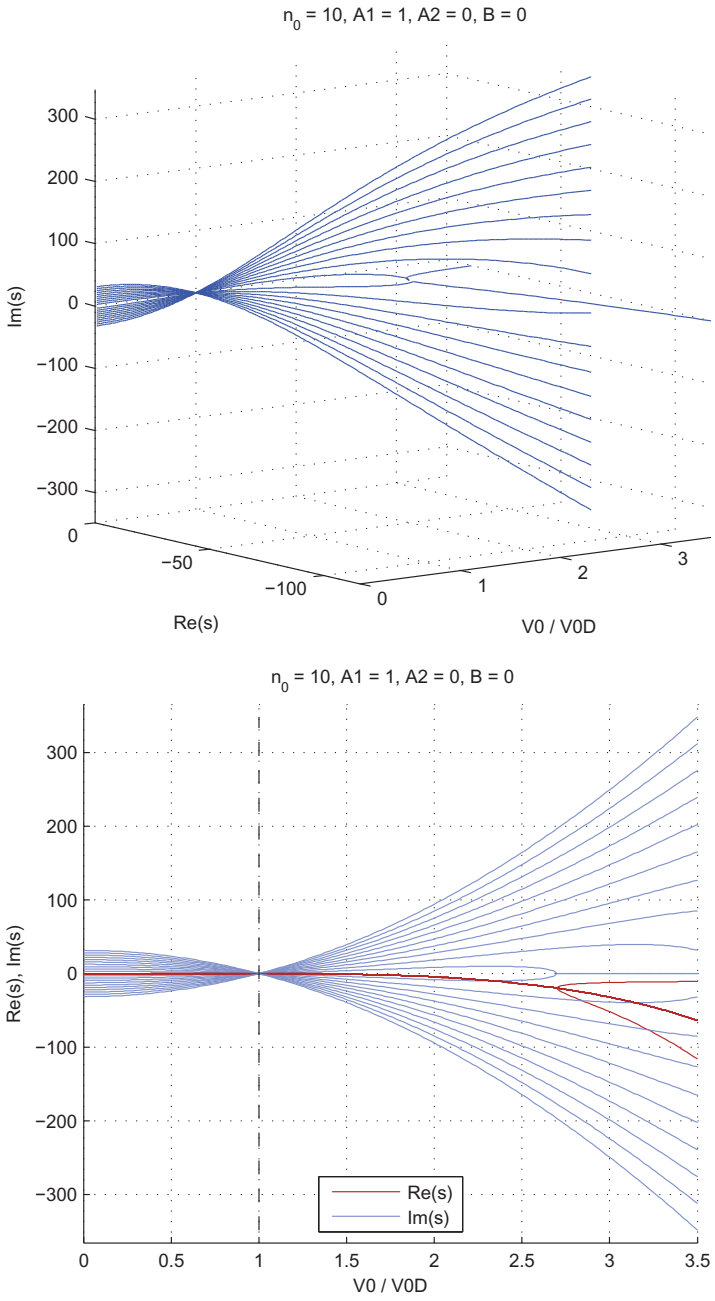

FIGURE 12 Eigenvalues of the damped moving string. Damping parameters $A_1 = 1$, $A_2 = 0$. Dimensionless velocity $\lambda = [0, 3.5]$, showing the point where the first mode becomes purely real. The solution is symmetric with respect to $\lambda = 0$, hence only the positive half is shown. *Top*: 3D plot in $(\lambda$, Re s, Im $s)$ space. *Bottom*: projections onto the $(\lambda$, Re $s)$ and $(\lambda$, Im $s)$ planes. In the projection, blue (light) line denotes imaginary part, red (dark) line real part.

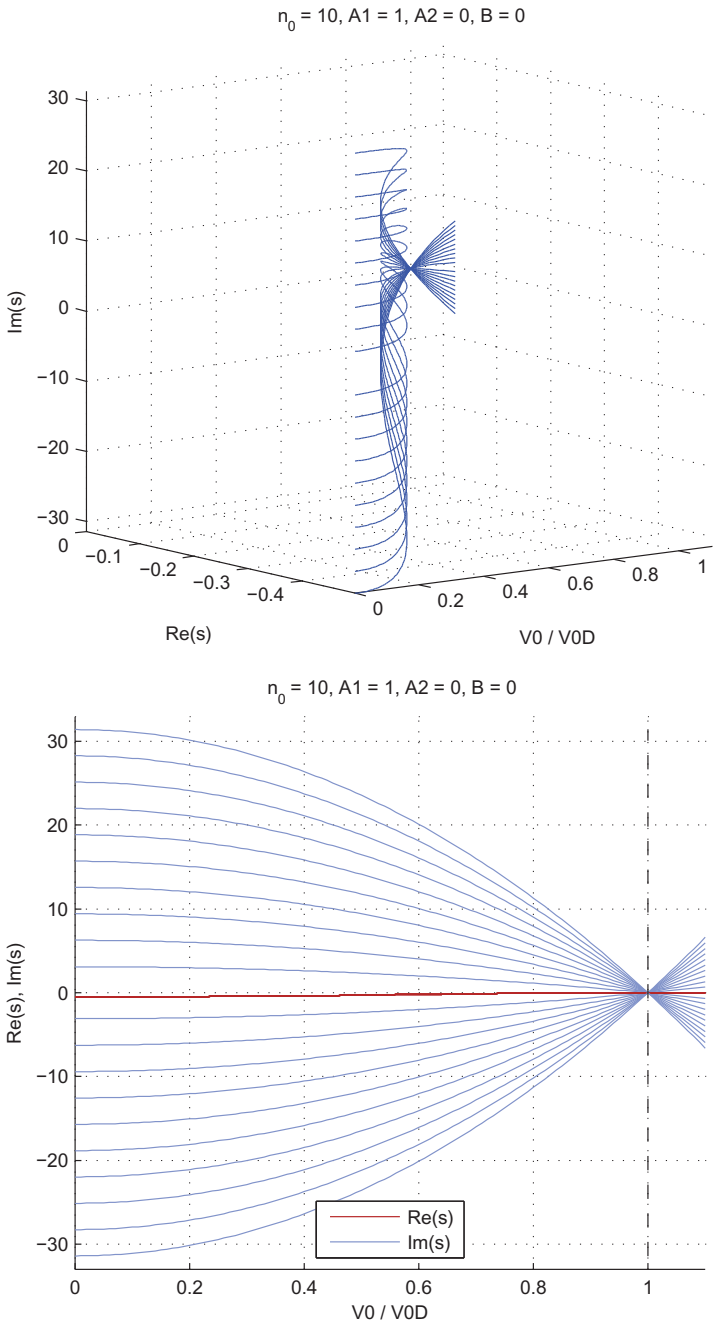

FIGURE 13 Eigenvalues of the damped moving string. Damping parameters $A_1 = 1$, $A_2 = 0$. Dimensionless velocity $\lambda = [0, 1.1]$, showing the subcritical regime. The solution is symmetric with respect to $\lambda = 0$, hence only the positive half is shown. *Top*: 3D plot in $(\lambda$, Re s, Im $s)$ space. *Bottom*: projections onto the $(\lambda$, Re $s)$ and $(\lambda$, Im $s)$ planes. In the projection, blue (light) line denotes imaginary part, red (dark) line real part.

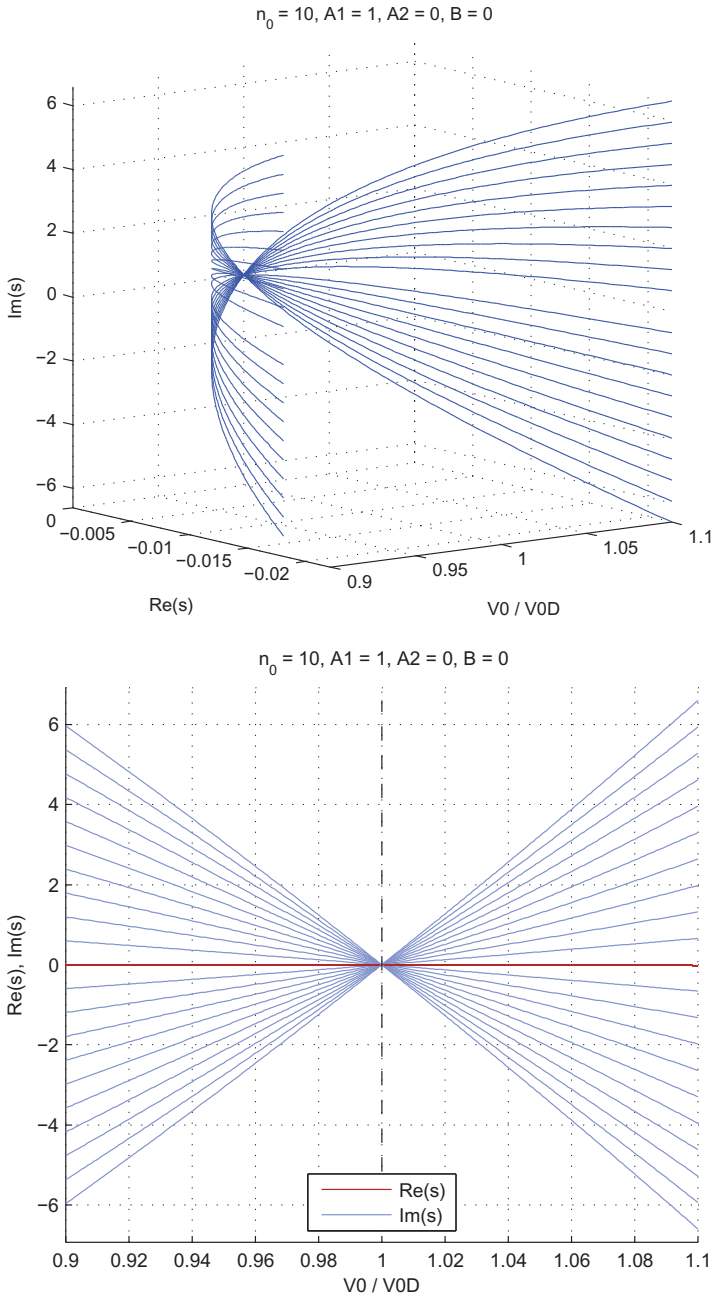

FIGURE 14 Eigenvalues of the damped moving string. Damping parameters $A_1 = 1$, $A_2 = 0$. Dimensionless velocity $\lambda = [0.9, 1.1]$, showing local behaviour near the critical point $\lambda = 1$. The solution is symmetric with respect to $\lambda = 0$, hence only the positive half is shown. *Top*: 3D plot in $(\lambda$, Re s, Im $s)$ space. *Bottom*: projections onto the $(\lambda$, Re $s)$ and $(\lambda$, Im $s)$ planes. In the projection, blue (light) line denotes imaginary part, red (dark) line real part.

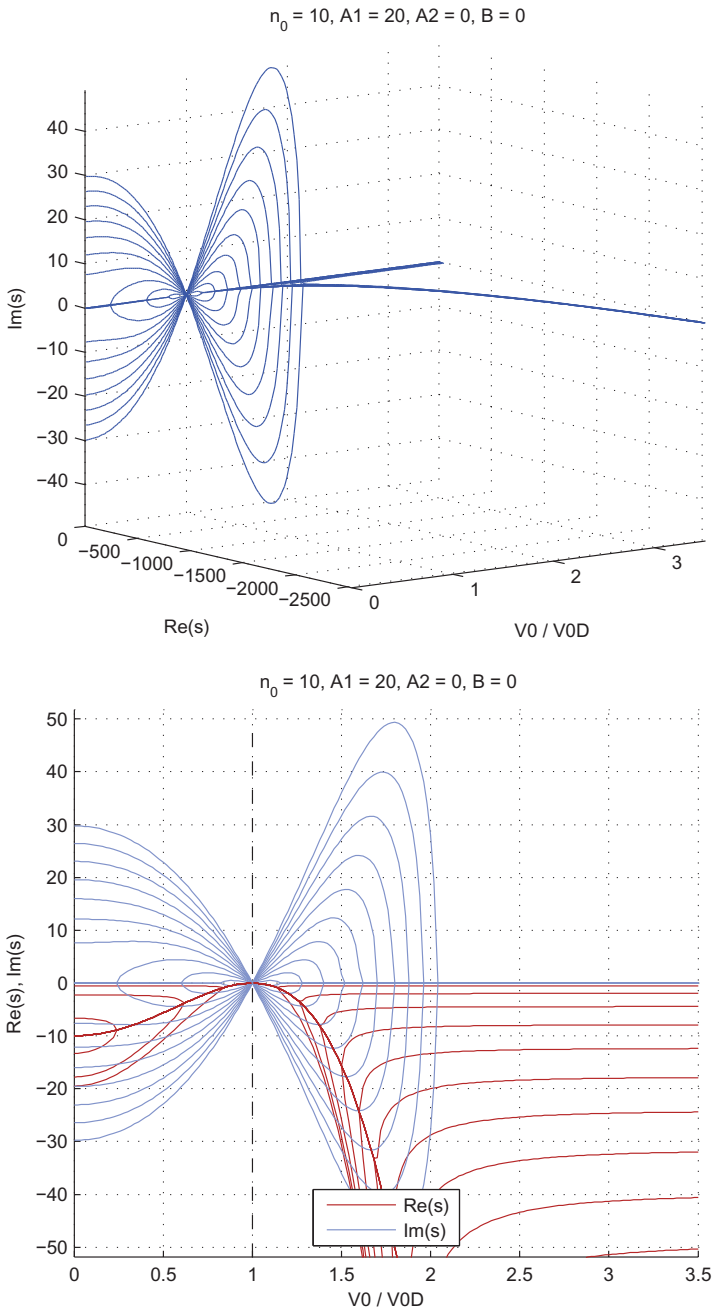

FIGURE 15 Eigenvalues of the damped moving string. Damping parameters $A_1 = 20$, $A_2 = 0$. Heavy damping generates some purely real eigenvalues at $\lambda = 0$. Dimensionless velocity $\lambda = [0, 3.5]$, showing asymptotic behaviour for large λ. The solution is symmetric with respect to $\lambda = 0$, hence only the positive half is shown. *Top*: 3D plot in (λ, Re s, Im s) space. *Bottom*: projections onto the (λ, Re s) and (λ, Im s) planes. In the projection, blue (light) line denotes imaginary part, red (dark) line real part.

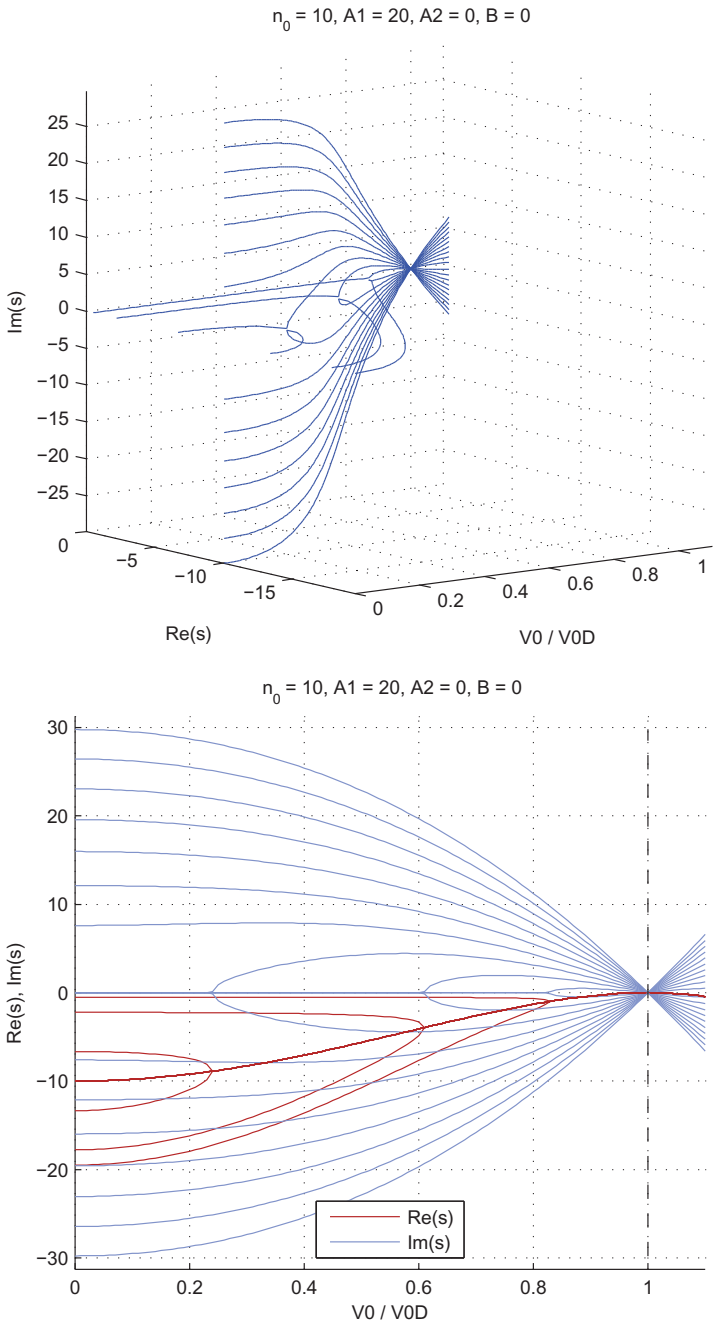

FIGURE 16 Eigenvalues of the damped moving string. Damping parameters $A_1 = 20$, $A_2 = 0$. Heavy damping generates some purely real eigenvalues at $\lambda = 0$. Dimensionless velocity $\lambda = [0, 1.1]$, showing the subcritical regime. The solution is symmetric with respect to $\lambda = 0$, hence only the positive half is shown. *Top*: 3D plot in (λ, Re s, Im s) space. *Bottom*: projections onto the (λ, Re s) and (λ, Im s) planes. In the projection, blue (light) line denotes imaginary part, red (dark) line real part.

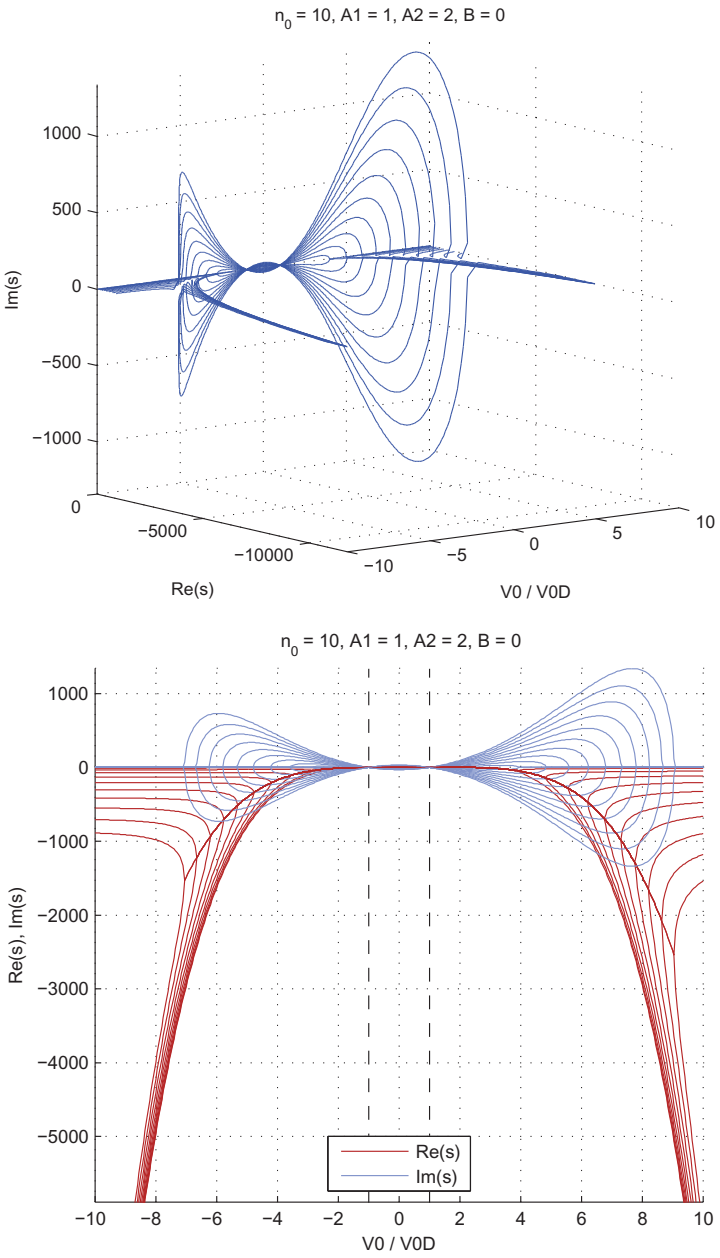

FIGURE 17 Eigenvalues of the damped moving string. Damping parameters $A_1 = 1$, $A_2 = 2$. Nonzero A_2 makes the spectrum non-symmetric with respect to λ. Dimensionless velocity $\lambda = [-10, 10]$, showing asymmetric global structure, and asymptotic behaviour for large λ. *Top*: 3D plot in $(\lambda$, Re s, Im $s)$ space. *Bottom*: projections onto the $(\lambda$, Re $s)$ and $(\lambda$, Im $s)$ planes. In the projection, blue (light) line denotes imaginary part, red (dark) line real part.

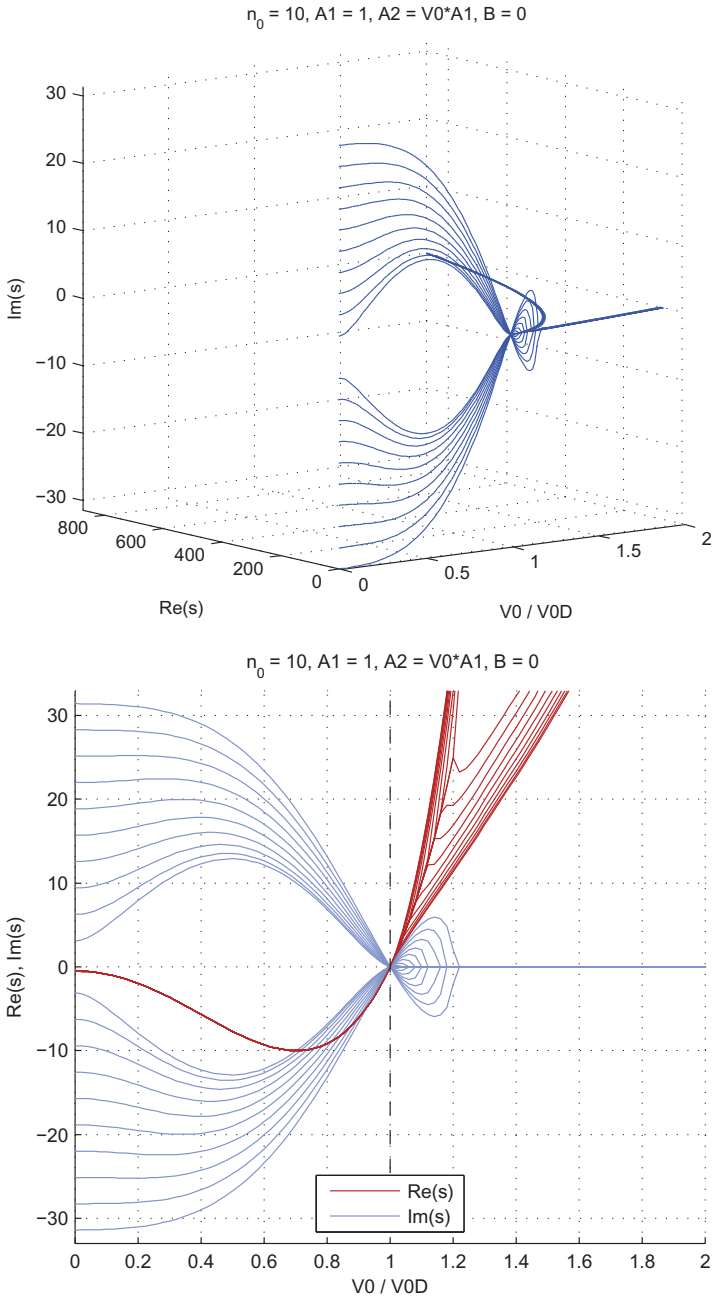

FIGURE 18 Eigenvalues of the damped moving string. Damping parameters $A_1 = 1$, $A_2 = V_0 A_1$. Dimensionless velocity $\lambda = [0, 3.5]$, showing asymptotic behaviour for large λ. The solution is symmetric with respect to $\lambda = 0$, hence only the positive half is shown. *Top*: 3D plot in (λ, Re s, Im s) space. *Bottom*: projections onto the (λ, Re s) and (λ, Im s) planes. In the projection, blue (light) line denotes imaginary part, red (dark) line real part.

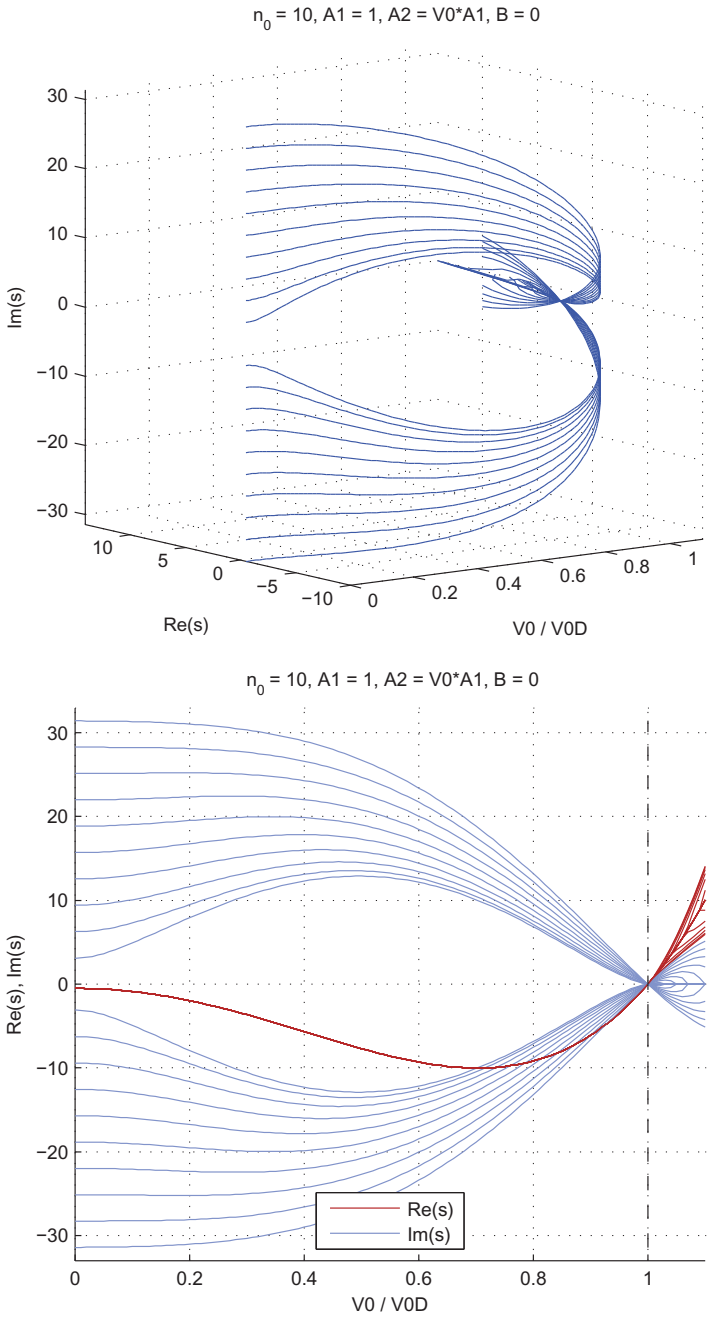

FIGURE 19 Eigenvalues of the damped moving string. Damping parameters $A_1 = 1$, $A_2 = V_0 A_1$. Dimensionless velocity $\lambda = [0, 1.1]$, showing the subcritical regime. The solution is symmetric with respect to $\lambda = 0$, hence only the positive half is shown. *Top*: 3D plot in (λ, Re s, Im s) space. *Bottom*: projections onto the (λ, Re s) and (λ, Im s) planes. In the projection, blue (light) line denotes imaginary part, red (dark) line real part.

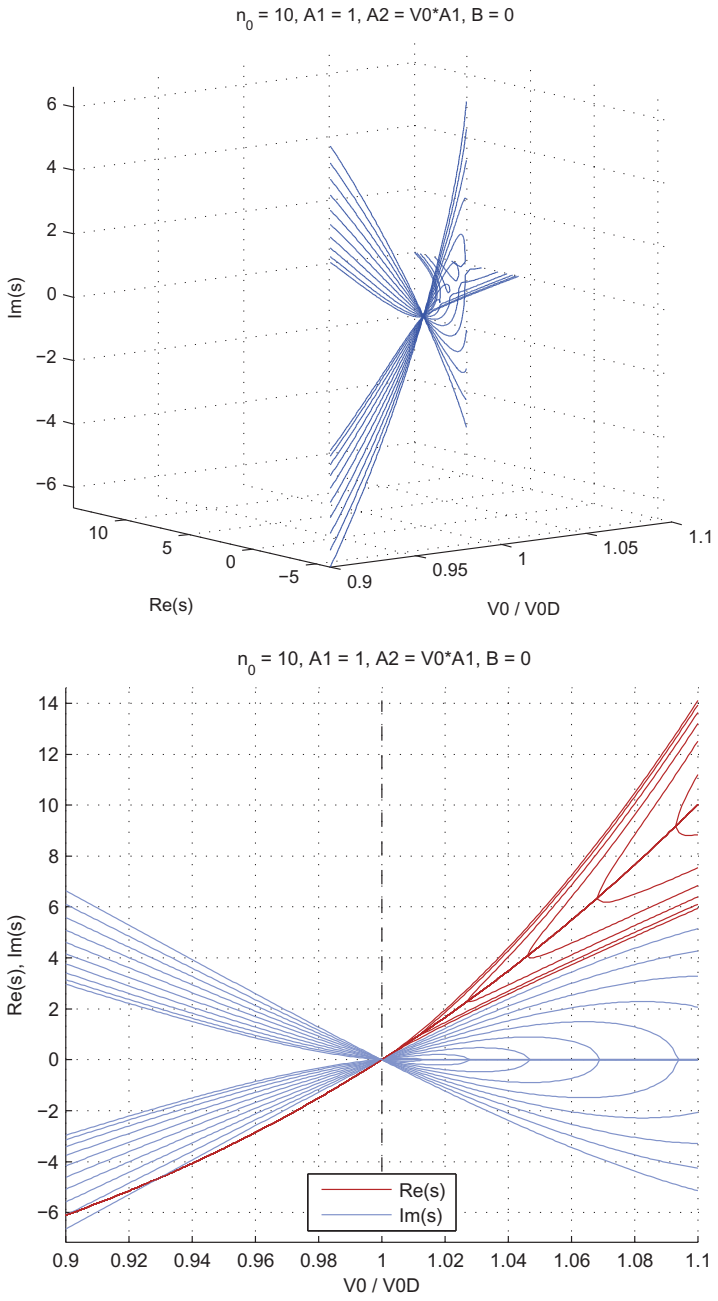

FIGURE 20 Eigenvalues of the damped moving string. Damping parameters $A_1 = 1$, $A_2 = V_0 A_1$. Dimensionless velocity $\lambda = [0.9, 1.1]$, showing local behaviour near the critical point $\lambda = 1$. The solution is symmetric with respect to $\lambda = 0$, hence only the positive half is shown. *Top*: 3D plot in (λ, Re s, Im s) space. *Bottom*: projections onto the (λ, Re s) and (λ, Im s) planes. In the projection, blue (light) line denotes imaginary part, red (dark) line real part.

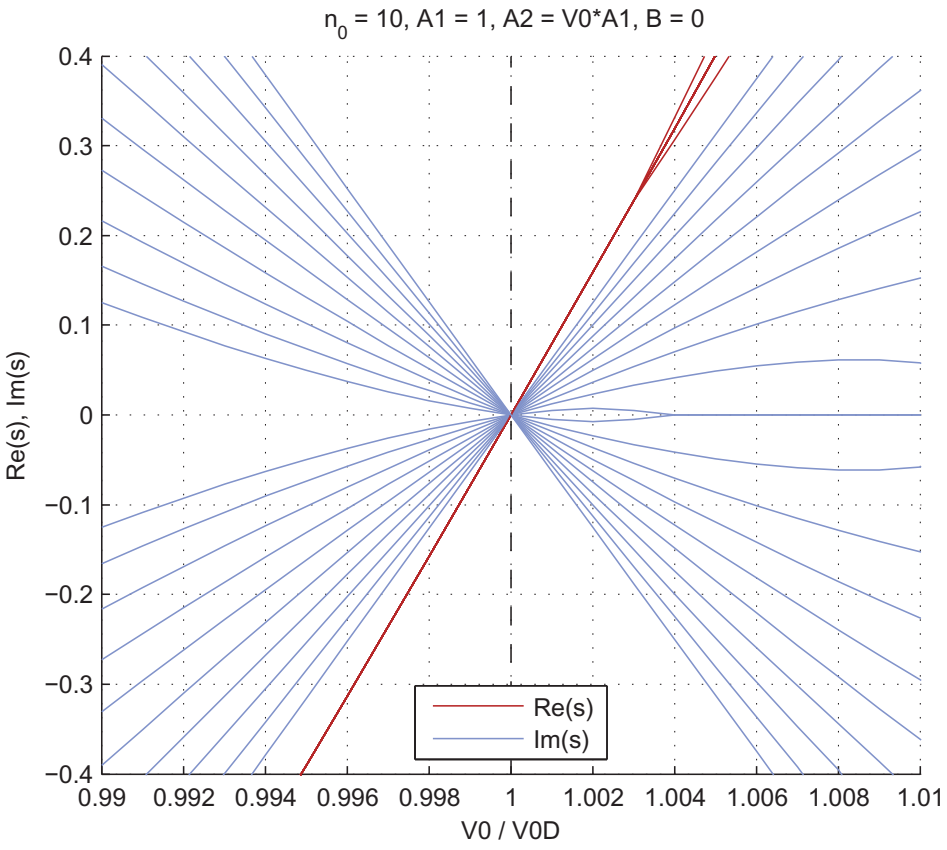

FIGURE 21 Eigenvalues of the damped moving string. Damping parameters $A_1 = 1$, $A_2 = V_0 A_1$. Dimensionless velocity $\lambda = [0.99, 1.01]$, showing the type of the instability. Projections onto the $(\lambda, \text{Re } s)$ and $(\lambda, \text{Im } s)$ planes. Blue (light) line denotes imaginary part, red (dark) line real part.

Im s_* becomes zero.

There may exist up to two flutter thresholds (in total, accounting for both signs of V_0), depending on the problem parameters. These thresholds are the same for all modes k.

An asymmetry (in terms of V_0 reflected upon the origin) may be introduced by the damping. This applies both to the flutter thresholds, if they exist, and to the thresholds of V_0 for Im $s_* = 0$ (governed by the polynomial $p_4(V_0; k)$, equation (62)). This is as expected for axially flowing fluid, which introduces an asymmetry to the physics of the situation.

At some values of V_0, different for each k, the zeroes of $p_4(V_0; k)$ may be reached. At these points, pairs of eigenvalues will switch between a complex conjugate state and a state of real values centered upon a common, moving point on the real axis. The common point is governed, as a function of V_0, by the other term of (54). The location of the common point is independent of the mode number k.

There may be up to four such switching points (in terms of V_0) for each mode k, and they occur at different V_0 for different k. We know that asymptotically in terms of $|V_0|$, the imaginary part of each mode becomes zero. Because (54) is continuous as a function of V_0 and all quantities under the square root are real, compatibility with the asymptotic result for any mode that has Im $s_* \neq 0$ at $V_0 = 0$ takes up one pair of switching points (one for each "direction", i.e., sign of V_0).

For such modes, we thus have up to two unallocated points left. If a second switch happened in each direction, this would make the mode imaginary again, and we would be left without remaining switches. This would contradict the asymptotic result. It follows that such modes can switch only once per direction, or — if the asymmetry is strong enough — possibly three times on one side of the origin and exactly once on the other side.

Modes that have Im $s_* = 0$ at $V_0 = 0$ (i.e. are initially purely real) may switch twice per direction, four times in one direction only, or not at all.

The conclusions from the performed analysis are as follows. From the eigenvalue problem it follows that there are a countably infinite number of modes k. As is clear from the equations for s_*, the eigenvalues form pairs due to the square roots, which admit both signs. The collision of two eigenvalues is a zero of the expression under the square root. This expression is a polynomial in V_0; thus a polynomial structure underlies the collisions. Especially, the number of possible collisions for each eigenvalue pair is finite and small. What the last two results mean is that in favourable circumstances, an eigenvalue pair may "bounce" a few times between complex conjugates and a pair of real values, until it runs out of polynomial zeroes, and (for the particular system just analyzed) settles upon real values that diverge from each other as $|V_0|$ is increased.

Together these facts fully explain qualitatively the "eigenvalue dynamics" of this system in terms of V_0: the complex conjugate symmetry, the pairing, and upon collision of eigenvalues, the switching between complex conjugates and a pair of real values centered upon a common point.

Note that in the system that was analyzed in this section, each eigenvalue pair (with matching k) is fully independent of all other pairs (with different k). It should be emphasized that in this particular system, each eigenvalue can interact only with its own pair, as a consequence of the square root structure. This will be seen, at least numerically, not to hold for the more complicated system that is the main topic of interest in the present work (see especially Figure 66 on page 202).

Nevertheless, the damped system is already one step up in complexity from the undamped case, where the eigenvalues come in pairs, but do not interact at all. In the undamped system, there is no square root in the expression for s_{xt}. Thus, the only thing that happens at $V_0 = C$ for that very simple system, is that each eigenvalue independently switches sign.

The damped moving string is one of the simplest representative examples that exhibits some of the eigenvalue dynamics of more complex problems in this class. As we saw, the analysis of this system already required some work, and not everything could be solved in a closed form (due to the fourth-degree polynomials determining the zero thresholds of Im s_*). It is clear that this is already close to the limit of what is sensible to do analytically. For more complex systems, numerical analysis is the only sensible possibility for investigating the behaviour of the eigenvalues. We will perform such an analysis on our main problem of interest in Section 6.3.

2.3 The axially moving panel

Now we will move on to the travelling panel, for which nonzero bending rigidity is allowed. From this point on, we will leave out damping, and study only the conservative model. The purpose of this section is to introduce the model of the moving panel, and review some results on the behaviour of the travelling panel in vacuum.

2.3.1 Governing equation and boundary conditions

The equation of small transverse vibrations of a travelling panel is

$$m w_{tt} + 2mV_0 w_{xt} + \left(mV_0^2 - T\right) w_{xx} + D w_{xxxx} = 0\,. \tag{64}$$

See setup in Figure 22.

A new term Dw_{xxxx} has been introduced, when compared to the string equation (12). This term represents the reaction force arising from bending resistance. The quantity D is the *bending rigidity* (Timoshenko and Woinowsky-Krieger, 1959, p. 5; also known as *cylindrical rigidity*):

$$D = \frac{Eh^3}{12(1-\nu^2)}\,, \tag{65}$$

where E is the Young modulus, h the thickness of the panel, and ν the Poisson ratio. Note that in beam theory, instead of the (cylindrical) bending rigidity, the

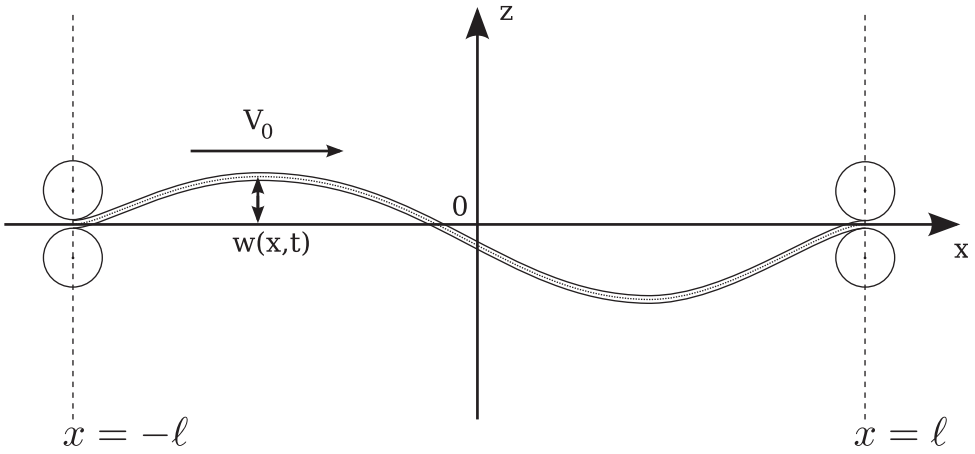

FIGURE 22 Axially moving panel. The finite thickness depicts bending rigidity. The roller symbols represent simple supports, with presence of axial motion. The function $w(x,t)$ is the transverse displacement of the midplane.

flexural stiffness EI is used, where E is the Young's modulus, and I is the second moment of inertia of the beam cross-section. This difference causes the units of D ($\text{Pa} \cdot \text{m}^3 = \text{Nm}$) and EI ($\text{Pa} \cdot \text{m}^4 = \text{Nm}^2$) to differ. This is not surprising, since the interpretation of the panel and beam models is different, even though they share some of their mathematical form.

Again, for the panel, the consistent choice is to take m as the mass per unit area, while for the beam, mass per unit length is used. For the panel, equation (64) represents pressures.

Equation (64) is of the fourth order in x (and, respectively in Lagrange coordinates, in ξ), so we need two more boundary conditions when compared to the case of the string. Just like in beam theory, the two customary choices for panel boundary conditions are as follows. Refer to Figure 23 for illustrations.

The *simply supported* (also known as *pinned*, *hinged* and by the abbreviation *S*) boundary conditions are

$$w(-\ell,t) = w(\ell,t) = 0 \tag{66}$$

$$w_{xx}(-\ell,t) = w_{xx}(\ell,t) = 0\,. \tag{67}$$

The condition (67) arises by requiring that the bending moment at the boundary points is zero. Since w_{xx} on the other hand is a rough measure of the curvature[9] in the small displacement regime, an alternative (convenient, but not fundamental) way to view this is that (67) requires that the curvature of the panel is zero at the boundaries. The simply supported conditions represent a panel (or beam), which is free to rotate (but supported) at its endpoints.

[9] The *curvature* is defined as $1/R$, where R is the *radius of curvature*. See Figure 23, and footnote 3 on p. 57.

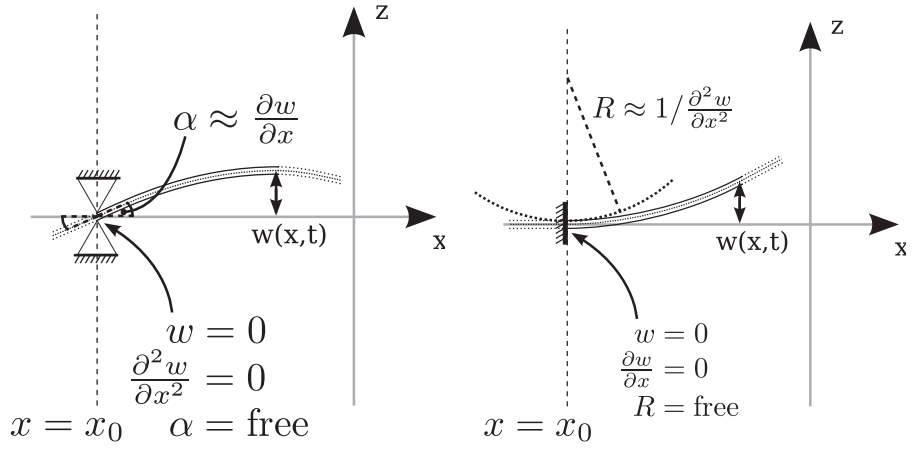

FIGURE 23 Standard boundary condition types for the panel, illustrated for a stationary panel. *Left*: simply supported. *Right*: clamped.

The *clamped* (or *built-in*, abbreviation *C*) boundary conditions are

$$w(-\ell, t) = w(\ell, t) = 0$$
$$w_x(-\ell, t) = w_x(\ell, t) = 0 \, .$$

The condition on w_x ensures that the panel leaves each clamped end perfectly horizontally. The physical situation being modelled by the clamped boundary conditions is usually depicted as having some of the panel (or beam) at its ends extending into a rigid wall.

Sometimes asymmetric boundary conditions are used, such as *SC* or *CS*, where one boundary point is simply supported and the other is clamped. In this work, we will concentrate on the symmetric *SS* case only.

Recall from the Introduction that we have ignored the viscoelasticity of the paper web, which would have introduced dissipation into the model. In this context it should be noted that if the boundary conditions are not symmetric, dissipation may have either a stabilizing or an instabilizing effect. See e.g. Païdoussis (1998), Sugiyama and Langthjem (2007), and Doaré (2010). Compare also subsection 2.2.5, where we observed that even for symmetric boundary conditions, velocity-dependent damping may cause destabilization.

In dimensionless coordinates, (13) from section 2.1.2, we have after multiplication of (64) by τ^2/m the equation

$$w_{tt} + 2V_0 \frac{\tau}{\ell} w_{xt} + \left(V_0^2 - \frac{T}{m} \right) \frac{\tau^2}{\ell^2} w_{xx} + \frac{D}{m} \frac{\tau^2}{\ell^4} w_{xxxx} = 0 \, , \tag{68}$$

where $x \in [-1, 1]$ and $t \in [0, \infty)$. The primes have been omitted. The scaling factor of w' cancels out.

Note the (arbitrary but convenient) placement of boundary points in (66)–(67); now the dimensionless $x \in [-1, 1]$. The symbol ℓ denotes the half-span length; refer to Figure 22.

2.3.2 Steady-state solution

In the steady state, the travelling panel equation is mathematically identical to the equation of the axially compressed Euler–Bernoulli beam. We will review the solution in this section, and explicitly derive the critical velocities, which for this model play the role of Euler's critical values of the compression force for the beam.

Setting the dynamical terms to zero and eliminating common factors, equation (68) becomes

$$\left(mV_0^2 - T\right)\frac{\mathrm{d}^2 w}{\mathrm{d}x^2} + \frac{D}{\ell^2}\frac{\mathrm{d}^4 w}{\mathrm{d}x^4} = 0\,. \tag{69}$$

We see that a steady-state solution may arise from a balance between the second- and fourth-order time-independent terms. (Cf. the moving string, where the steady-state solution arose by elimination of the w_{xx} term.)

Because (69) contains only second and fourth derivatives, we can introduce an auxiliary function

$$\psi(x) \equiv \frac{\mathrm{d}^2 w}{\mathrm{d}x^2}\,, \tag{70}$$

describing the curvature of the panel, and formulate the corresponding eigenvalue problem for it:

$$\frac{\mathrm{d}^2 \psi}{\mathrm{d}x^2} + \lambda\psi = 0\,, \quad -1 \le x \le 1 \tag{71}$$

$$\psi\,(-1) = 0\,, \quad \psi\,(1) = 0\,, \tag{72}$$

where the boundary conditions follow from those for w_{xx}, equation (67).

The parameter λ in (71),

$$\lambda = \frac{\ell^2\left[mV_0^2 - T\right]}{D}\,, \tag{73}$$

plays the role of the eigenvalue. The nontrivial solutions, i.e., eigenfunctions, of the eigenvalue problem (71)–(72) are determined as

$$\psi\,(x) = A\sin\left(\sqrt{\lambda}\frac{x+1}{2}\right) + B\cos\left(\sqrt{\lambda}\frac{x+1}{2}\right),$$

with two unknown coefficients A and B and an unknown eigenvalue λ. Applying the boundary conditions (72), we obtain

$$\psi\,(x) = A\sin\left(j\pi\frac{x+1}{2}\right) \tag{74}$$

$$\lambda = j^2\pi^2, \quad j = 1, 2, \ldots \tag{75}$$

where $A \neq 0$ is an arbitrary constant. In divergence analysis made in the frame of the Eulerian concept of static instability, the amplitudes of the eigenfunctions

are unknown. Integrating (74) twice and accounting for the boundary conditions for w, equation (66), we have for the displacement of the jth mode the function

$$w(x) = C \sin\left(j\pi \frac{x+1}{2}\right), \quad -1 \leq x \leq 1\,, \tag{76}$$

where $C = -(2/j\pi)^2 A$ is an arbitrary constant. We have from (73) and (75) that the corresponding critical velocity is

$$\left(V_{0\,\mathrm{vac}}^{\mathrm{div}\,j}\right)^2 = \frac{T + j^2\pi^2 D/\ell^2}{m}\,. \tag{77}$$

Thus, we observe that the shape of the eigenmode coincides with the membrane ($D = 0$) eigenmode regardless of the value of the bending rigidity D, but the bending rigidity contributes an additional term to the divergence speed.

Only the critical divergence speed has physical significance. It corresponds to the minimal eigenvalue, i.e., $j = 1$. By (77), the critical divergence speed is

$$\left(V_{0\,\mathrm{vac}}^{\mathrm{div}}\right)^2 = \frac{\pi^2 D}{m\ell^2} + \frac{T}{m}. \tag{78}$$

In the theory of paper web dynamics, the bending rigidity D is a small parameter. If D tends to zero, then the divergence speed tends to the limit value,

$$V_{0\,\mathrm{vac}}^{\mathrm{div}} \to \sqrt{\frac{T}{m}} = V_{0\,\mathrm{mem\ vac}}^{\mathrm{div}}\,, \tag{79}$$

which corresponds to the critical divergence speed of a moving membrane (see, e.g., Chang and Moretti, 1991).

We also observe by letting $D \to 0$ in (77) that in the membrane limit, in vacuum, there is only one (degenerate) eigenvalue, and thus all displacement modes (76) correspond to the critical divergence speed. Because (76) is an infinite Fourier basis, this implies that a membrane in vacuum may take any shape (that satisfies the boundary conditions) as it approaches divergence (just like the ideal string moving at critical velocity, as we recall from subsection 2.1.3). This is in contrast with the case with surrounding fluid (to be analyzed later, in Section 6.1), and also that of a travelling plate in a vacuum (see Banichuk et al., 2010a), for both of which the divergence shape is unique.

2.3.3 Free vibrations

Because equation (68) is of the fourth order in x, finding the free vibrations of the panel is much more difficult than for the simpler, second-order models that were considered in subsections 2.1.4 and 2.2.2.

An exact, short closed-form solution for this problem is probably impossible. Using the time-harmonic trial function, the general solution of the homogeneous, constant-coefficient ODE for the space component is not difficult to find, but finding the roots of the fourth-degree characteristic polynomial in the general case is not reasonable to do analytically. The special case of a travelling beam

with no applied tension ($T = 0$), which permits factorization of the characteristic polynomial, has been solved analytically by Simpson (1973).

In the case of paper production, the bending rigidity parameter D is typically small. Hence, for this application, it is possible to use singular perturbation theory (see e.g. Lagerstrom and Casten, 1972; Bender and Orszag, 1978; Chen et al., 1996) to produce an approximate free vibration solution. Singular perturbation theory is required, because the small parameter is the coefficient of the sole leading-order term. At the limit of vanishing D, the order of the model jumps down by two.

Because the model is linear and has constant coefficients, it is also possible to look directly for free vibration solutions of the plane wave form in the (x, t) plane, and solve the resulting dispersion equation. This approach requires only algebraic singular perturbation for polynomials. Such an algebraic singular perturbation analysis, utilizing the phase closure principle to take into account the boundary conditions (cases SS, CC, SC and CS), has been performed for the corresponding beam-theoretical problem by Kong and Parker (2004).

The solution by Kong and Parker, which is useful as a reference point, can be summarized as follows. Let the panel be located in the interval $x \in [0, \ell]$. The dynamical equation is (64), i.e.,

$$m w_{tt} + 2 m V_0 w_{xt} + \left(m V_0^2 - T \right) w_{xx} + D w_{xxxx} = 0 \, .$$

Define

$$\hat{x} \equiv \frac{x}{\ell} \, , \quad \hat{w} \equiv \frac{w}{\ell} \, , \quad \hat{t} \equiv t \sqrt{\frac{T}{m \ell^2}} \, , \quad \varepsilon^2 \equiv \frac{D}{T \ell^2} \, , \quad \hat{v} \equiv V_0 \sqrt{\frac{m}{T}} \, , \tag{80}$$

where the small bending rigidity assumption is $\varepsilon^2 \ll 1$. After an analysis using the plane wave trial function, singular perturbation for polynomials and the phase closure principle, the eigenfrequencies of the simply supported beam (or panel) are obtained as

$$\omega_n = n \pi \left[1 - v^2 + \varepsilon^2 n^2 \pi^2 \left(v^4 + 6 v^2 + 1 \right) / 2 + \ldots \right] \, . \tag{81}$$

Equation (81) is valid in the subcritical regime. Kong and Parker's plane-wave trial function is $w(x, t) = \exp [\, i \, (rx - \omega t) \,]$; hence, our $s_* = -i\omega$.

We see that for any given n, the root $\omega_n(v) = 0$ must have $|v| > 1$. Also, the location of the root depends on n. Both properties agree with the steady-state solution (77).

Kong and Parker compare (81) with numerically exact solutions for various parameter values, and note that if either the beam velocity v is low, or the dimensionless bending rigidity ε is small, the approximation (81) is good. No explicit recommendations are given in the text, but from their Figure 3 (on p. 465 in the reference), the agreement looks good for $v = 0.3$ up to about $\varepsilon \approx 0.07$, for $v = 0.6$ up to about $\varepsilon \approx 0.05$, and at $v = 0.9$ up to about $\varepsilon \approx 0.03$. For $v = 0$, the agreement is good for any tested ε, which validates the approximation.

Even the most stringent requirement for ε, of those above, is easily satisfied for typical papermaking cases. Thus, the formula provides a very fast and simple way to estimate the eigenfrequencies in this context — albeit with the limitation that fluid-structure interaction is not accounted for. To remedy this in a simple way without disturbing the analytical structure of the model, an added-mass approximation can be used (of which there are several available in the literature).

2.3.4 Applicability of the panel model

The last question to be answered in this section is: under which conditions can one simplify a plate into a panel? It should be kept in mind that all real-world objects that can be modelled as a thin plate are, even after reduction of one dimension by the plate model, still effectively two-dimensional. Thus, to determine the validity of the panel model in a wider context (while still staying in the mathematical landscape of linear models), we must consider the more complex plate model, and then see which limiting cases tend to the panel model, as some parameter either vanishes or increases without bound.

Keeping the intended application in mind, let us consider what kind of travelling plates occur in papermaking science. In this context, the case of a rectangular, classical Kirchhoff plate with $SFSF$ boundary conditions is especially interesting. The $SFSF$ plate is simply supported on two opposite edges, and free (zero normal stress and shear stress: $\sigma_{yy} = 0$, $\tau_{xy} = 0$) on the two others. This is a fairly good model for the mechanics of the paper web in an open draw, where the web momentarily travels without support while it is moving from one supporting roller to another (recall the photo in Figure 2, p. 33; cf. the schematic illustration below, in Figure 24, p. 101).

This is an important situation in practice, because as was noted in the introduction, in a practical paper machine there is always at least one open draw, in the transfer from the press nip (which squeezes out most of the water) to the dryer section. Also, as was mentioned, if the dryer section is of the classical heated cylinder type, an open draw exists between each successive pair of cylinders. (Karlsson, 2000)

Our research suggests that in situations of the $SFSF$ type, the panel model works the best for a long, narrow plate (Banichuk et al., 2010a,b). For the steady-state problem, the plate model reduces to the panel model when the width tends to zero. For plates which are wider than long, the eigenmodes of transverse vibrations can no longer be approximated as cylindrical. (Banichuk et al., 2010a) At least in the steady-state eigenmodes that were the object of the study, most of the transverse displacement occurs near the free edges. See the aforementioned Banichuk et al. (2010a) for the travelling plate case, and the $SFSF$ case for the classical stationary plate in the classic book by Gorman (1982). The connection is that the buckling shape of the moving plate is that of eigenfunctions of free vibrations of a stationary rectangular plate (which are given, e.g., in Gorman's book). Orthotropicity of the material introduces no qualitative changes (Banichuk et al., 2011a).

The above applies to wide plates of any finite width. For infinitely wide plates, on the other hand, the classical recommendation is to use cylindrical displacement theory (Timoshenko and Woinowsky-Krieger, 1959, ch. 1). This leads one to ask, what is going on here?

The apparent paradox can be explained by examining the limit as the width of the plate tends to infinity. Although the displacement becomes localized near the free edges for any finite width, it is never exactly zero at the center, but only very small compared to the displacement near the edges. As the width increases indefinitely, the center region takes up more and more of the total area of the plate. The localization to the edges grows stronger, but the width dependence of the displacement near the center grows ever weaker. At the limit of infinite width, the edges vanish and the center region takes up all of the plate. At this point, the width dependence at any finite y (width coordinate) has vanished, and the panel model is again applicable.

Thus, we conclude that the panel model is applicable to two cases: long and narrow bands, and the center region of very wide plates.

2.3.5 Summary and conclusion

The model of the axially travelling panel (in vacuum), allowing for nonzero bending rigidity, was briefly introduced.

The steady-state equation was solved and the critical velocities predicted by the linear model explicitly determined. The approximate eigenfrequency solution of Kong and Parker (2004) was given for reference, and the applicability of the panel model was discussed.

This simplified vacuum model is the last logical step before our main problems of interest, in which we will consider a travelling panel submerged in ideal fluid.

3 THE FLOW PROBLEM OF THE SURROUNDING AIR

As was noted in the introduction, in order to accurately model an open draw, or indeed the dynamics and stability of any lightweight moving material, the interaction between the material and the surrounding air must be taken into account somehow.

In this chapter, we will set up and solve analytically the aerodynamic problem for potential flow obstructed by the axially moving panel. See Figures 24–26. We will also derive an added-mass approximation from the exact solution, and compare it to some known results in literature.

Consider a travelling panel submerged in ideal fluid, where the free stream flows toward the right at velocity v_∞ (in Euler coordinates). See Figure 25. The governing equation for the dynamical behaviour of the panel is

$$mw_{tt} + 2mV_0 w_{xt} + \left(mV_0^2 - T\right) w_{xx} + Dw_{xxxx} = q_f + g \,, \tag{82}$$

where D is the bending rigidity (p. 92), $q_f \equiv q_f(w)$ is the aerodynamic reaction pressure and $g \equiv g(x,t)$ represents external forces inside the domain. The aerodynamic reaction is unknown, to be solved from the flow model (in terms of the panel displacement $w(x,t)$), and the external forces are considered given. The external forces are allowed to vary dynamically, if desired.

For solving the flow problem of the fluid component, we will apply techniques that are considered classical in the aerodynamics of thin aerofoils, constructing a Green's function type solution via complex analysis. More information on thin airfoil theory is available in the books by Ashley and Landahl (1985), Bisplinghoff and Ashley (1962), and Anderson (1985). Especially the first one is recommended for its clear presentation and similarity of approach.

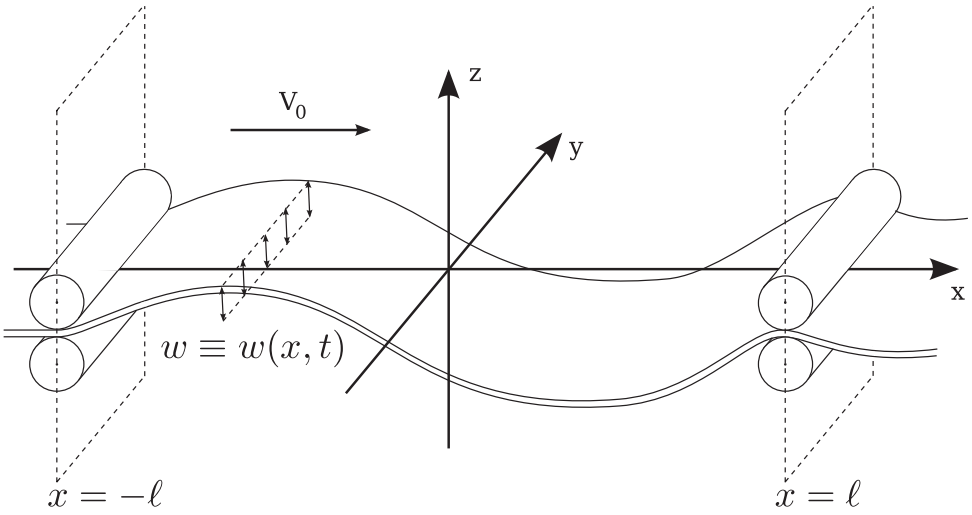

FIGURE 24 Axially moving thin plate with *SFSF* boundary conditions, undergoing cylindrical deformation. The three-dimensional physical situation.

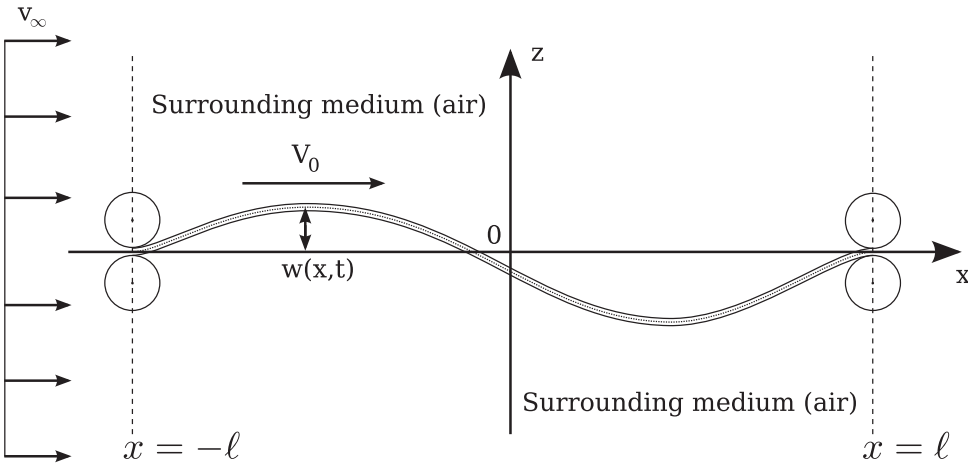

FIGURE 25 Axially moving panel submerged in axially flowing, two-dimensional ideal fluid. The roller symbols represent simple supports, with presence of axial motion.

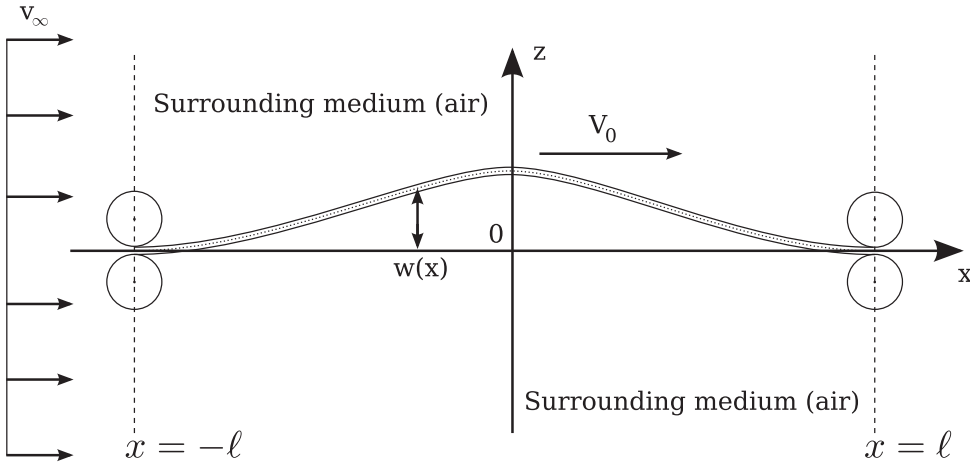

FIGURE 26 Steady-state problem for the eigenshapes of the axially moving panel submerged in axially flowing, two-dimensional ideal fluid. The roller symbols represent simple supports, with presence of axial motion. Now the panel velocity V_0 is the eigenvalue, and $w = w(x)$ only (i.e. the panel material undergoes steady-state flow, unrelated to the flow of the surrounding fluid).

3.1 Aerodynamic reaction as a function of the fluid velocity potential

In laboratory coordinates, the velocity potential of the disturbed stream is

$$\Phi(x,z,t) = xv_\infty + \varphi(x,z,t)\ , \tag{83}$$

where the first term is the free-stream potential, and the second term is a disturbance potential due to the obstacle. The Cauchy–Lagrange integral (see, e.g., Sedov 1972, ch. 9) is

$$\frac{\partial\Phi}{\partial t} + \frac{1}{2}\left(\nabla\Phi\right)^2 + \frac{p}{\rho_f} - \mathcal{U} = f(t)\ , \tag{84}$$

where we have assumed that the fluid is incompressible ($\mathcal{P} = p/\rho_f$, with ρ_f constant). The symbol $\mathcal{U}$ represents the scalar potential of the external forces affecting the flow, $F = \nabla\mathcal{U}$. The force potential must exist, based on the derivation of the Cauchy–Lagrange integral. On the right-hand side, $f(t)$ is the arbitrary function of time that comes from the integration leading to (84).

In the following, let us assume that there are no external forces, $\mathcal{U} \equiv 0$. Solving (84) for p, we have

$$p = \rho_f\left[f(t) - \frac{\partial\Phi}{\partial t} - \frac{1}{2}\left(\nabla\Phi\right)^2\right]\ . \tag{85}$$

The aerodynamic reaction is the pressure difference

$$q_f(x,t) \equiv p^-(x,t) - p^+(x,t)\ , \tag{86}$$

where the superscript notation is defined as

$$f^{\pm}(x,t) \equiv \lim_{z\to 0^{\pm}} f(x,z,t) \ , \tag{87}$$

where the upper (respectively lower) signs correspond to each other. The pressure difference is the jump in pressure, caused by the discontinuity introduced by the obstacle through which no flow can occur. Note the sign of (86): a positive reaction pushes upwards, i.e., toward positive z. Physically, it is obvious that this occurs when the pressure on the lower surface is greater than that on the upper surface.

From (83), the gradient giving the fluid velocity is

$$\mathbf{v}_f \equiv \nabla\Phi = \left(\ v_\infty + \frac{\partial\varphi}{\partial x} \, , \ \frac{\partial\varphi}{\partial z} \ \right) , \tag{88}$$

where $\mathbf{v}_f$ denotes the fluid velocity field. The square of the gradient, needed in (85), is

$$\begin{aligned} (\nabla\Phi)^2 &\equiv (\nabla\Phi)\cdot(\nabla\Phi) \\ &= \left(v_\infty + \frac{\partial\varphi}{\partial x} \right)^2 + \left(\frac{\partial\varphi}{\partial z} \right)^2 \\ &= v_\infty^2 + 2v_\infty \frac{\partial\varphi}{\partial x} + \left(\frac{\partial\varphi}{\partial x} \right)^2 + \left(\frac{\partial\varphi}{\partial z} \right)^2 \ . \end{aligned}$$

Let us assume that the disturbance velocities $\partial\varphi/\partial x$ and $\partial\varphi/\partial z$ are first-order small.[1] The linearized squared gradient becomes

$$(\nabla\Phi)^2 \approx v_\infty^2 + 2v_\infty \frac{\partial\varphi}{\partial x} \ . \tag{89}$$

We write (86) in terms of (85) and insert (89):

$$\begin{aligned} q_f &= \rho_f \left[\left(\frac{\partial\Phi}{\partial t} \right)^+ - \left(\frac{\partial\Phi}{\partial t} \right)^- + v_\infty \left(\frac{\partial\varphi}{\partial x} \right)^+ - v_\infty \left(\frac{\partial\varphi}{\partial x} \right)^- \right] \\ &= \rho_f \left(\frac{\partial}{\partial t} + v_\infty \frac{\partial}{\partial x} \right) \left(\varphi^+ - \varphi^- \right) \ . \end{aligned} \tag{90}$$

The function $f(t)$ vanishes from this jump expression, because it only depends on time. Also the v_∞^2 term vanishes, because it is a constant. Finally, $\partial\Phi/\partial t = \partial\varphi/\partial t$ everywhere, because our free-stream potential does not depend on time.

---

[1] Strictly speaking, this assumption is not needed. The continuity of the squares v_∞^2, $(\partial\varphi/\partial x)^2$ and $(\partial\varphi/\partial z)^2$ across the panel surface is enough to eliminate them from the pressure difference equation. Both ways are valid; if we choose this option, we must utilize the geometry of the flow configuration, which is not needed in the linearization approach.

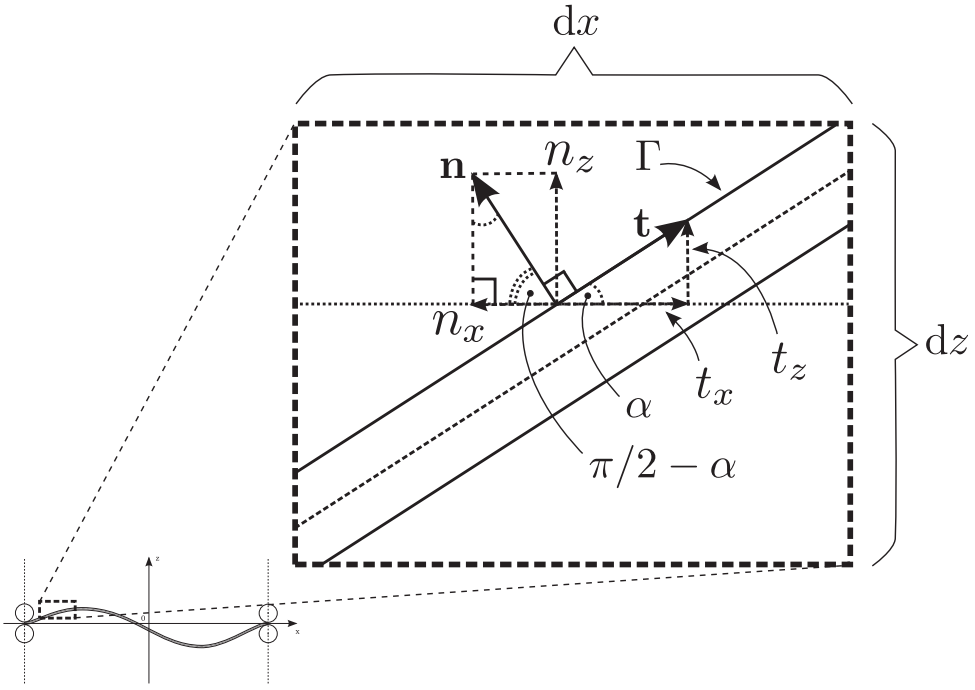

FIGURE 27 Close-up of the panel surface showing the (local) normal and tangent vectors.

3.2 The slip boundary condition

We aim to solve the fluid flow in the (x, z) plane region exterior to the panel. On the panel surface, we need a boundary condition for the fluid flow.

The classical choice, which we will also use, is that flow cannot cross the surface of the panel. However, we are now allowing axial motion for both the panel and the free stream. It is easy to make mistakes in the derivation of this boundary condition, so we will work through the details explicitly. We begin with its statement in terms of the velocity fields in the laboratory (Euler) coordinates,

$$\mathbf{n} \cdot \mathbf{v}_f = \mathbf{n} \cdot \frac{\mathrm{d}\mathbf{U}}{\mathrm{d}t} \quad \text{on } \Gamma \,, \tag{91}$$

where $\mathbf{n}$ is the unit surface normal vector of the panel, $\mathbf{v}_f$ is the fluid velocity field, and $\mathbf{U}$ is the (vector-valued) displacement field of the panel. The symbol $\mathrm{d}/\mathrm{d}t$ denotes the Lagrange derivative. The boundary Γ is the surface of the panel.

Simple trigonometry (see Figure 27) obtains that the local normal vector of the panel surface is

$$\mathbf{n} = \begin{pmatrix} -\sin\alpha & \cos\alpha \end{pmatrix}^T \,, \tag{92}$$

where α is the (counterclockwise) angle between the positive x axis and the local tangent vector of the panel, and T is the transpose. The vector $\mathbf{n}$ was chosen so

that it points toward positive z when $\alpha = 0$. It does not matter which choice we use, as long as we use the same choice for both sides of equation (91).

To find (92), consider a differential element of the panel, and in it, the upper 180^o angle between the positive and negative x axis, which is divided by the panel surface and $\mathbf{n}$ into α, a straight angle and $(\pi/2) - \alpha$. Then consider the triangle formed by $\mathbf{n}$, n_z and n_x, and the angles in this triangle. These must be the same three angles, but in a different order. Refer to Figure 27.

Alternatively, the normal vector is easily found algebraically. Take the positively oriented tangent vector of the panel and the counterclockwise 2D rotation matrix

$$\mathbf{t} = \begin{pmatrix} \cos\alpha \\ \sin\alpha \end{pmatrix} , \qquad R(\theta) = \begin{pmatrix} \cos\theta & -\sin\theta \\ \sin\theta & \cos\theta \end{pmatrix} . \tag{93}$$

Then, note that

$$\mathbf{n} = R(\pi/2)\mathbf{t} , \tag{94}$$

and evaluate to obtain (92). Refer to Figure 27.

By the definitions of the tangent function, and on the other hand the derivative, we have from the geometry of the situation that

$$\tan\alpha = \frac{\partial w}{\partial x} \tag{95}$$

at the obvious limit.

The panel moves axially at a constant velocity V_0. Keeping in mind (7) and (5) (p. 56), the displacement field of the panel, written in the Euler coordinates, is

$$\mathbf{U}(x,t) = (\ V_0 t + \tilde{u}(\xi(x,t),t)\ ,\ \tilde{w}(\xi(x,t),t)\ ) , \tag{96}$$

where $\tilde{u}$ and $\tilde{w}$ are, respectively, the in-plane and out-of-plane displacement functions defined in terms of the Lagrange coordinates, and the $V_0 t$ term accounts for the global axial motion.

The form of (96) is critically important for deriving the slip boundary condition correctly, and warrants some attention before we move on.

First, it should be noted that in (96), we have assumed small displacements. It should be obvious that in the general case, $\tilde{u} = \tilde{u}(s,t)$ and $\tilde{w} = \tilde{w}(s,t)$, where s is the longitudinal coordinate along the panel. The displacements are, generally speaking, functions of s and not of ξ (or x). However, in the small displacement regime, we can approximate $s \approx \xi$. In addition to being valid for small displacements only, this approximation has a further important mathematical consequence: describing shapes which are not single-valued functions of ξ is impossible in terms of $\tilde{u}(\xi,t)$ and $\tilde{w}(\xi,t)$. This limits the class of shapes that can be described, but the limitation also induces a benefit: self-intersection of the panel surface is automatically prevented without the need for further constraints.

The second important item to note is that we have defined the displacement functions $\tilde{u}$ and $\tilde{w}$ as being concerned with the elastic behaviour only. Mathematically, they are the solutions of the PDEs governing the vibrations of the web in

the longitudinal and out-of-plane directions. This choice implies that if we wrote the displacement field in the Lagrange coordinates, we would have

$$\tilde{\mathbf{U}}(\xi, t) = (\ \tilde{u}(\xi, t)\ ,\ \tilde{w}(\xi, t)\ )\ . \tag{97}$$

This is because at any given point of time t, each particle is only displaced from its original position *in the co-moving coordinate system* by the effects of elastic vibration. The Lagrange coordinate system for this problem is defined precisely such that it accounts for the global axial motion. This is why a $V_0 t$ term appears in (96), but not in (97).

Finally, the axial tension in a paper machine is in practice generated by using a velocity difference between the rollers at the ends of each free span. This causes the web to stretch, which induces an x-dependent longitudinal strain. Typically these strains are small; we have neglected this effect in (96). If we wish to take it into account, we need to add a third, x-dependent term in the axial component of $\mathbf{U}$. Although this term is easier to add into the Euler version $\mathbf{U}$ than the Lagrange version $\tilde{\mathbf{U}}$ (where it will depend on both ξ and t), from the physics of the situation it is evident that this term (if added) must appear in both coordinate systems.

Recall the coordinate transformations from subsection 2.1.2. From (96) and (8), we obtain in (x, t) coordinates the velocity field of the panel,

$$\frac{\mathrm{d}\mathbf{U}}{\mathrm{d}t} = (\ V_0 + V_0 \frac{\partial u}{\partial x} + \frac{\partial u}{\partial t}\ ,\ V_0 \frac{\partial w}{\partial x} + \frac{\partial w}{\partial t}\ )\ , \tag{98}$$

where again $\mathrm{d}/\mathrm{d}t$ denotes the material derivative.

From (92) and (98), we have for the normal motion of the panel the expression

$$\mathbf{n} \cdot \frac{d\mathbf{U}}{dt} = -\sin\alpha \left[V_0 + \frac{\partial u}{\partial t} + V_0 \frac{\partial u}{\partial x} \right] + \cos\alpha \left[\frac{\partial w}{\partial t} + V_0 \frac{\partial w}{\partial x} \right]\ . \tag{99}$$

Similarly, from (92) and (88), for the normal fluid velocity we have

$$\mathbf{n} \cdot \mathbf{v}_f = -\sin\alpha \left[v_\infty + \frac{\partial \varphi}{\partial x} \right] + \cos\alpha \frac{\partial \varphi}{\partial z}\ . \tag{100}$$

Subtracting (99) from (100) and using (91) to eliminate the left-hand side gives

$$-\sin\alpha \left[v_\infty - V_0 - \frac{\partial u}{\partial t} - V_0 \frac{\partial u}{\partial x} + \frac{\partial \varphi}{\partial x} \right] + \cos\alpha \left[\frac{\partial \varphi}{\partial z} - \frac{\partial w}{\partial t} - V_0 \frac{\partial w}{\partial x} \right] = 0\ .$$

Dividing by $\cos\alpha$, substituting (95) for $\tan\alpha$, and multiplying the equation by -1 obtains

$$\frac{\partial w}{\partial x} \left[v_\infty - V_0 - \frac{\partial u}{\partial t} - V_0 \frac{\partial u}{\partial x} + \frac{\partial \varphi}{\partial x} \right] - \left[\frac{\partial \varphi}{\partial z} - \frac{\partial w}{\partial t} - V_0 \frac{\partial w}{\partial x} \right] = 0\ . \tag{101}$$

Note that the $V_0 \partial w/\partial x$ terms cancel exactly; all other terms remain. Equation (101) is the *exact* small-displacement slip boundary condition.

Finally, in small-displacement theory it is customary to assume that $\partial w/\partial x$, $\partial u/\partial t$, $\partial u/\partial x$, and $\partial \varphi/\partial x$ are small, and discard second-order small terms. Note

that this will approximate the panel as perfectly horizontal. (This approximation will be used to set up the geometry for the fluid flow problem, in Section 3.3. It is a useful simplification in order to obtain an analytical solution for the flow.)

Rearranging terms, we obtain the linear approximation

$$\frac{\partial \varphi}{\partial z} = \frac{\partial w}{\partial t} + v_\infty \frac{\partial w}{\partial x} \equiv \gamma(x,t) \ , \tag{102}$$

which is the *approximate* small-displacement slip boundary condition on the panel surface. It ensures that the flow will not cross the surface of the panel, accounting for up to first-order small terms.

Equation (102) is more convenient to use than (101), because it contains only $\partial\varphi/\partial z$ and has no $\partial\varphi/\partial x$ term. Also, it does not require considering the longitudinal displacement u at all. This is another manifestation of the rather general phenomenon that in the small-displacement approximation, the in-plane and out-of-plane components become decoupled from each other.

Note especially that the boundary condition (102) does not have a term including V_0, although in Lagrange coordinates, what the system experiences is indeed the axial velocity difference $v_\infty - V_0$. This is easily confirmed by repeating the steps (96)–(102) in the Lagrange coordinates.[2] The $V_0 t$ term (which caused the cancellation) is not present in $\tilde{\mathbf{U}}$, and the velocity coefficient in the corresponding Lagrange boundary condition will indeed be $(v_\infty - V_0)$.

On the other hand, the lack of a V_0 term in (102) is not very surprising, since both axial motions are accounted for independently in the Euler coordinate system. The free-stream fluid velocity was given in the Euler coordinates to begin with. By transforming the mechanics of the panel from the Lagrange into the Euler system, we have written both axial velocities with respect to the same coordinate system. The approach of writing the boundary condition in the Lagrange coordinate system, on the other hand, transforms the fluid velocity into the coordinates axially moving with the panel, introducing a shift by $-V_0$ as expected.

3.2.1 Accounting for fluid viscosity

As was alluded to in subsection 2.2.4, the empirical fluid viscosity terms for the damped system require similar treatment. Physically, the panel experiences a stream of fluid at the axial velocity $(v_\infty - V_0)$, and the friction in the fluid causes damping in the vibrations of the panel. In the Lagrange coordinate system of the panel, the damping is dependent only on w_t.

It is clear, by an argument similar to what was done above, that to a first approximation the physically correct coefficient for the $\partial/\partial x$ damping term (in Euler coordinates) is $A_2 = v_\infty A_1$. Just like equation (102), this does not depend on the panel axial velocity V_0, unless we make the assumption that the whole air mass moves along with the panel.

---

[2] Here one must be careful to use $\partial\xi/\partial t = -V_0$ instead of $\partial x/\partial t = V_0$, as was done in the Euler coordinates.

For the viscosity term, the velocity v_∞ is approximate, because the contribution of the disturbance velocity $\partial\varphi/\partial x$ has been neglected, as far as the fluid velocity in the viscosity coefficient is concerned. This is a zeroth-order approximation, which should be fine (even if highly approximate) in the small-displacement regime. Note that no velocity approximation was done in (102); indeed, the whole point was to derive a consistent condition for the (transverse) disturbance velocity $\partial\varphi/\partial z$ when the free-stream velocity v_∞ is given.

If a more accurate solution for the connection between the damping coefficients is desired, it first comes to mind that one could calculate $\partial\varphi/\partial x$ on the panel surface from the solution of the flow problem that will be obtained below, and to use that to form $A_2 = (\partial\Phi/\partial x)\, A_1 = (v_\infty + \partial\varphi/\partial x)\, A_1$, which would be consistent with (102). However, this expression depends on a single value of $\partial\varphi/\partial x$ at $z = 0$, instead of its jump across $z = 0$ like the pressure difference (equation (90)). This is problematic, since we will see that φ^+ is discontinuous and antisymmetric with respect to $z = 0$, i.e. $2\varphi^+ = \varphi^+ - \varphi^-$. Thus, φ has no well-defined value at $z = 0$ and this approach does not work. We conclude that better approximations require modifying the fluid model in a less ad hoc manner (such as by using boundary layer theory; see e.g. Ashley and Landahl, 1985 and the standard Schlichting, 1960).

However, due to the antisymmetricity, $\partial\varphi/\partial x$ shifts in opposite directions on different sides of the panel. For the fluid velocity, v_∞ is the average. The shifts $\partial\varphi/\partial x$ were assumed first-order small. Together these facts suggest that the single approximation v_∞ may be adequate in practice to obtain some insight into the viscous behaviour using the modified ideal fluid model. Another, even more approximate, way is to use added masses to account for the fluid-structure interaction, with which approach the ad hoc damping approach is consistent.

3.3 Problem statement

As is well-known, ideal fluid velocity potentials fulfill Laplace's equation, as also do harmonic functions in complex analysis. Thus a classical way to approach two-dimensional ideal fluid flow problems is to use complex analysis, and seek a harmonic function such that it fulfills the given boundary conditions (see e.g. Ashley and Landahl, 1985).

We thus identify the complex plane $\mathbb{C}$ with the (x, z) plane in the model,

$$\eta \equiv x + zi \ \in \mathbb{C} \qquad \Leftrightarrow \qquad (x, z) \ \in \mathbb{R}^2 \, .$$

Because we work in the small deformation range, we can approximate the panel as a linear cut in the complex plane, located completely on the real axis. The domain of the aerodynamic flow problem is the region exterior to the panel; see Figure 28.

As in equation (83), we consider the disturbed flow as a superposition of a constant-velocity free stream and a disturbance term representing the effect of

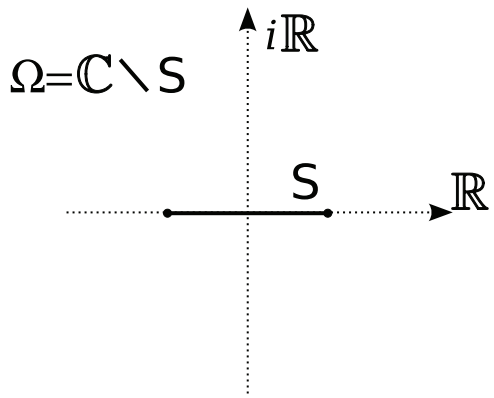

FIGURE 28 Domain of the problem for the surrounding airflow. The plate is geometrically approximated as the infinitely thin linear cut $S \equiv \{z = 0,\ -1 \leq x \leq 1\}$. The symbol i denotes the imaginary unit, $i \equiv \sqrt{-1}$.

the obstacle. The free-stream potential is linear in x; thus it is trivially harmonic. Also, it fulfills the slip condition along all of the real axis.

Therefore, we only need to solve the first-order correction to the free stream, i.e. the flow problem for the disturbance potential. This problem can be stated as

$$\triangle\varphi \equiv \frac{\partial^2\varphi}{\partial x^2} + \frac{\partial^2\varphi}{\partial z^2} = 0 \qquad \text{in } \Omega \tag{103}$$

$$\left(\frac{\partial\varphi}{\partial z}\right)^{\pm} = \gamma(x,t)\,, \qquad \text{along } S \tag{104}$$

$$(\nabla\varphi)_\infty = 0\,, \tag{105}$$

where (103) is the Laplace equation for the disturbance potential, (104) is the linearized slip boundary condition where $\gamma(x,t)$ is given by (102), and (105) requires that the disturbance in the fluid velocity field vanishes at infinity. The $\pm$ notation is defined as earlier, (87), and the subscript infinity denotes the limit

$$(\cdot)_\infty \equiv \lim_{|\eta|\to\infty} (\cdot)\,, \tag{106}$$

where $|\eta| \equiv \sqrt{x^2 + z^2}$ is the complex modulus.

Because we have a Laplace problem with only Neumann boundary conditions, the value of the potential φ can only be unique up to an additive constant. This ambiguity can, however, be resolved in an arbitrary manner, because the value of the velocity potential is of no physical interest. To obtain the velocity field, we need only its gradient, on which a global additive constant clearly has no effect.

The doubly connected topology of our fluid domain introduces an additional complication. From potential flow theory, we know that in a doubly connected domain, $\nabla\varphi$ is unique if and only if we prescribe the value of circulation around the cut. Suppose that we have found a (two-dimensional) velocity potential of the noncirculatory flow, $\Gamma = 0$, satisfying the slip boundary condition on a

given surface S. Now, it is possible to add to this flow a simple (inviscid) vortex of arbitrary strength Γ_0, for which one of the circular streamlines has been conformally transformed into the surface S. The general mapping theorem (also known as Riemann's mapping theorem; see e.g. Nehari, 1952, p. 175 for the mathematics) guarantees that this can always be done. By superposition of the two flows, a new irrotational flow has been created, still satisfying the slip boundary condition on S, but now $\Gamma = \Gamma_0$, which was arbitrary. Hence, the circulation Γ must be specified if we wish to have a unique irrotational flow in a doubly connected two-dimensional domain. (Ashley and Landahl, 1985, pp. 42–43)

This ambiguity is commonly resolved by requiring the so-called Kutta condition (or Kutta–Zhukowski condition) at the trailing edge. The condition picks a unique solution, makes the pressure continuous at the trailing edge, and also moves the trailing stagnation point of the flow to the tip of the airfoil, removing a singularity in the flow velocity field that would otherwise occur there for shapes with sharp trailing edges. See e.g. Ashley and Landahl (1985), and Lighthill (1986). In our solution, we will use a regularity condition by Sherman (1952), which comes from a problem in elastics sharing some of the mathematical form with our flow problem.

The problem (103)–(105) involves several approximations. Some are obvious, such as the two-dimensional problem setup and the ideal fluid model. Thus, width-directional variation both in the flow and in the behaviour of the moving web are neglected, as are fluid rotation and viscosity. A further approximation is that the boundary condition (104) is only valid up to first-order small terms, as was discussed during the derivation of (102).

A more subtle approximation concerns the panel geometry. The domain of the aerodynamic problem is infinite. It consists of the whole xz plane with the exception of the cut at $S \equiv \{z = 0,\ -1 \leq x \leq 1\}$, which is our linearised representation of the space occupied by the panel (see Figure 28). Thus: although we consider an axially moving panel, for the purposes of this aerodynamic problem the panel only exists on the interval $-1 \leq x \leq 1$. Effectively, in the panel domain, there is a material source at $x = -1$ and a sink at $x = +1$ (assuming positive V_0). Also, the rollers are ignored in the flow problem, being represented only in the boundary conditions for the panel displacement.

This is of course just one possible choice to build a model for this kind of situation; alternatively, it could be assumed that the elastic panel is embedded in a rigid baffle of infinite extent, splitting the xz plane into two parts (as in Kornecki et al., 1976). Note that this choice leads to a flow topology different from ours.

A third alternative is to model also the rollers and some of the surrounding panel surface, but then a more purely numerical approach is required. Available methods include, for example, the classical vortex panel method (see e.g. Anderson, 1985), and the much more general and more modern finite element method (FEM), as was mentioned in the introduction (see e.g. Johnson, 1987; Krizek and Neittaanmäki, 1990; Hughes, 2000; Gresho and Sani, 1999; Haataja et al., 2002; Hämäläinen and Järvinen, 2006).

Finally, whereas the geometry of the panel is simplified into the straight line

segment S (as far as the flow problem is concerned), the transverse velocity w_t, and the local angle with respect to the x-axis, w_x, are both allowed to be nonzero (in the slip boundary condition). Strictly speaking this is of course impossible (aside from artificial pathological cases), but it is a reasonable approximation in the small-deformation range.

The shape (and hence dynamic motion) of the surface will affect the boundary condition (104), which creates a nonzero disturbance velocity in the fluid along the line segment S. This in turn affects the $q_f(x,t)$ term in the panel equation, feeding back into the motion of the panel. This way the two-way aeroelastic coupling is taken into account. The model works in the small-displacement range, i.e., as long as the straight line segment assumption is approximately valid.

3.4 Solution

Because potential flow is memory-free, the flow field reconfigures itself instantly at each time t, independent of its previous history. Therefore, as far as the flow problem is concerned, the time t in the function $\gamma(x,t)$ in boundary condition (104) is just a parameter. This is the only time-dependent part in problem (103)–(105). Hence, in the following, we consider an arbitrary fixed value for t, and treat only x and z as variables.

In accordance with the complex analysis approach to 2D potential flows, we introduce an auxiliary analytic function

$$W(\eta,t) = \Psi(x,z,t) + i\varphi(x,z,t) \tag{107}$$

of the complex variable $\eta = x + iz$, where $i^2 = -1$. The Cauchy-Riemann equations and boundary conditions (104) imply that

$$\frac{\partial \Psi}{\partial x}|_{z=0} = \frac{\partial \varphi}{\partial z}|_{z=0} = \gamma(x,t) \ . \tag{108}$$

Let us denote $\Psi(x,t) \equiv \Psi(x,0,t)$. We have

$$\Psi(x,t) = \chi(x,t) + C(t) \ , \tag{109}$$

where

$$\chi(x,t) = \int_{-1}^{x} \gamma(\xi,t)\, \mathrm{d}\xi \ , \tag{110}$$

and $C(t)$ is a real constant of integration for each fixed t. Thus, finding the velocity potential φ reduces to the computation of the imaginary part of the analytic function (107), whose real part on $[-1,1]$ is (109).

In other words, the idea of introducing the auxiliary function W is that we may use the Neumann boundary data (104) for the original (unknown) potential φ to generate Dirichlet boundary data for the (similarly unknown) stream function Ψ, as per equations (109) and (110). Note that unlike the usual convention,

the real part of W is here the stream function, and the imaginary part is the real-valued potential for which the original problem was formulated.

We use the results given by Sherman (1952) (compare also Ashley and Landahl, 1985, chap. 5-3) and represent the solution of this problem as

$$W(\eta,t) = \frac{1}{2\pi i}\left(\frac{\eta-1}{\eta+1}\right)^{1/2}\int_{-1}^{1}\left(\frac{\xi+1}{\xi-1}\right)^{1/2}\frac{\chi(\xi,t)+C(t)}{\xi-\eta}d\xi\,. \quad (111)$$

The real constant $C(t)$ is determined with the help of the following equation:

$$\frac{1}{2\pi i}\int_{-1}^{1}\frac{\chi(\xi,t)+C(t)}{\sqrt{\xi^2-1}}\,\mathrm{d}\xi = 0\,, \quad (112)$$

which represents a regularity condition for the function W. The condition comes from Sherman (1952). The left-hand side of (112) is obtained by taking the limit $\eta \to -1$ in (111), and using $(\xi-1)(\xi+1) = \xi^2-1$ in the denominator. The condition requires that the integral factor in (111) vanishes at $\eta = -1$.

From condition (112), we have

$$C(t) = \frac{1}{\pi i}\int_{-1}^{1}\frac{\chi(\xi,t)\,\mathrm{d}\xi}{\sqrt{\xi^2-1}}. \quad (113)$$

Using expression (113) and the formula (cf. Ashley and Landahl, 1985, pp. 94–95, but note the slight difference in form)

$$\frac{1}{2\pi i}\int_{-1}^{1}\left(\frac{\xi+1}{\xi-1}\right)^{1/2}\frac{\mathrm{d}\xi}{\xi-\eta} = \frac{1}{2}\left(\frac{\eta+1}{\eta-1}\right)^{1/2} - \frac{1}{2}\,, \quad (114)$$

we perform substitutions into expression (111) and elementary transformations and obtain

$$\begin{aligned} W = {} & \frac{1}{2\pi i}\left(\frac{\eta-1}{\eta+1}\right)^{1/2}\int_{-1}^{1}\left(\frac{\xi+1}{\xi-1}\right)^{1/2}\frac{\chi(\xi,t)\,\mathrm{d}\xi}{\xi-\eta} \\ & + \frac{C(t)}{2}\left[1-\left(\frac{\eta-1}{\eta+1}\right)^{1/2}\right] \\ = {} & \frac{\sqrt{\eta^2-1}}{2\pi i}\int_{-1}^{1}\frac{\chi(\xi,t)\,\mathrm{d}\xi}{(\xi-\eta)\sqrt{\xi^2-1}} + \frac{C(t)}{2}. \end{aligned} \quad (115)$$

From the representation (115), we can compute the quantity φ^+:

$$\begin{aligned} \varphi^+ = {} & \lim_{z\to 0^+}\left[\mathrm{Im}\,W(x+iz)\right] \\ = {} & \mathrm{p.v.}\left(-\frac{\sqrt{1-x^2}}{2\pi}\int_{-1}^{1}\frac{\chi(\xi,t)\,\mathrm{d}\xi}{(\xi-x)\sqrt{1-\xi^2}}\right)\,. \end{aligned} \quad (116)$$

Here, we took into account that the constant $C(t)$ on the right-hand side of (115) is real, and consequently must be omitted when the limit of the imaginary part is computed in (116). Note also that the integration in (116) is understood in the sense of Cauchy's principal value, here denoted $\mathrm{p.v.}(\cdot)$.

We have

$$\varphi^+ - \varphi^- = 2\varphi^+ \tag{117}$$

because the flow is antisymmetric with respect to the linearised plate surface (see, e.g., Eloy et al. 2007 for a similar case). Alternatively, we can take the corresponding limit of (115) at $\eta = x - iz \;\to\; x - i \cdot 0 \;\; (z \to 0^-)$ and obtain the same result.

By definition of the principal value, we have

$$\begin{aligned} 2\varphi^+ = \;& \text{p.v.} \left(-\frac{1}{\pi} \int_{-1}^{1} \left(\frac{1-x^2}{1-\xi^2} \right)^{1/2} \frac{\chi\,(\xi,t)\;\mathrm{d}\xi}{\xi - x} \right) \\ \equiv \;& \lim_{\varepsilon \to 0} \; -\frac{1}{\pi} \left[\int_{-1}^{x-\varepsilon} \left(\frac{1-x^2}{1-\xi^2} \right)^{1/2} \frac{\chi\,(\xi,t)\;\mathrm{d}\xi}{\xi - x} \right. \\ & \left. + \int_{x+\varepsilon}^{1} \left(\frac{1-x^2}{1-\xi^2} \right)^{1/2} \frac{\chi\,(\xi,t)\;\mathrm{d}\xi}{\xi - x} \right]. \end{aligned} \tag{118}$$

Integrating by parts, and substituting expression (110) for $\chi\,(x)$, we have[3]

$$\begin{aligned} 2\varphi^+ = \;& \lim_{\varepsilon \to 0} \left[N\,(x-\varepsilon, x) \int_{-1}^{x-\varepsilon} \gamma\,(\xi,t)\;\mathrm{d}\xi \right. \\ & -N\,(x+\varepsilon, x) \int_{-1}^{x+\varepsilon} \gamma\,(\xi,t)\;\mathrm{d}\xi \\ & - \int_{-1}^{x-\varepsilon} N\,(\xi, x)\,\gamma\,(\xi,t)\;\mathrm{d}\xi \\ & \left. - \int_{x+\varepsilon}^{1} N\,(\xi, x)\,\gamma\,(\xi,t)\;\mathrm{d}\xi \right], \end{aligned} \tag{119}$$

where we have defined

$$\begin{aligned} N\,(\xi, x) &\equiv \frac{1}{\pi} \ln \left| \frac{1 + \Lambda(\xi, x)}{1 - \Lambda(\xi, x)} \right| , \qquad \text{where} \\ \Lambda\,(\xi, x) &\equiv \left[\frac{(1-x)\,(1+\xi)}{(1-\xi)\,(1+x)} \right]^{1/2} . \end{aligned} \tag{120}$$

See Figures 29 and 30 for a qualitative picture of the functions Λ and N, and Figure 31 for contour plots.

We observe that all terms on the right-hand side of (119) are finite; therefore the integration by parts is legitimate. As $\varepsilon \to 0$, the sum of the first two terms in

[3] In the integration by parts formula, set $u' = \sqrt{(1-x^2)/(1-\xi^2)}/(\xi - x)$, and $v = \chi(\xi, t)$. The first term in (119) is the boundary term uv, evaluated at the upper limit $x - \varepsilon$. The lower limit produces no term, because $\chi(x, t)$ is defined with the help of an integral from -1 to x; hence, $\chi(-1, t) = 0$. The second term in (119) is uv, evaluated at the *lower* limit $x + \varepsilon$. The limits of integration that may look weird at first glance are due to evaluating $\chi(x + \varepsilon, t)$. Now the upper limit produces no term, because $N(\xi, x) \to 0$ as $\xi \to 1$. The last two terms in (119) are the straightforward integrated-by-parts terms of the form uv'.

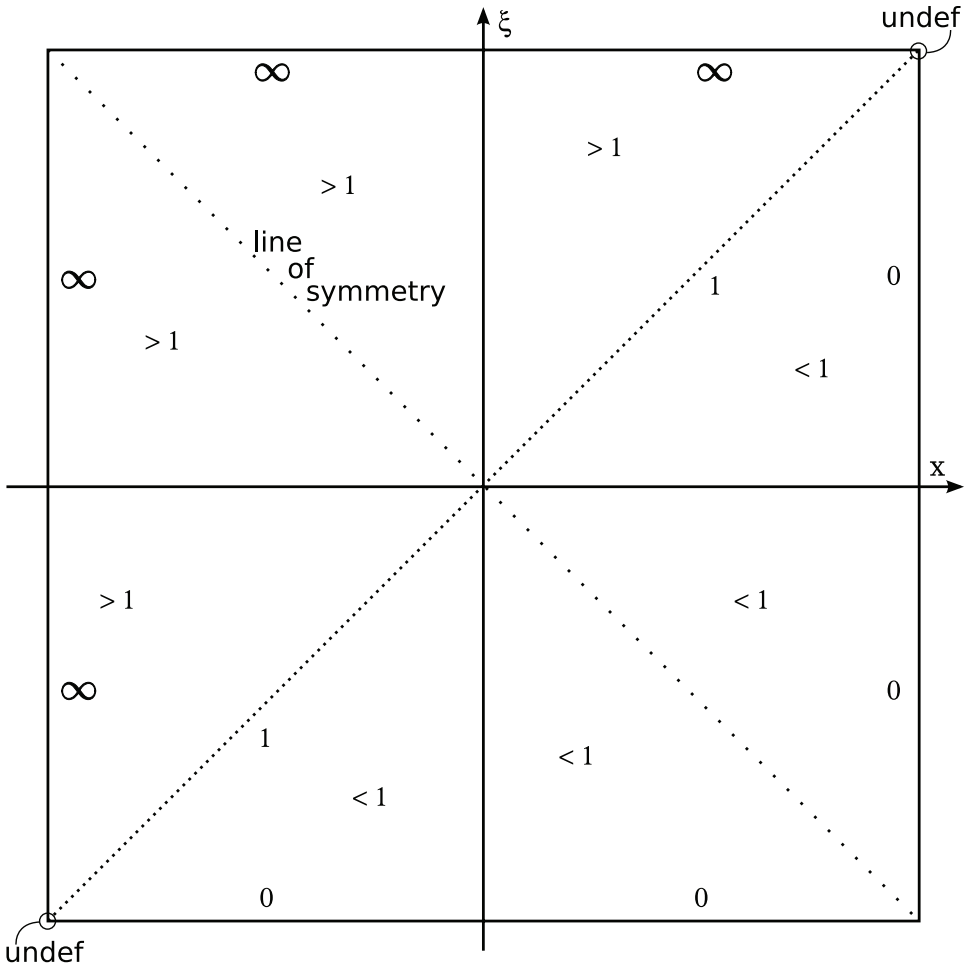

FIGURE 29 Auxiliary function $\Lambda(\xi, x)$ in $[-1, 1] \times [-1, 1]$. Qualitative drawing. The infinities should be understood in the sense of limits.

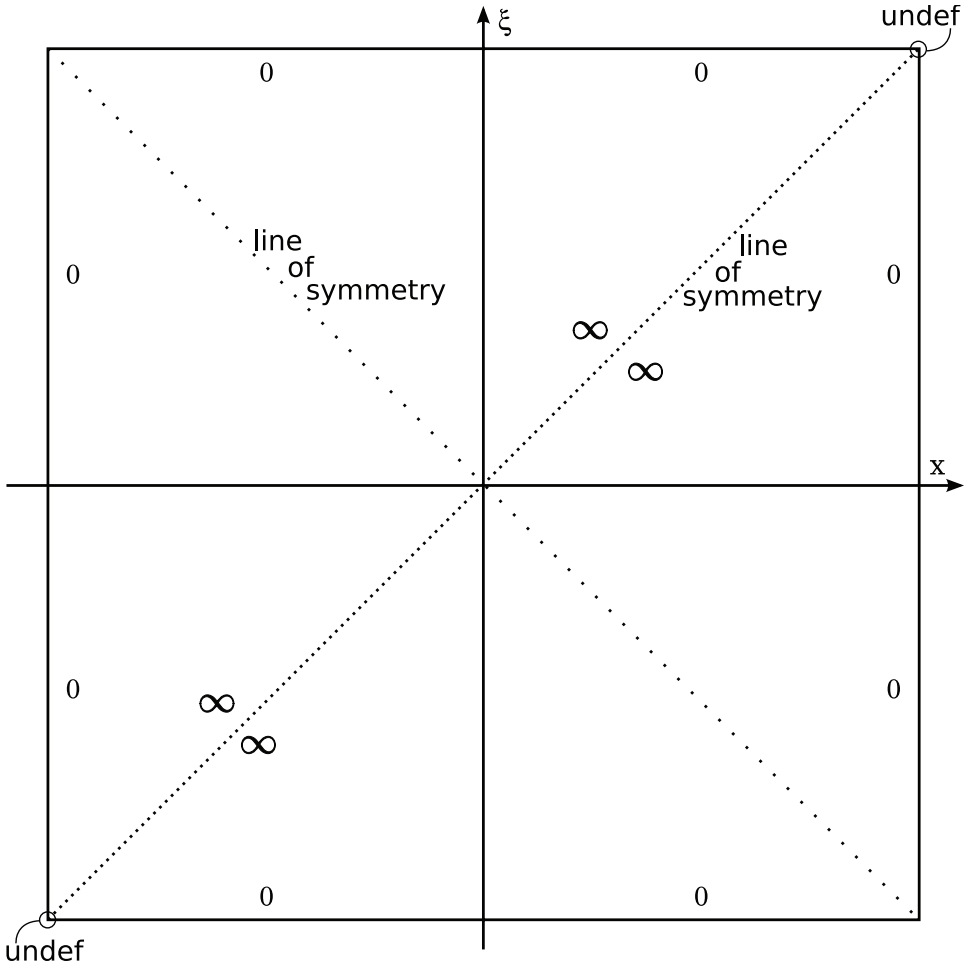

FIGURE 30 Aerodynamic kernel $N(\xi, x)$ in $[-1, 1] \times [-1, 1]$. Qualitative drawing. The infinities, and the upper and left edges (which are outside the domain of the auxiliary function $\Lambda(\xi, x)$, needed by $N(\xi, x)$), should be understood in the sense of limits.

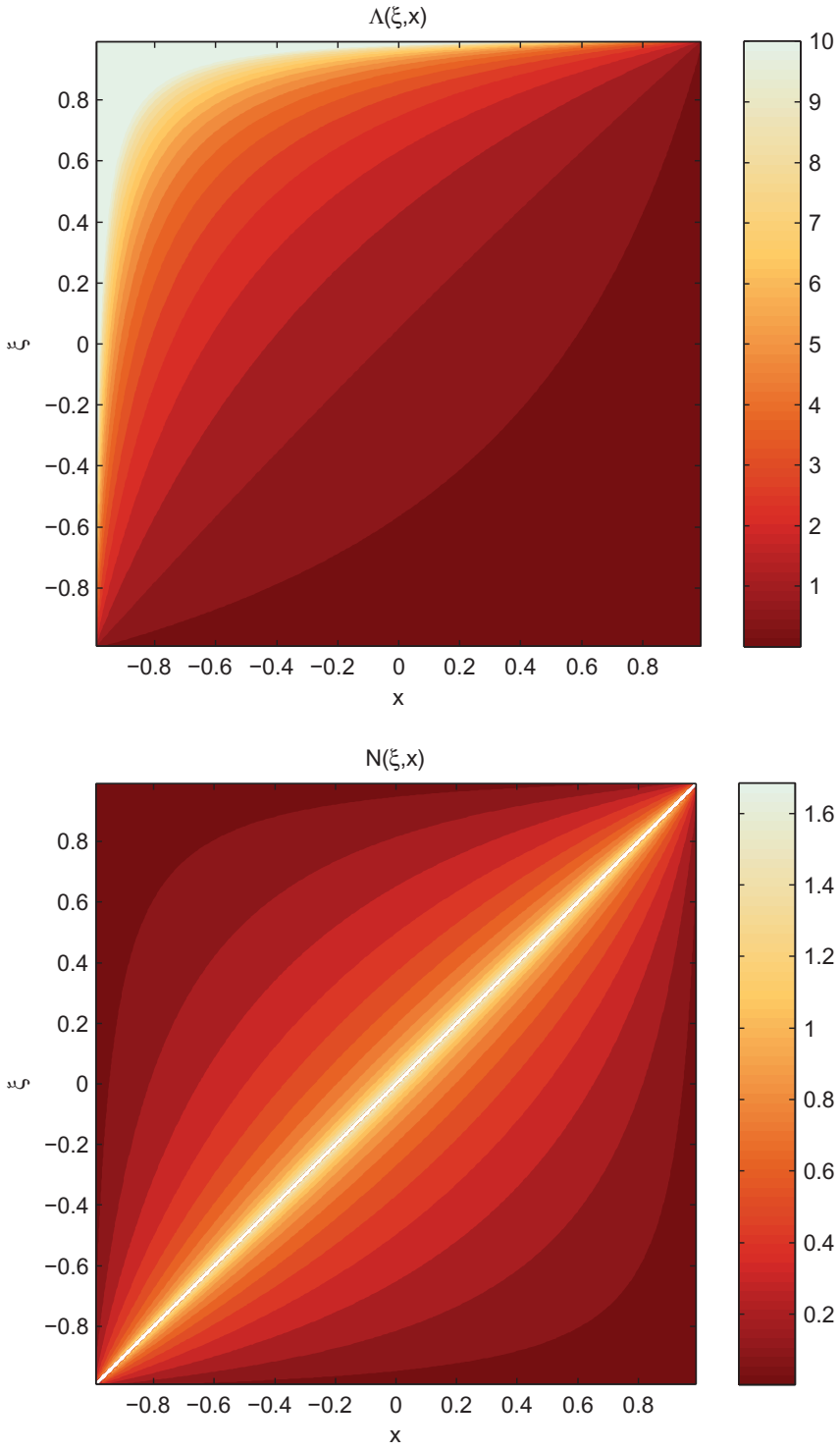

FIGURE 31 Contour plots of the functions $\Lambda(\xi, x)$ and $N(\xi, x)$. *Top*: Λ. *Bottom*: N.

(119) approaches zero. It can be shown that the last two integrals converge (we will do this below).[4] Therefore, the required functional dependence is of the form

$$2\varphi^+(x,t) = -\int_{-1}^{1} N(\xi,x)\,\gamma(\xi,t)\;\mathrm{d}\xi. \tag{121}$$

With the help of (90), (102), (120) and (121), we arrive at the expression for the aerodynamic reaction of the fluid. Writing out the dimensionless coordinate scaling factors τ and ℓ explicitly, we have:

$$\begin{aligned}
q_f(x,t) &= p^-(x,t) - p^+(x,t) \\
&= \rho_f\left(\frac{1}{\tau}\frac{\partial}{\partial t} + \frac{1}{\ell}v_\infty\frac{\partial}{\partial x}\right)\left(\varphi^+(x,t) - \varphi^-(x,t)\right) \\
&= \rho_f\left(\frac{1}{\tau}\frac{\partial}{\partial t} + \frac{1}{\ell}v_\infty\frac{\partial}{\partial x}\right)\left(2\varphi^+(x,t)\right) \\
&= -\rho_f\left(\frac{1}{\tau}\frac{\partial}{\partial t} + \frac{1}{\ell}v_\infty\frac{\partial}{\partial x}\right)\int_{-1}^{1} N(\xi,x)\,\gamma(\xi,t)\;\mathrm{d}\xi \\
&= -\rho_f\left(\frac{1}{\tau}\frac{\partial}{\partial t} + \frac{1}{\ell}v_\infty\frac{\partial}{\partial x}\right)\int_{-1}^{1} N(\xi,x)\left(\frac{\ell}{\tau}\frac{\partial}{\partial t} + v_\infty\frac{\partial}{\partial x}\right)w(\xi,t)\,\mathrm{d}\xi \\
&= -\rho_f\frac{1}{\ell}\left(\frac{\ell}{\tau}\frac{\partial}{\partial t} + v_\infty\frac{\partial}{\partial x}\right)\int_{-1}^{1} N(\xi,x)\left(\frac{\ell}{\tau}\frac{\partial}{\partial t} + v_\infty\frac{\partial}{\partial x}\right)w(\xi,t)\,\mathrm{d}\xi\,. \qquad (122)
\end{aligned}$$

The expression (122) is valid, because $N(\xi,x)$ is a Green's function of Laplace's equation, and thus, the improper integral (121) converges (see, e.g., Evans, 1998). The convergence can also be established in a more direct manner, which we will do in the following section.

3.5 Properties of the aerodynamic kernel

In this section, we will show that $N(\xi,x)$ is symmetric with respect to reflection by the lines $x = \pm\xi$, and that it is integrable.

The symmetricity can be obtained by inspection of (120) and some algebraic manipulation. We will present it here briefly for completeness. First, note that the domain of Λ is $(-1,1)\times(-1,1)$, and that of N is $\{(-1,1)\times(-1,1)\}\setminus\{\xi = x\}$.

Consider $\Lambda(\xi,x)$, defined in equation (120). Reflecting the point (ξ,x) with respect to $x=\xi$, let us evaluate $\Lambda(x,\xi)$:

$$\Lambda(x,\xi) = \left[\frac{(1-\xi)(1+x)}{(1-x)(1+\xi)}\right]^{1/2} = \left[\frac{(1-x)(1+\xi)}{(1-\xi)(1+x)}\right]^{-1/2} = \frac{1}{\Lambda(\xi,x)}\,. \tag{123}$$

[4] Note that (119) came from (116), which only converges in the sense of the principal value. Thus, strict convergence of these improper integrals is not required, but it will lead to cleaner-looking equations, as we can use the usual kind of improper integral instead of the principal value. This distinction is of course a purely analytical one, because numerically, even the improper integral will be in practice computed via an approximation of the corresponding principal value.

Then, using (123) we have

$$N(x,\xi) = \frac{1}{\pi}\ln\left|\frac{1+\frac{1}{\Lambda}}{1-\frac{1}{\Lambda}}\right| = \frac{1}{\pi}\ln\left|\frac{\Lambda+1}{\Lambda-1}\right| = \frac{1}{\pi}\ln\left|-\frac{1+\Lambda}{1-\Lambda}\right| = \frac{1}{\pi}\ln\left|\frac{1+\Lambda}{1-\Lambda}\right| = N(\xi,x)\ . \tag{124}$$

Similarly, for reflection with respect to $x = -\xi$, we have

$$\Lambda(-x,-\xi) = \Lambda(\xi,x)\ ,$$

and thus also

$$N(-x,-\xi) = N(\xi,x)\ ,$$

because N depends on ξ and x only implicitly via $\Lambda(\xi,x)$. Thus N is symmetric in reflection with respect to the lines $x = \pm\xi$.

Now, consider the integrability. For the aerodynamic problem, we need to show that the integral (121) converges. We will show directly that the L_1 norm of $N(\xi,x)$ is finite, from which the convergence of (121) follows. Assume that $x \in (-1,1)$ and $t \in [0,\infty)$ are fixed.

Let

$$I_1(x) \equiv \int_{-1}^{1} N(\xi,x)\, f(\xi)\, \mathrm{d}\xi\ , \tag{125}$$

where $f(\xi) = f(\xi;t)$, i.e. f is allowed to depend on t, but this dependence is omitted from the notation since we hold t fixed and thus it can be treated as a parameter. We require that $f(\xi)$ is bounded for $-1 < \xi < 1$.

We estimate (125) from above by

$$\begin{aligned} I_1(x) \le |I_1(x)| &\equiv \left|\int_{-1}^{1} N(\xi,x)\, f(\xi)\, \mathrm{d}\xi\right| \le \int_{-1}^{1} |N(\xi,x)\, f(\xi)|\, \mathrm{d}\xi \\ &\equiv \|N(\xi,x)\, f(\xi)\|_{L_1} \le \|N(\xi,x)\|_{L_1}\, \|f(\xi)\|_{L_\infty} \\ &\equiv \int_{-1}^{1} |N(\xi,x)|\, \mathrm{d}\xi \ \cdot \max_{\xi\in[-1,1]} |f(\xi)| \\ &\equiv M(t)\ \cdot \int_{-1}^{1} |N(\xi,x)|\, \mathrm{d}\xi\ , \end{aligned}$$

where on the second line we have used Hölder's inequality, and on the last line, we have defined $M(t) \equiv \max_{\xi\in[-1,1]} |f(\xi)|$.

The factor $M(t)$ is clearly a nonnegative, finite number for each fixed t, so it does not affect the convergence. Also, because $N(\xi,x) \ge 0$ over the whole domain, we can omit the absolute value in the integral on the last line above. Thus, it is sufficient to prove that the integral

$$I_2(x) \equiv \int_{-1}^{1} N(\xi,x)\ \mathrm{d}\xi \tag{126}$$

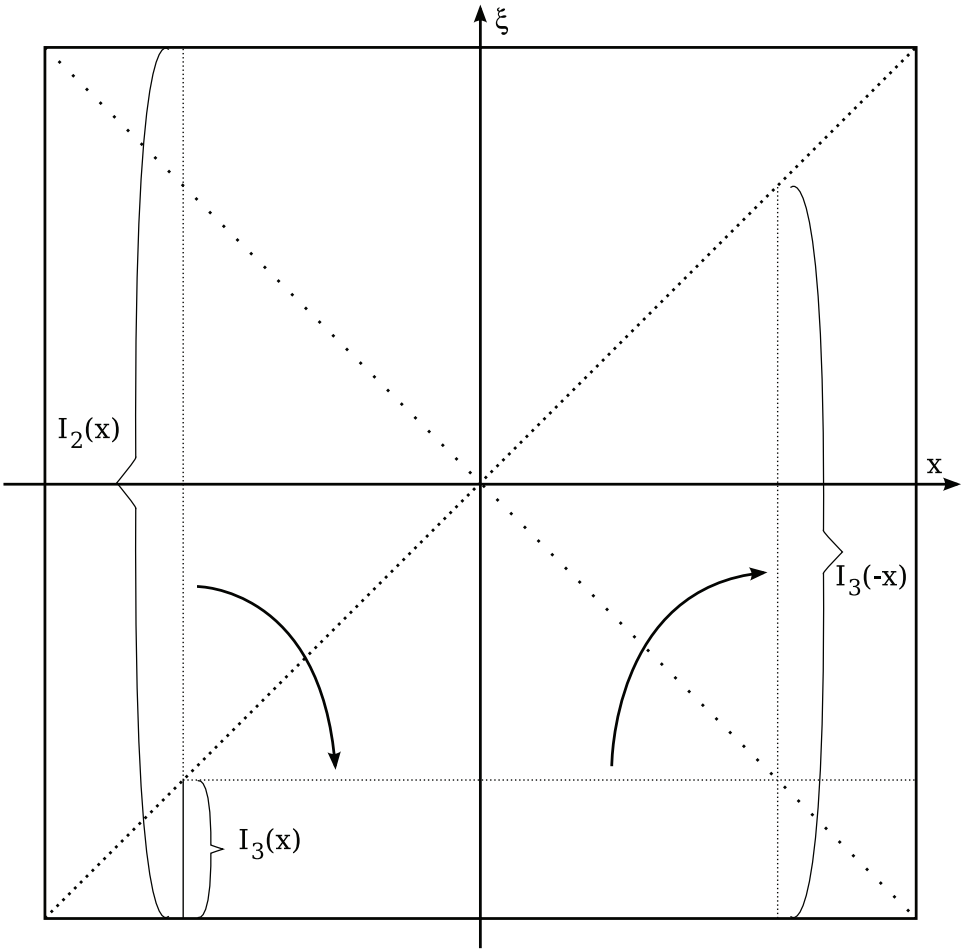

FIGURE 32 Effect of the symmetries of $N(\xi, x)$ on the integral $I_2(x)$.

converges. Furthermore, as was shown above, the function $N(\xi, x)$ is symmetric with respect to the lines $\xi = x$ and $\xi = -x$. Define

$$I_3(x) \equiv \int_{-1}^{x} N(\xi, x)\ \mathrm{d}\xi\ . \tag{127}$$

Due to the symmetries, it holds that $I_2(x) = I_3(x) + I_3(-x)$ for all $x \in [-1, 1]$. See Figure 32 for an illustration. Therefore, it is sufficient to consider the convergence of only the integral (127).

Note that (127) is of the form of the third integral in (119), when taken to the limit, so the following argument will prove the convergence of that limit, too. Due to the symmetry, it is also sufficient for proving the convergence of the fourth integral in the same equation.

Now, to show that (127) converges, we can use the elementary sandwich theorem (dominated convergence) from analysis. The outline of the argument is as follows.

Due to the symmetry of $N(\xi, x)$ with respect to $\xi = x$, it is sufficient to consider just one half of the domain. Let $\xi < x$ (we leave out strict equality to avoid the singularity of $N(\xi, x)$ at $x = \xi$). Consider the set $D_1 = \{\,(-1,1) \times (-1,1)\,\} \cap \{\xi < x\}$. We observe that $0 \leq \Lambda(\xi, x) < 1$ for all $(x, \xi) \in D_1$. Taking this into account, we can estimate N from above, simplifying the expression slightly:

$$N(\xi, x) \equiv \frac{1}{\pi} \ln \left| \frac{1+\Lambda}{1-\Lambda} \right| \overset{\text{for } \xi < x}{=} \frac{1}{\pi} \ln \frac{1+\Lambda}{1-\Lambda} < \ln \frac{2}{1-\Lambda} \equiv s(\xi, x)\,, \tag{128}$$

where $s(\xi, x)$ is defined as indicated. This simplifies the numerator and gets rid of the absolute value.

Define $\eta \equiv x - \xi$ and $\zeta \equiv x + \xi$. Let $r(\eta) \equiv \ln(4/\eta)$, and $r(\xi, x) \equiv r(\eta) \equiv r(x - \xi)$. In the set D_1, it holds that $\eta \in (0, 2)$. In this range, the function r is positive and integrable; $\int r(x - \xi)\, \mathrm{d}\xi < \infty$. Once we show that on lines parallel with $x = -\xi$, for the function s it holds that $s(\eta, \zeta) \leq s(\eta, 0)$, the argument reduces into one dimension. Then, it is sufficient to show that for $\eta \in (0, 2)$, we have $s(\eta, 0) < r(\eta)$; the sandwich theorem does the rest. Details are given in Appendix 1.

As a final remark to this section, we see that $N(\xi, x)$ decreases quickly — quantitatively speaking, faster than $\ln(4/\eta)$ — as the distance $\eta \equiv |\xi - x|$ from the singularity $\xi = x$ increases (Figure 76 in Appendix 1).

3.6 Construction and analysis of an added-mass approximation

As was seen in the literature review, added-mass models are often used for taking into account the inertial effects of fluid-structure interaction when the ideal fluid model is used for the fluid component. In this section, we will construct an added-mass approximation for our model and compare the result to some existing added-mass models.

Note that in the main part of this thesis (Chapters 4 and 6), we will not use this approximation, but we will use the original model directly.

We saw that $N(\xi, x)$ has the following properties:

- $N(\xi, x) \to \infty$ as $\xi \to x$,
- $N(\xi, x) \in L^1([-1, 1] \times [-1, 1])$, and
- The value of $N(\xi, x)$ decreases quickly as the distance from the singularity increases.

Motivated by these properties, let us make the following simplifying approximation:

$$\int_{-1}^{1} N(\xi, x)\, f(\xi)\, \mathrm{d}\xi \approx \mu \int_{-1}^{1} \delta(\xi, x)\, f(\xi)\, \mathrm{d}\xi\,, \tag{129}$$

where $\delta(\xi, x)$ is the Dirac delta distribution, $f(\xi) = f(\xi; t)$ is any admissible func-

tion, and μ is the constant

$$\mu \equiv \operatorname*{mean}_{x\in(-1,1)} \int_{-1}^{1} N(\xi, x)\, \mathrm{d}\xi = \frac{1}{2} \int_{-1}^{1} \left[\int_{-1}^{1} N(\xi, x)\, \mathrm{d}\xi \right] \mathrm{dx} \,. \tag{130}$$

The approximated integral in (129) is easy to evaluate. Using the definition of the Dirac delta, we have

$$\mu \int_{-1}^{1} \delta(\xi, x)\, f(\xi)\, \mathrm{d}\xi = \mu\, f(x) \quad \forall x \in [-1, 1] \,. \tag{131}$$

Numerically, it is easy to find that the required mean value is $\mu \approx \pi/4$. To do this, the formula (130) can be evaluated in several ways. One way is to use the Monte Carlo method: take the middle form of the expression (130), replace the mean by the sample mean, and sample the integral for e.g. $n = 1000$ uniformly distributed random values of x. The sample mean then gives an approximation for μ.

Alternatively, it is possible to use the rightmost form of (130), and evaluate the double integral directly by applying a (possibly adaptive) quadrature method to both the outer and inner integrals. This approach requires a lot of evaluations of the inner integral, and is thus fairly slow, but it gives a more accurate result.

Whichever method is used, due to the singularity of $N(\xi, x)$ at $\xi = x$, in practice the (inner) integral must be numerically approximated as

$$\int_{-1}^{1} N(\xi, x)\, \mathrm{d}\xi \approx \int_{-1}^{x-\varepsilon} N(\xi, x)\, \mathrm{d}\xi + \int_{x+\varepsilon}^{1} N(\xi, x)\, \mathrm{d}\xi \,, \tag{132}$$

where ε is small, e.g. 10^{-8}.

It is important to note that the added-mass model, by replacing the exact aerodynamic kernel by the Dirac delta approximation as per equation (129), approximates the fluid-structure interaction as pointwise local. Thus, the added-mass model can be seen as performing mass lumping on the original model; the factor μ approximates the total strength of the aerodynamic reaction on one point of the panel surface.

Of course, a global mean value is not the only way to perform mass lumping. Alternatively, one could approximate

$$\int_{-1}^{1} N(\xi, x)\, f(\xi)\, \mathrm{d}\xi \approx S(x) \int_{-1}^{1} \delta(\xi, x)\, f(\xi)\, \mathrm{d}\xi \,,$$

where

$$S(x) \equiv \int_{-1}^{1} N(\xi, x)\, \mathrm{d}\xi \,. \tag{133}$$

This choice is slightly more sophisticated in that it accounts for differences in the strength of the coupling at different values of x. It approximates the effect of the kernel with the local mean at each fixed x, instead of the global mean $\pi/4$. For a plot of $S(x)$, see Figure 33. If fast computation is desired, a polynomial approximation can be used. A least squares fit (by the method of normal equations, see

Appendix 4) using the functions $\phi_0(x) \equiv 1$, $\phi_1(x) = x^2$, $\phi_2(x) = x^4$ gives coefficients $c_0 = 0.9892$, $c_1 = -0.3195$, and $c_2 = -0.4872$. This approach leads to a variable-coefficient PDE, and is in spirit similar to the approach of Frondelius et al. (2006), where an added-mass model was used, with the added masses taken as functions of x derived from boundary layer theory (although here we use thin airfoil theory instead of boundary layer theory).

In any case, how accurate the added-mass approximation is depends on the physical situation being considered. In Païdoussis (2008), it is pointed out that the problem of plates subjected to axial flow is more complex than the otherwise very similar, canonical problem of the fluid-carrying pipe, exactly due to the nonlocal coupling effect that is ignored by the added-mass model.

With this reservation, let us work out the added masses predicted by our model. For simplicity, consider only the inertial terms and q_f in (82). That is, in (82), assume $T = 0$, $D = 0$ and $g \equiv 0$ for simplicity (we can easily add these terms back when we are done). We approximate q_f by inserting (129) and $\mu = \pi/4$ into (122). Then, we evaluate the approximated aerodynamic integral by (131).

In dimensionless coordinates, we have the result

$$\frac{m}{\tau^2}\frac{\partial^2 w}{\partial t^2} + 2\frac{mV_0}{\ell\tau}\frac{\partial^2 w}{\partial x \partial t} + \frac{mV_0^2}{\ell^2}\frac{\partial^2 w}{\partial x^2} = -\rho_f \frac{\pi}{4}\left[\frac{\ell}{\tau^2}\frac{\partial^2 w}{\partial t^2} + 2\frac{v_\infty}{\tau}\frac{\partial^2 w}{\partial x \partial t} + \frac{v_\infty^2}{\ell}\frac{\partial^2 w}{\partial x^2}\right] ,$$

from which we obtain

$$\frac{1}{\tau^2}\left[m + m_a\right]\frac{\partial^2 w}{\partial t^2} + 2\frac{V_0}{\ell\tau}\left[m + m_a r_v\right]\frac{\partial^2 w}{\partial x \partial t} + \frac{V_0^2}{\ell^2}\left[m + m_a r_v^2\right]\frac{\partial^2 w}{\partial x^2} = 0 , \qquad (134)$$

where

$$m_a \equiv \ell\rho_f \pi/4 \qquad \text{and} \qquad r_v \equiv v_\infty / V_0 . \qquad (135)$$

This reduces to a classical one- or three-term single-parameter added-mass model by choosing $r_v = 0$ (i.e. $v_\infty = 0$, no free-stream flow in laboratory coordinates) or $r_v = 1$ (i.e. $v_\infty = V_0$, whole air mass moves with the web).

The prediction for the added mass m_a thus derived, in equation (135), agrees with eq. (12a) of Pramila (1986), if we take $\alpha = 0.5$ in Pramila's eq. (12a). Note that our ℓ denotes the span half-length and Pramila's a denotes the full length. According to Pramila (1986, Table II), the choice $\alpha = 0.5$ corresponds to an aspect ratio slightly larger than 1.0 (span slightly longer than wide).

Compare also eq. (13) of Pramila (1987), due to T. Y.-T. Wu, reported to hold for long and narrow spans. Here the corresponding added mass becomes $b\rho_f\pi/4$, when the force per unit area is considered. This formulation, instead of ℓ, uses the plate width b as the length scale. Comparing to our approximation in (134), $\ell\rho_f\pi/4$, the best agreement is obtained when $\ell/b \approx 1$, i.e. aspect ratio $2\ell/b \approx 2$.

Finally, note that in the special case $V_0 = 0$, the effect of fluid cannot be included in the mass only, because for $V_0 = 0$ the quantity r_v in (135) becomes undefined. However, the added mass m_a is still well-defined. The added mass m_a and the fluid axial velocity v_∞ together fully characterize the approximated effect of the fluid.

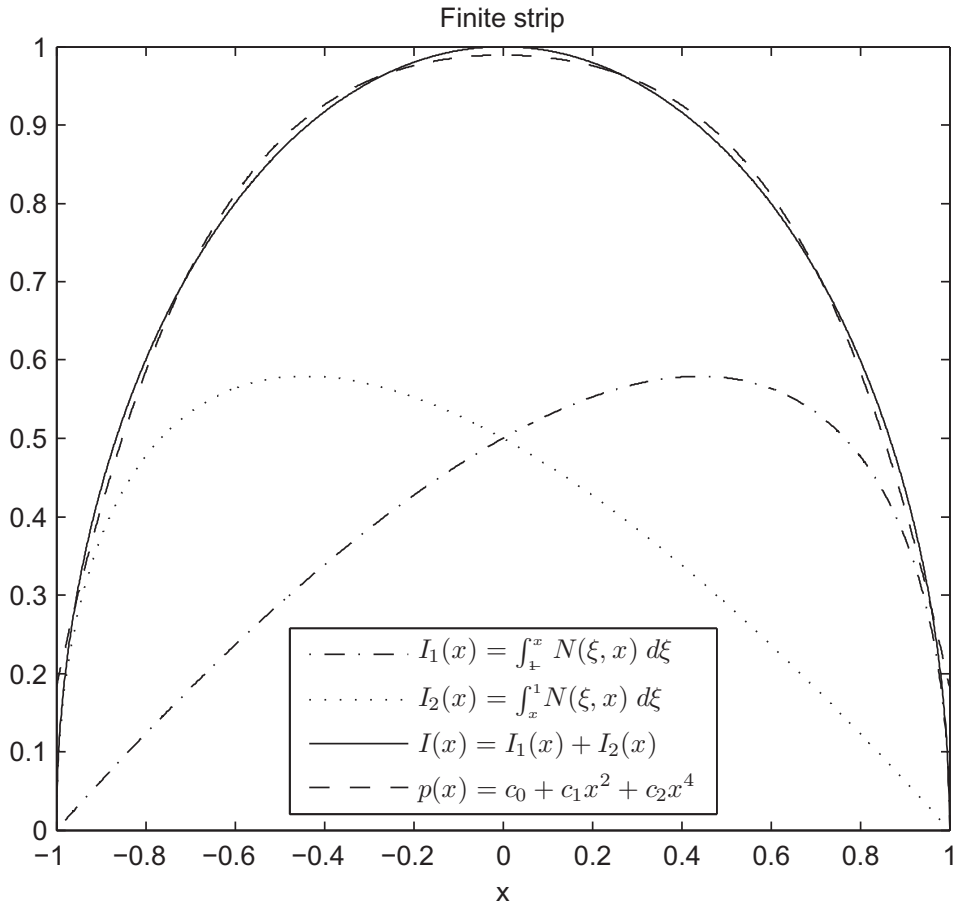

FIGURE 33 The function $S(x)$ defined by equation (133), for local approximation of the aerodynamic reaction. Both the original function and its three-term polynomial approximation are shown. The polynomial fit coefficients are $c_0 = 0.9892$, $c_1 = -0.3195$, and $c_2 = -0.4872$. Note that the original function touches zero at both ends of the domain.

In the general case, instead of writing (134), we can use added mass for the w_{tt} term ($m_{\text{total}} = m + m_a$), added linear momentum (per unit of surface area) for w_{xt} ($p_{\text{total}} = mV_0 + m_a v_\infty$), and added kinetic energy (per unit of surface area) for w_{xx} ($2K_{\text{total}} = mV_0^2 + m_a v_\infty^2$). We have

$$\frac{1}{\tau^2} m_{\text{total}} \frac{\partial^2 w}{\partial t^2} + 2\frac{1}{\ell\tau} p_{\text{total}} \frac{\partial^2 w}{\partial x \partial t} + \frac{1}{\ell^2} 2K_{\text{total}} \frac{\partial^2 w}{\partial x^2} = 0 \ ,$$

or, equivalently,

$$\frac{1}{\tau^2} \left[m + m_a\right] \frac{\partial^2 w}{\partial t^2} + 2\frac{1}{\ell\tau} \left[mV_0 + m_a v_\infty\right] \frac{\partial^2 w}{\partial x \partial t} + \frac{1}{\ell^2} \left[mV_0^2 + m_a v_\infty^2\right] \frac{\partial^2 w}{\partial x^2} = 0 \ . \quad (136)$$

This generalized added-mass type approximation covers all values of V_0.

Note that due to the forms of (134) and (136), neither approximation can qualitatively change the dynamic stability of the system when compared to the vacuum case. These approximations only modify the coefficients of the original constant-coefficient PDE; the PDE itself remains identical to the vacuum case.

Thus, the dynamic stability results of the corresponding vacuum case fully qualitatively govern the stability of this approximated FSI model. We will see later, in the numerical results of Section 6.3, that this property does not hold for the original model; introduction of the exact analytical aerodynamic reaction may introduce an instability, much like the introduction of damping did in subsection 2.2.2.

3.7 Summary and conclusion

We set up the aerodynamic problem and derived its solution in a functional form, using the techniques of thin airfoil analysis. We obtained a Green's function solution in terms of the aerodynamic kernel $N(\xi, x)$, determined explicitly in closed form, and the panel displacement $w(x,t)$. This solution was used to produce an explicit formula for the aerodynamic reaction $q_f(w)$.

We proved certain symmetry properties and the absolute integrability of the aerodynamic kernel. We also established an analytical upper limit for its values across its whole domain. Finally, we derived an added-mass approximation for the present FSI model, and suggested a second, more sophisticated added-mass approximation with coefficients depending on x.

The assumptions behind the obtained solution are as follows. The fluid is ideal; that is, only potential flow occurs, and fluid rotation and viscosity are neglected. The panel displacement w, the fluid disturbance potential φ, and their derivatives are small. Especially, the panel undergoes small deformation only; geometrically, it can be approximated as a straight line segment on the x axis. In the flow problem, only the no-penetration boundary condition depends on the panel's transverse displacement w. Although an axially moving panel is studied, in the fluid flow problem the panel only exists in the interval $x \in [-1, 1]$. Thus,

in the panel domain, there is a material source at $x = -1$ and a sink at $x = +1$ (for positive V_0). The rollers supporting the panel, and any surrounding parts of the panel itself, are neglected in the flow analysis.

The approach is thus highly approximate, but it is fairly simple and it accounts for two-way coupling between the panel and fluid components of the FSI model. The deformation of the panel pushes the fluid, which then pushes back on the panel surface. The linearity of the model is preserved, because potential flow is memory-free.

Finally, it should be noted that our solution for the aerodynamic problem does not require the simply supported boundary conditions for the panel that we use in the present work. Any choice of boundary conditions for the panel can be used, as long as the panel displacement w and its derivatives inside the domain remain small. For one example, the same aerodynamic reaction is applicable also with the nonsymmetric boundary conditions introduced by Garziera and Amabili (2000), in which study the case of tape winding onto a reel was investigated. In the papermaking context, those boundary conditions could be used for modelling the end of the paper machine, where the finished product is similarly wound onto a reel.

4 THE AXIALLY MOVING PANEL SUBMERGED IN IDEAL FLUID

We will now begin analyzing the axially moving panel submerged in ideal fluid. We will use the solution of the flow problem from Chapter 3.

The analysis has been split into several chapters to facilitate logical organization. In this first, short chapter, we set up our three problems for the travelling panel submerged in ideal fluid, and perform the space discretization to obtain the semidiscrete form. The latter is done just once, because much of the work in the space discretization is identical in the steady-state and dynamic cases.

Starting from the semidiscrete form, the three main problems will be analyzed one at a time in Chapter 6. These are the steady-state stability problem, the dynamical behaviour problem, and the eigenfrequency problem. The presentation of problem-specific numerical approaches is deferred until the handling of each problem.

The numerical eigenfrequency problem requires some further consideration; practical tools for it will be developed in the intervening Chapter 5.

Let us begin by defining some common notation for all the problems. Let

$$V_{0D} \equiv \sqrt{T/m}\,, \tag{137}$$

which is the critical velocity of a membrane in vacuum (see, e.g., Chang and Moretti, 1991). Define also the dimensionless quantities

$$\gamma \equiv \ell\,\frac{\rho_f}{m}\,, \tag{138}$$

$$\beta \equiv \frac{D}{mV_{0D}^2\ell^2} = \frac{D}{\ell^2 T}\,, \tag{139}$$

$$\lambda \equiv V_0/V_{0D}\,, \tag{140}$$

$$\theta \equiv v_\infty/V_{0D}\,, \tag{141}$$

$$\alpha \equiv \frac{\ell/\tau}{V_{0D}}\,. \tag{142}$$

These denote a fluid effect coefficient, dimensionless bending rigidity, dimensionless axial velocities for the panel and the fluid, and dynamic time scale, respec-

tively. The quantities (138)–(141) appear in both steady-state and dynamic cases; the quantity (142) only in the dynamic case.

All three problems that will be analyzed can be expressed in abstract integro-differential form as

$$\mathcal{L}(w;\, V_0) + \gamma \mathcal{K}(w;\, v_\infty) = \mathcal{G}\ , \tag{143}$$

where $\mathcal{L}$ is the differential operator of the corresponding vacuum problem, γ is the fluid effect coefficient, $\mathcal{K}$ is the integro-differential operator accounting for fluid-structure interaction, and $\mathcal{G} = \mathcal{G}(x,t)$ is the (optional) external load function (which does not depend on w). The operator $\mathcal{L}$ has the panel velocity V_0 as parameter, while $\mathcal{K}$ has the fluid free-stream velocity v_∞. As the dynamical behaviour problem is the most general of those considered, equation (150), below, can be used as a definition for $\mathcal{L}$, $\mathcal{K}$ and $\mathcal{G}$.

4.1 Steady-state problem

We use the Euler approach of determining nontrivial steady-state solutions, and the associated critical values of the problem parameter of interest. Like in subsection 2.3.2, we concentrate on finding the critical velocities, which play the role analogous to Euler's critical compression force for the axially compressed beam.

Recall equation (82) (from p. 100), which describes the dynamical behaviour of the moving panel submerged in ideal fluid. Setting the time-dependent terms to zero, and assuming zero external forces ($g \equiv 0$), we obtain the steady-state equation

$$\left(mV_0^2 - T\right) w_{xx} + D w_{xxxx} = q_f\ , \tag{144}$$

which describes the buckling of a travelling panel submerged in ideal fluid. Refer to Figure 26 (p. 102).

It is convenient to transform the problem into nondimensional form for analysis. This should be done before we proceed any further, because the aerodynamic reaction, which we wish to insert here, was derived in dimensionless coordinates. Let us use $x' = x/\ell$ (recall equation (13), p. 58); hence each differentiation will produce a factor of $1/\ell$. Note that since we will be considering eigenvalue problems only, the scaling of w is of no concern. Let us choose $w'(x',t') \equiv w(x,t)$ (scaling factor of unity).

In dimensionless coordinates, we have

$$\left(mV_0^2 - T\right) \frac{1}{\ell^2} w_{xx} + D \frac{1}{\ell^4} w_{xxxx} = q_f\ ,$$

where $x \in [-1,1]$. The prime has been omitted from notation. Moving q_f to the left-hand side, inserting the final solution for the aerodynamic reaction from equation (122), and dropping the time dependence in it, we obtain

$$\left(mV_0^2 - T\right) \frac{1}{\ell^2} w_{xx} + D \frac{1}{\ell^4} w_{xxxx} + \rho_f \frac{1}{\ell} v_\infty \frac{\partial}{\partial x} \int_{-1}^{1} N(\xi, x)\, v_\infty \frac{\partial}{\partial x} w(\xi)\, \mathrm{d}\xi = 0\ . \tag{145}$$

Multiplying (145) by ℓ^2/mV_{0D}^2, and applying (138)–(141), we obtain

$$(\lambda^2-1)w_{xx}+\beta w_{xxxx}+\gamma\theta^2\frac{\partial}{\partial x}\left[\int_{-1}^{1}N(\xi,x)\left(\frac{\partial}{\partial x}w(\xi)\right)\,\mathrm{d}\xi\right]=0\,. \qquad (146)$$

This is the fourth-order integro-differential equation that will be solved for investigating the static stability. As was mentioned, the domain is $x\in[-1,1]$. For the boundary conditions, we take the simply supported conditions (66)–(67) (p. 93).

We fix all parameters but one, and treat the remaining parameter as an eigenvalue. In this study, we consider only the axial velocities V_0 (dimensionless: λ) and v_∞ (dimensionless: θ) as eigenvalues.

The static stability problem is: what are the critical values of the chosen parameter, such that (145) admits nontrivial solutions $w(x)\not\equiv 0$, and what are those nontrivial solutions?

The steady-state solution of the moving panel in vacuum (subsection 2.3.2) will be of interest as a point of comparison.

We will derive the discrete form of this problem from the semidiscrete form in Section 6.1.

4.2 Dynamical behaviour

For this problem, we investigate the full dynamic equation (82),

$$mw_{tt}+2mV_0w_{xt}+\left(mV_0^2-T\right)w_{xx}+Dw_{xxxx}=q_f+g\,.$$

Refer to Figure 25 (p. 101) for the setup. The external load $g\equiv g(x,t)$ is allowed to be nonzero, and is considered given.

Let us move into dimensionless coordinates. We will scale $x'=x/\ell$ and $t'=t/\tau$ as in (13), but for w, we choose the scaling $w'=w/\ell$ (which is especially convenient for this problem). We have

$$m\frac{1}{\tau^2}w_{tt}+2mV_0\frac{1}{\ell\tau}w_{xt}+\left(mV_0^2-T\right)\frac{1}{\ell^2}w_{xx}+D\frac{1}{\ell^4}w_{xxxx}=\frac{1}{\ell}q_f+\frac{1}{\ell}g\,. \qquad (147)$$

The $1/\ell$ factor on the right-hand side comes from the scaling of $w=\ell w'$ (after division of both sides by ℓ). The dimensionless variables $x\in[-1,1]$ and $t\in[0,\infty)$. Primes have been dropped from the notation.

Now we can insert the aerodynamic reaction $q_f\equiv q_f(w)$, which is given in dimensionless coordinates in equation (122),

$$q_f=-\rho_f\frac{1}{\ell}\left(\frac{\ell}{\tau}\frac{\partial}{\partial t}+v_\infty\frac{\partial}{\partial x}\right)\int_{-1}^{1}N(\xi,x)\left(\frac{\ell}{\tau}\frac{\partial}{\partial t}+v_\infty\frac{\partial}{\partial x}\right)w(\xi,t)\,\mathrm{d}\xi\,.$$

In the formula for the aerodynamic reaction, the scaling of w has not been applied yet; only dimensionless x' and t' are used. We must apply it now, to get an equation which depends only on the scaled w'. Inserting $w=\ell w'$ into (122) eliminates

the leading $1/\ell$. However, when we insert the resulting expression into (147), the same factor will be brought back by the $1/\ell$ multiplying the q_f.

Summarizing, we obtain

$$\begin{aligned} & m\frac{1}{\tau^2}w_{tt} + 2mV_0\frac{1}{\ell\tau}w_{xt} + \left(mV_0^2 - T\right)\frac{1}{\ell^2}w_{xx} + D\frac{1}{\ell^4}w_{xxxx} \\ & \quad = -\rho_f\frac{1}{\ell}\left(\frac{\ell}{\tau}\frac{\partial}{\partial t} + v_\infty\frac{\partial}{\partial x}\right)\int_{-1}^{1} N(\xi,x)\left(\frac{\ell}{\tau}\frac{\partial}{\partial t} + v_\infty\frac{\partial}{\partial x}\right)w(\xi,t)\,\mathrm{d}\xi + \frac{1}{\ell}g(x,t)\ . \end{aligned} \tag{148}$$

Anticipating upcoming manipulations, let us define the dimensionless external load (here spelling out the primes for the sake of clarity)

$$g''(x',t') \equiv \frac{\ell}{mV_{0D}^2}\,g'(x',t') = \frac{\ell}{T}\,g'(x',t')\ . \tag{149}$$

The double-prime is just notation to distinguish g'' (dimensionless) and g' (dimensional, but function of dimensionless variables). Explicitly,

$$g'(x',t') \equiv g(x,t) = g(\,\ell\,x',\,\tau\,t'\,)\ .$$

Hence, to actually evaluate g'', we can use

$$g''(x',t') = (\ell/T)\cdot g(\,\ell\,x',\,\tau\,t'\,)\ ,$$

where g is the original (dimensional) load function.

We multiply (148) by ℓ^2/mV_{0D}^2, and in the q_f term, distribute the $1/V_{0D}^2$ into the operators (one $1/V_{0D}$ per instance of the operator). Applying (138)–(142) to the result, and moving q_f to the left-hand side, we have

$$\begin{aligned} & \alpha^2 w_{tt} + 2\alpha\lambda w_{xt} + (\lambda^2-1)w_{xx} + \beta w_{xxxx} \\ & \qquad + \gamma\left(\alpha\frac{\partial}{\partial t} + \theta\frac{\partial}{\partial x}\right)\int_{-1}^{1} N(\xi,x)\left(\alpha\frac{\partial}{\partial t} + \theta\frac{\partial}{\partial x}\right)w(\xi,t)\,\mathrm{d}\xi = g''(x,t)\ . \end{aligned} \tag{150}$$

The domain of equation (150) is $(x,t) \in (\,[-1,1],\ [0,\infty)\,)$. This is the equation that will be solved to determine the dynamical behaviour.

As the boundary conditions, we use the simply supported conditions (66)–(67) (p. 93). Uniqueness of dynamic behaviour requires two initial conditions, as the equation is of the second order in time. We set

$$w(x,0) = g_1(x) \tag{151}$$

$$w_t(x,0) = g_2(x)\ , \tag{152}$$

where $g_1(x)$ and $g_2(x)$ are given functions.

The dynamic problem is to solve the initial boundary value problem (150), (66)–(67), (151)–(152) to find the time-dependent behaviour $w(x,t)$.

We will derive the discrete form of this problem from the semidiscrete form in Section 6.2.

4.3 Eigenfrequencies

The eigenfrequency problem is concerned with finding the unloaded time-harmonic behaviour. We start from equation (150), and set $g \equiv 0$. By inserting the standard time-harmonic trial function

$$w(x,t) \equiv e^{st} W(x) \tag{153}$$

into (150), and ignoring the common exp factor, we have the pseudo-steady-state problem

$$\alpha^2 s^2 W + 2\alpha\lambda s W_x + (\lambda^2 - 1) W_{xx} + \beta W_{xxxx} + \gamma \left(\alpha s + \theta \frac{\partial}{\partial x}\right) \int_{-1}^{1} N(\xi, x) \left(\alpha s + \theta \frac{\partial}{\partial x}\right) W(\xi)\, \mathrm{d}\xi = 0\,. \tag{154}$$

Because our original operator is linear in w, and the original coefficients are real, the complex-valued time-harmonic approach is justified, as was noted in the introduction (Section 1.5, page 47). As usual, s will be complex, and the coefficients of the space-component problem (154) will be complex-valued.

As the boundary conditions for $W(x)$, we choose the simply supported conditions (66)–(67) (p. 93). In the eigenfrequency analysis, we just look for possible modes for free vibrations, so initial conditions are not needed. Instead, we have an eigenvalue problem for pairs (s, W).

As a point of comparison, it is useful to keep in mind the qualitative aspects of the free-vibration solutions from Chapter 2 (subsections 2.1.4, 2.2.2 and 2.3.3).

We will derive the discrete form of this problem from the semidiscrete form in Section 6.3.

4.4 Derivation of semi-discrete form

For the purposes of numerical analysis, a discrete approximation will be used for the partial differential equations as usual. Also in the traditional manner, the space discretization will be performed first, producing a semi-discrete form. Deriving the semi-discrete form is the purpose of the present section. Practical hints for computing the fluid-structure interaction matrices, which will arise in the discretization, are included in Appendix 2.

In the dynamic behaviour problem, we will also need a time discretization; this will be performed during the analysis of the dynamic problem, in Section 6.2. For the other two problems, the space discretization is sufficient. The steady-state problem is by definition time-independent; and for the eigenfrequency problem, the time component is known analytically.

Galerkin methods are especially convenient for numerical handling of integro-differential equations. We will space-discretize using the Fourier–Galerkin

method (see e.g. Canuto et al. 1988). The Fourier–Galerkin method is a traditional spectral method of the Galerkin type. According to Canuto et al. (1988), the first serious application of spectral methods to partial differential equations was made by Silberman (1954) for meteorological modelling. For a stability analysis of the method and some further references, see Tadmor (1987). Recently, the method has been applied, e.g., in computing the stationary solutions of two-dimensional generalised wave equations (Christou and Christov, 2007).

We represent the displacement w as a Galerkin series,

$$w(x,t) = \sum_{n=1}^{\infty} f_n(t)\,\Psi_n(x)\ , \tag{155}$$

Note that we are working in dimensionless coordinates, so there is no scaling factor, and w (which is actually w' with the prime omitted from notation) is dimensionless. The functions f_n and Ψ_n are both dimensionless.

For the shape functions Ψ_n, we choose the eigenmodes of free vibrations of a membrane in vacuum,

$$\Psi_n(x) \equiv \sin\left(n\pi\frac{x+1}{2}\right), \quad x \in [-1,1]\,. \tag{156}$$

This is a Fourier sine basis that splits the space component of the solution into a frequency domain along the x axis.[1] By its construction, it automatically accounts for the simply supported boundary conditions (66)–(67). The basis is equivalent to the standard Fourier sine basis, up to a constant factor of 2, if the solution is considered to have period 4, and to be antisymmetric with regard to the (fictitious) midpoint $x = 1$.

We start the development of the semi-discrete form from the dimensionless integro-differential equation (150), which we repeat here:

$$\alpha^2 w_{tt} + 2\alpha\lambda w_{xt} + (\lambda^2-1)w_{xx} + \beta w_{xxxx} + \gamma\left(\alpha\frac{\partial}{\partial t} + \theta\frac{\partial}{\partial x}\right)\int_{-1}^{1} N(\xi,x)\left(\alpha\frac{\partial}{\partial t} + \theta\frac{\partial}{\partial x}\right) w(\xi,t)\,\mathrm{d}\xi = g''(x,t)\ .$$

We must be careful with the $\partial/\partial x$ in front of the integral in the fluid term, because the aerodynamic kernel $N(\xi,x)$ is singular. We cannot directly take the derivative operator into the integral, because the L_1 norm of $\partial N/\partial x$ is not finite. A straightforward, but somewhat lengthy, calculation finds that $\partial N/\partial x$ has singularities of type $1/x^{\alpha}$, where $\alpha \geq 1$. The singularities are located at $x = \pm 1$ with $\alpha = 3/2$, and at $x = \xi$ with $\alpha = 1$.

However, as was shown, the integral in (121) is absolutely convergent, and thus the function φ^+ is bounded. We can choose from two approaches. The first approach is to integrate first, and then differentiate the result by any method.

[1] This use of the word *frequency* has nothing to do with time, but represents the decomposition of the space axis in a manner somewhat similar to what Fourier analysis does to time signals. Note that the functions f_n are functions of the time t directly; hence our frequency domain is only spatial.

The second approach, more applicable here because we will work in the weak form and do not have a closed-form antiderivative, is to integrate by parts against the test function as usual. This is legitimate despite the singularity, because the integrand of the weak form is a product of two bounded, integrable functions.

We now consider the system of equations corresponding to the dynamics of the web, expressed by the weak form of (150). As was mentioned earlier, (150) is of the abstract form

$$\mathcal{L}(w;\, V_0) + \gamma \mathcal{K}(w;\, v_\infty) = \mathcal{G}\ .$$

We multiply equation (150) by the test function $\Psi_j(x)$ and integrate over the dimensionless space domain $\Omega = [-1, 1]$. We have

$$\begin{aligned}
&\alpha^2 \int_{-1}^{1} w_{tt}\Psi_j \,\mathrm{d}x + 2\alpha\lambda \int_{-1}^{1} w_{xt}\Psi_j \,\mathrm{d}x \\
+(\lambda^2-1) &\int_{-1}^{1} w_{xx}\Psi_j \,\mathrm{d}x + \beta \int_{-1}^{1} w_{xxxx}\Psi_j \,\mathrm{d}x \\
&+\gamma \int_{-1}^{1} \left[\left(\alpha\frac{\partial}{\partial t} + \theta\frac{\partial}{\partial x} \right) \int_{-1}^{1} N\left(\xi, x\right) \left(\alpha\frac{\partial}{\partial t} + \theta\frac{\partial}{\partial x} \right) w(\xi, t)\,\mathrm{d}\xi \right] \Psi_j(x)\,\mathrm{d}x \\
&= \int_{-1}^{1} g''(x,t)\Psi_j \,\mathrm{d}x\ . \qquad (157)
\end{aligned}$$

The brackets emphasize that the aerodynamic reaction is one function. In the same term, the x in $\Psi_j(x)$ is indicated explicitly, because there are two integrations: first, over ξ to determine $q_f(x,t)$ at a fixed x, and then over x from the weak form. From (157), the choices of functions for integration by parts should be more apparent, and it should be clear what to do in practice in order to transfer the outer $\partial/\partial x$ to the factor $\Psi_j(x)$.

That takes care of the space derivative. What about the outer $\partial/\partial t$? Once we insert the Galerkin series (155), for each term n in the sum, the function w will separate into a product of space- and time-dependent parts. We make the standard assumption that the series is "convergent enough" so that the order of spatial integration and series summation can be exchanged. Once the summation has been taken outside both (nested) integrals, we can use the fact that the time part is constant in space, and hence it too can be taken outside the integrals.

To sum up, as long as care is taken with the outer $\partial/\partial x$ in the aerodynamic term, the rest can be done in the standard manner. The result is as follows. Inserting the Galerkin series (155) into the weak form (157) gives us the following expressions for the weak equivalents of the operators $\mathcal{L}$ and $\mathcal{K}$:

$$\begin{aligned}
\int_{-1}^{1} \mathcal{L}\left(w;\lambda\right)\, \Psi_j \,\mathrm{d}x &= \int_{-1}^{1} \mathcal{L}\left(\sum_{n=1}^{\infty} f_n \Psi_n \ ;\lambda \right) \Psi_j \,\mathrm{d}x \\
&= \sum_{n=1}^{\infty} \left[\alpha^2 A_{jn} \frac{\mathrm{d}^2 f_n}{\mathrm{d}t^2} + 2\alpha\lambda B_{jn} \frac{\mathrm{d}f_n}{\mathrm{d}t} + (\lambda^2-1) C_{jn} f_n + \beta D_{jn} f_n \right] \qquad (158)
\end{aligned}$$

$$\int_{-1}^{1} \mathcal{K}\left(w;\theta\right)\, \Psi_j \,\mathrm{d}x = \int_{-1}^{1} \mathcal{K}\left(\sum_{n=1}^{\infty} f_n \Psi_n \;;\theta\right) \Psi_j \,\mathrm{d}x$$
$$= \sum_{n=1}^{\infty} \left[\alpha^2 a_{jn} \frac{\mathrm{d}^2 f_n}{\mathrm{d}t^2} + 2\alpha\theta b_{jn} \frac{\mathrm{d}f_n}{\mathrm{d}t} + \theta^2 c_{jn} f_n\right]. \qquad (159)$$

The operator $\mathcal{L}$ depends on the dimensionless panel velocity λ, while $\mathcal{K}$ depends on the dimensionless fluid velocity θ. Both operators are nonzero even at zero velocity.

The formal matrices A_{jn}, B_{jn}, C_{jn}, D_{jn}, a_{jn}, b_{jn} and c_{jn} are defined by

$$A_{jn} = \int_{-1}^{1} \Psi_n(x)\Psi_j(x)\,\mathrm{d}x = \delta_{jn} \qquad (160)$$

$$B_{jn} = \int_{-1}^{1} \frac{\mathrm{d}\Psi_n}{\mathrm{d}x}(x)\Psi_j(x)\,\mathrm{d}x = \begin{cases} 0, & j = n \\ \dfrac{nj}{n^2 - j^2}\left((-1)^{j+n} - 1\right), & j \neq n \end{cases} \qquad (161)$$

$$C_{jn} = \int_{-1}^{1} \frac{\mathrm{d}^2\Psi_n}{\mathrm{d}x^2}(x)\Psi_j(x)\,\mathrm{d}x = -\left(\frac{j\pi}{2}\right)^2 \delta_{jn} \qquad (162)$$

$$D_{jn} = \int_{-1}^{1} \frac{\mathrm{d}^4\Psi_n}{\mathrm{d}x^4}(x)\Psi_j(x)\,\mathrm{d}x = \left(\frac{j\pi}{2}\right)^4 \delta_{jn} \qquad (163)$$

$$a_{jn} = \int_{-1}^{1}\int_{-1}^{1} \Psi_n(\xi) N\left(\xi, x\right) \Psi_j(x)\,\mathrm{d}\xi\mathrm{d}x \qquad (164)$$

$$b_{jn} = \frac{1}{2}\left(I_{jn} - I_{nj}\right) \quad \text{and} \qquad (165)$$

$$c_{jn} = -\int_{-1}^{1}\int_{-1}^{1} \frac{\mathrm{d}\Psi_n}{\mathrm{d}x}\left(\xi\right) N\left(\xi, x\right) \frac{\mathrm{d}\Psi_j}{\mathrm{d}x}\left(x\right)\,\mathrm{d}\xi\mathrm{d}x\,, \qquad (166)$$

where $j, n = 1, 2, 3, \ldots$ and δ_{jn} is the Kronecker delta. In equation (165), we have defined

$$I_{jn} \equiv \int_{-1}^{1}\int_{-1}^{1} \frac{\mathrm{d}\Psi_n}{\mathrm{d}x}\left(\xi\right) N\left(\xi, x\right) \Psi_j\left(x\right)\,\mathrm{d}\xi\mathrm{d}x\,. \qquad (167)$$

The test functions are indexed by j; the Galerkin series is summed over n.

In equation (166), and in the I_{nj} term in (165), we have carried out the mentioned integration by parts. No boundary terms appear, because $N(\xi, \pm 1) = 0$ either directly (at $x = +1$) or in the sense of limits (at $x = -1$). This holds for any choice of boundary conditions for w. (Additionally, if the chosen boundary conditions require $w|_{x=\pm 1} = 0$, it follows that $\Psi_j(\pm 1) = 0$ for all j.)

Although we use a global sine basis which is infinitely smooth, the integration by parts is compulsory due to the singularity of $N(\xi, x)$, as mentioned above.

The closed-form solutions of (160)–(163) are, obviously, specific to the basis (156). In all other respects, the definitions (160)–(167) always hold, regardless of the basis or boundary conditions chosen.

The integrals in (164)–(167) have no closed-form solution, but some useful properties may be obtained analytically, assuming the basis (156). A summary

follows; see Appendix 2 for the details. If $j+n$ is odd, then $a_{jn} = c_{jn} = 0$ by considering the symmetries of each integrand. The matrix b_{jn} is antisymmetric, and if $j+n$ is even, then $b_{jn} = 0$. The matrices a_{jn} and c_{jn} are symmetric by the symmetry of $N(\xi, x)$ with respect to the line $x = \xi$ and the application of Fubini's theorem. When $j+n$ is even, each integrand a_{jn} and c_{jn} is symmetric with respect to the lines $x = \xi$ and $x = -\xi$.

Summarizing, we have obtained the semidiscrete weak form,

$$\sum_{n=1}^{\infty} \left(\alpha^2 \left[A_{jn} + \gamma a_{jn} \right] \frac{\mathrm{d}^2 f_n}{\mathrm{d}t^2} + 2\alpha \left[\lambda B_{jn} + \gamma\theta b_{jn} \right] \frac{\mathrm{d}f_n}{\mathrm{d}t} + \left[(\lambda^2 - 1) C_{jn} + \gamma\theta^2 c_{jn} + \beta D_{jn} \right] f_n \right) - G_j = 0 \,, \quad (168)$$

where definitions (138)–(142), (149), and (160)–(167) have been used. Additionally, we have defined the space-discrete load vector, whose jth component is (spelling out the primes)

$$G_j(t') \equiv \int_{-1}^{1} g''(x', t') \, \Psi_j(x') \, \mathrm{d}x' \,. \quad (169)$$

Finally, consider the initial conditions for direct temporal simulation. We insert (155) into (151)–(152) (page 129), multiply both sides by $\Psi_j(x)$, integrate over the domain, and use (160) to eliminate all cross terms on the left-hand side. We have

$$f_j(0) = \frac{1}{\ell} \int_{-1}^{1} \Psi_j(x) g_1(x) \, dx, \quad j = 1, 2, 3, \ldots \quad (170)$$

$$\frac{df_j}{dt}(0) = \frac{1}{\ell} \int_{-1}^{1} \Psi_j(x) g_2(x) \, dx, \quad j = 1, 2, 3, \ldots \,. \quad (171)$$

The leading $1/\ell$ comes from the scaling $w = \ell w'$, by dividing both sides of each equation by ℓ. (This scaling is inherited from (150).)

This completes the semi-discrete form. The original initial boundary value problem (150), (66)–(67), (151)–(152), has been transformed into a Cauchy problem for the system of ordinary differential equations (168) with initial conditions (170)–(171).

For a practical numerical implementation, we truncate the Galerkin series at a given value of $n = n_0$. The resulting finite equation corresponding to (168) is a linear, second-order, non-homogeneous, system of ordinary differential equations with constant coefficients.

5 SOLUTION AND VISUALIZATION OF EIGENFREQUENCIES

One final task remains before we can solve all three problems that we set up in Chapter 4. In this section, we will look at the computation and visualization of as many eigenfrequencies as the discretization allows. For now, we assume that we have obtained the eigenfrequencies of the discrete problem; how to do this will be reviewed in Section 6.3.

Although the solution of complex eigenfrequencies itself is an often recurring theme in the literature (see e.g. Bolotin, 1963; Ulsoy and Mote, 1982; Renshaw and Mote, 1996; Lin, 1997; Parker, 1998; Guo and Païdoussis, 2000; Kim et al., 2003; Païdoussis, 2004; Lee and Oh, 2005; Zhou and Wang, 2007; Vaughan and Raman, 2010), this is a topic that is not often discussed. Parker (1999) has previously made some remarks in this area for some models of the same class, but did not consider the problem of connecting the solution points in visualization.

When we solve the eigenfrequency problem, we will keep the rest of the problem parameters fixed, and scan through the V_0 axis. We will discretize the V_0 axis into steps, and record the set of eigenvalues for each step. Even with $n_0 = 50$ basis functions, one scan is completed in a few seconds. Since the problem is continuous in V_0, the scan, when plotted in $\mathbb{R}^3$ with $(V_0,\ \mathrm{Re}\, s,\ \mathrm{Im}\, s)$ as the axes, consists of $2n_0$ continuous curves. We will then repeat the process for different values of v_∞ to see the effect of axial motion of the free stream.

However, since standard eigenvalue solvers return the results in a random order, the indices corresponding to points on the same curve may switch around randomly at adjacent V_0 steps. A trivial solution is to forget about drawing lines, and to simply use a scatter plot (see e.g. Parker, 1999, p. 212–213, and Guo and Païdoussis, 2000). In a way, this is the most accurate view of the discrete data.

However, a representation based on piecewise linear curve segments is somewhat easier to read visually. In order to be able to draw lines in $\mathbb{R}^3$ connecting the corresponding points in the discrete data for two adjacent values of V_0, we must detect at each V_0 step which of the solutions is which. Obviously a general solution is to take advantage of continuity; the purpose of this chapter is to present two practical methods to address this.

There is also a second issue here that deserves attention. Before the truncation of the Galerkin series, the original frequency-domain problem is infinite-dimensional. In a practical numerical solution, naturally only a finite number of terms are kept, leading to a matrix M of size $2n_0 \times 2n_0$. The matrix has $2n_0$ complex eigenvalues[1].

With n_0 basis functions used to construct the Galerkin approximation (155) (page 131), obviously only some of the $2n_0$ eigenfunctions can be approximated to reasonable accuracy in the general case. In practice, it is seen that the lowest modes are approximated the most accurately. The question naturally arises: is the accuracy of the eigenfrequencies affected by the discretization, too?

5.1 Demonstration of qualitative artifacts introduced by discretization

One might guess, correctly, that the answer is yes. We will see that in general, the discretization can be expected to introduce even qualitative artifacts into the eigenfrequency solution. Detailed analysis of this phenomenon is beyond the scope of the present study; the purpose of this section is simply to raise awareness of the phenomenon, and to demonstrate it on a simple problem for which a closed-form solution is known. Compare the study by Parker (1999, p. 212–213), who has noted the same problem.

To demonstrate the issue numerically, let us consider the problem of the moving ideal string, travelling through two pinholes (which was solved analytically in subsection 2.1.4). We will concentrate on the phenomenon itself; the techniques used will be presented in detail in the following Sections 5.2 and 5.3.

In the Fourier–Galerkin basis, for this problem specifically, all modes are correct at $V_0 = 0$, because at this point the basis functions are exactly the eigenfunctions of the system (recall that they were chosen this way). As $|V_0|$ increases, the approximation quality suffers, as the basis functions drift (continuously) further and further away from the eigenfunctions.[2]

By comparing the numerical results to a plot of the analytical solution (33) (p. 64), it is seen that the lowest n_0 eigenfrequencies are reproduced reasonably accurately up to the critical velocity (and maybe a slight bit beyond). However, the other half of the numerical solution is simply wrong: the highest n_0 modes seemingly introduce flutter instabilities, whereas it is analytically known that this particular system is stable for all V_0. We also see that the values of the incorrect solutions depend on the space discretization used.

---

1 These are not necessarily distinct; but in practice multiplicities higher than one only appear during eigenvalue pair collisions, and when passing through the origin.

2 A natural idea for improving the results would be to use the velocity-dependent eigenfunctions of the moving string as the basis, instead of the eigenfunctions of the stationary string. Parker (1999) indeed suggests this, referring to Mote and Wickert (1991) (see discussion of the Rayleigh quotient from p. S282 onward).

The numerical results are produced as follows. We first discretize the ideal string problem in space using Fourier–Galerkin. This produces the matrices (160)–(162), given in Section 4.4 (page 133). We solve the flutter equation (206) (below, page 183). Refer to equations (168) and (190)–(193) (pages 134 and 171–172, respectively) for the necessary definitions.

We also discretize the same problem using standard linear Lagrange FEM (i.e. linear finite elements) on a uniform grid with spacing h. Working out the weak form produces the well-known tridiagonal matrices

$$\tilde{A}_{jn} \equiv \int_\Omega \phi_j \phi_n \,\mathrm{d}x = \begin{cases} 2h/3\,, & \text{if } j = n \\ h/6\,, & \text{if } |j-n| = 1 \\ 0 & \text{otherwise} \end{cases} \tag{172}$$

$$\tilde{B}_{jn} \equiv \int_\Omega \phi_j \frac{\mathrm{d}}{\mathrm{d}x}(\phi_n) \,\mathrm{d}x = \begin{cases} +1/2\,, & \text{if } n = j+1 \\ -1/2\,, & \text{if } n = j-1 \\ 0 & \text{otherwise} \end{cases} \tag{173}$$

$$\tilde{C}_{jn} \equiv -\int_\Omega \frac{\mathrm{d}}{\mathrm{d}x}(\phi_j) \frac{\mathrm{d}}{\mathrm{d}x}(\phi_n) \,\mathrm{d}x = \begin{cases} 2/h\,, & \text{if } j = n \\ -1/h\,, & \text{if } |j-n| = 1 \\ 0 & \text{otherwise}\,, \end{cases} \tag{174}$$

which correspond to the local inertia, Coriolis, and centrifugal terms, respectively. As before, the index j refers to the test function; summation in the Galerkin series is taken over n. The symbol ϕ is used for the basis functions of the piecewise linear basis simply to distinguish it from the sine basis.

Note that the boundary conditions imply that the first and last nodes have $w = 0$; the degrees of freedom are related only to the interior of the domain. Also, the boundary term (from integration by parts in $\tilde{C}_{jn}$) vanishes. The flutter equation (206) for the linear FEM case is formed in the exact same manner as above, now using (172)–(174) in place of (160)–(162) when assembling the matrices M_2, M_1 and M_0. Because there is no fluid, the matrices $\tilde{a}_{jn} \equiv \tilde{b}_{jn} \equiv \tilde{c}_{jn} \equiv 0$, and no bending rigidity; hence also $\tilde{D}_{jn} \equiv 0$. (If there were bending rigidity, we would need a C^1 FEM.)

We solve (206) for each of the two discretizations using the eigenvalue approach, Section 6.3. The numerical results are shown in Figure 34. Compare the plot of the analytical result in Figure 10 on page 65; in the analytical solution, Re $s \equiv 0$.

The difference in the scaling of Im s (and also Re s, although this is obviously not visible in a problem where Re $s \equiv 0$) arises from a difference in the length of the domain. Here the length is two units, whereas in Figure 10, one unit; see footnote 3 on page 168.

Figure 35 shows the filtered numerical result, where only those parts of the solutions flagged as correct are shown. Methods to do this will be discussed in Section 5.3.

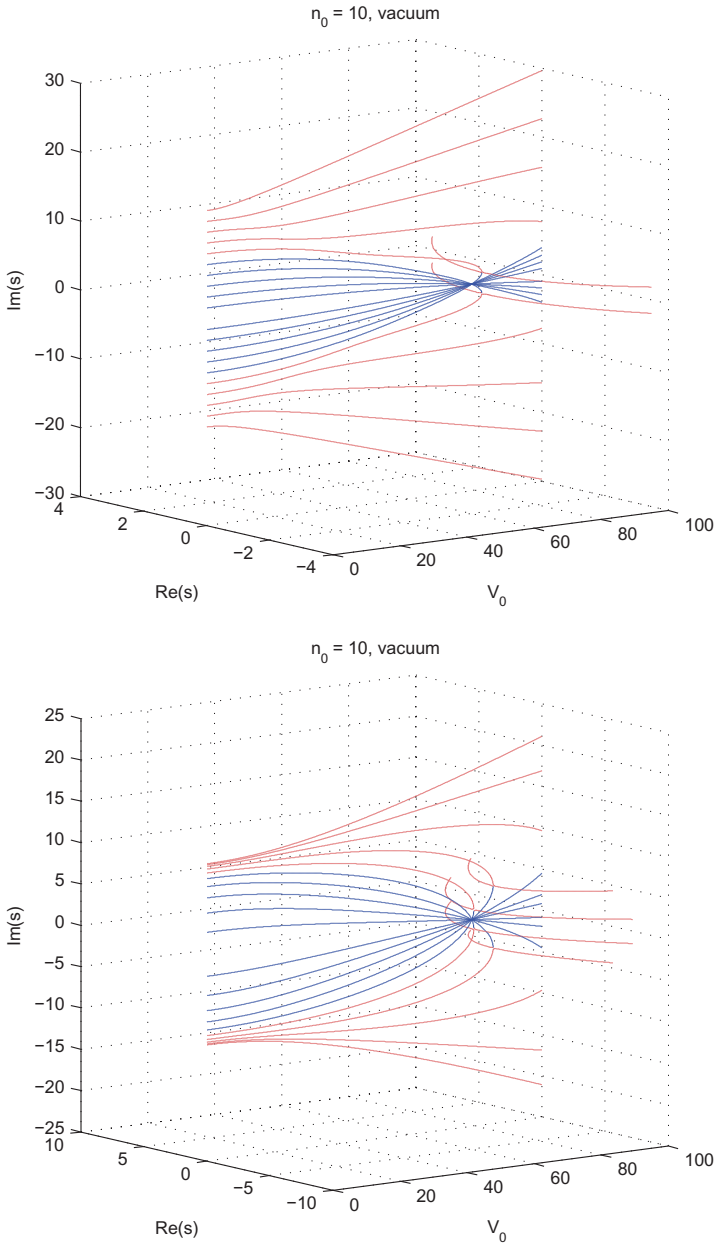

FIGURE 34 Eigenvalues of the moving ideal string. *Top*: Fourier–Galerkin discretization, MAC tracking (see Section 5.2). *Bottom*: Linear FEM discretization, Taylor tracking. In both plots, blue (dark) line denotes parts of solution flagged as correct, red (light) line parts flagged as numerical artifacts. Compare analytical result in Figure 10 (p. 65), for which $\operatorname{Re} s \equiv 0$.

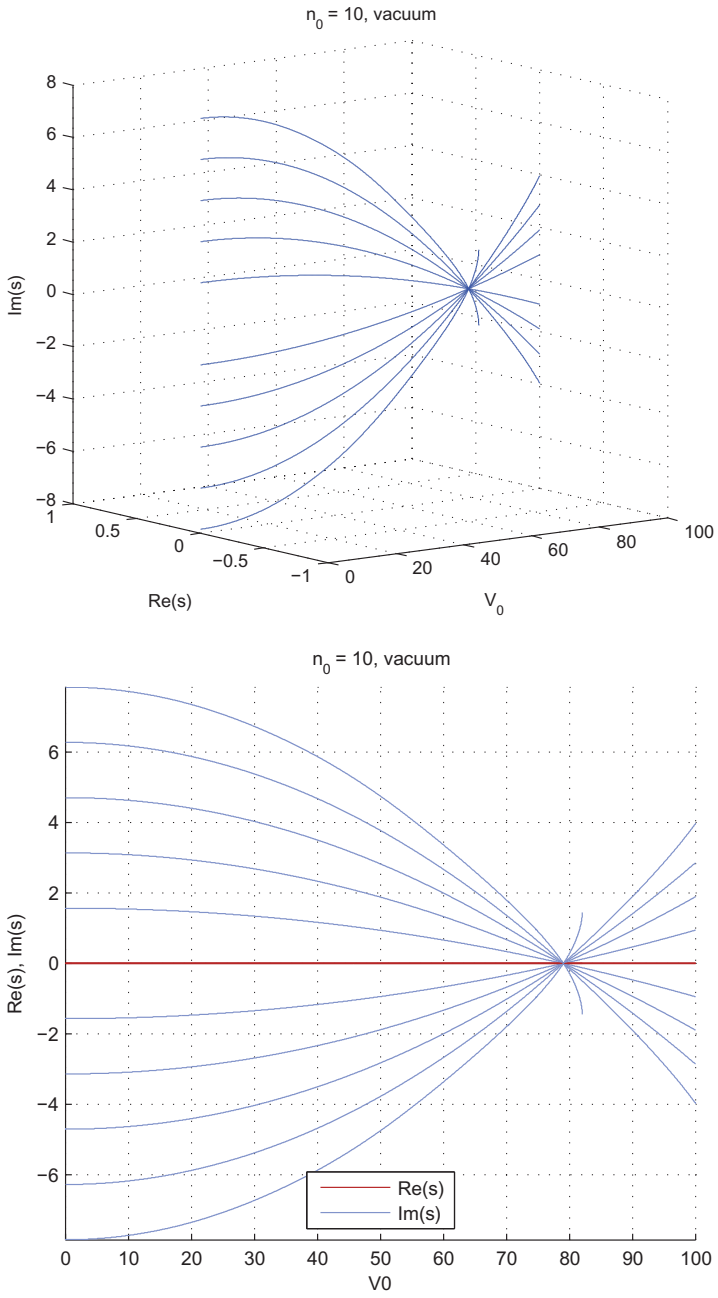

FIGURE 35 Eigenvalues of the moving ideal string. After filtering (Section 5.3); only those parts of the solutions flagged as correct are shown. Fourier–Galerkin discretization with MAC tracking (Section 5.2). In the projection, blue (light) line denotes imaginary part, red (dark) line real part.

5.2 Tracking the solutions

As was mentioned above, the identities of the solutions must be tracked somehow if we are to be able to plot piecewise linear curves in $\mathbb{R}^3$.

There are at least two different ways to utilize the continuity of the problem. If we have no desire to compute the eigenfunctions (or do not have them available), a natural approach is to assume that the curve traced by each eigenvalue is C^1 with respect to V_0 (physically, continuous with continuous "velocity" $\mathrm{d}s/\mathrm{d}V_0$). Then one can use local Taylor series (approximated, e.g., up to the 2nd derivative order, using e.g. backward differences of second-order accuracy in h) to predict where the eigenvalue "should" go in the next V_0 step.

In collision-free or "sparsely populated" areas, this is a fairly good approach. The advantage is that the eigenfunctions do not need to be known. It is also very fast to compute. However, this approach requires that the velocity grid is "tight enough" so that the derivative approximations are valid. Also, when an eigenvalue collision occurs, re-catching each solution requires a backup plan (e.g. picking the solution closest to the previous value), until enough "old" points on a continuous path are gathered to use the Taylor approximations again. If lots of eigenvalues crowd near each other (especially just after a collision), the algorithm may make mistakes.

Another way is to use the modal assurance criterion (MAC) from modal analysis. The advantage is that this approach is not sensitive to the size of the V_0 step. It can reliably identify the solutions even when the eigenvalues pass through each other (e.g. at the critical point of the ideal string). The main disadvantage is that it requires the solution of the eigenmode corresponding to each eigenvalue at each V_0 step; this adds a lot of computational effort. The approach is good, but not perfect; it was observed in practice that depending on the case, either algorithm may provide better tracking.

Whichever approach is used, some bookkeeping is required to ensure that the same solution is used only once during each V_0 step. Otherwise, when multiple matches occur (to within numerical accuracy), the same solution at the new step may get assigned to two or more solutions at the old step, leaving one or more solutions at the new step unassigned (and corrupting the tracking from that point on).

5.2.1 Taylor-based tracking algorithm

The Taylor-based algorithm works as follows. To approximate the derivatives in the Taylor series, we use the following backward differences of second-order asymptotic accuracy:

$$\frac{\partial u}{\partial x}|_{x=x_k} = \frac{1}{2h}\left(3u_k - 4u_{k-1} + u_{k-2}\right) + O(h^2)\ ,$$
$$\frac{\partial^2 u}{\partial x^2}|_{x=x_k} = \frac{1}{h^2}\left(2u_k - 5u_{k-1} + 4u_{k-2} - u_{k-3}\right) + O(h^2)\ ,$$

where we have used the standard notation $u_k \equiv u(x_k)$, and $x_0, x_1 = x_0 + h, x_2 = x_0 + 2h \ldots, x_n = x_0 + nh$ is a uniform grid with spacing h. These formulas are assumed well-known; for derivations, see a textbook, or refer to online sources[3].

In the algorithm, the symbols are defined as follows. Let h denote the spacing of a uniform grid on the V_0 axis. Let $\mathbf{s}^{(j)}$ denote all solutions at V_0 step j, and $s_k^{(j)}$ solution k at V_0 step j. Let N be the total number of V_0 steps. Let $M = 2n_0$, the number of solutions at one V_0 step. Let $\|s\| \equiv \sqrt{s\,\bar{s}} \equiv \sqrt{(\operatorname{Re} s)^2 + (\operatorname{Im} s)^2}$.

Taking into account the vectorized nature of modern numerical programming languages including MATLAB, Python with NumPy and Fortran 90, the algorithm is given in a vector form. This makes the presentation more compact, shows the logical structure more clearly, and is directly suited for programming in vectorized languages. The conversion to a scalar form, if needed, can be done trivially by adding the appropriate loops taken over the elements. If the target language is object-oriented, implementing a custom data type obeying the vector semantics is likewise easy, and may be conceptually cleaner (by keeping the abstraction at a reasonably high level at each point in the code).

The bold symbols denote vectors of length M. Operations are assumed elementwise unless otherwise noted. For instance, if $\mathbf{s} = (s_1, s_2, \ldots, s_M)$, in the vector notation $\|\mathbf{s}\| \equiv (\|s_1\|, \|s_2\|, \ldots, \|s_M\|)$. Assigning a scalar $\mathbf{u} \leftarrow r$ means setting all elements $u_k \leftarrow r$.

We also use the logical indexing notation that is common in vectorized languages. For example, the logical test $\mathbf{u} = 1$ performed on a vector $\mathbf{u}$ produces a logical vector $\mathbf{b}$, of the same length as $\mathbf{u}$, with ones (logical true) in positions where the condition matches, and zeroes (logical false) in positions where it does not match. Indexing a vector $\mathbf{v}$ by a logical vector $\mathbf{b}$, denoted as $\mathbf{v_b}$, refers to taking (or applying some operation to) those elements v_k where $b_k = 1$. The compacted notation $\mathbf{v}_{\mathbf{u}=1}$ means "those elements v_k where $u_k = 1$". When logical indexing is used, the vectors $\mathbf{v}$ and $\mathbf{u}$ must be of the same length.

Finally, the notation $(a, b) \leftarrow \min_k \mathbf{u}$ means taking both the minimal element (min) of $\mathbf{u}$ and its index (arg min), and assigning the pair to the scalar variables a and b, respectively.

With these in mind, the Taylor-based tracker is given in Algorithm 1. For simplicity, the algorithm is presented for the case when the data contain only solutions for $V_0 \geq 0$, with the data for $V_0 = 0$ located at index $j = 1$. If $V_0 = 0$ is located in the middle of the data, it is more convenient (for reasons that will become clear below) to do the tracking in two passes (one pass in each direction), beginning each pass at the index j_0 where $V_0 = 0$. If this is done, all step indices will of course need to be adjusted in the obvious manner.

For the backward pass, in the difference formula for $\partial u/\partial x$ given above, in addition to replacing $k - 1$ with $k + 1$ and $k - 2$ with $k + 2$, all signs on the

[3] For example, the online document `http://www.geometrictools.com/Documentation/FiniteDifferences.pdf` by David Eberly of Geometric Tools, LLC, contains a primer for creating custom finite difference formulas. (Published in 2001, last updated in 2008. Link referred 18th October 2011.)

right-hand side must be switched. The formula for $\partial^2 u/\partial x^2$ needs only the index changes.

In the algorithm, the prediction for the new position comes from combining the following sequence of operations:

$$
\begin{aligned}
v_k &\leftarrow 1/2h \ \cdot \ (3s_k^{(j-1)} - 4s_k^{(j-2)} + s_k^{(j-3)}) \ , \\
a_k &\leftarrow 1/h^2 \ \cdot \ (2s_k^{(j-1)} - 5s_k^{(j-2)} + 4s_k^{(j-3)} - s_k^{(j-4)}) \ , \\
\tilde{s}_k^{(j)} &\leftarrow s_k^{(j-1)} + v_k h + \frac{1}{2} a_k h^2 \ .
\end{aligned}
$$

When these operations are combined as in Algorithm 1, we avoid the unnecessary divisions and multiplications by h, thus avoiding rounding errors. In this original form, the origin of the expression as a Taylor expansion is more evident. Note that the formula for $\tilde{s}_k^{(j)}$ also corresponds to Newtonian mechanics for a mass point undergoing a constant acceleration a_k over a time interval h, with initial velocity v_k and initial position $s_k^{(j-1)}$.

5.2.2 Modal assurance criterion (MAC) based tracking algorithm

The modal assurance criterion (MAC), which is a well-known technique in modal analysis, is a tool designed exactly for the kind of task encountered here — assuming that the eigenfunctions are available. It is commonly used, e.g., to pair the modes of a damaged beam with the modes of a perfect beam, making it possible to identify how the damage has changed the eigenfunctions. Of course, instead of damage, in this context we are interested in small changes in V_0.

The MAC is based on the pairwise L_2 projection of eigenfunctions,

$$
\Pi(w_1, w_2) \equiv < w_1, w_2 > \equiv \int_\Omega w_1(x) \cdot \overline{w_2(x)} \, \mathrm{d}x \ , \tag{175}
$$

where we use the normalization

$$
< w_j, w_j > \equiv \left\| w_j \right\|^2 = 1 \ . \tag{176}
$$

In addition to removing the need for a scaling factor in the projection, this normalization is particularly convenient, as we will see below. The choice of having the complex conjugate in our inner product is naturally motivated by the fact that this version induces a norm for complex-valued functions.

The MAC for matching a new function u against a given function w is

$$
\mathrm{MAC}(u; w) \equiv |\Pi(w, u)| \ . \tag{177}
$$

The absolute value protects against complex-valued phase changes (e.g. multiplication by $\sqrt{-1}$). In practice, the solver really generates such phase changes randomly, so this is very much necessary.

Obviously, $0 \leq \mathrm{MAC}(u; w) \leq 1$ for all admissible u and w. The closer the value is to 1, the closer the match between u and w. Hence, $1 - \mathrm{MAC}(u; w)$ is

Algorithm 1 Taylor-based tracking for complex eigenvalue spectrum.

▷ **Input**: randomly ordered eigenvalues $\mathbf{s}^{(j)}$ for $j = 1, 2, \ldots, N$

▷ **Output**: permuted eigenvalues $\boldsymbol{\sigma}^{(j)}$, where $\mathbf{s}^{(j)} \mapsto \boldsymbol{\sigma}^{(j)}$ with each $\sigma_k^{(j)}$ continuous over j

▷ **Initialization**
▷ Initialize output array $\boldsymbol{\sigma}$, copying input from first V_0 step at $j = 1$.
▷ This establishes a random numbering, which we will try to keep consistent.
$\boldsymbol{\sigma}^{(1)} \leftarrow \mathbf{s}^{(1)}$
▷ The output for other steps can be left uninitialized for now, or can be zeroed.
for $j = 2 : N$ **do**
    $\boldsymbol{\sigma}^{(j)} \leftarrow 0$
end for
▷ Initialize tracking reset indices $\mathbf{r}$.
$\mathbf{r} \leftarrow 1$

▷ **Main loop**
for $j = 2 : N$ **do**
    ▷ Mark all solutions unused for step j. When $u_k = 1$, sol. k has been used.
    $\mathbf{u} \leftarrow 0$
    for $k = 1 : M$ **do**
        ▷ Distance of each new solution from prev. known value of sol. k.
        $\mathbf{d}^{\text{null}} \leftarrow \left\| \mathbf{s}^{(j)} - s_k^{(j-1)} \right\|$
        ▷ Invalidate distances of used sols. to match each only once per step.
        $\left(\mathbf{d}^{\text{null}}\right)_{\mathbf{u}=\mathbf{1}} \leftarrow +\infty$
        ▷ Pick the winner.
        $(d_1, k_1) \leftarrow \min_k \mathbf{d}^{\text{null}}$
        ▷ Do Taylor prediction if possible (need some history for Taylor series).
        $d_2 \leftarrow +\infty$
        if $j \geq r_k + 4$ **then**
            ▷ Predict new position
            $\tilde{s}_k^{(j)} \leftarrow \frac{1}{2}\left[\, 7s_k^{(j-1)} - 9s_k^{(j-2)} + 5s_k^{(j-3)} - s_k^{(j-4)} \,\right]$
            ▷ Distance of each new solution from predicted pos. of sol. k.
            $\mathbf{d}^{\text{taylor}} \leftarrow \left\| \mathbf{s}^{(j)} - \tilde{s}_k^{(j)} \right\|$
            $\left(\mathbf{d}^{\text{taylor}}\right)_{\mathbf{u}=\mathbf{1}} \leftarrow +\infty$ ▷ Invalidate distances of used solutions.
            $(d_2, k_2) \leftarrow \min_k \mathbf{d}^{\text{taylor}}$ ▷ Pick the winner.
        end if

Algorithm 1 Taylor-based tracking for complex eigenvalue spectrum (continued).

```
        ▷ Pick the winner k̂ based on which prediction was closer.
        if d_2 < d_1 then
            k̂ ← k_2
        else
            k̂ ← k_1
            if d_2 < +∞ then
                ▷ Discontinuity in trajectory detected.
                ▷ Reset the tracking for solution k.
                r_k ← j
            end if
        end if
        ▷ Update output array and mark solution k̂ as used for step j.
        σ_k^(j) ← s_k̂
        u_k̂ ← 1
    end for
end for
```

an indicator of an "eigenfunction distance" between u and w, with 0 meaning "same" and 1 meaning L^2-orthogonal.[4]

The final remaining issue is coping with the case of multiple winners. In certain situations, such as starting from $V_0 = 0$ in our system, it happens that two eigenfunctions are initially identical, and then become complex conjugates as soon as $V_0 = \varepsilon$. In this case, which mode should win in a MAC comparison?

First, to detect multiple winners, given the reality of floating point rounding errors, one should have some tolerance in picking the maximum — in case several functions w_k would have produced the same value in the L^2 projection for the MAC if exact arithmetic was used.

Then, to pick the correct winner from the candidates, it is possible to use the fact that distances look very different in the MAC and complex plane euclidean (direct eigenvalue distance) senses. It is not only the distance of eigenvalues at successive V_0 steps which determines the identity of each solution (like in the Taylor approach above), and neither is it only the eigenfunction distance, but it is a combination of both. These two "views" into distances within the data set complement each other in a natural way, giving an easy method for conflict resolution.

In case of multiple matches within numerical accuracy, the correct winner is obtained by picking the minimal eigenvalue distance out of the candidate set, while making sure that each solution can only be used once (per V_0 step).

Finally, before laying down the actual algorithm, let us see how to compute the L^2 projection of two given Galerkin approximations. Consider a (possibly

[4] We could also define $d(u, w) \equiv 1/\mathrm{MAC}(u; w) - 1$, which would map "same" to 0 and L^2-orthogonal to $+\infty$.

complex-valued) function $w_m(x)$ given in some basis ϕ_j:

$$w_m(x) \equiv \sum_{j=1}^{n_0} c_j^{(m)} \phi_j(x) \ .$$

The inner product of two such functions, w_1 and w_2, is

$$\begin{aligned} < w_1,\ w_2 > &\equiv \int_\Omega [w_1(x)]\ \overline{[w_2(x)]}\ \mathrm{d}x \\ &= \int_\Omega \left[\sum_{j=1}^{n_0} c_j^{(1)} \phi_j(x)\right]\ \overline{\left[\sum_{k=1}^{n_0} c_k^{(2)} \phi_k(x)\right]}\ \mathrm{d}x \\ &= \sum_{j=1}^{n_0}\sum_{k=1}^{n_0} c_j^{(1)} \overline{c_k^{(2)}} \int_\Omega \left[\phi_j(x)\right]\ \overline{[\phi_k(x)]}\ \mathrm{d}x \ . \end{aligned} \tag{178}$$

In our problem we have

$$\Omega \equiv [-1, 1] \ , \quad \phi_j(x) \equiv \sin(j\pi \frac{x+1}{2}) \ ,$$

which leads to orthonormality, i.e.,

$$< \phi_j, \phi_k >= \delta_{jk} \ ,$$

where δ_{jk} is the Kronecker delta. Therefore, all but the diagonal terms in the double sum (178) vanish, and we obtain

$$\begin{aligned} < w_1,\ w_2 > &= \sum_{j=1}^{n_0} c_j^{(1)} \overline{c_j^{(2)}}\ < \phi_j, \phi_j > \\ &= \sum_{j=1}^{n_0} c_j^{(1)} \overline{c_j^{(2)}} \\ &\equiv \mathbf{c}^{(1)} \cdot \overline{\mathbf{c}^{(2)}} \ . \end{aligned} \tag{179}$$

In other words: in the sine basis, the L^2 projection of two Galerkin approximations w_1, w_2 is the dot product of the coefficient vectors, with the complex conjugate taken of the coefficients of w_2.

The Galerkin coefficients for our eigenfunctions will be, as per subsection 6.3.1 further below, determined from the rows of a unitary matrix. Hence, in light of the requirement (176) and equation (179), they are already normalized (this is the convenient feature suggested above).

Let us define notation for this algorithm. Let $\mathbf{f}_k^{(j)}$ denote the Galerkin coefficient vector (of length n_0) for the eigenfunction corresponding to solution k at V_0 step j. As above, let N be the total number of V_0 steps, and $M = 2n_0$, the number of solutions at one V_0 step.

Define the extraction of an index set from a logical vector, denoted $K \leftleftarrows \mathbf{b}$: the set K will contain those integers k, for which $b_k = 1$. Finally, denote the elementwise logical AND of two logical vectors $\mathbf{b}_1$ and $\mathbf{b}_2$ as $\mathbf{b}_1 \cap \mathbf{b}_2$.

The MAC-based tracker is given in Algorithm 2. This algorithm, too, is presented for the case when the data contain only solutions for $V_0 \geq 0$. The same remark applies as for the previous algorithm.

Algorithm 2 MAC-based tracking for complex eigenvalue spectrum.

▷ **Input**: randomly ordered eigenvalues $\mathbf{s}^{(j)}$, and corresponding discretized eigenfunctions $\mathbf{F}^{(j)}$, for $j = 1, 2, \ldots, N$. The eigenfunction $\mathbf{f}_k^{(j)}$ corresponds to the eigenvalue $s_k^{(j)}$.

▷ **Output**: permuted eigenvalues $\boldsymbol{\sigma}^{(j)}$, where $\mathbf{s}^{(j)} \mapsto \boldsymbol{\sigma}^{(j)}$ with each $\sigma_k^{(j)}$ continuous over j.

▷ **Initialization**
▷ Initialize output array $\boldsymbol{\sigma}$, copying input from first V_0 step at $j = 1$.
▷ This establishes a random numbering, which we will try to keep consistent.
$\boldsymbol{\sigma}^{(1)} \leftarrow \mathbf{s}^{(1)}$
▷ The output for other steps can be left uninitialized for now, or can be zeroed.
for $j = 2 : N$ **do**
    $\boldsymbol{\sigma}^{(j)} \leftarrow 0$
end for
▷ Initialize the previous eigenmode vectors from data at $j = 1$.
for $k = 1 : M$ **do**
    $\tilde{\mathbf{f}}_k \leftarrow \mathbf{f}_k^{(1)}$
end for

▷ **Main loop**
for $j = 2 : N$ **do**
    ▷ Mark all solutions unused for step j. When $u_k = 1$, sol. k has been used.
    $\mathbf{u} \leftarrow 0$
    ▷ Initialize permuted eigenmode array for this step
    for $k = 1 : M$ **do**
        $\hat{\mathbf{f}}_k \leftarrow 0$
    end for
    for $k = 1 : M$ **do**
        ▷ Match all new eigenmodes against known old eigenmode of sol. k.
        $\mathbf{C} \leftarrow 0$
        for $n = 1 : M$ **do**
            $C_n \leftarrow \left| \Pi(\mathbf{f}_n^{(j)}, \tilde{\mathbf{f}}_k) \right|$
        end for
        ▷ Define set K: indices of all unused matches having projection within ε from maximum. Recommended value $\varepsilon = 10^{-4}$.
        $c \leftarrow \max_n \mathbf{C}$
        $K \leftleftarrows \Big((|\mathbf{C} - c| < \varepsilon) \cap (\mathbf{u} = 0) \Big)$

Algorithm 2 MAC-based tracking for complex eigenvalue spectrum (continued).

```
        ▷ Eigenvalue distance of each new sol. from prev. known value of sol. k.
        d ← ‖ s^(j) − s_k^(j−1) ‖
        ▷ Pick the MAC match with the smallest eigenvalue distance.
        k̂ ← arg min_{k∈K} d
        ▷ Store a copy of the eigenmode vector of solution k̂.
        ▷ We shift the new (garbled) index k̂ to the old (consistent) k.
        f̂_k ← f_k̂^(j)
        ▷ Update output array and mark solution k̂ as used for step j.
        σ_k^(j) ← s_k̂
        u_k̂ ← 1
    end for
    ▷ Using stored copies, permute prev. eigenmode array to correct indexing.
    for k = 1 : M do
        f̃_k ← f̂_k
    end for
end for
```

5.3 Detecting when good solutions go bad

Keeping in mind what was said about valid and invalid solutions in the motivation, it is possible to develop the visualization methodology slightly further. We will work with the assumption that an initially valid solution becomes invalid, if it interacts with a solution which is at that point invalid.

If we have some data on which solutions are initially valid (e.g. at $V_0 = 0$), by tracking collisions between the solutions it is possible to detect "when a good solution goes bad". (This is the reason behind the strategy of one pass per direction.)

This information can be used for automatic visual flagging of valid and invalid parts of the plot. Alternatively, it is possible to use it for simply visualizing only the parts that are (likely to be) valid.

5.3.1 Collision detection in Taylor-based algorithm

Collision tracking in the Taylor approach comes naturally: when the prediction $\mathbf{d}_{\text{null}}$ wins against $\mathbf{d}_{\text{taylor}}$, this suggests that the continuity of the trajectory has been disturbed, i.e., it is likely that a collision has occurred.

An easy way to track collisions is to use two processing passes at each V_0 step. During the first pass, the solutions are identified and potential colliders flagged (if during the identification it happens that $d_2 \geq d_1$, set a collision flag for solution k at this frame).

In the second pass, it is then detected which of the other solutions each collider most likely hit. This can be computed from the minimal distance $\min_k \|\mathbf{s}^{(j)} -$

$s_k^{(j)}\|$, when the point $s_k^{(j)}$ itself is excluded from $\mathbf{s}^{(j)}$. (When the inner loop (over k) completes in Algorithm 1, the solutions have been identified at step j, so we have the value of $s_k^{(j)}$ for each k.) Again, each solution should be matched in only one collision. A flagging mechanism similar to the one presented above (to keep track of solutions already used) can be used for this.

5.3.2 Collision detection in MAC-based algorithm

The MAC approach is a bit more involved in this respect. Because of the reliable one-pass identification however, it is possible to do the collision checking in a separate full pass over the data, once it is already known which solution is which.

In this approach, one can track the (in the MAC spirit, directional cosines of) angles drawn between the successive differences $d_k^{(j)} \equiv s_k^{(j)} - s_k^{(j-1)}$ and $d_k^{(j-1)} \equiv s_k^{(j-1)} - s_k^{(j-2)}$, when viewed as vectors in the complex plane. At a collision, the pair of eigenvalues should rebound at angles of $\pi/2$ ($= 90^\text{o}$) with regard to their original flight directions (if we view the V_0 axis as "time").

However, the exact collision point almost never contains a sample. Hence, the discretized collision — when we look at four successive points of the same solution — looks like a rectangle with its corner sawed off, splitting the angle $\pi/2$ into α and $\beta = \pi/2 - \alpha$. Depending on whether the "older" or "newer" angle triggers the collision detector, these cases need to be handled differently in order to correctly detect between which frames of the sampled data the collision occurred. See Figures 36–37 for an illustration.

In Algorithm 3, we give a flag-and-track approach for collision detection and validity flagging of the sorted eigenvalue data produced by the MAC-based tracker (Algorithm 2). Given the ideas presented above, most of this is easy; the difficult part is to keep the indices correct.

Let $\varepsilon_1 = \pi/6$ ($= 30^\text{o}$) and $\varepsilon_2 = \pi/18$ ($= 10^\text{o}$). We present the algorithm in the same vectorized form as Algorithms 1 and 2, although those parts, where doing so improves the readability, have been left in a traditional serial form.

We will use the following elementary arithmetic properties. First, the dot product of two unit vectors is the directional cosine of the angle between them. Secondly, note that for any two complex numbers of the general form $z_m = a_m + b_m i$ (where $a_m, b_m \in \mathbb{R}$), we have

$$z_1 \overline{z_2} = (a_1 a_2 + b_1 b_2) + (a_1 b_2 - b_1 a_2)\, i \; .$$

Hence, it is convenient to calculate dot products of vectors in $\mathbb{R}^2$, which have been encoded as complex numbers, by taking $(a_1, b_1) \cdot (a_2, b_2) = \text{Re}\,(z_1 \overline{z_2})$, when z_1 and z_2 are each seen as a vector in $\mathbb{R}^2$. Of course, we have also $z_1 \overline{z_1} = \|z_1\|^2$. (The imaginary part $\text{Im}\,(z_1 \overline{z_2}) = -(a_1, b_1) \times (a_2, b_2)$ for the "2D cross product"; it is not needed here.)

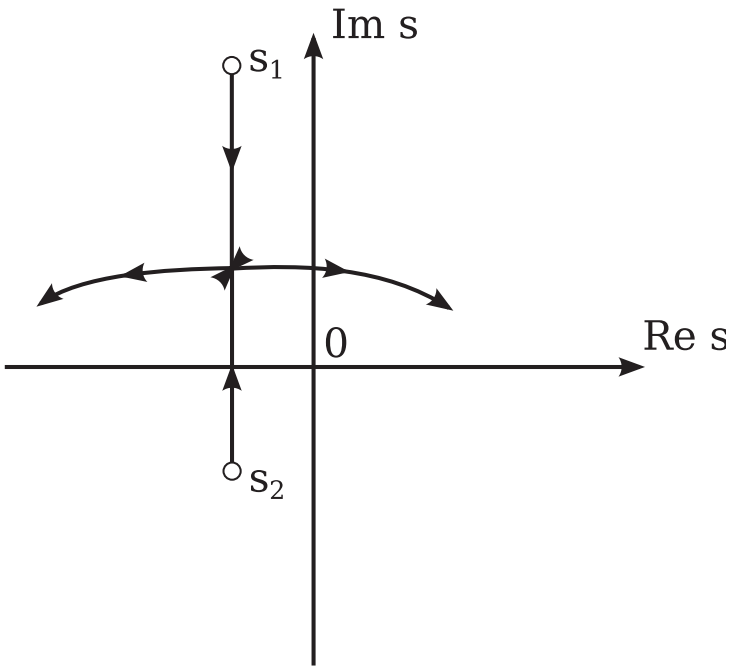

FIGURE 36 Continuum behaviour of a general eigenvalue collision. Now the coordinates are represented as-is (in contrast to Figure 6 on p. 48, where an offset was used for legibility).

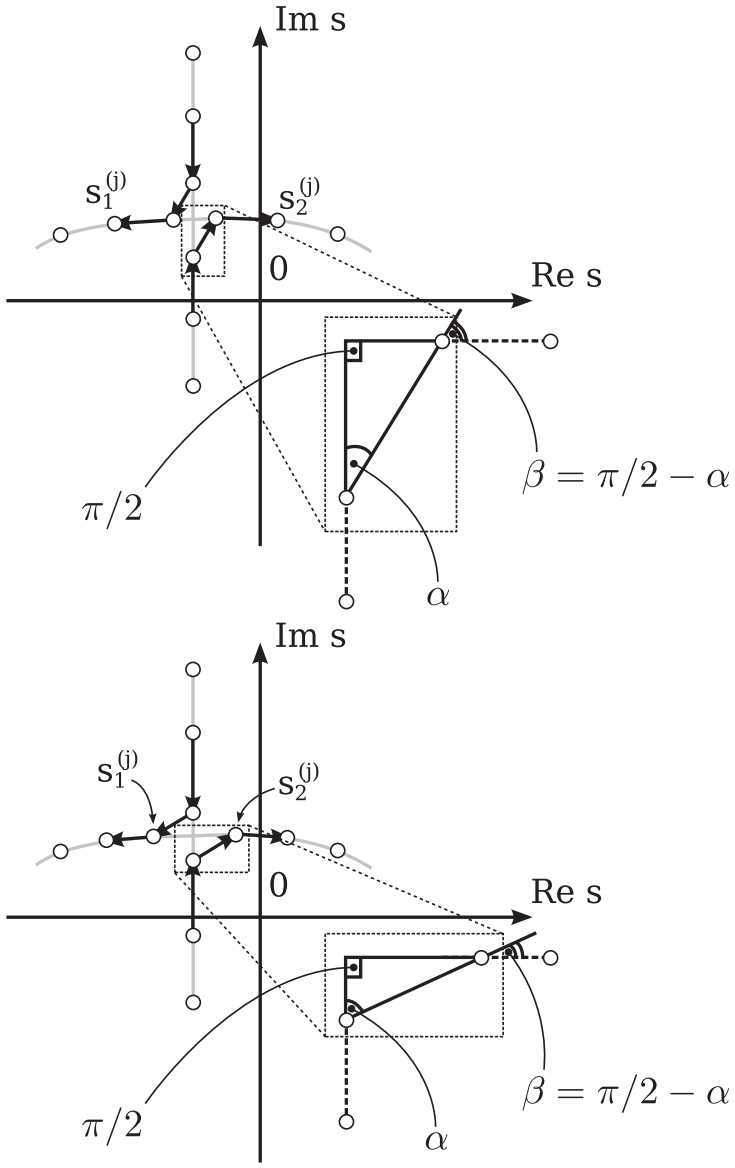

FIGURE 37 Discretized eigenvalue collisions. *Top*: angle $\beta > \alpha$. *Bottom*: angle $\alpha > \beta$.

Algorithm 3 Collision detection and validity flagging for MAC-based tracking.

▷ **Input**: ordered eigenvalues $\boldsymbol{\sigma}^{(j)}$, with each $\sigma_k^{(j)}$ continuous over j. Validity vector $\mathbf{b}$, where $b_k = 1$ if $\sigma_k^{(1)}$ is valid (where $j = 1$ corresponds to $V_0 = 0$), and $b_k = 0$ otherwise.
▷ **Output**: vector $\mathbf{v}$. Each solution k is valid in the range $j = 1, 2, \ldots, (v_k - 1)$.

▷ **Initialization**
$\mathbf{v}_{\mathbf{b}=1} \leftarrow N + 1$
$\mathbf{v}_{\mathbf{b}=0} \leftarrow 1$
▷ Old flight directions. The superscript indicates how many steps behind current value of j.
$\tilde{\mathbf{d}}^{(2)} \leftarrow 0 + 0\mathrm{i}$
$\tilde{\mathbf{d}}^{(1)} \leftarrow 0 + 0\mathrm{i}$

▷ **Main loop**
$\mathbf{d} \leftarrow 0 + 0\mathrm{i}$
for $j = 2 : N$ **do**
  ▷ Compute latest flight directions, normalizing to unit vectors.
  for $k = 1 : M$ **do**
    $d_k \leftarrow \sigma_k^{(j)} - \sigma_k^{(j-1)}$
    $d_k \leftarrow d_k / \left\| d_k \right\|$
  end for
  ▷ If history initialized, do actual processing.
  if $j \geq 4$ **then**
    ▷ Compute current and old directional cosines, and the corresponding combined angle γ. This is used to detect sudden changes in flight direction.
    $\mathbf{c}^{(\beta)} \leftarrow 0$
    $\mathbf{c}^{(\alpha)} \leftarrow 0$
    $\boldsymbol{\gamma} \leftarrow 0$
    for $k = 1 : M$ **do**
      $c_k^{(\beta)} \leftarrow \mathrm{Re}\ (\tilde{d}_k^{(1)} \overline{d_k})$
      $c_k^{(\alpha)} \leftarrow \mathrm{Re}\ (\tilde{d}_k^{(2)} \overline{\tilde{d}_k^{(1)}})$
      $\gamma_k \leftarrow \arccos(c_k^{(\beta)}) + \arccos(c_k^{(\alpha)})$
    end for
    ▷ Make index set of colliders by considering angles β_k closer to $\pi/2$ than threshold. Smaller cos, larger angle. Absolute value is taken elementwise.
    $C \leftleftarrows \left(\left| \mathbf{c}^{(\beta)} \right| < \cos \varepsilon_1 \right)$
    ▷ Make index set of collisions of type A. The rest will be of type B. See Figure 37. Absolute value is taken elementwise.
    $A \leftleftarrows \left(|\pi/2 - \boldsymbol{\gamma}| < \varepsilon_2 \right)$

Algorithm 3 Collision detection and validity flagging for MAC-based tracking (continued).

for $k \in C$ **do**
  $m_1 \leftarrow j - 1$ ▷ Used for indexing $\sigma_k^{(m_1)}$
  $m_2 \leftarrow 1$ ▷ Used for indexing $\vec{d}_k^{(m_2)}$
  if $k \in A$ **then**
    $m_1 \leftarrow m_1 - 1$
    $m_2 \leftarrow 2$
  end if
  ▷ Potential collision partners.
  $P \leftarrow \{C \setminus k\}$
  ▷ The following vectors contain $\#P$ elements each.
  $\mathbf{n} \leftarrow j - 1$
  $\mathbf{q} \leftarrow 1$
  $\mathbf{r} \leftarrow +\infty$ ▷ Squared distances
  $\Delta\mathbf{x} \leftarrow 0$ ▷ Relative position
  $\Delta\mathbf{v} \leftarrow 0$ ▷ Relative flight direction
  $\mathbf{z} \leftarrow 0$ ▷ Relative flight direction check
  ▷ In the following loop, the set P is understood as a vector, which can be indexed (subscripted) from 1 to $\#P$ to get the corresponding element.
  for $k' = 1, 2, \ldots, \#P$ **do**
    if $P_{k'} \in A$ **then**
      $n_{k'} \leftarrow n_{k'} - 1$
      $q_{k'} \leftarrow 2$
    end if
    $r_{k'} \leftarrow \left\| \sigma_{P_{k'}}^{n_{k'}} - \sigma_k^m \right\|^2$
    $\Delta x_{k'} \leftarrow \sigma_{P_{k'}}^{(n_{k'})} - \sigma_k^{(m_1)}$
    $\Delta v_{k'} \leftarrow d_{P_{k'}}^{(q_{k'})} - d_k^{(m_2)}$
    $z_{k'} \leftarrow \mathrm{Re}\left(\Delta x_{k'} \overline{\Delta v_{k'}}\right)$
  end for
  ▷ Filter out impossible collision partners. Set indexing P_Q is shorthand for $\{P_k : k \in Q\}$, where P is understood as a vector.
  $Q \leftleftarrows (\mathbf{z} > 0)$
  $P \leftarrow P \setminus P_Q$

Algorithm 3 Collision detection and validity flagging for MAC-based tracking (continued).

▷ If any possible partners were found, pick the winner based on minimal eigenvalue distance.

if $\#P > 0$ **then**

$k' \leftarrow \underset{k'=1,2,\ldots,\#P}{\arg\min}\ r_{k'}$

$\hat{k} \leftarrow P_{k'}$

▷ In a collision between a valid and invalid solution, mark the previously valid solution as invalid from now on, and set its first invalid step number. Otherwise, do nothing.

if $b_{\hat{k}} = 0$ **and** $b_k = 1$ **then**

$b_k \leftarrow 0$

$v_k \leftarrow m_1 + 1$

else if $b_{\hat{k}} = 1$ **and** $b_k = 0$ **then**

$b_{\hat{k}} \leftarrow 0$

$v_{\hat{k}} \leftarrow n_{k'} + 1$

end if

end if

end for

end if

▷ Update history.

$\mathbf{d}^{(2)} \leftarrow \mathbf{d}^{(1)}$

$\mathbf{d}^{(1)} \leftarrow \mathbf{d}$

end for

The index set A may require an explanation. The idea is to check that the last two angles approximately sum to $\pi/2$. This flags collisions, where the newer angle β is larger than the threshold ε_1, i.e. collisions of type A (Figure 37). If the older angle α is larger, it already triggered the collision check (index set C) during the previous step $(j-1)$, but did not trigger this "type A" check. Hence it got handled as a type B collision. If the newer angle β is exactly $\pi/2$, the collision will be detected as type A; hence the unlikely special case is handled correctly.

The $\mathrm{Re}\,(\Delta x\overline{\Delta v}) > 0$ check comes from a necessary (but not sufficient) condition for collision: the vectors Δx and Δv must point to opposite half-spaces. This additional check makes the algorithm slightly more robust.

This algorithm, too, is presented for the case when the data contains only solutions for $V_0 \geq 0$. The same remark applies as for the previous algorithms.

Finally, the presented algorithm does not handle the case of two or more collisions within the same frame j. These could be detected from a directional cosine having value -1. There are two possible cases: $d_k^{(j)} \cdot d_k^{(j-1)} = -1$, and the unlikely but possible $d_k^{(j-1)} = 0$, $d_k^{(j)} \cdot d_k^{(j-2)} = -1$ (if the samples $j-1$ and $j-2$ are exactly equidistant from their corresponding nearest points of collision).

In subsection 6.3.3, we will apply Algorithms 1–3 to the relevant main problem of interest.

6 NUMERICAL CONSIDERATIONS AND RESULTS

In this section, we will consider the three main problems one at a time. We will discuss the steady-state problem, some direct temporal simulations, and the eigenfrequency problem. The handling of the last one is split into two parts. We will first look at the lowest eigenfrequency problem, and then at computing as many eigenfrequencies as the discretization allows.

For each problem, we will first explain the solution strategy, starting from the semi-discrete form that was derived above. We will then report the numerical results. The handling of each problem ends with a short summary and conclusion.

Problem parameters used in all numerical solutions are given in Table 1. The physical parameters were chosen as typical for a paper web surrounded by air. For the bending rigidity D, zero is used for some calculations; this is mentioned when it is the case. Otherwise, the value in Table 1 is used.

The results displayed in the numerical result subsections were computed using a set of custom, single-purpose numerical codes developed in the MATLAB programming language. The present model of the axially travelling panel

TABLE 1 Problem parameters used. For definitions, see the Nomenclature. Note that ℓ is the half-length; refer to Figure 25 on p. 101.

ρ_f [kg/m^3]	T [N/m]	m [kg/m]	ℓ [m]	h [m]	E [N/m]	ν	$\Rightarrow$ D [Nm]
1.25	500	0.08	1	10^{-4}	10^9	0.3	$9.16 \cdot 10^{-5}$

$\Rightarrow$ α	β	$\Rightarrow$ γ	θ	λ
1	$*$	15.625; $\times$	e.v. eq. (183), (184); else $*$	e.v. eq. (181), (182); else $*$

τ [s]
$\ell/\sqrt{T/m}$

Legend	
$\Rightarrow$	Derived parameter (from others)
$*$	Case-dependent; see text
$\times$	Except when plot axis variable
e.v.	Eigenvalue to be solved

submerged in axially flowing ideal fluid was thus implemented. With repeatability of results in mind, the codes are open source, and archived online[1]. The codes are (mostly) compatible also with GNU Octave, version 3.2.4 and above. The MATLAB version used for all displayed computations and visualizations was 2009b.

6.1 Steady-state problem

As promised, let us first outline the numerical solution strategy. The discrete steady-state problem can be obtained directly from the semidiscrete form, (168), by setting the time scale parameter to $\alpha = 0$ (i.e., $\tau \to \infty$) and taking zero external load, $G_j \equiv 0$. We have

$$\sum_{n=1}^{\infty} \left[(\lambda^2 - 1) C_{jn} + \gamma \theta^2 c_{jn} + \beta D_{jn} \right] f_n = 0 \,. \tag{180}$$

Compare the continuum formulation in equation (146), p. 128. (But when comparing, note that (180) is in weak form, while the original equation (146) is in strong form.)

The finite equation corresponding to (180) is an algebraic, linear equation system. The question for the discrete problem is: what are the critical values of the chosen parameter, such that (180) admits nontrivial solutions $\mathbf{f} \not\equiv 0$, and what are those nontrivial solutions?

Let us truncate the series (180) at some n_0. First, consider the panel velocity V_0 (resp. λ) as the eigenvalue. If v_∞ is independent of V_0, we can rearrange the terms of (180) to produce the following generalized linear eigenvalue problem in $(\lambda^2, \mathbf{f})$:

$$\sum_{n=1}^{n_0} \left[C_{jn} - \gamma \theta^2 c_{jn} - \beta D_{jn} \right] f_n = \lambda^2 \sum_{n=1}^{n_0} C_{jn} f_n \,. \tag{181}$$

If $v_\infty = V_0$ (resp. $\theta = \lambda$; the whole air mass moves with the panel), the problem for $(\lambda^2, \mathbf{f})$ reads

$$\sum_{n=1}^{n_0} \left[C_{jn} - \beta D_{jn} \right] f_n = \lambda^2 \sum_{n=1}^{n_0} \left(C_{jn} + \gamma c_{jn} \right) f_n \,. \tag{182}$$

From this discrete form, it is apparent that the model described by (182) is similar in spirit to the corresponding vacuum model, as there is only one independent velocity. Indeed, the form of the equation is a perturbed vacuum model with the additional term γc_{jn} on the right-hand side. In the limit of zero dimensionless fluid density, $\gamma \to 0$, it reduces to the vacuum model. Compare (181), which

[1] As of this writing,
`http://yousource.it.jyu.fi/banichuk-panel/codes`
Link referred 18th October 2011.

reduces to the vacuum model also when the dimensionless fluid velocity $\theta \to 0$.[2] Thus we can expect different behaviour from the two cases.

Finally, consider the fluid velocity v_∞ (resp. θ) as the eigenvalue. The problem for $(\theta^2, \mathbf{f})$ (now for fixed V_0, i.e., λ) reads

$$\sum_{n=1}^{n_0} \left[(1-\lambda^2)C_{jn} - \beta D_{jn}\right] f_n = \theta^2 \sum_{n=1}^{n_0} \gamma c_{jn} f_n \,. \tag{183}$$

The special case $\lambda = 0$ of equation (183) corresponds to a stationary, tensioned panel subjected to axial flow; see e.g. Kornecki et al. (1976); Païdoussis (2004, 2008). This case has been experimentally tested in a wind tunnel, for a stationary web held fixed at two edges and free to move at two others, by Chang and Moretti (1991). On the theoretical side, they considered a threadline model for cylindrical displacement, with added masses to account for the surrounding flow. We obtain the corresponding problem (in the limit of an infinitely wide wind tunnel, i.e., assuming the walls are far enough not to disturb the flow near the panel) by setting $\beta = 0$ and $\lambda = 0$ in equation (183). We have

$$\sum_{n=1}^{n_0} C_{jn} f_n = \theta^2 \sum_{n=1}^{n_0} \gamma c_{jn} f_n \,, \tag{184}$$

which is the eigenvalue problem for $(\theta^2, \mathbf{f})$ corresponding to Chang and Moretti (1991).

The classical non-tensioned panel requires different treatment, because we divided by the tension T to produce our dimensionless form. Guo and Païdoussis (2000) (see also Païdoussis, 2004) considered the stability of a classical non-tensioned plate subjected to two-dimensional axial flow in a channel. In our notation, the continuum formulation reads

$$D w_{xxxx} = \ell^3 q_f \,.$$

Let us rewrite (180) without the dimensionless forms (138)–(141):

$$\sum_{n=1}^{\infty} \left[\left(\frac{m}{\ell} V_0^2 - \frac{T}{\ell} \right) C_{jn} + \frac{D}{\ell^3} D_{jn} + \rho_f v_\infty^2 \, c_{jn} \right] f_n = 0 \,. \tag{185}$$

By setting $T = 0$ and $V_0 = 0$, from equation (185) we can formulate this problem (again, in the limit of an infinitely wide channel) for $(\overline{U}^2, \mathbf{f})$:

$$-\sum_{n=1}^{\infty} D_{jn} \, f_n = \overline{U}^2 \sum_{n=1}^{\infty} c_{jn} \, f_n \,, \tag{186}$$

where the eigenvalue $\overline{U}^2$ is the dimensionless dynamic pressure (Païdoussis, 2004, p. 1149)

$$\overline{U}^2 = \frac{\rho_f \, \ell^3}{D} v_\infty^2 \,, \tag{187}$$

[2] This is because in the steady-state problem, the part of the operator $\mathcal{K}$ that does not depend on the velocity θ is not present; it would be in the term with the second-order time derivative. In the dynamic case, where this part is present, the model differs from the vacuum model even for $\theta = 0$.

which is the square of the dimensionless flow velocity $\overline{U}$. The critical fluid flow velocity for divergence, v_∞^{div}, can be found from $\overline{U_{cd}}^2$, the minimal positive eigenvalue $\overline{U}^2$ of the problem (186).

Note that all the problems (181)–(184), (186) are generalized linear eigenvalue problems; i.e. are of the general form

$$A_1\mathbf{x} = \varkappa A_2\mathbf{x} \tag{188}$$

with A_2 a non-identity matrix. Here A_1 is an arbitrary matrix, $\varkappa$ is the (scalar) eigenvalue and $\mathbf{x}$ is the corresponding eigenvector. Standard eigenvalue solvers can be used to solve (188).

Now, we will look into the numerical results obtained from these steady-state problems.

6.1.1 Numerical results

In this subsection, a parametric study will be made into problems (181) and (182). The critical velocities predicted from (182) will be compared to Pramila (1986). Additionally, the results of (184) will be compared to those in Chang and Moretti (1991), and the results from (186) will be compared to Guo and Païdoussis (2000). The main item of interest here is the parametric study; the comparisons are done mainly for validation purposes.

In all cases, the Galerkin series was truncated at $n_0 = 56$. For problems (181) and (182), physical parameters given in Table 1 on page 155 were used.

For problem (184), the physical parameters were chosen as corresponding to those of Chang and Moretti (1991). The parameter values were $D = 0$, $m = 0.076680634$ kg/m^2 (0.0155 lb/in^2), $\lambda = 0$. The width of the plate, needed in the theory of Chang and Moretti (1991), was $b = 0.1524$ m (6 in). Note that our model does not use the width. Two cases were tested; in case A, plate length was $2\ell = 0.508$ m (20 in). In case B, length $2\ell = 0.254$ m (10 in). See Appendix 3 for the experimental tension values and wind speeds. The compared theoretical results are calculated from Chang and Moretti (1991, eq. (20)), which states

$$v_\infty^{\text{div}} = \sqrt{\frac{T}{m_a}}, \quad \text{where} \quad m_a = \frac{\pi}{4}\rho_f b\,. \tag{189}$$

The symbol T represents the tension per unit width of web, and b is the web width. Because the web itself is stationary, only the added mass m_a appears in the expression for v_∞^{div} (it does not depend on the web mass m).

Now, let us look at the effect of problem parameters on the critical panel velocity λ. Figures 38–41 show results from problem (181), where the dimensionless fluid velocity θ is a parameter. Figure 38 shows an example of the critical shape, and the difference between the vacuum mode and the with-fluid mode for some parameter values.

Consider Figure 39. As expected, the region of stability (the region where the eigenvalue $\lambda > 0$) expands toward materials having a larger bending stiffness

D, or as the length of the span ℓ becomes shorter. Both of these changes increase β. However, as the tension T is increased, β decreases. This is counterintuitive, as one would expect a stabilising effect resulting from increased tension. A stabilising effect is indeed present, because increasing the tension also increases the vacuum divergence velocity (equation (79), p. 96), which is used in the dimensionless normalization. This causes θ to decrease if the dimensional fluid velocity is kept constant, and at $\theta = 0$, λ stays constant with increasing T. Thus, one needs to be careful when interpreting the dimensionless results with respect to tension (T) or panel area mass (m).

Because static instability analysis is only concerned with the critical velocity, and not the (complex-valued) eigenfrequencies, the present analysis cannot tell apart the type of the interval between the origin ($V_0 = 0$) and the minimal positive eigenvalue, i.e., whether the behaviour in the interval is stable or unstable. Of course, by physical considerations this interval is known to be stable when the fluid velocity is zero.

We have concentrated in this analysis only on the lowest region of stability, given by the interval between the two eigenvalues that, at zero fluid velocity, are the maximal negative and the minimal positive eigenvalue. Once either end of this region crosses the origin (as θ is varied), the results become physically meaningless. The figures shown have been filtered to show only the physically meaningful data.

The critical value of $\theta = \theta_{\text{critical}}$, where the lowest region of stability ends, can be found for each fixed pair (β, γ) numerically e.g. with a linear-logarithmic search procedure. That is, start from $\theta = 0$, increase θ in fixed steps until $\lambda^2 < 0$, then go back one step, halve the step size and repeat the procedure until desired tolerance is achieved. However, in order for this to work correctly, the starting step size should be "small enough". Otherwise the search may hit a higher stability region, where again $\lambda^2 > 0$, which is (incorrectly) predicted by the linear model to begin at some value of θ larger than θ_{critical}.

Figure 40 shows the effects of γ and θ on the critical velocity λ. The contour plot is symmetric with respect to θ, and hence only the positive half has been plotted. This feature is to be expected, because equation (181) only depends on θ^2. Figure 41 shows axis-oriented slices of the contour at various parameter values.

Figures 42–44 show results from problem (182), where the whole air mass moves with the panel, i.e., $v_\infty = V_0$, and $\theta = \lambda =$ eigenvalue. Figure 42 again shows an example of the critical shape, and its difference from the vacuum solution for some values of the dimensionless bending rigidity β.

In Figure 43 we see the effects of β and γ on the critical velocity λ. Figure 44 again shows axis-oriented slices of the same effect at various parameter values. As expected, an increase in the bending stiffness β stabilizes (increases the critical velocity), while an increase in the fluid density γ destabilizes (decreases the critical velocity).

Table 2 gives the numerical values of the critical velocity for the reference values of the problem parameters (refer to Table 1 on p. 155) at various v_∞. The values of v_∞ correspond to the choices in Figure 54 in the upcoming first eigenfre-

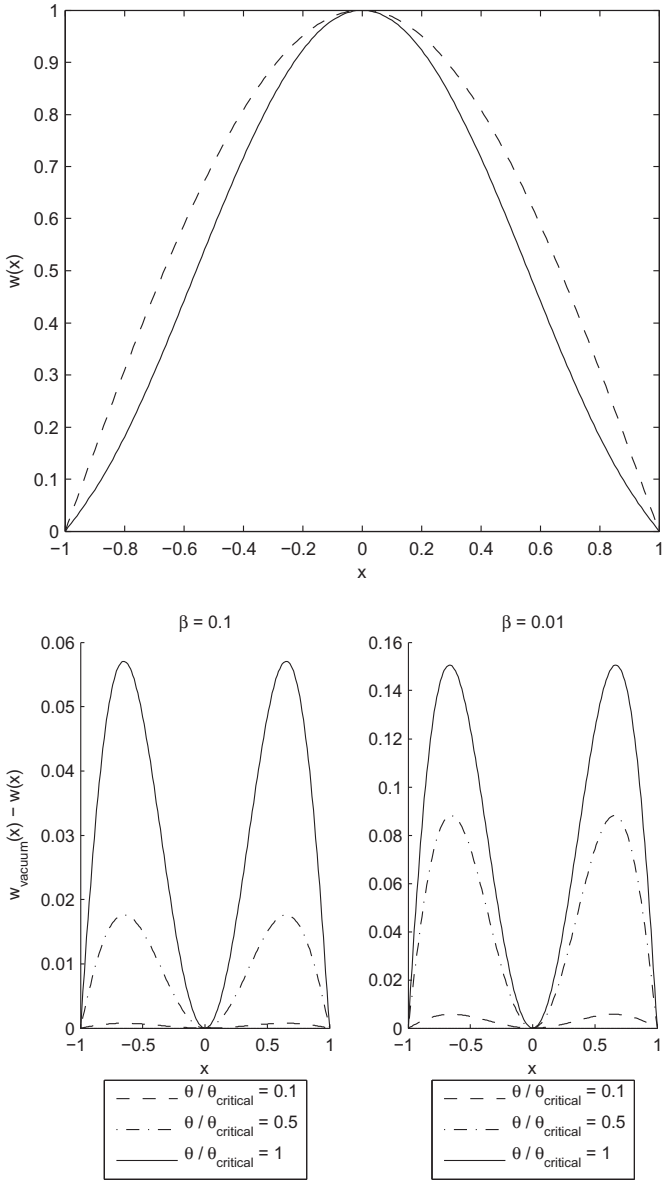

FIGURE 38 Some solutions of problem (181), where the dimensionless fluid velocity θ is a parameter. The dimensionless density $\gamma = 15.625$. *Top*: Critical eigenmode (solid line). The dashed line shows the corresponding vacuum mode. Both modes normalized such that the maximum is 1. Shapes are very similar for any admissible θ. *Bottom*: the difference between the vacuum and with-fluid solutions at two dimensionless bending rigidities β, for different fluid velocities θ. Differences were computed using the same normalization for the solutions as at the top. The symbol θ_{critical} denotes the smallest value of θ at which the dimensionless critical web velocity λ becomes zero (see Figure 39).

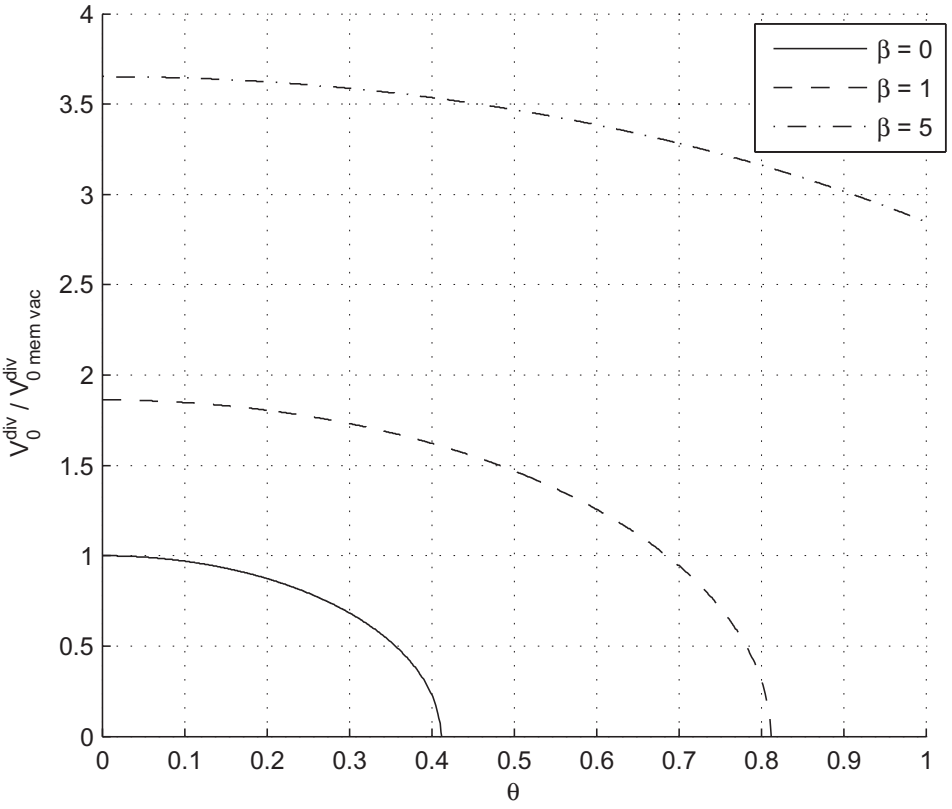

FIGURE 39 Problem (181). Effects of the dimensionless fluid velocity θ and the dimensionless bending rigidity β on the dimensionless critical web velocity λ. The dimensionless density $\gamma = 15.625$. The result is symmetric for $-\theta$; hence only one half is shown. The axis intersection points on the horizontal axis are the values θ_{critical} (for the corresponding parameter point (β, γ)).

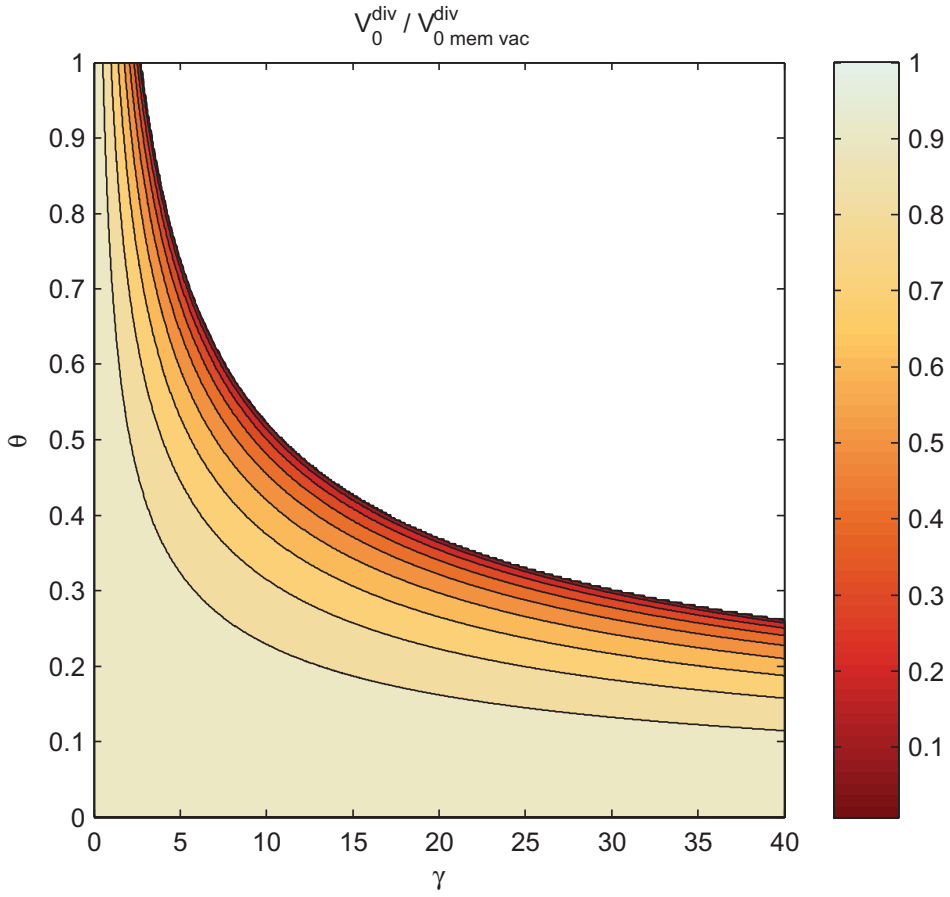

FIGURE 40 Problem (181). Effects of the dimensionless fluid density γ and the dimensionless fluid velocity θ on the dimensionless critical web velocity λ. The result is symmetric for $-\theta$; hence only the positive half is shown. The bending rigidity is fixed to $\beta = 0$; the solution is representative for small bending rigidities. On the axes, $\lambda \equiv 1$. In the blank area, the problem has no physically meaningful solution. See also slices in Figure 41.

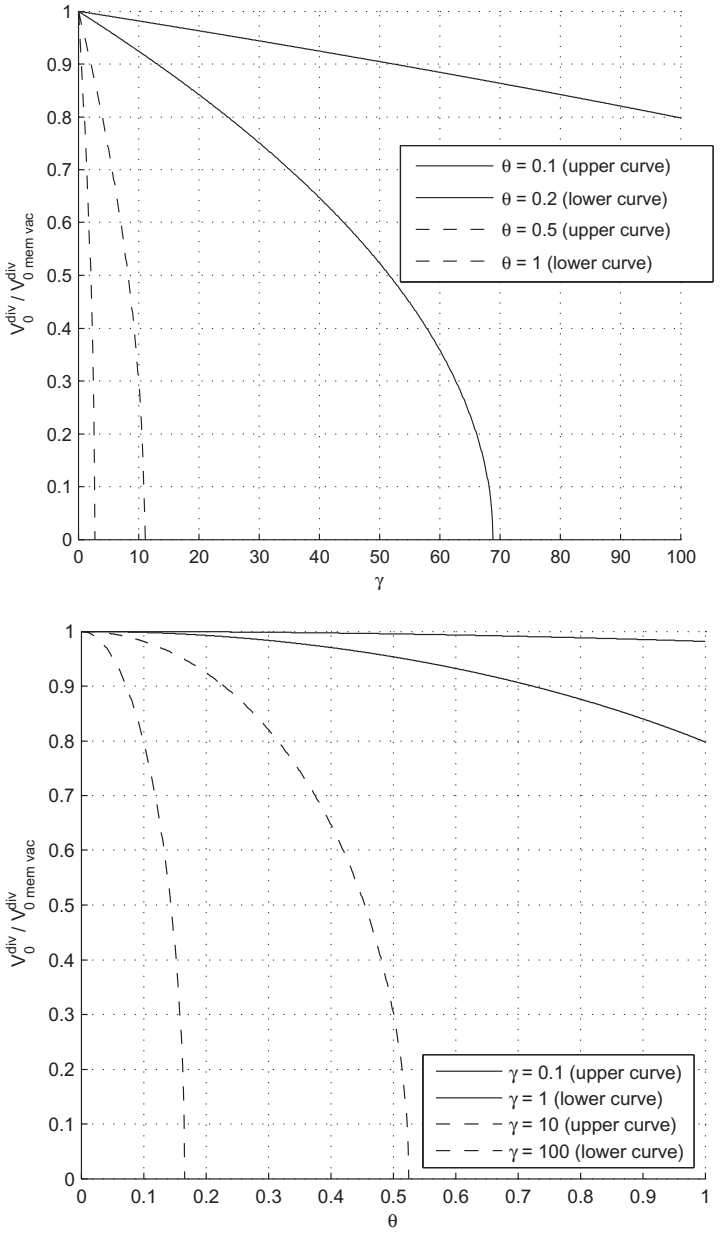

FIGURE 41 Problem (181). Effects of the dimensionless fluid density γ and the dimensionless fluid velocity θ on the dimensionless critical web velocity λ. *Top*: effect of density γ. For $\theta = 0$, $\lambda \equiv 1$ (not plotted). *Bottom*: effect of fluid velocity θ. For $\gamma = 0$, $\lambda \equiv 1$ (not plotted). The bending rigidity is fixed to $\beta = 0$; the solution is representative for small bending rigidities. See also sheet in Figure 40.

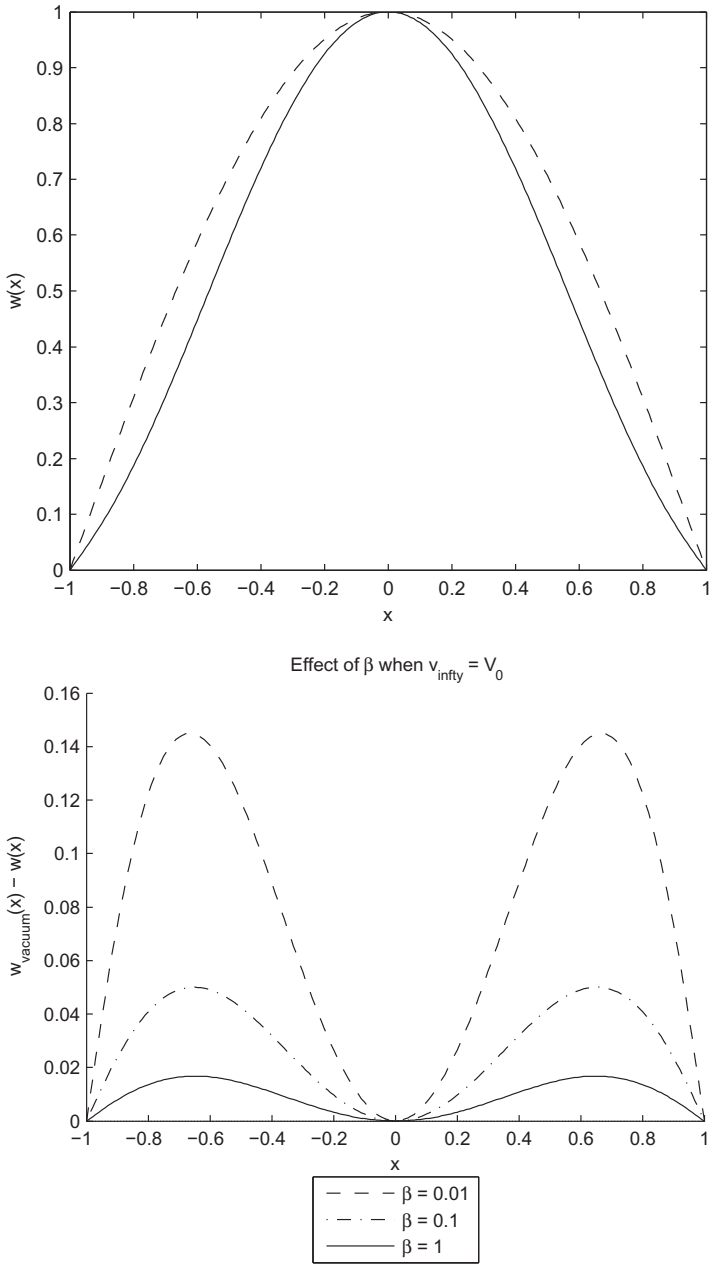

FIGURE 42 Some solutions of problem (182), where the air mass moves with the panel. The dimensionless density $\gamma = 15.625$. *Top*: Critical eigenmode (solid line). The dashed line shows the corresponding vacuum mode. Both modes normalized such that the maximum is 1. *Bottom*: the difference between the vacuum and with-fluid solutions at different values for the dimensionless bending rigidity β. Differences computed using the same normalization for the solutions as at the top.

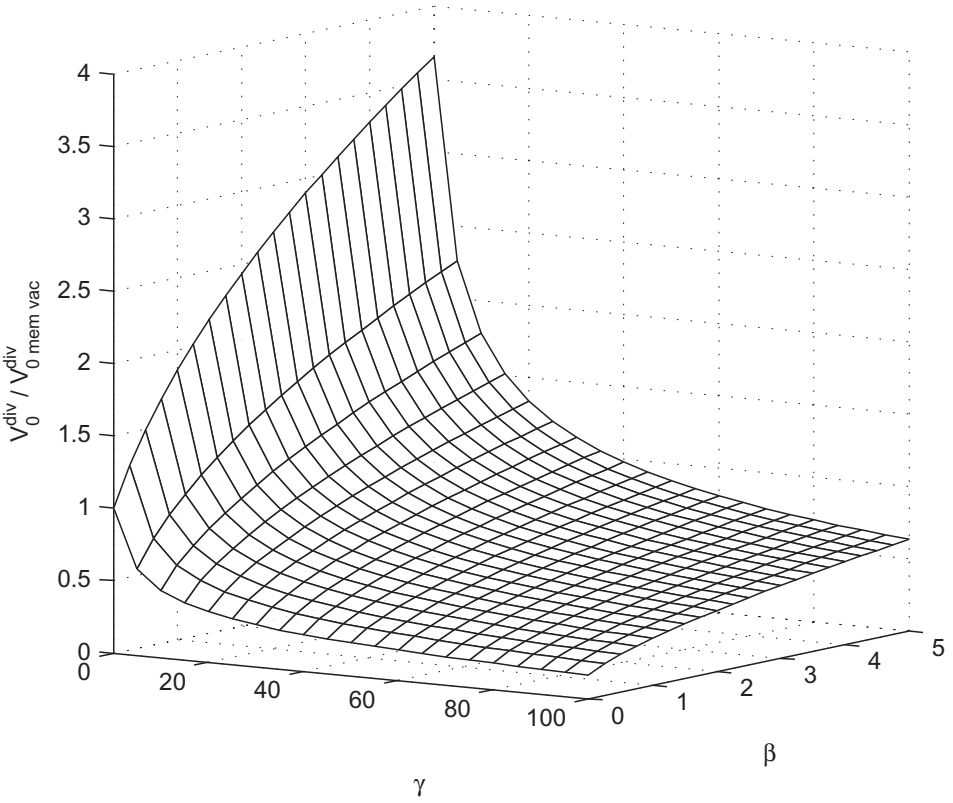

FIGURE 43 Problem (182). Effects of the dimensionless fluid density γ and the dimensionless bending rigidity β on the dimensionless critical web velocity λ. See also slices in Figure 44.

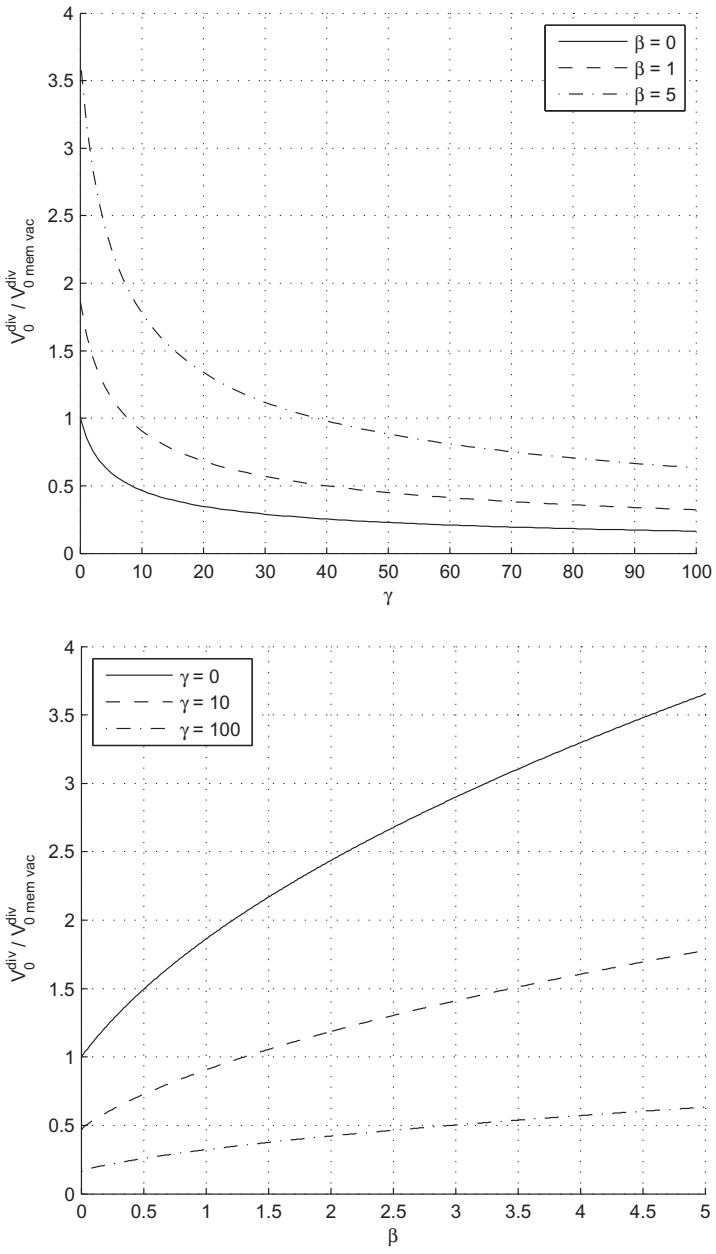

FIGURE 44 Problem (182). Effects of the dimensionless fluid density γ and the dimensionless bending rigidity β on the dimensionless critical web velocity λ. *Top*: effect of density γ. *Bottom*: effect of bending rigidity β. See also the 3D plot in Figure 43.

TABLE 2 Critical web velocity V_0 as a function of fluid velocity v_∞. The solution does not depend on the signs of the velocities. The same data are given in both dimensional and dimensionless forms; given a value of v_∞ (respectively θ), the critical web velocity is V_0^{div} (respectively λ^{div}). The dimensionless critical velocities λ^{div} give the axis intersection points of Figure 54 (p. 188).

v_∞ [m/s]	0	10	15	20	25	30	$v_\infty = V_0$
V_0^{div} [m/s]	79.057	75.385	70.526	63.098	52.012	33.845	30.607
θ	0	0.13	0.19	0.25	0.32	0.38	$\theta = \lambda$
λ^{div}	1	0.95355	0.89209	0.79813	0.65791	0.42811	0.38715

quency analysis. The case with no fluid (vacuum) gives the same critical velocity as $v_\infty = 0$, so it is not reported separately. This is expected; recall the comments on the structure of equation (181). The special case $v_\infty = V_0$ is also shown; we see that with this assumption, using our parameter values we get a critical velocity that is about 39% of the corresponding vacuum value.

On this note, let us compare our results to known ones for validation. The study by Pramila (1986) is well suited for comparison, because in it an axially moving web submerged in ideal fluid was considered. In Pramila's study, we have $v_\infty = 0$ for the stationary air, $D = 0$ for the threadline model (corresponding to an ideal membrane in the panel model), and $\rho_f = 1.2$ kg/m^3. However, since our model does not change the critical velocity for $v_\infty = 0$, it is more natural to assume $v_\infty = V_0$ as an alternative model for the case with no free stream.

In his study, Pramila gives the nondimensional first natural frequency as a function of the nondimensional velocity for some example cases. We will compare our natural frequency predictions with Pramila's later (in subsection 6.3.2); currently we are interested in the nondimensional velocity where the natural frequency becomes zero, denoted λ in our eigenvalue problem.

From added mass considerations, Pramila obtains a scaling factor, r. In his model, the first natural frequency and the critical velocity (computed from the vacuum case) both become scaled with the factor r, when the ideal fluid is taken into account. In our model, λ is the scaling factor for the critical velocity, and the steady-state analysis makes no prediction concerning the natural frequency.

For $m = 35.5$ g/m^2, Pramila's Figure 5 (Pramila, 1986, p. 74) suggests that r is in the range 20%–30%, depending on which added mass expression is used. Similarly, his Figure 6 suggests that for $m = 54$ g/m^2, the factor r is in the range 22%–35%. For both these examples, the dimensions of the open draw are span length $2\ell = 2.4$ m and web width $b = 0.47$ m, leading to an aspect ratio of $\text{AR} = 2\ell/b \approx 5.1$, i.e. a narrow strip. We will not need the width in our model.

In both cases, we have the dimensionless parameter $\beta = 0$. Noting that in problem (182) ($v_\infty = V_0$, i.e., $\theta = \lambda$), the value of T only affects the absolute value of V_0^{div} and not λ, our model predicts that for the first case ($\gamma = 40.5634$), the factor $r \approx 25.2\%$ regardless of tension. For the second case ($\gamma = 26.6667$), we have $r \approx 30.6\%$ regardless of tension. Both cases show good agreement with Pramila's results.

Let us compare the results using another aspect ratio, too. In Pramila's numerical example (Pramila, 1986, p. 72), the geometry is a wide plate with $2\ell = 0.75$ m and $b = 7.5$ m, giving an aspect ratio of AR $= 2\ell/b = 0.1$. The physical parameters are $T = 16$ N/m and $m = 50$ g/m^2. This gives a vacuum divergence velocity of ${V_0^{\text{div}}}_{\text{vac}} = \sqrt{T/m} \approx 18$ m/s. Pramila predicts that with these values, depending on the added mass expression used, the critical velocity is found to be between 2.7–4.6 m/s, or 15%–26% of the vacuum case.

Inserting the numbers to our model, we have $\beta = 0$ and $\gamma = 9.0$. Solving the eigenvalue problem (182) gives $V_0^{\text{div}} \approx 8.66$ m/s, or 48.4% of the vacuum case. Here the only agreement is qualitative: according to both models, the divergence velocity decreases when compared to the vacuum case. The quantitative difference is probably due to the deformation localisation effect, which renders the cylindrical deformation assumption invalid in the case of a wide plate.

Moving on to the next case, in Figure 45, we have considered the problem of Chang and Moretti (1991) for the critical flow velocity v_∞^{div}, (our) equation (184). In this problem, the panel is stationary (dimensionless panel velocity $\lambda = 0$) and is assumed to have zero bending rigidity ($D = 0$). The results for v_∞^{div} from our model, computed by solving (184), are shown together with the theoretical results and experimental data of Chang and Moretti (1991). We see that our model gives a more accurate prediction for case A (20×6 in, AR$\approx$3.33), than the original model. However, in case B (10×6 in, AR$\approx$1.67), our model almost systematically overestimates. The critical velocity, according to the measurements, increases more slowly in terms of the applied tension value than predicted. The increasing trend is predicted correctly, but the original model gives a better quantitative approximation. Comparatively better agreement with experiment in case A is to be expected, since the cylindrical deformation assumption holds best for long and narrow plates (see subsection 2.3.4 and Banichuk et al., 2010a, 2011a).

Finally, consider the classical stationary, non-tensioned panel subjected to axial flow. This problem is parameter-free, if we are only interested in the dimensionless $\overline{U_{cd}}$, so one solution is sufficient. The book by Païdoussis (2004, p. 1155) states that in the limit of a wide channel, the dimensionless critical flow velocity for a pinned-pinned plate with flow on both sides is $\overline{U_{cd\,\text{ref}}} \approx 3.3$. By solving the eigenvalue problem (186), we obtain $\overline{U_{cd}}^2 \approx 2.7788$, from which $\overline{U_{cd}} \approx 1.6670$. Our domain is $x \in [-1, 1]$, while the standard is $x \in [0, 1]$. Hence, we should scale our eigenvalue $\overline{U_{cd}}$ by 2 to make the results comparable.[3] Scaling produces $2\overline{U_{cd}} \approx 3.3339$, which agrees with the reference value.

Païdoussis (2004, p. 1150) also lists the quantity $\overline{U_{cd}}^2/\pi^3$ for several different studies, where flow on one side only has been investigated. In this case $\overline{U_{cd\,\text{ref}}}$ must be scaled by a factor of 2 to account for flow on one side of the plate only

[3] For an illustration of this issue, consider the eigenvalue problem of the 1D Laplace operator with zero Dirichlet boundary conditions. For $-w_{xx} = \lambda^2 w$, the eigenvalues λ are inversely proportional to the length of the domain. Hence, if the same problem is solved on a domain that is twice longer (different nondimensionalization of x), the eigenvalues will be halved. The present problem is similar enough (1D, and has a difference in derivative order by 2 between the terms) to behave in a similar manner.

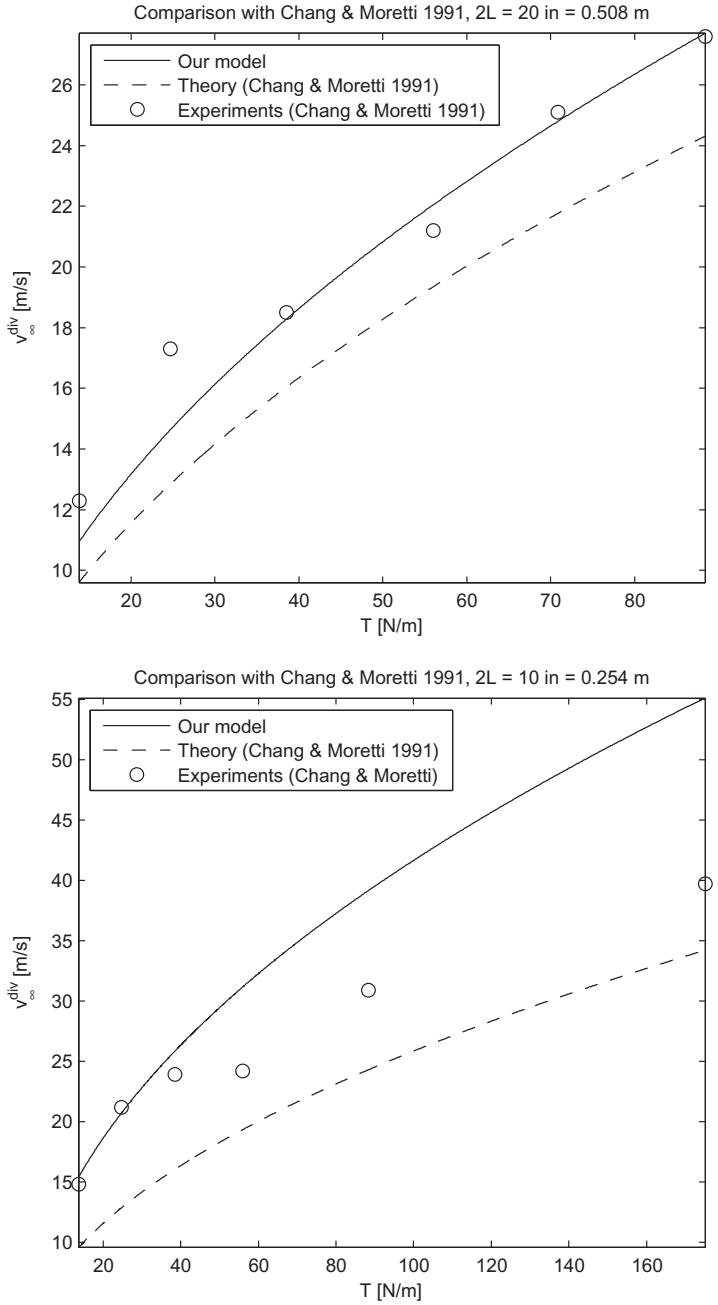

FIGURE 45 Static stability problem of Chang and Moretti (1991). A stationary panel is subjected to steady-state flow in a wind tunnel; the quantity of interest is the critical flow velocity v_∞^{div} at a given value of tension T. *Top*: case A, $2\ell = 0.508$ m (20 in). *Bottom*: case B, $2\ell = 0.254$ m (10 in).

(see Païdoussis, 2004, p. 1155). This scaling by 2 is independent of the one due to the difference in domain lengths. For our result, we obtain $(4\,\overline{U_{cd}})^2/\pi^3 \approx 1.43$, which obviously agrees with $(2\overline{U_{cd\,\mathrm{ref}}})^2/\pi^3 \approx 1.4$. Païdoussis remarks that this is a bit higher than the tabulated values (in the book), which are in the range $1.00 \ldots 1.35$.

We observe that the choice of n_0 does not matter; the change in the computed $\overline{U_{cd}}^2$ between $n_0 = 1$ and $n_0 = 56$ is less than 0.5%. The fast convergence agrees with the remark in the article Guo and Païdoussis (2000).

6.1.2 Summary and conclusion

The critical velocity of the system was investigated numerically as a function of problem parameters. The results were summarized in graphical form. It was found that, quite intuitively, increasing fluid density decreases the critical velocity, while increasing the bending rigidity increases it. The value of the computations is in giving quantitative predictions for the critical velocity with given parameter values.

What was less intuitive is that, by this model, any nonzero free-stream velocity for the fluid decreases the critical velocity of the panel. This was found to be the case even if the fluid and the panel move in the same direction. This is unintuitive, because one would expect any setup with a smaller velocity difference $(v_\infty - V_0)$ to resemble more the case of a non-moving panel in stationary air; however this is not the case. The effect of the given free-stream velocity was investigated parametrically, as well as the effects of bending rigidity and fluid density.

In the present model, as is often the case, discretization was necessary to make the model solvable. The validation suggests that the accuracy of the discretization is good in practice, although the convergence properties (and the size of the discretization error) have not been investigated with a mathematically rigorous approach.

In the analysis performed, four different steady-state problems were solved. The first two were related to the critical velocity of the panel, as follows. In the first problem, the free-stream velocity of the fluid v_∞ (dimensionless form: θ) was given as a problem parameter, while the panel velocity V_0 (respectively λ) was the unknown eigenvalue.

In the second problem, the whole air mass was assumed to move along with the panel; $v_\infty = V_0$. In this case, there was only one velocity, which was treated as the unknown eigenvalue λ. The structure of the equation then becomes that of a perturbed vacuum model. It was found that if the whole air mass moves with the panel, the critical panel velocity is decreased. The decrease is significant; values between 25.2%–48.4% of the corresponding vacuum value were observed.

The other two investigated steady-state problems were related to the flow divergence of stationary panels. As these do not concern axially moving panels, they were of interest mainly for validation, and for seeing how the predictions from the present model differ from known values in literature.

The third problem was the divergence of the stationary tensioned panel when subjected to axial flow. The panel velocity was zero, $V_0 = 0$ (resp. $\lambda = 0$), and the free-stream velocity of the fluid, v_∞ (resp. θ), was the unknown eigenvalue. The critical fluid velocity was thus determined. The results were compared to Chang and Moretti (1991). In the case of a long, narrow strip (20×6 in, AR$\approx$3.33), the present model improves on the theoretical predictions of Chang and Moretti, in terms of matching experimental data. In the case of a relatively wider span (10×6 in, AR$\approx$1.67), the agreement is not as good, although the qualitative trend is predicted correctly. This supports our earlier findings of the validity of the panel model; see subsection 2.3.4 and Banichuk et al. (2010a).

The last problem was the classical non-tensioned stationary panel subjected to axial flow. Again, the panel velocity was zero, $V_0 = 0$ (resp. $\lambda = 0$), and the free-stream velocity of the fluid, v_∞ (resp. θ), was the unknown eigenvalue. This was a parameter-free problem with just the dimensionless lowest critical velocity as the solution. The result was compared to those summarized in the book by Païdoussis (2004). The agreement was found to be good.

To sum up, the performed parametric study gives insight into the behaviour of the critical panel velocity, when fluid-structure interaction is accounted for. The present model was validated, and found to work especially well for long, narrow strips. Overall it can be said that the model works well for aspect ratios AR $= 2\ell/b$ of 3 and higher. The qualitative trends are correct for lower aspect ratios, too, but then the critical velocity may be overestimated by the model.

6.2 Dynamical behaviour

Our next problem is the dynamical behaviour of the system. As above, we will first look into the numerical solution strategy used, and then report the numerical results.

The time integration of (168), which is a system of ordinary differential equations (ODEs), proceeds using order reduction, and then numerical diagonalization. For completeness, let us briefly review the techniques.

6.2.1 Order reduction

Let us truncate the Galerkin series at $n = n_0$. The finite equation corresponding to (168) is of the general form

$$M_2 \frac{\mathrm{d}^2 \mathbf{f}(t)}{\mathrm{d}t^2} + M_1 \frac{\mathrm{d}\mathbf{f}(t)}{\mathrm{d}t} + M_0 \mathbf{f}(t) = \mathbf{G}(t) \,, \tag{190}$$

where the coefficient matrices are defined by the obvious identifications (compare equations (190) and (168), p. 134), and $\mathbf{G}$ is a vector consisting of the components

G_j defined by (169), p. 134. For convenience, we give them explicitly here:

$$(M_2)_{jn} \equiv \alpha^2 \left[A_{jn} + \gamma a_{jn} \right] \tag{191}$$

$$(M_1)_{jn} \equiv 2\alpha \left[\lambda B_{jn} + \gamma\theta b_{jn} \right] \tag{192}$$

$$(M_0)_{jn} \equiv (\lambda^2 - 1) C_{jn} + \gamma\theta^2 c_{jn} + \beta D_{jn} \tag{193}$$

$$G_j(t') \equiv \frac{\ell}{T} \int_{-1}^{1} g(\, \ell\, x',\, \tau\, t'\,)\, \Psi_j(x')\, \mathrm{d}x' \,. \tag{194}$$

In (194), the primes explicitly indicate dimensionless quantities. The load function g is the original, dimensional load function (the factor ℓ/T then makes G_j dimensionless), expressed in the original, unscaled (x, t) coordinates.

System (190) can be reduced to a twice larger first-order one by standard techniques; let us define

$$\mathbf{u} \equiv \begin{bmatrix} \mathbf{f}' \\ \mathbf{f} \end{bmatrix} , \tag{195}$$

where the prime denotes the time derivative. Taking into account that M_2 is small enough to invert numerically, the expanded equation system becomes

$$\frac{\mathrm{d}}{\mathrm{d}t} \begin{bmatrix} \mathbf{f}' \\ \mathbf{f} \end{bmatrix} = \begin{bmatrix} -M_2^{-1} M_1 & -M_2^{-1} M_0 \\ I & 0 \end{bmatrix} \begin{bmatrix} \mathbf{f}' \\ \mathbf{f} \end{bmatrix} + \begin{bmatrix} M_2^{-1} \mathbf{G} \\ 0 \end{bmatrix} , \tag{196}$$

which can be written as

$$\mathbf{u}' = M\mathbf{u} + \mathbf{g}(t) \,, \tag{197}$$

where

$$M = \begin{bmatrix} -M_2^{-1} M_1 & -M_2^{-1} M_0 \\ I & 0 \end{bmatrix} , \qquad \mathbf{g}(t) = \begin{bmatrix} M_2^{-1} \mathbf{G}(t) \\ 0 \end{bmatrix} . \tag{198}$$

The quantities (198) are the mass matrix and the force vector of the reduced-order problem.

6.2.2 ODE system integration by diagonalization

Standard integration techniques, such as the Fourth-order Runge–Kutta method, are directly applicable to the first-order system (197). However, we have only one space dimension in the original problem, and the Fourier basis typically does not require many modes along each space dimension in order to get acceptable results. This motivates the use of a diagonalization method (see, e.g., Kreyszig, 1993), which can take advantage of the small size of the equation system.

To diagonalize the system (197), we assume that M has a full eigenvector basis (in practice, this holds). Define Λ, X, $\mathbf{z}$, and $\mathbf{h}(t)$:

$$\Lambda \equiv X^{-1} M X \,, \qquad \mathbf{u} \equiv X\mathbf{z} \,, \qquad X\mathbf{h}(t) \equiv \mathbf{g}(t) \,, \tag{199}$$

where Λ is a diagonal matrix with the (complex) eigenvalues λ_j of M on the diagonal, and X is a unitary matrix containing the eigenvectors of M in its columns. Using the relations (199), equation (197) becomes

$$\mathbf{z}' = \Lambda\mathbf{z} + \mathbf{h}(t) \,, \tag{200}$$

The solution for the jth component of $\mathbf{z}$ is (Kreyszig, 1993, p. 191)

$$z_j(t) = e^{\lambda_j t}\left[z_j(0) + \int_{\hat{t}=0}^{t} e^{-\lambda_j \hat{t}} h_j(\hat{t})\,\mathrm{d}\hat{t}\right] , \tag{201}$$

where $\hat{t}$ is a dummy variable for integration and $j = 1, 2, \ldots, 2 \cdot n_0$. The initial value $\mathbf{z}(0)$ is evaluated by using (170)–(171) and (195), and solving the linear system in (199) for $\mathbf{z}$. Using (201), (199) and (195), the space-discrete solution $\mathbf{f}(t)$ and its time derivative $\mathbf{f}'(t)$ may then be computed at any desired time t without the need for timestepping. Especially, there is no requirement on the size of the intervals between consecutive time values.

Because the equation system is small, and M is constant in time, it is not expensive to compute Λ and X using a standard numerical eigenvalue solver.

Next, let us look into the relevant numerical results.

6.2.3 Numerical results

As in the steady-state cases, the Galerkin series was truncated at $n_0 = 56$. Physical parameters were again chosen as typical for a paper web surrounded by air; refer to Table 1 on page 155. The timescale parameter was chosen as $\tau = \ell/\sqrt{T/m}$, which leads to $\alpha = 1$ (equation (142), p. 126).

Each simulation is presented as a figure consisting of three parts. The top half displays a space–time plot of the displacement function $w(x,t)$. The horizontal axis represents dimensionless time t and the vertical axis designates the position x between the rollers at $x = \pm 1$ (note the orientation, positive x up). The shade of each point in the image indicates the height, measured from zero displacement.

The bottom half of each figure is made up of two graphs. The graph on the left shows the displacement of the panel as a function of x at a few selected times t. The graph on the right shows the time behaviour of the centre point of the panel, $w(0,t)$. The corresponding points in the lower two graphs are marked with circles.

All computations were performed with a configuration where the initial position of the panel was given. For the cases in Figures 46–51, the initial condition for position was

$$w\,(x,0) \equiv g_1\,(x) \equiv a \cdot \sin(\pi\,\frac{x+1}{2})\ , \tag{202}$$

where the initial amplitude at the center point was $a = 5 \cdot 10^{-3}$. The initial transverse velocity was zero,

$$\frac{\partial w}{\partial t}\,(x,0) \equiv g_2\,(x) \equiv 0\ , \tag{203}$$

and there were no external disturbances,

$$g\,(x,t) \equiv 0\ . \tag{204}$$

Note that (203)–(204) are not fundamental limitations of the model, but are simply choices made to simplify the cases studied.

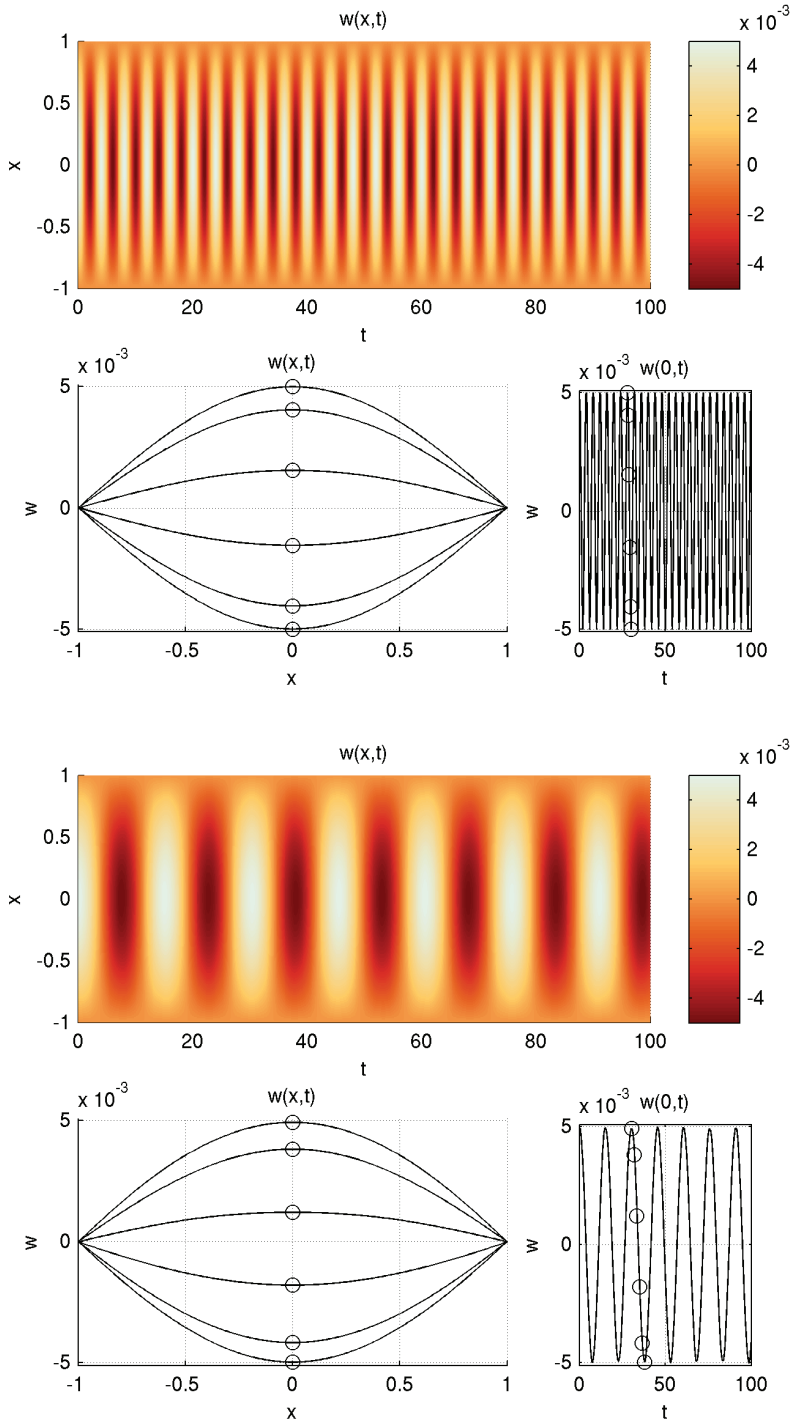

FIGURE 46 Dynamic response of the panel in vacuum and in stationary fluid. $V_0 = 0$ m/s. *Top*: Vacuum case for comparison. *Bottom*: $v_\infty = 0$ m/s (submerged in stationary fluid).

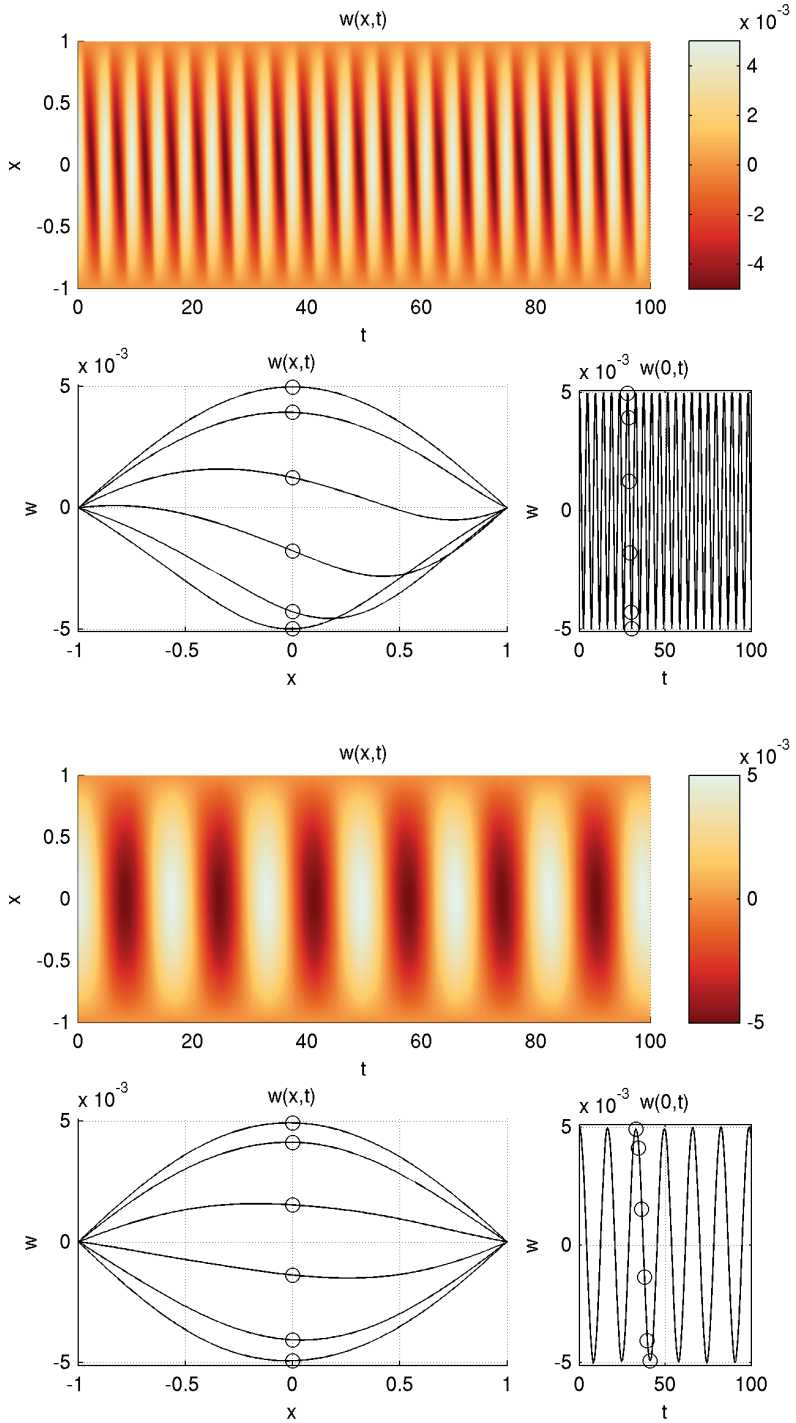

FIGURE 47 Dynamic response of the panel in vacuum and in stationary fluid. $V_0 = 30$ m/s. *Top*: Vacuum case for comparison. *Bottom*: $v_\infty = 0$ m/s (submerged in stationary fluid).

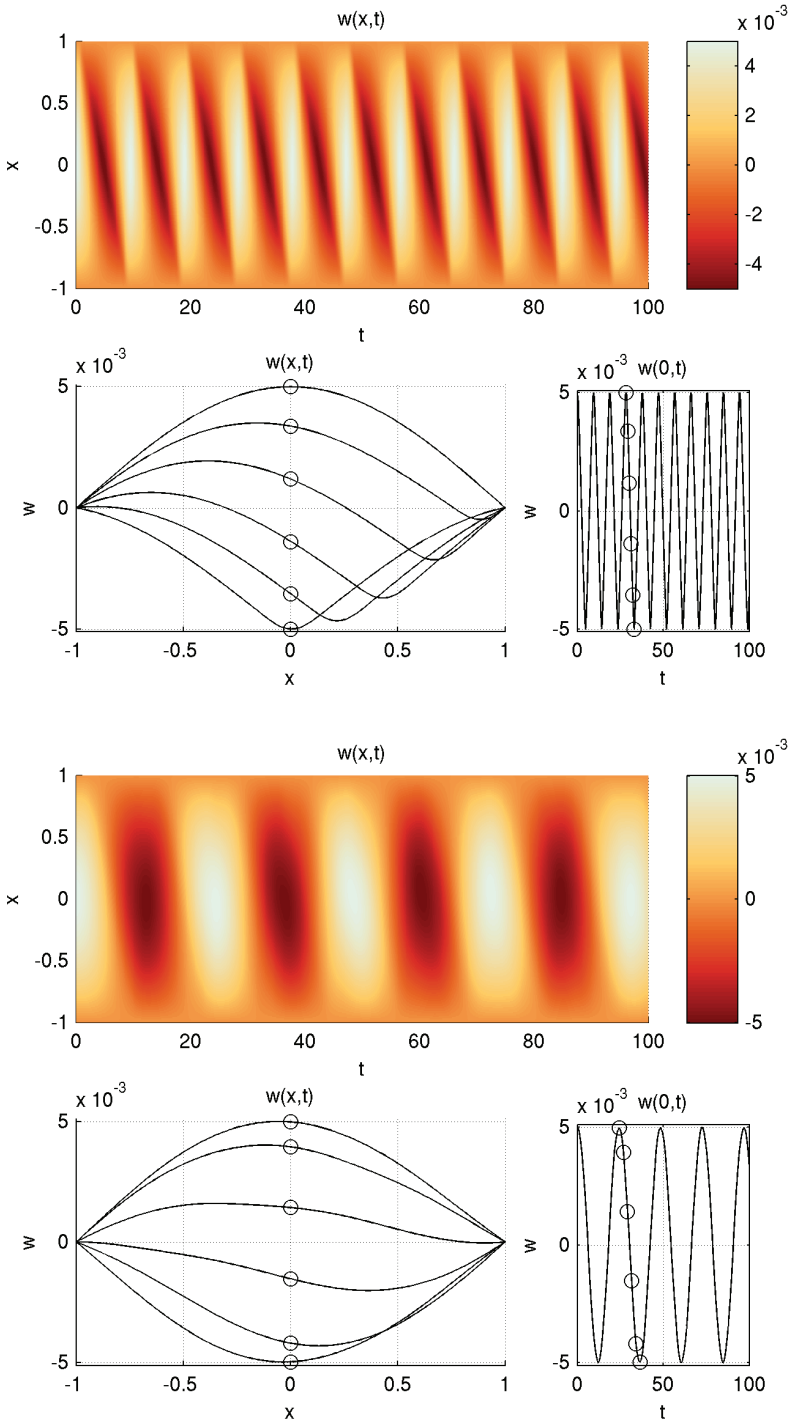

FIGURE 48 Dynamic response of the panel in vacuum and in stationary fluid. $V_0 = 60$ m/s. *Top*: Vacuum case for comparison. *Bottom*: $v_\infty = 0$ m/s (submerged in stationary fluid).

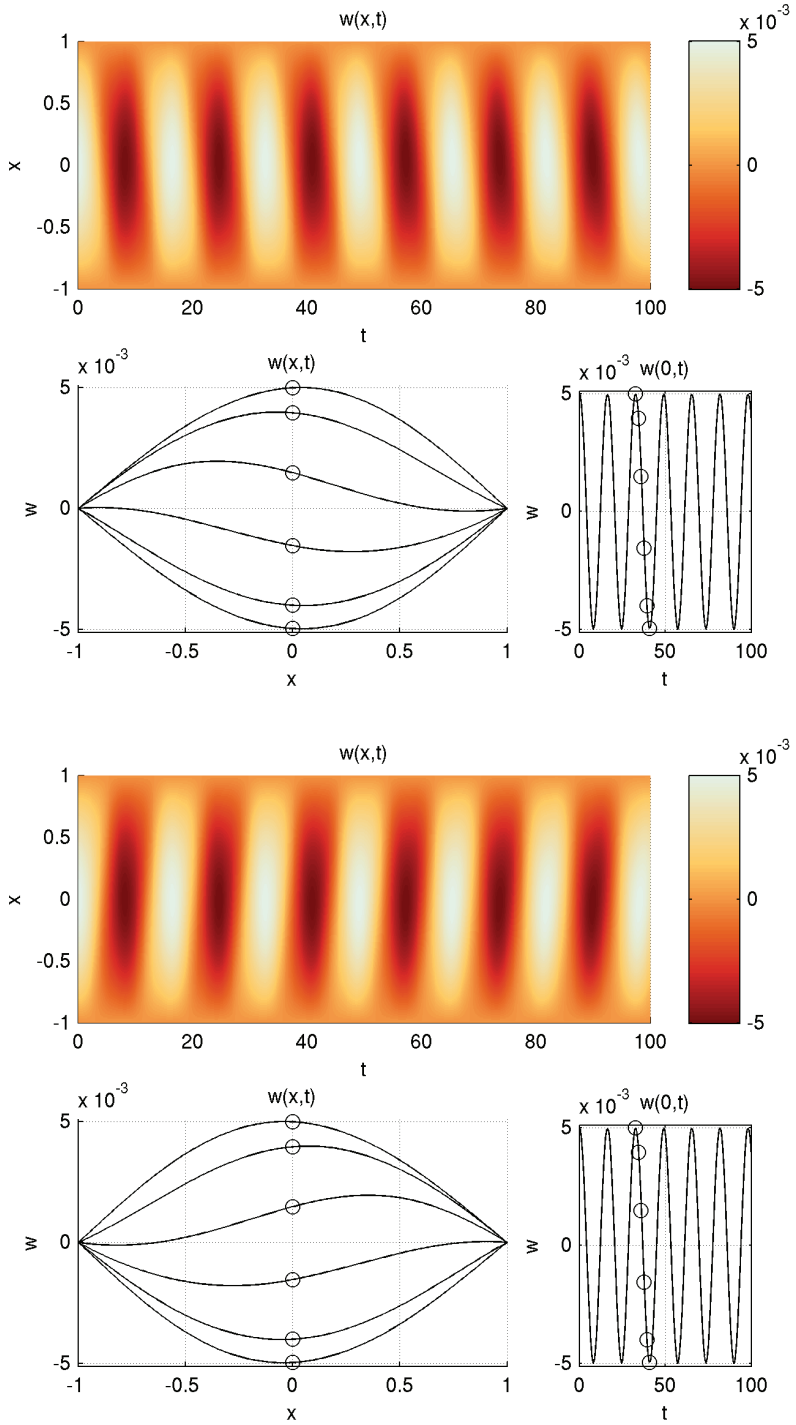

FIGURE 49 Dynamic response of the panel in axially moving fluid. $V_0 = 0$ m/s. *Top*: $v_\infty = +10$ m/s. *Bottom*: $v_\infty = -10$ m/s.

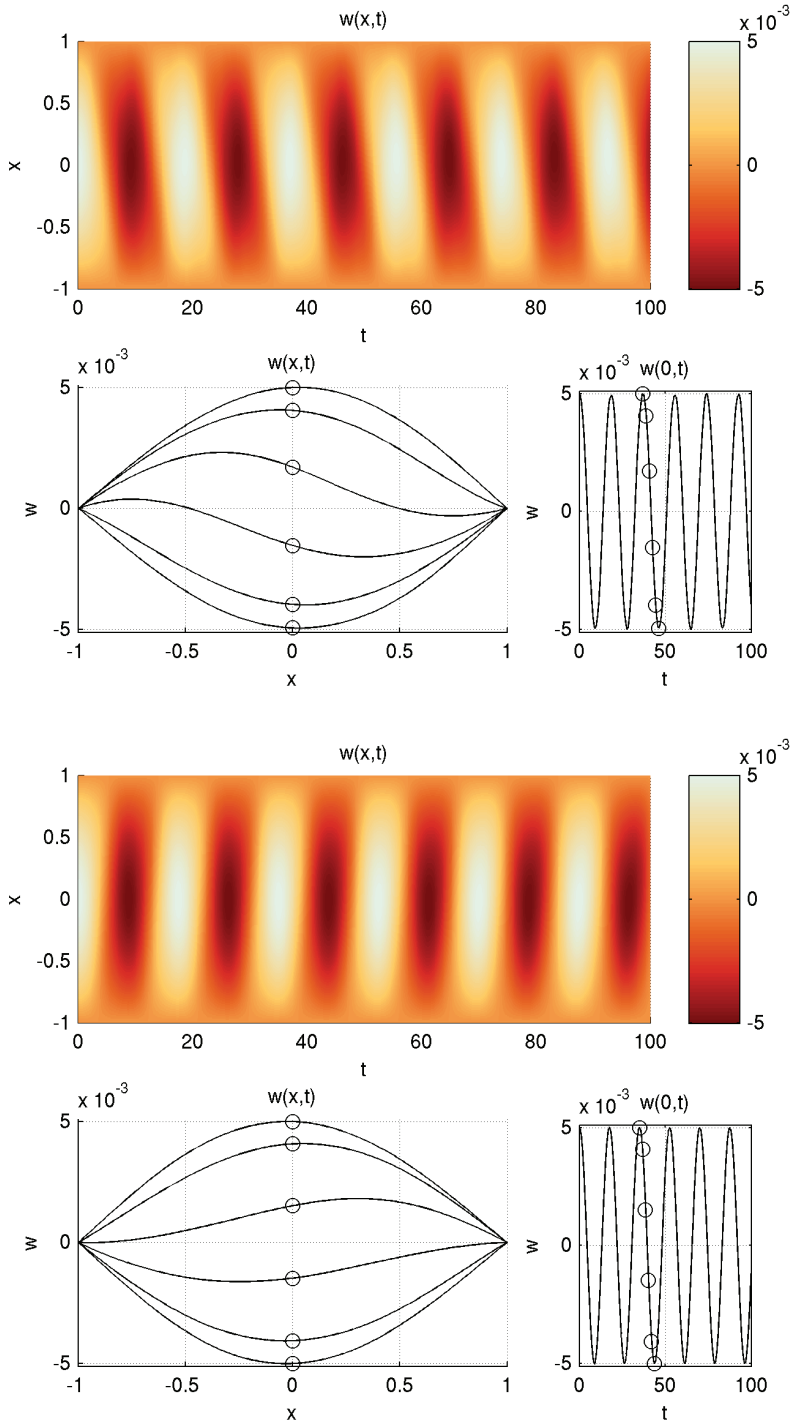

FIGURE 50 Dynamic response of the panel in axially moving fluid. $V_0 = 30$ m/s. *Top*: $v_\infty = +10$ m/s. *Bottom*: $v_\infty = -10$ m/s.

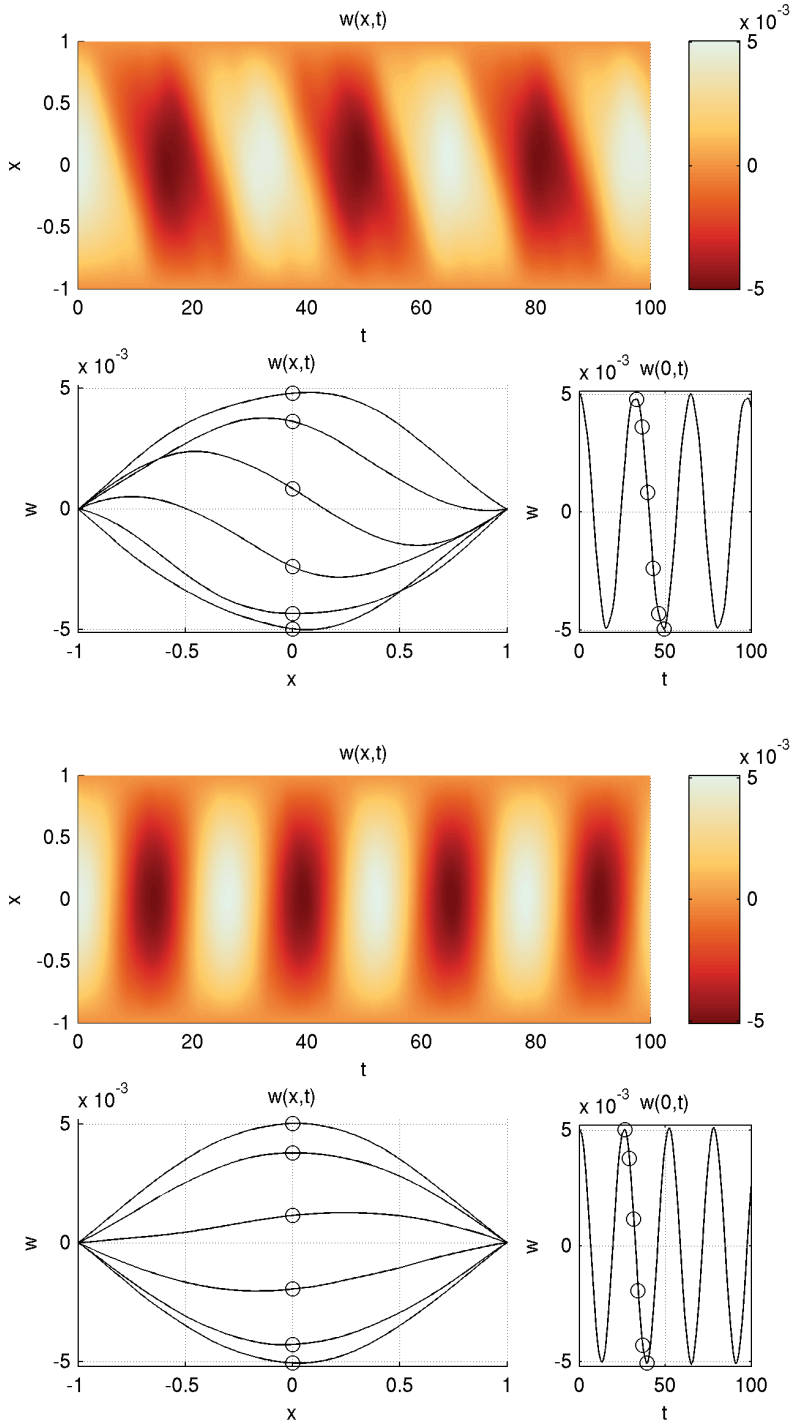

FIGURE 51 Dynamic response of the panel in axially moving fluid. $V_0 = 60$ m/s. *Top*: $v_\infty = +10$ m/s. *Bottom*: $v_\infty = -10$ m/s.

In the upper part of Figures 46–48, we have as a fundamental test case a panel in vacuum, travelling at various speeds and undergoing a steady, cylindrical vibration. Figure 46 represents the classical non-travelling case. In Figures 47–48, the shapes are aligned at an angle to the x axis. Due to the axial motion toward the positive x direction, the positive-x half of the plate experiences each maximum (minimum) of the vibration before the negative-x half does. Physically, as is well known, the wave travelling to the direction of travel on an axially moving medium moves at a higher velocity than the wave travelling in the opposite direction. Mathematically, the phenomenon can be seen as the velocity-dependent phase shift in the eigenmodes of axially travelling strings and beams that was discussed by Wickert and Mote (1990). As was noted in the problem setup, the flat panel model shares the mathematical formulation with the beam model, so we can expect the same phenomenon to occur.

Let us now move onto the focus of the present study, and consider the effect of fluid-structure interaction. The lower parts of Figures 46–48 represent the dynamic response of the panel in stationary ideal fluid. The axial velocity of the panel is the same in both the upper and lower parts of each Figure, to facilitate easy comparison.

Figures 49–51 represent the response in axially moving fluid. The upper part of each Figure shows the response at $v_\infty = +10$ m/s, and the lower part at $v_\infty = -10$ m/s. The axial velocity of the panel is the same in both the upper and lower parts of each Figure.

The qualitative behaviour in our Figures 46–51 is seen to be similar to Figure 2 in Chang et al. (1991), where a free vibration cycle of a travelling threadline from a direct simulation was plotted.

In a kind of cross-validation between the steady-state and dynamic cases, we conclude this section with a direct simulation of a special case. The solutions shown in Figures 46–51 are periodic and stable. Figure 52 represents the limiting case where a nontrivial steady-state solution exists. For this case, the starting position of the panel was specified as the critical eigenmode of the corresponding steady-state problem.

The steady-state problem was solved as described in Section 6.1, and the obtained numerical Fourier–Galerkin coefficients and the critical velocity were used as input data for the dynamic solution process. In this configuration, the initial transverse velocity was zero as per equation (203), and there were no external disturbances, as per equation (204). It was found, as shown in Figure 52, that the computed solution stays constant in time, as expected.

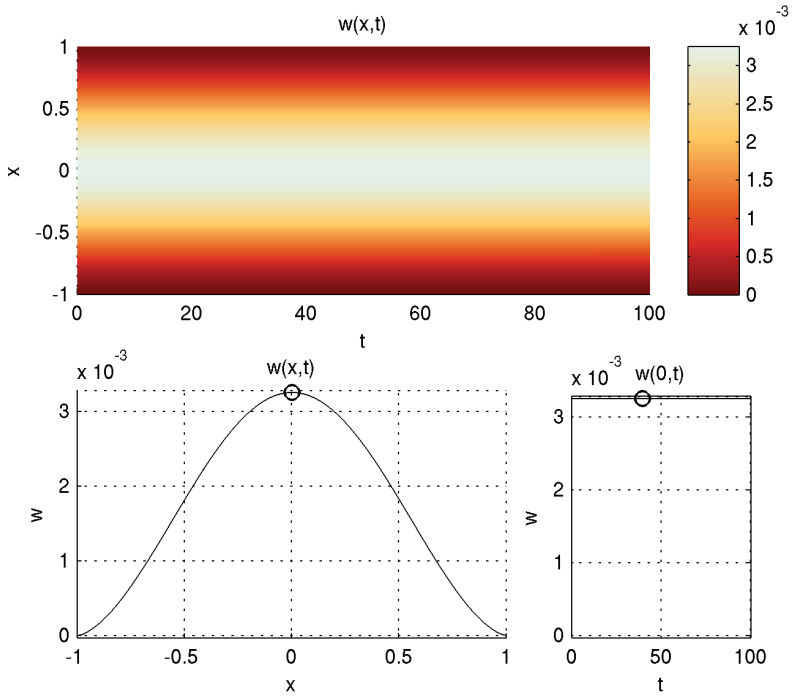

FIGURE 52 Steady state solution. $V_0 = 70.5257$ m/s. $v_\infty = -15$ m/s, $t_{\text{fin}} = 1$ s, $g_1(x)$ set to critical eigenmode, $g(x,t) \equiv 0$, $g_2(x) \equiv 0$.

6.2.4 Discussion

The following observations were made about the numerical solutions.

Although the eigenvalues λ_j are in general complex, the exact solution $\mathbf{u}$ stays real-valued for real-valued initial data.

The diagonalization method does not cause numerical dissipation, because the qualitative behaviour of the first-order system (200) is captured by (201).

The initialization of this method requires computing Λ and X. The asymptotic cost of this initialization is $O(n_0^3)$ (with e.g. the QR algorithm; see Golub and van Loan, 1996), so this method is only applicable to small equation systems. After the initialization, the cost of evaluating the solution at one point of time t is $O(n_0^2)$ due to the full vector-matrix multiplication. The advantage is that there is no timestep limitation.

As can be seen from equation (201), any numerical approximation of the transformed solution $\mathbf{z}$ will drift away from the exact one at a rate which depends on the amount of numerical error in the eigenvalues λ_j. The error in the numerical approximation of $\mathbf{u}$ then behaves as a linear combination of these errors, by the transformation (199). The error is independent of the spacing of the points of time at which the solution is evaluated.

Numerical error in the eigenvalues may cause small imaginary components to be introduced into the Galerkin coefficients $\mathbf{u}$, which are known a priori to be real. This can be avoided by inspecting the imaginary part of the solution at each point of time for which it is computed, and then either ignoring the imaginary part (if small) or stopping computation. In our tests, to keep the computation consistent, we chose to test for imaginary parts in the original solution vector, but discard them only in visualization (assembly of the Galerkin approximation). The validity criterion used was $\left|\mathrm{Im}(u_j)\right| < 10^{-8}$ separately for each component $j = 1, 2, \ldots, 2 \cdot n_0$. In practice, this criterion was never violated.

The method was also tested against standard fourth-order Runge–Kutta (RK4); no difference was observed when the timestep was small enough for RK4 to converge. This suggests that the used eigenvalue solver was accurate enough in order for the drift problem to remain theoretical in the cases tested.

6.2.5 Summary and conclusion

Direct temporal simulations of panel behaviour were made, with and without the effect of the surrounding air. The simulations showed the response of the system as it starts from a given initial position. This gives some intuitive insight into the time evolution of the system.

The time integration method was validated against a widely used one. The dynamic solution was cross-validated against the steady-state one, by using as input the critical velocity and eigenmode obtained from steady-state analysis.

The cases analyzed were given initial position only, but the approach allows for given initial velocity and given, dynamic external disturbances (load functions inside the domain).

6.3 Eigenfrequencies

Our final problem are the eigenfrequencies of the system. The solution was obtained as follows.

Consider the free vibration problem of the space-discrete system (190). Let us set the external forces to zero, $\mathbf{G}(t) \equiv 0$, and use the standard time-harmonic trial function:

$$\mathbf{f}(t) = \mathbf{F}e^{st} \,, \tag{205}$$

where $\mathbf{F}$ is a constant vector. We wish to find all $s \in \mathbb{C}$ (and optionally, also the corresponding nontrivial $\mathbf{F} \in \mathbb{C}^{n_0}$) such that

$$\left[\left(M_2 s^2 + M_1 s + M_0\right)\mathbf{F}\right] e^{st} \equiv L(s)\,\mathbf{F}\,e^{st} = 0 \,.$$

The matrices M_j are given by (191)–(193), p. 172.

Obviously, the common exp factor does not matter, so we have

$$\left(M_2 s^2 + M_1 s + M_0\right)\mathbf{F} \equiv L(s)\,\mathbf{F} = 0 \,. \tag{206}$$

To find s, we use the determinant method. In order to admit nontrivial $\mathbf{F}$ in (206), the matrix $L(s)$ must be singular. It is easily seen that the zeroes of $\det(L(s))$ (as a function of s) are exactly the eigenvalues of M, the $2 \cdot n_0 \times 2 \cdot n_0$ matrix defined by equation (198) (p. 172). Thus, there are up to $2 \cdot n_0$ distinct solutions, all of which can be readily obtained by computing the eigenvalues.

To see the equivalence, expand $\det(M - \lambda_j I)$ as a block determinant, noting that the necessary blocks commute. Multiply (206) from the left by M_2^{-1}. Compare the zero determinant conditions to find that $s = \lambda_j$.

The solutions s give us the eigenfrequency response of the system, e.g., for various values of V_0 with the other parameters kept fixed. The critical velocity at which $s_j = 0$ for all $j = 1, 2, \ldots, 2 \cdot n_0$, obtained by a numerical search procedure, matches the critical velocity predicted by the static instability analysis.

Finally, note that $L(s) \in \mathbb{C}^{n_0 \times n_0}$, while $M \in \mathbb{R}^{2n_0 \times 2n_0}$ (but with complex eigenvalues). The matrix $L(s)$ is gyroscopic (because M_2 and M_0 are symmetric, while M_1 is skew-symmetric). The presented method for computing the eigenfrequencies is classical and simple, but other methods also exist specifically for gyroscopic systems. See e.g. Qian and Lin (2007) for a method which works directly on (206) without requiring M.

6.3.1 Finding the corresponding eigenvectors

The eigenfunctions (and hence, eigenvectors) will be needed below, so before moving on to the results, we will briefly review on how to find the eigenvectors $\mathbf{F}$, once the eigenvalues s are known.

Consider $L(s)$ defined in equation (206), and a fixed s, which is a solution of $\det(L(s)) = 0$. The singular value decomposition (SVD) can be used. Write the SVD of the matrix L as

$$L = USV \,, \tag{207}$$

where U and V are unitary, and S is a diagonal matrix containing the singular values of L on the diagonal. Standard numerical solvers can be used to perform the SVD in practice. The algorithmic details for implementing one, if needed, can be found in the book Golub and van Loan (1996).

The right-hand side of (207) represents a rotation (plus possibly a reflection) V, followed by a scaling S, followed by another rotation (plus possibly reflection) U. In the once-rotated space, the nontrivial kernel of L must correspond to the zero rows of S, because these rows are then scaled to zero before applying the second rotation U. The question becomes: which vectors in the input space map to the corresponding vector elements?

Let us denote the index set of the zero rows of S as

$$I_0 = \{i : \ S_{ii} = 0\} \ . \tag{208}$$

In this definition, it is sufficient to use the diagonal element, because S is a diagonal matrix.

The matrix L can be viewed as a linear operator in $\mathbb{C}^{n_0} \to \mathbb{C}^{n_0} : \ \mathbf{a} \mapsto L\mathbf{a}$. On the other hand, $L = USV$ as was mentioned. Consider the linear mapping

$$\mathbf{b} = V\mathbf{a} \ , \tag{209}$$

where $\mathbf{a}$ and $\mathbf{b}$ are (complex) vectors with n_0 elements. In the next step of applying the product $L = USV$ to the vector $\mathbf{a}$, the elements $\{b_j : \ j \in I_0\}$ of the vector $\mathbf{b} = (b_1, b_2, \ldots, b_{n_0})^{\mathrm{T}}$ will be zeroed out in the matrix-vector product $S\mathbf{b}$. Because V is unitary, multiplying (209) from the left by V^{H} (the Hermitian conjugate of V) gives

$$V^{\mathrm{H}}\mathbf{b} = \mathbf{a} \ . \tag{210}$$

Since the index set I_0 can be obtained directly (by inspection of the SVD result), we can choose a set of vectors $\{\mathbf{b}_k\} = \{\hat{\mathbf{e}}_k : \ k \in I_0\}$ (the kth standard basis vector of unit length, with k in I_0), and see how each of them maps through (210). This procedure gives the corresponding vectors $\mathbf{a}_k$ in the original, untransformed space. These vectors represent the directions that are in the null space of L; thus, they are the eigenvectors of the discretized free vibration problem (206).

From an implementation viewpoint, we do not need to compute anything more once we have the SVD. The product $V^{\mathrm{H}}\hat{\mathbf{e}}_k$ simply picks the kth column of the matrix V^{H}. Because V^{H} is the Hermitian conjugate of V, this is equivalent with picking the complex conjugate of the kth row of the original V.

The conclusion is that the eigenvectors, corresponding to one fixed eigenfrequency s, are

$$E \equiv \{\mathbf{v}_k : \ k \in I_0\} \ , \quad \text{where} \quad (\mathbf{v}_k)_j = \mathrm{conj}(V_{kj}) \ , \tag{211}$$

where $(\mathbf{v}_k)_j$ denotes the jth component of the vector $\mathbf{v}_k$, and $\mathrm{conj}(\cdot)$ the complex conjugate. The matrix V comes from the SVD of $L(s)$, and the index set I_0 is defined by (208). Note that, via the SVD, the set E has the eigenvalue s as a parameter; thus the set of eigenvectors must be evaluated separately for each solution s of the equation $\det(L(s)) = 0$.

Usually, it happens in practice that $\#I_0 = 1$, i.e., there is only one eigenvector for each eigenvalue s.

Now we have all the tools; let us move on to the results. The results for the first (lowest) eigenfrequency will be discussed first. Then we will discuss results on the solution of the eigenfrequency spectrum, which is the final topic in the analysis of our main problems.

6.3.2 Numerical results: first eigenvalue

Let us look at some solutions of the dimensionless first (lowest) eigenfrequency of the system. The physical problem parameters were as in Table 1 on page 155, except that the bending rigidity was assumed to be zero, $D = 0$ (membrane limit). As in the dynamic simulations, the timescale parameter was chosen as $\tau = \ell/\sqrt{T/m}$, which leads to $\alpha = 1$ (equation (142), p. 126).

The dimensionless first eigenfrequency of the system is plotted as a function of dimensionless panel velocity λ in Figure 53. Two cases are shown: stationary air ($v_\infty = 0$), and the case where the whole air mass moves with the web ($v_\infty = V_0$). Again, the assumption in the second case makes it similar in spirit to the vacuum case, as there is only one independent velocity. It can be seen that the presence of fluid decreases the first natural frequency, as expected (Pramila, 1986, Frondelius et al., 2006 and Kulachenko et al., 2007b).

The eigenfrequency is non-dimensionalized by ω_0, the lowest eigenfrequency of the same system, in vacuum at $V_0 = 0$. The normalization factor was computed numerically, using the same numerical code, but with the fluid terms omitted (effectively setting $q_f(x,t) \equiv 0$).

The results were obtained by solving (206) (page 183) as explained in Section 6.3, and taking the lowest eigenfrequency as $\omega_{\min}(V_0) \equiv \min_j \left|\operatorname{Im} s_j(V_0)\right|$. Then the dimensionless eigenfrequency, shown on the vertical axis of the plots, is $\omega'(V_0) \equiv \omega_{\min}(V_0)/\omega_0$ (the prime denotes a dimensionless variable).

For validation, three pairs of classical analytical results from two added-mass models from a study by Pramila (1987) are included in Figure 53, plotted for our problem parameters. Each pair begins at a single point at $V_0 = 0$, and the different pairs correspond to different aspect ratios ($\mathrm{AR} = 2\ell/b$, span length per width). The added masses are constants, which are affected by β_{Pr}, the β value of Pramila (1986, Table II), which depends on the AR. For the results shown here, this dependence was modelled in the form $\mathrm{AR} = \mathrm{AR}(\beta_{\mathrm{Pr}}) = c_1/\beta_{\mathrm{Pr}} + c_2/\beta_{\mathrm{Pr}}^2$.

To determine the coefficients in the function $\mathrm{AR}(\beta_{\mathrm{Pr}})$, a least squares fit to Pramila's tabulated data was performed using the method of normal equations (see Appendix 4). The variable $x = \beta_{\mathrm{Pr}}$, and (x_j, f_j) are the tabulated (β_{Pr}, AR) pairs. We used the functions $\phi_1(x) = 1/x$ and $\phi_2(x) = 1/x^2$. The coefficients $c_1 = 0.1387$ and $c_2 = 0.5318$ were obtained. Alternative forms, with just the first term $1/x$, and a three-term form including $1/x^3$, were also tried. The two-term form given here was found to produce the most satisfactory fit.

In Figure 53, the curve marked as eq. (16) corresponds to an added-mass model modifying all three masses (local inertia, Coriolis and centrifugal), while

the one labelled as eq. (22) corresponds to a model modifying only the local inertia mass.

For convenience, the equations (16) and (22) from Pramila (1987), converted to our notation, are reproduced below. The real part of the complex eigenfrequency, in both cases, is zero. The imaginary parts are:

$$s_{\mathrm{Im}}^{(\mathrm{Pr},\,16)} = \left[1 - \frac{(m+m_a)}{T} V_0^2\right] \cdot \sqrt{\frac{T}{m+m_a}} \cdot \frac{1}{4\ell} \tag{212}$$

$$s_{\mathrm{Im}}^{(\mathrm{Pr},\,22)} = \frac{1 - \frac{m}{T} V_0^2}{\sqrt{1 + \frac{m_a}{m} - \frac{m_a}{T} V_0^2}} \cdot \sqrt{\frac{T}{m}} \cdot \frac{1}{4\ell}\,, \tag{213}$$

where the superscript on the left-hand side corresponds to Pramila's equation numbering. Note that we use 4ℓ instead of Pramila's 2ℓ, because in our notation ℓ denotes the half-length of the span. In both equations, (212) and (213), the added mass m_a is computed as

$$m_a = 2\ell\, \rho_f\, \beta_{\mathrm{Pr}}\,, \tag{214}$$

where we similarly use 2ℓ instead of Pramila's ℓ.

For the eq. (16) model, all three added masses are equal. Note that Pramila used mass per unit length in his study (Pramila, 1987), whereas we use mass per unit area. Because the frequency expressions contain only ratios of the parameters, the width can be cancelled out and the results are directly comparable, once the span length and time scaling are taken into account.

Our model at $v_\infty = 0$ agrees closely with Pramila's eq. (22) one, as expected. From the discretization (168) we see that in this case, only the matrix a_{jn} has an effect. This corresponds in first approximation to a local inertia mass increase. The magnitude of the decrease in eigenfrequency is similar to that reported by Pramila (about 75% according to Pramila, 1986). For a certain aspect ratio (AR $\approx$ 3.1989, $\beta_{\mathrm{Pr}} = 0.43$), the predictions coincide for the problem parameters used.

In the case $v_\infty = V_0$, the models qualitatively agree. If we again use $\beta_{\mathrm{Pr}} = 0.43$ for Pramila's model, we see that the prediction given by our model for the critical velocity is approximately 60% higher than that from the corresponding added-mass approach (Pramila's eq. (16)). On the other hand, if the value $\beta_{\mathrm{Pr}} = 0.18$ (corresponding to AR $\approx$ 17.1850) is used, then the predictions of critical velocity agree, but the eigenfrequency given by the added-mass model is approximately 60% higher. Values of β_{Pr} between these two cases produce results that vary continuously from the first case to the second. See Figure 53 for an example. It is seen that the primary difference between the present functional approach and the classical results being compared, as far as the lowest eigenfrequency is concerned, is that the predictions change in the case where all three inertia terms are modified. The aspect ratio never explicitly enters this model, so which prediction differs more, depends on the aspect ratio.

This effect has a simple mathematical explanation. In Pramila's eq. (16), changing the added mass changes the scaling of both axes equally. For each pair of added-mass curves in Figure 53, it is seen that the axis intersection points of

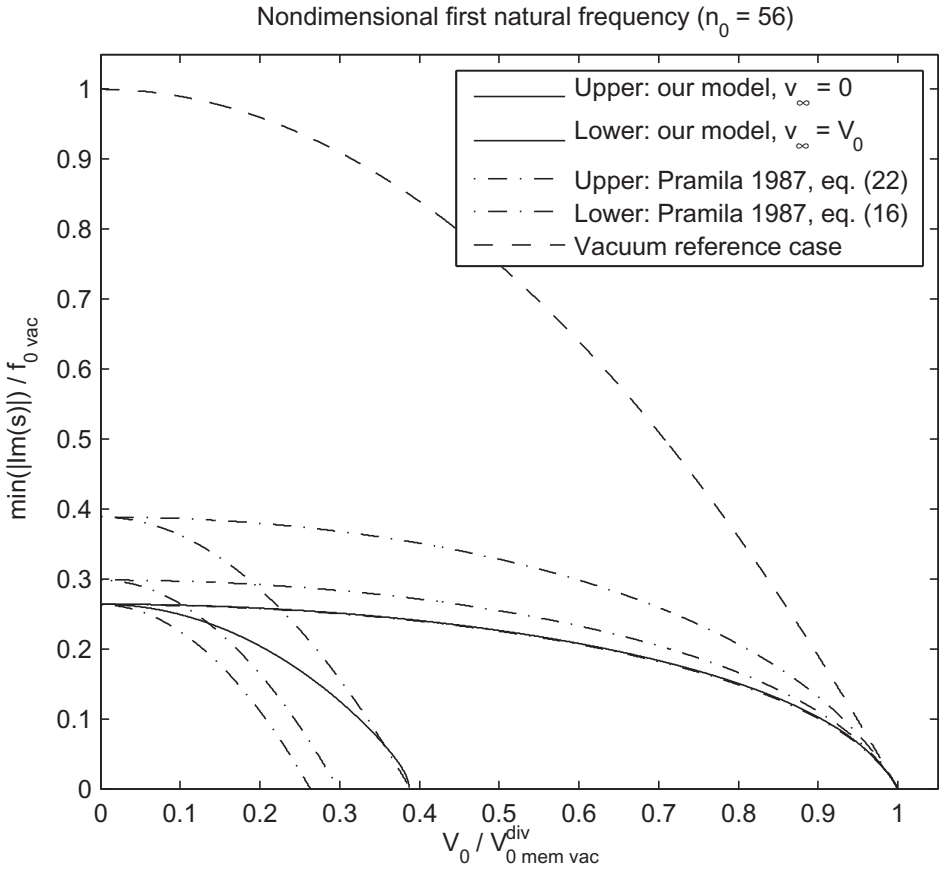

FIGURE 53 Behaviour of the nondimensional first natural frequency as a function of the nondimensional velocity of the panel. Normalized by the axis intersecting values in vacuum. For the upper solid line, fluid velocity $v_\infty = 0$. For the lower solid line, $v_\infty = V_0$, i.e. the air mass moves with the web. For comparison, the vacuum case (dashed line) and three pairs of results corresponding to Pramila's added-mass formulas (dash-dot lines) from the study Pramila (1987) are shown. Each pair begins at a single point at $V_0 = 0$. The different pairs correspond to different aspect ratios (AR, length per width). From top to bottom, AR $\approx$ 17.1850 ($\beta_{\mathrm{Pr}} = 0.18$); AR $\approx$ 5.1064 ($\beta_{\mathrm{Pr}} = 0.3275$); and AR $\approx$ 3.1989 ($\beta_{\mathrm{Pr}} = 0.43$; in this particular case, the upper curves coincide). The symbol β_{Pr} refers to the β value of Pramila (1986, Table II). See also Figure 67 on p. 203 for a view in the $(V_0,\, v_\infty)$ plane. Axis intersection point for $v_\infty = V_0$ in our model is given as λ^{div} in Table 2 (p. 167).

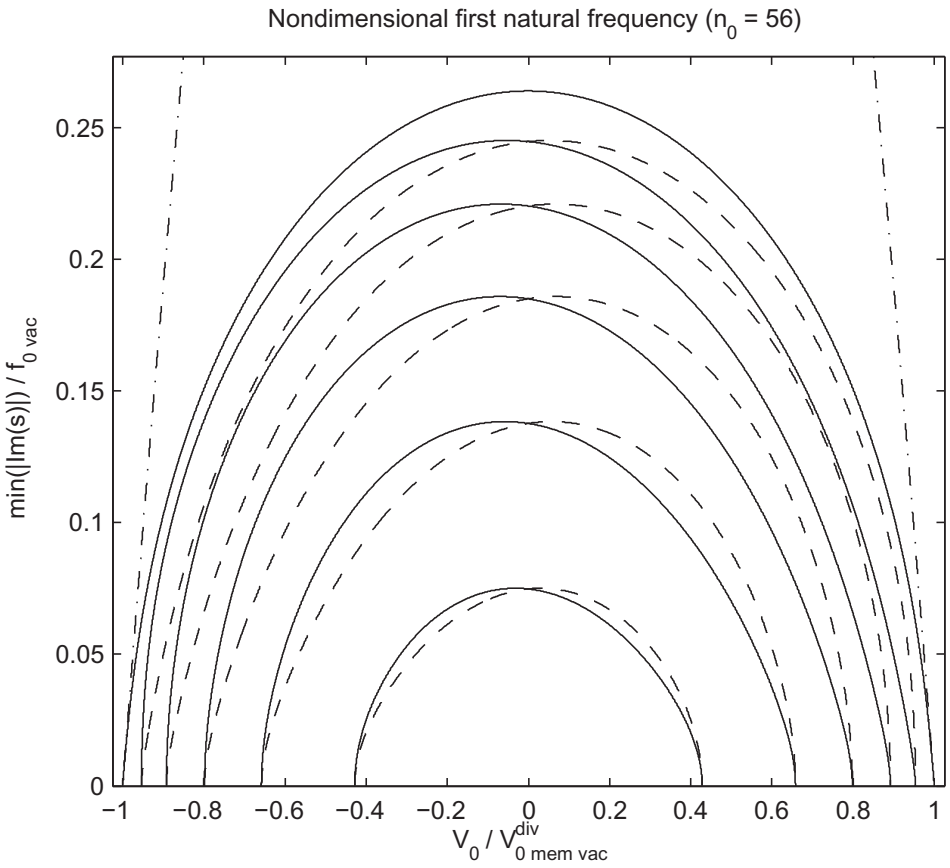

FIGURE 54 Behaviour of the nondimensional first natural frequency as a function of the nondimensional velocity of the panel. Normalized by the axis intersecting values in vacuum. The vacuum case is partly shown for comparison (dash-dot line). Solid lines indicate $v_\infty \geq 0$, dashed lines $v_\infty < 0$. From top to bottom, the absolute values of the fluid velocities are 0 (corresponds to upper solid line of Fig. 53), 10 ($\theta \approx 0.13$), 15 ($\theta \approx 0.19$), 20 ($\theta \approx 0.25$), 25 ($\theta \approx 0.32$), and 30 m/s ($\theta \approx 0.38$). Note the scaling of the vertical axis. See also Figure 67 on p. 203 for a view in the (V_0, v_∞) plane. See values λ^{div} in Table 2 (p. 167) for the axis intersection points.

the curve corresponding to Pramila's eq. (16) are equal. The present model does not make any such assumption, and thus the scalings, which arise naturally by solving the integro-differential equation, may be different. To summarize, the fact that we may match either the first natural frequency at $V_0 = 0$, or the critical velocity, but not both, arises from a difference in how mass is handled in the two models.

The equal scaling is not an inherent limitation of the added-mass approach, but is due to the specific form of Pramila's eq. (16). See Chang et al. (1991) for a discussion on how different (but still constant) added masses in each term affect the eigenfrequency behaviour. For an approach utilizing boundary layer theory to compute added masses as functions of x, also resulting in different scalings for the axes, see Frondelius et al. (2006).

In addition to the two classical cases presented in Figure 53, our model opens the possibility for studying the problem with an arbitrary axial flow velocity for the surrounding air. In Figure 54, we have plotted first eigenfrequency curves similar to those in Figure 53 for several different fluid velocities v_∞. The normalization procedure is the same as in Figure 53.

Note that as is evident from Figure 54, if v_∞ is nonzero and independent of V_0, the eigenfrequency curves are no longer symmetric with respect to $V_0 = 0$. This reflects the asymmetry in the physics of the situation: the velocities V_0 and v_∞ can have either the same or different signs. We will see by consideration of the higher eigenfrequencies, in subsection 6.3.3, that the effect of the asymmetry on the eigenfrequency spectrum is much more dramatic than Figure 54 alone would suggest. (Compare, especially, Figures 60–61 and 62–63 for different signs of V_0 in the asymmetric case.)

6.3.3 Numerical results: higher eigenvalues

In this final numerics section, let us solve the flutter problem (206) for the main topic of this study. As was explained above, we will use Fourier–Galerkin for the space discretization. For tracking the solutions, we will use both the Taylor and MAC based methods (in the Figures, it will be indicated which method was used).

Since no analytical algorithm is known for producing this solution, we will simply assume that the observed general properties of the Fourier–Galerkin discretization of a moving string carry over to this more complex case, and apply the same validity flagging algorithm as in the moving string example. In the flagging, the "correct" solutions are chosen as having the n_0 lowest (i.e. $\min |\mathrm{Im}\,\cdot|$) eigenfrequencies at $V_0 = 0$. The rest is handled by continuity and collision detection, as discussed.

For legibility of plots, we use $n_0 = 10$. The rest of the parameters are the same as for the first eigenfrequency computations (bending rigidity $D = 0$; for the rest, refer to Table 1 on page 155).

In all the 3D plots in this Section, the blue (dark) lines denote parts of the solution flagged as correct; red (light) lines denote parts flagged as numerical

artifacts. The axes are $(V_0, \operatorname{Re} s, \operatorname{Im} s)$. No scaling has been applied; the raw data values are shown as-is. Although the plots are shown at an angle to better display their qualitative structure, in each Figure the eigenfrequencies start with $\operatorname{Re} s_j = 0$ (for all j) at $V_0 = 0$.

In some Figures, we will show the filtered data, containing only the part of the solution flagged as correct. In this case, the 3D plot will have only the blue (dark) lines. For these plots, as in subsection 2.2.5, we will also show projections onto the $(\lambda, \operatorname{Re} s)$ and $(\lambda, \operatorname{Im} s)$ planes. Both projections are plotted into the same image, with red (dark) lines denoting the real parts and blue (light) lines the imaginary parts.

Numerical solutions are shown for three cases. First, in Figures 55–57, the fluid free-stream velocity $v_\infty = 0$. Second, in Figures 58–63, we have taken $v_\infty = 20$ m/s. This case is asymmetric in V_0 due to the asymmetry of the physics, as was noted further above; the velocities V_0 and v_∞ may have either the same or different signs. These Figures together cover both situations. Finally, in the third case, $v_\infty = V_0$, i.e. it is assumed that the whole air mass moves axially with the panel. This situation is shown in Figures 64–66. Compare these plots to the previous Figures 53–54, which show only the first eigenfrequency up to the lowest critical velocity.

If the correct and incorrect solutions were classified correctly, it seems by the spectra illustrated here that the moving panel with $v_\infty = 0$, in the membrane limit, has no instability at its first critical point (V_0 such that $s = 0$). If the free stream of air moves at a given axial velocity v_∞, the panel experiences a lowest-mode divergence state at the first critical point for both positive and negative V_0, even in the membrane limit. It seems this happens already at relatively low free-stream velocities; $v_\infty = 1$ m/s was also tested and found to exhibit this effect.

In the case where the air mass moves with the web, a lowest-mode divergence state is likewise formed at the first critical point. By the ideal fluid model, the existence of time-harmonic instability seems to depend on whether the free stream is stationary (in laboratory coordinates) or not.

For this phenomenon, it does not matter whether the free-stream velocity is a separate parameter, or fixed to the web velocity. This has a natural mathematical explanation. In the (V_0, v_∞) plane, fixing $v_\infty = V_0$ explores a line angled at 45°, passing through the origin. Both velocities are still parameters with given, constant values for each eigenvalue problem solved. Fixing v_∞ and varying only V_0 explores lines angled at 0° (horizontally) in this same plane. See Figure 67 for an illustration. The critical point for the 45° line corresponds to the critical point of one of the 0° lines. Similarly, any point at a distance ε from the critical point along this line corresponds to a point in one of the other solutions.

In reality, because of the boundary layer, some of the air indeed moves with the web, so extrapolating from the present model, an instability can be expected in practice (although this is by no means a rigorous argument).

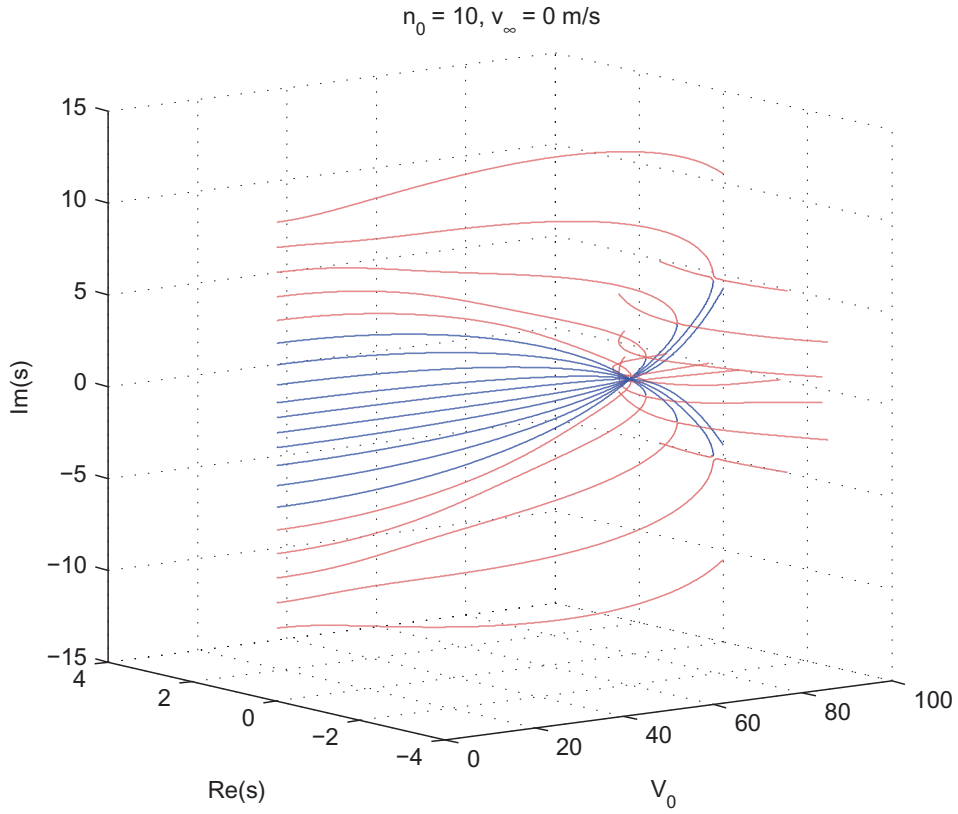

FIGURE 55 Spectrum of axially moving panel submerged in ideal fluid. Fluid free-stream velocity $v_\infty = 0$. Full solution, Fourier–Galerkin discretization with MAC tracking. Blue (dark) line denotes parts of solution flagged as correct, red (light) line parts flagged as numerical artifacts. See Figure 56 for some zoom-ins of the same data.

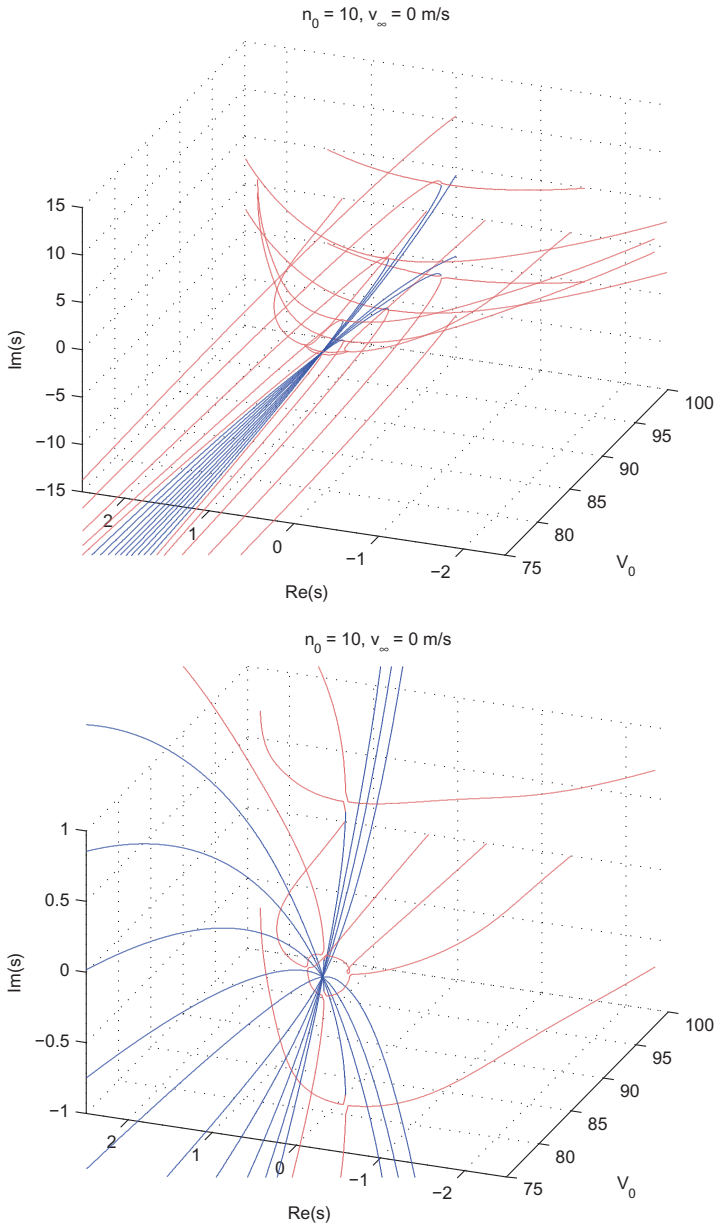

FIGURE 56 Spectrum of axially moving panel submerged in ideal fluid. Fluid free-stream velocity $v_\infty = 0$. MAC tracking. Detail near critical velocity. Two zoom-ins of data in Figure 55. At the bottom, the vertical direction has been zoomed further in; other axes have the same scaling in both pictures. Blue (dark) line denotes parts of solution flagged as correct, red (light) line parts flagged as numerical artifacts.

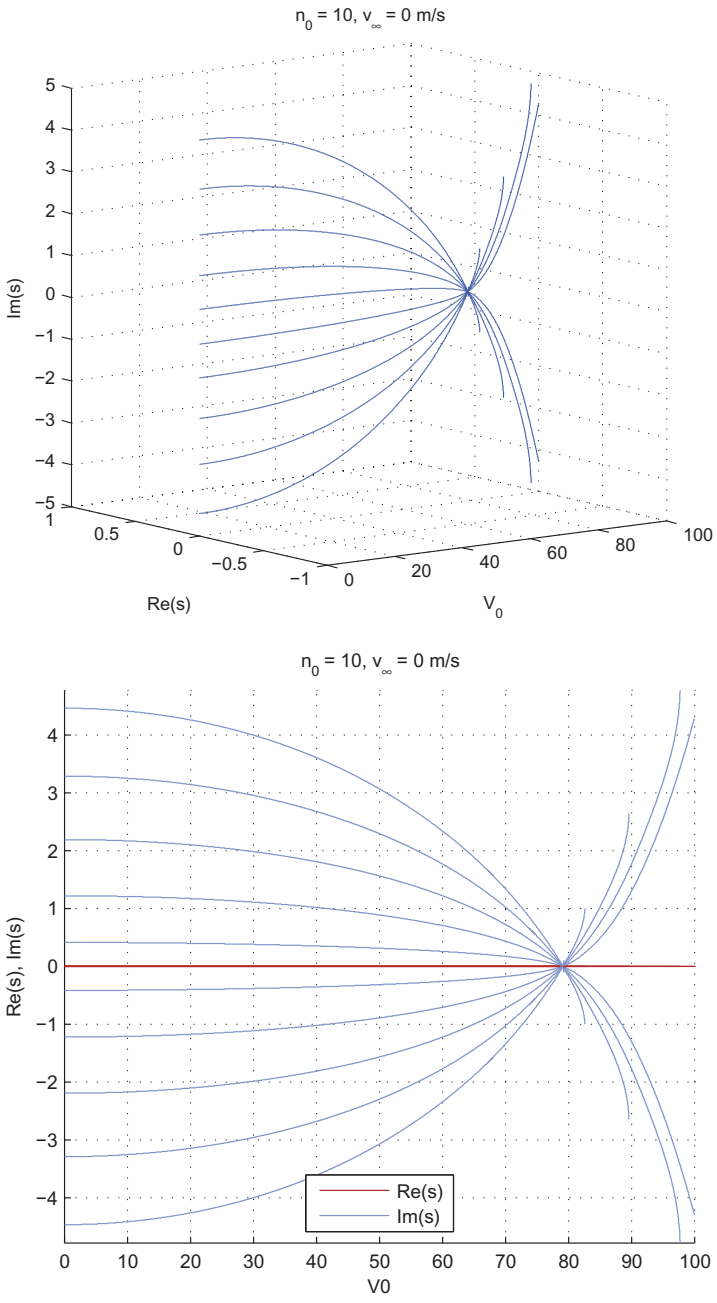

FIGURE 57 Spectrum of axially moving panel submerged in ideal fluid. Fluid free-stream velocity $v_\infty = 0$. After filtering; only parts flagged as correct are shown. Fourier–Galerkin discretization with MAC tracking. In the projection, blue (light) line denotes imaginary part, red (dark) line real part. Note that Re $s \equiv 0$.

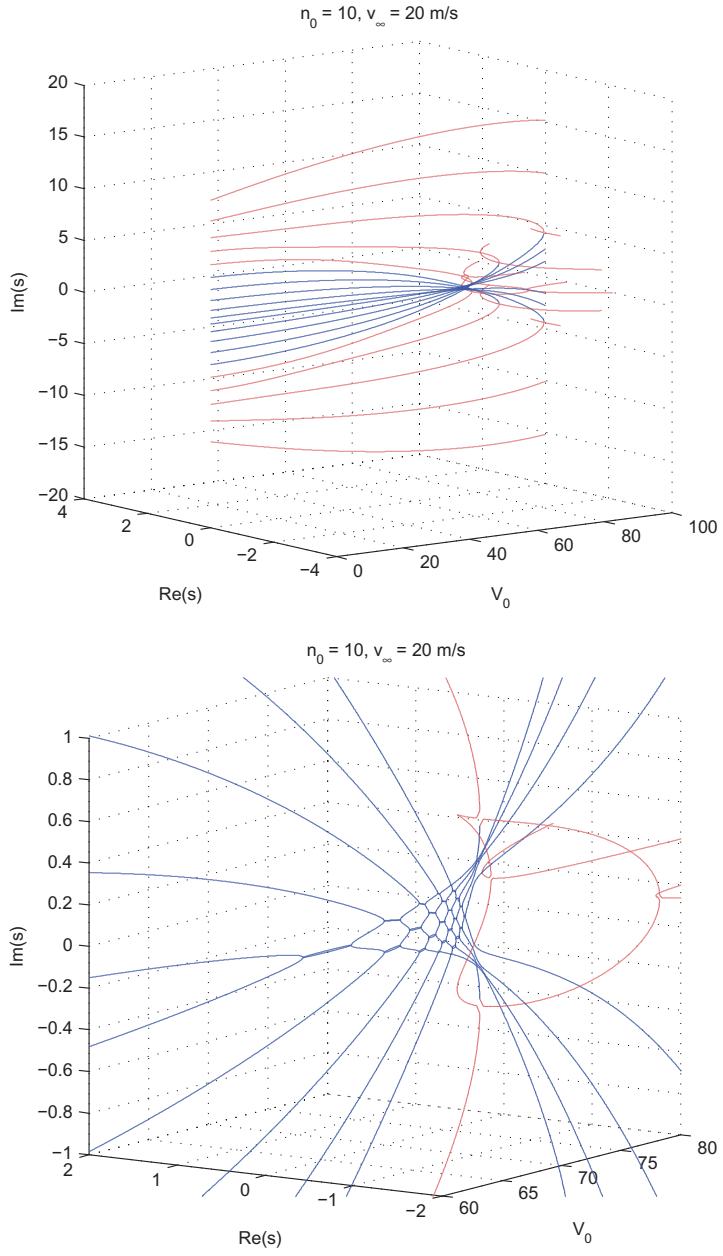

FIGURE 58 Spectrum of axially moving panel submerged in axially flowing ideal fluid. Fluid free-stream velocity $v_\infty = 20$ m/s. Solution for positive V_0. MAC tracking. Blue (dark) line denotes parts of solution flagged as correct, red (light) line parts flagged as numerical artifacts. *Top*: Full solution (Fourier–Galerkin). *Bottom*: Detail near critical velocity.

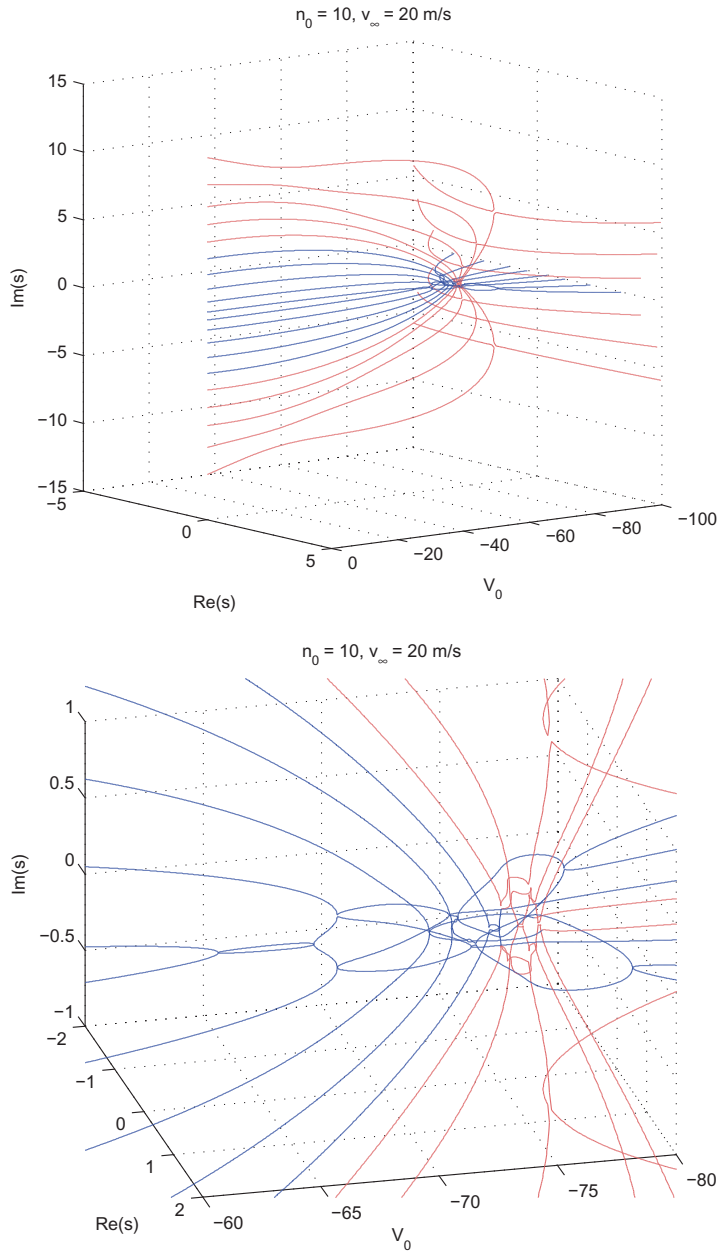

FIGURE 59 Spectrum of axially moving panel submerged in axially flowing ideal fluid. Fluid free-stream velocity $v_\infty = 20$ m/s. Solution for negative V_0. Taylor tracking. Blue (dark) line denotes parts of solution flagged as correct, red (light) line parts flagged as numerical artifacts. *Top*: Full solution (Fourier–Galerkin). *Bottom*: Detail near critical velocity.

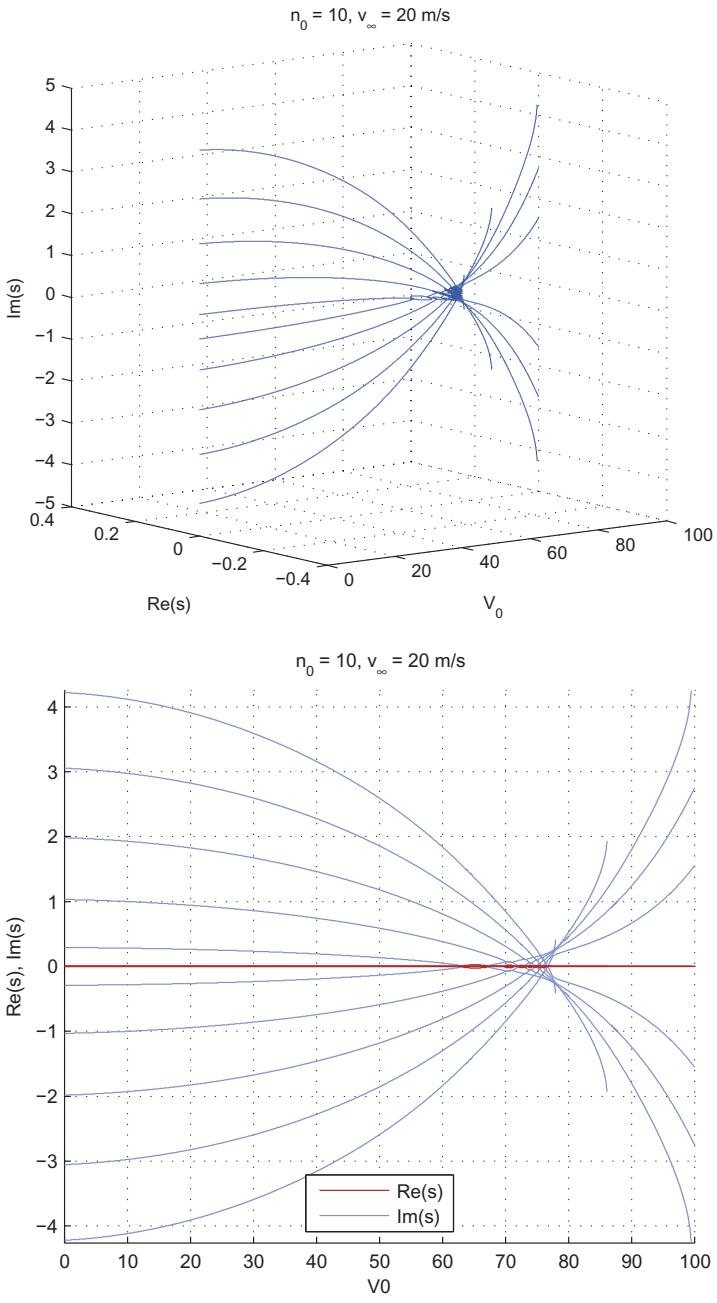

FIGURE 60 Spectrum of axially moving panel submerged in ideal fluid. Fluid free-stream velocity $v_\infty = 20$ m/s. Solution for positive V_0. After filtering; only parts flagged as correct are shown. Fourier–Galerkin discretization with MAC tracking. In the projection, blue (light) line denotes imaginary part, red (dark) line real part.

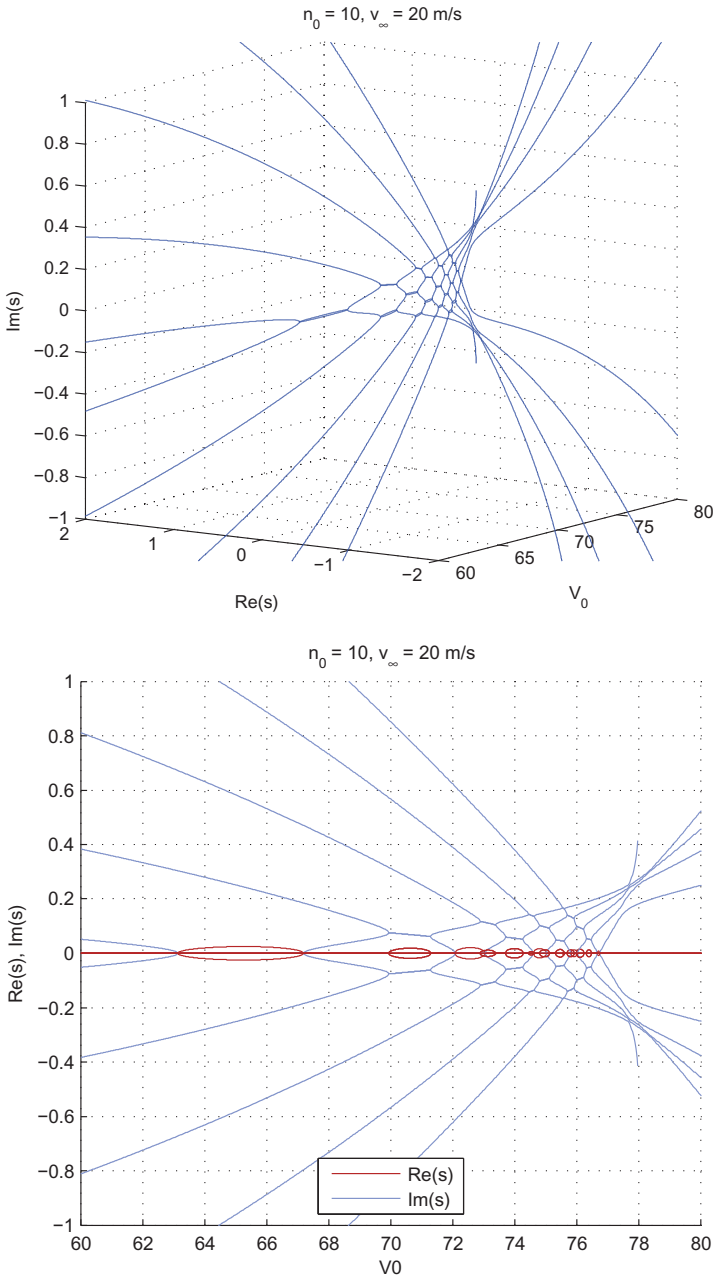

FIGURE 61 Spectrum of axially moving panel submerged in ideal fluid. Fluid free-stream velocity $v_\infty = 20$ m/s. Solution for positive V_0. Detail near critical velocity. After filtering; only parts flagged as correct are shown. Fourier–Galerkin discretization with MAC tracking. In the projection, blue (light) line denotes imaginary part, red (dark) line real part.

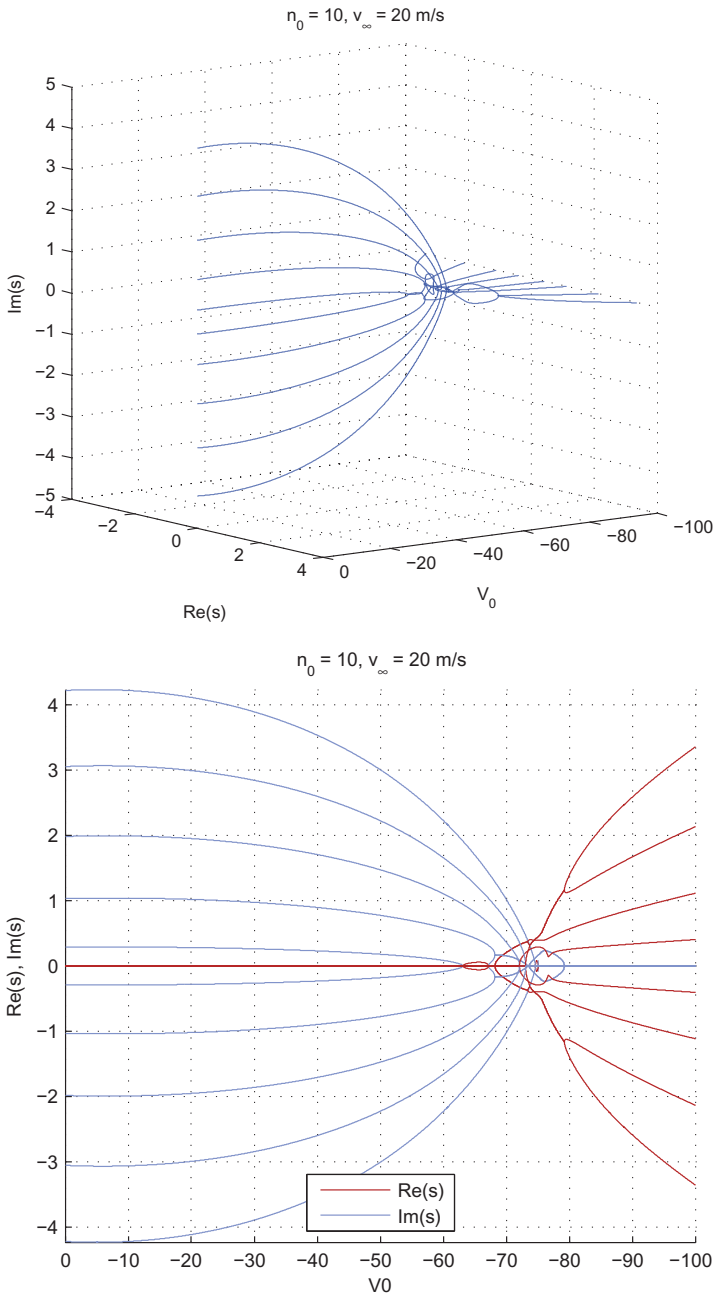

FIGURE 62 Spectrum of axially moving panel submerged in ideal fluid. Fluid free-stream velocity $v_\infty = 20$ m/s. Solution for negative V_0. After filtering; only parts flagged as correct are shown. Fourier–Galerkin discretization with Taylor tracking. In the projection, blue (light) line denotes imaginary part, red (dark) line real part.

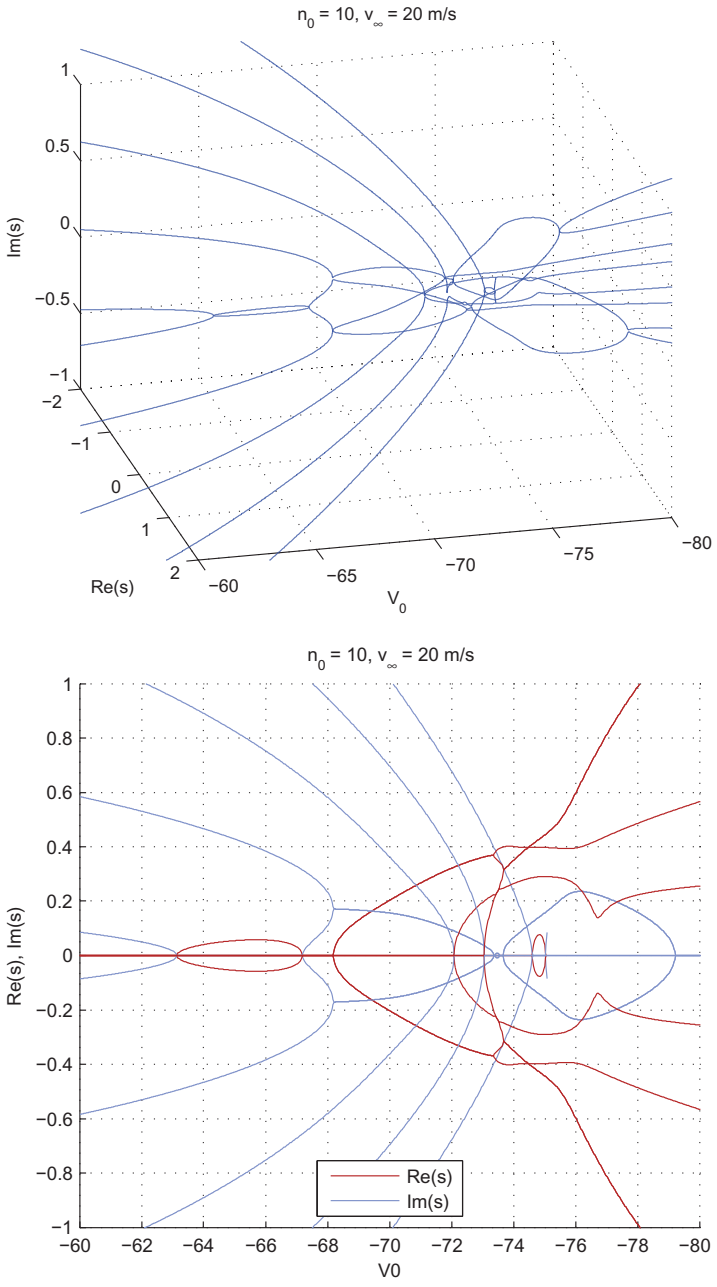

FIGURE 63 Spectrum of axially moving panel submerged in ideal fluid. Fluid free-stream velocity $v_\infty = 20$ m/s. Solution for negative V_0. Detail near critical velocity. After filtering; only parts flagged as correct are shown. Fourier–Galerkin discretization with Taylor tracking. In the projection, blue (light) line denotes imaginary part, red (dark) line real part.

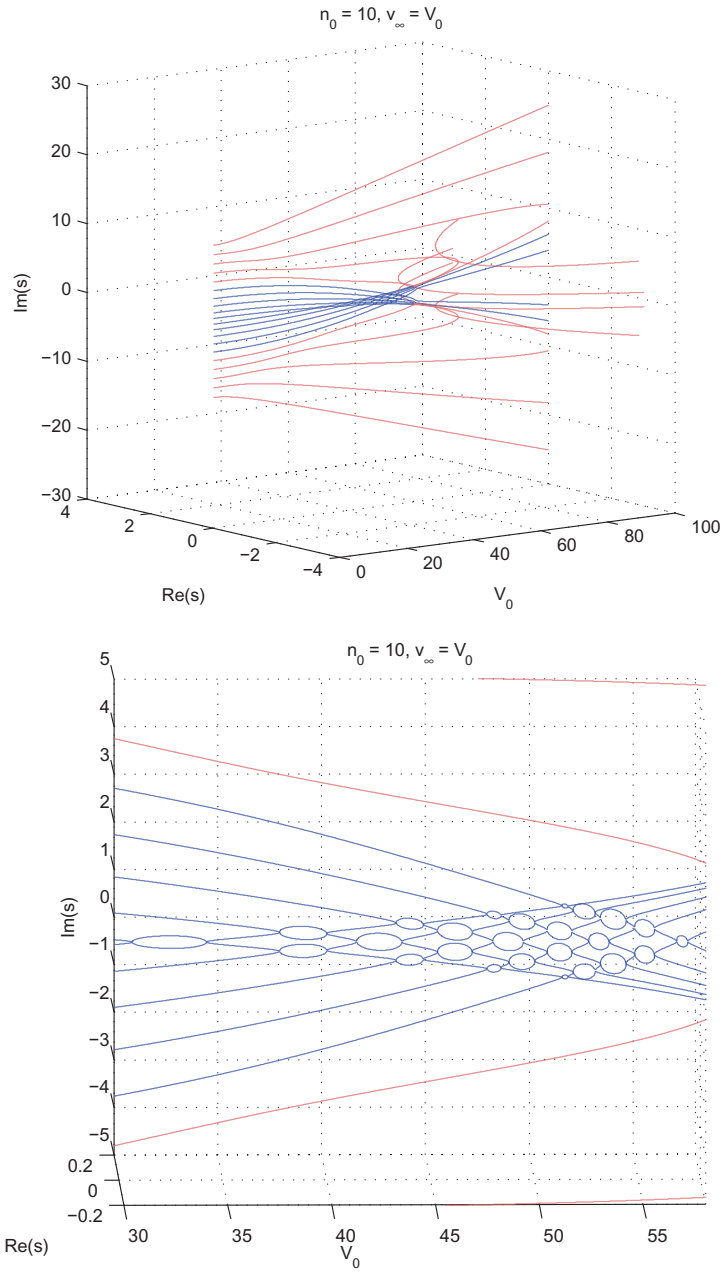

FIGURE 64 Spectrum of axially moving panel submerged in axially flowing ideal fluid. Fluid free-stream velocity $v_\infty = V_0$, i.e. whole air mass moves axially with the panel. Taylor tracking. Blue (dark) line denotes parts of solution flagged as correct, red (light) line parts flagged as numerical artifacts. *Top*: Full solution (Fourier–Galerkin). *Bottom*: Detail near critical velocity.

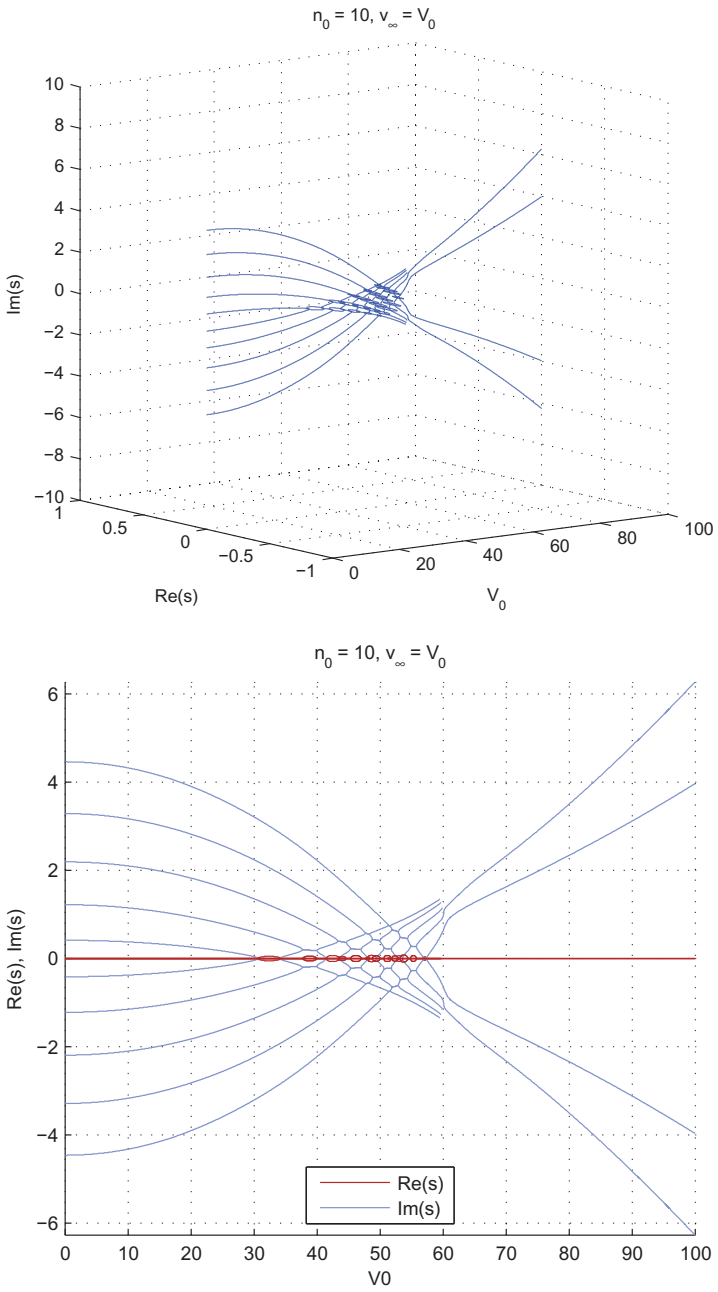

FIGURE 65 Spectrum of axially moving panel submerged in axially flowing ideal fluid. Fluid free-stream velocity $v_\infty = V_0$, i.e. whole air mass moves axially with the panel. Taylor tracking. After filtering; only parts flagged as correct are shown. In the projection, blue (light) line denotes imaginary part, red (dark) line real part.

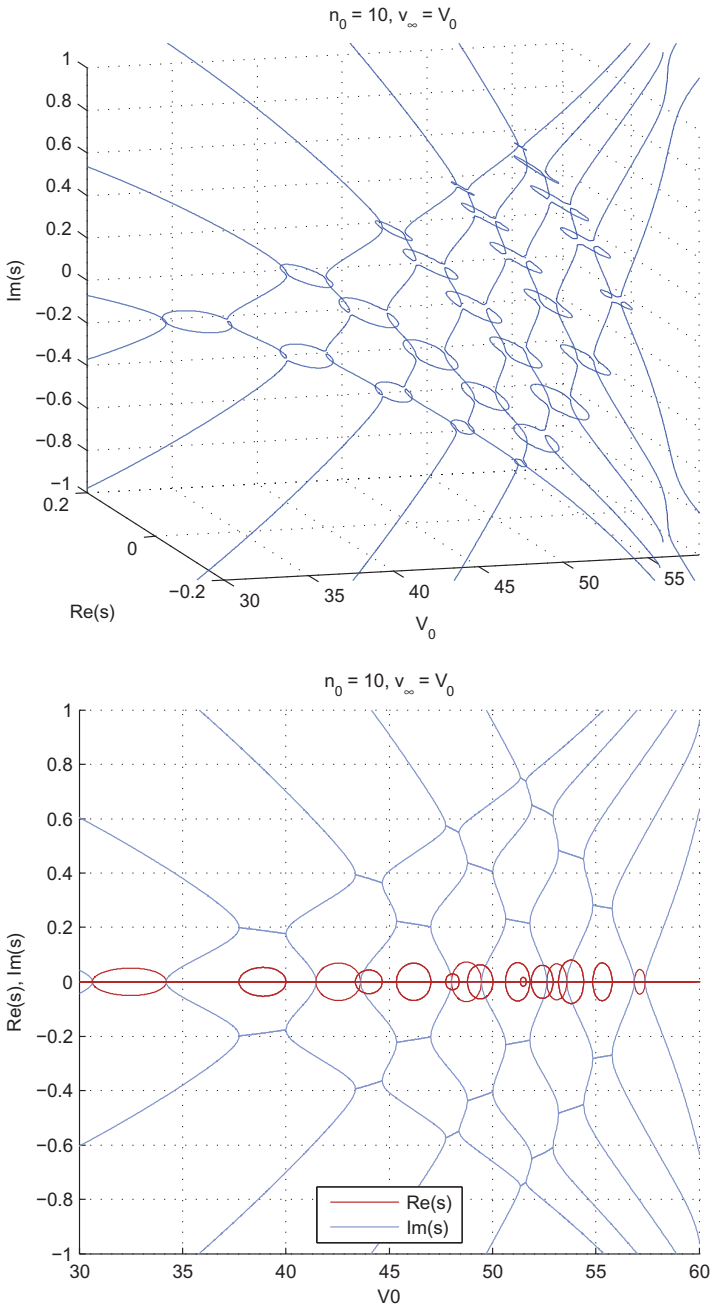

FIGURE 66 Spectrum of axially moving panel submerged in axially flowing ideal fluid. Fluid free-stream velocity $v_\infty = V_0$, i.e. whole air mass moves axially with the panel. Taylor tracking. After filtering; only parts flagged as correct are shown. In the projection, blue (light) line denotes imaginary part, red (dark) line real part. The V_0 grid is not dense enough to pick up the eigenvalue collision points in the 3D view. The elliptical shapes become incomplete toward the right, although the solution identities are tracked correctly.

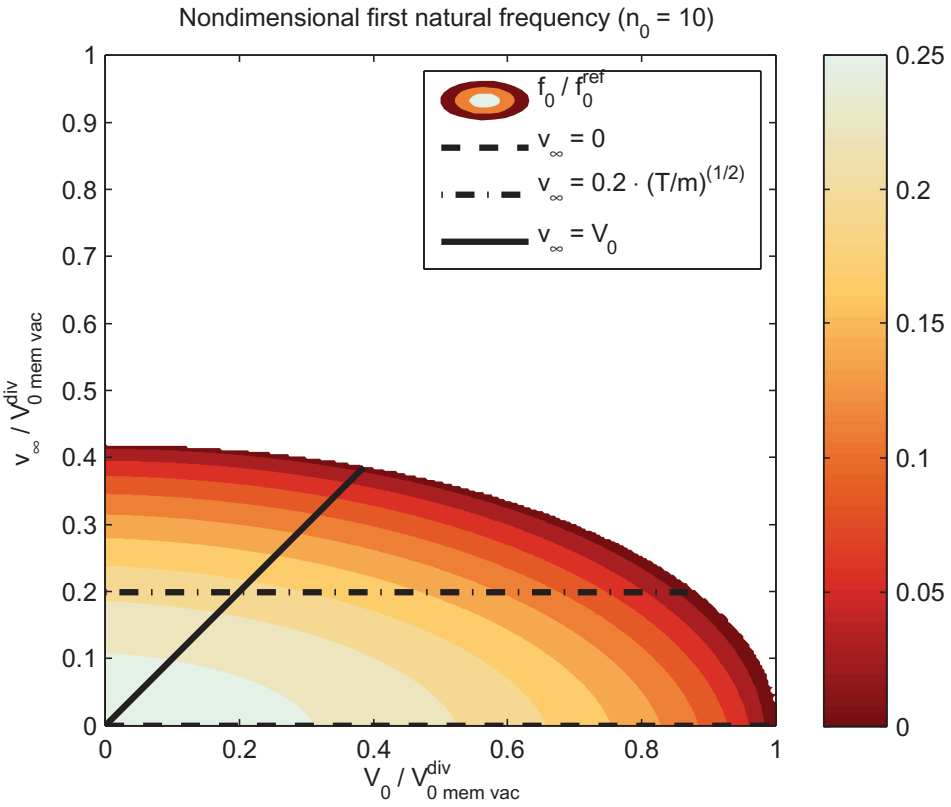

FIGURE 67 View of the lowest eigenfrequency in the (V_0, v_∞) plane, computed using $n_0 = 10$ modes. When v_∞ is a parameter, the spectra (Figures 55–63; also lowest eigenfrequencies in Figures 53–54) are taken along horizontal lines in this plane (two examples indicated). When $v_\infty = V_0$, the spectra (Figures 64–66; also the $v_\infty = V_0$ case in Figure 53) are taken along the indicated line angled at 45°.

Finally, in Figures 68–71 we include some plots of eigenfunctions $W(x)$ at various V_0. The plots are normalized such that the maximum complex amplitude is unity, i.e. $\max_x W(x)\overline{W}(x) = 1$. These were produced by the method given in subsection 6.3.1. In Figure 68, the panel is in vacuum. In Figure 69, stationary ideal fluid is added. In Figure 70, the fluid moves at $v_\infty = 20$ m/s. The last case shown is Figure 71, where $v_\infty = V_0$, i.e. the whole air mass moves axially with the panel.

The complex conjugate structure of the eigenfunction pairs is clearly visible in the figures. If (s, W) are an eigenvalue-eigenfunction pair, then so are $(\overline{s}, \overline{W})$. The functions at $V_0 = 0$ are the same for the vacuum case, for $v_\infty = 0$, and for the case $v_\infty = V_0$ (which, for $V_0 = 0$, reduces to the previous case). If v_∞ is nonzero, the eigenfunctions become different even for $V_0 = 0$ (Figure 70, left; compare the left column of the other three Figures 68–69, 71).

6.3.4 Summary and conclusion

In the eigenfrequency analysis, both the panel (V_0) and fluid (v_∞) velocities were considered as given problem parameters. Eigenfrequencies were studied parametrically, and some examples of eigenmodes were plotted.

The tracking algorithms developed in Chapter 5 were used to produce continuous eigenfrequency curves out of randomly ordered eigenvalue data. The effectiveness of those algorithms on the present problem was thus demonstrated. Furthermore, the flagging approach was used to help filtering the solution, in order to show just the correct parts.

Here we return to the question of the accuracy of the discretization. As was seen in Chapter 5, discretization may introduce artificial instabilities in the problem for the eigenfrequency spectrum.

In the present analysis, this issue was handled in a practically oriented manner, by analogy with the moving string problem. It was assumed that the lowest n_0 modes are reproduced correctly. The tracking and flagging approaches developed in Chapter 5 were used to classify parts of the solution as either correct, or as numerical artifact.

The assumption seems reasonable, as the two problems are (loosely speaking) similar, and it is supported by the qualitative aspects of the obtained numerical results. The flutter modes that were judged as spurious by the algorithms, look qualitatively very similar to the spurious flutter modes of the moving ideal string problem (Section 5.1).

The discrete eigenfrequency spectrum of the system was solved in three cases: zero free-stream fluid velocity ($v_\infty = 0$), nonzero free-stream fluid velocity (as an example, $v_\infty = 20$ m/s was used), and with the whole air mass following the panel ($v_\infty = V_0$). The eigenfrequencies were visualized using the same kind of plots as for the damped string in subsection 2.2.5. This was done to facilitate direct comparison.

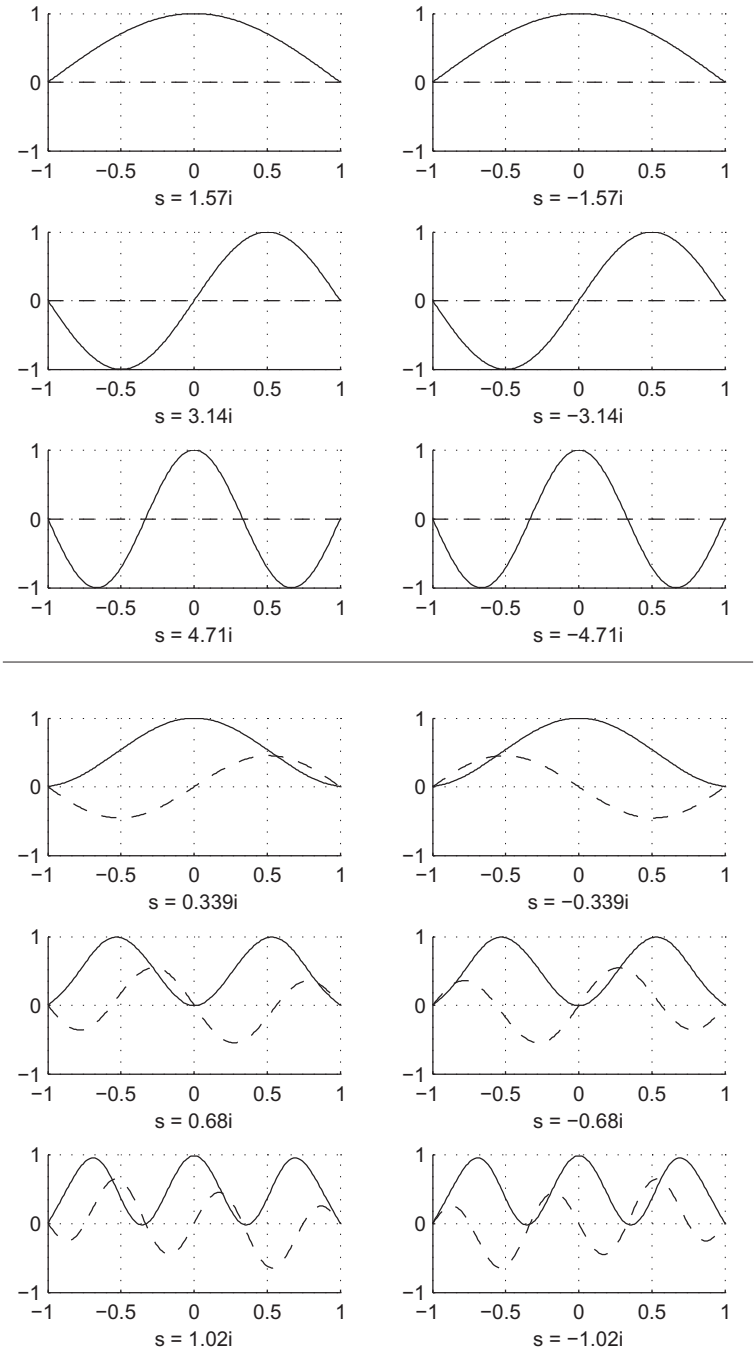

FIGURE 68 Lowest free vibration eigenmodes of an axially moving panel. Vacuum case. Horizontal axis dimensionless x, vertical axis $w(x)$. Solid line is real part, dashed line imaginary part. *Top*: $V_0 = 0$. *Bottom*: $V_0 = 70$ m/s (near critical, $V_{0D} = \sqrt{T/m} = 79.0569$ m/s).

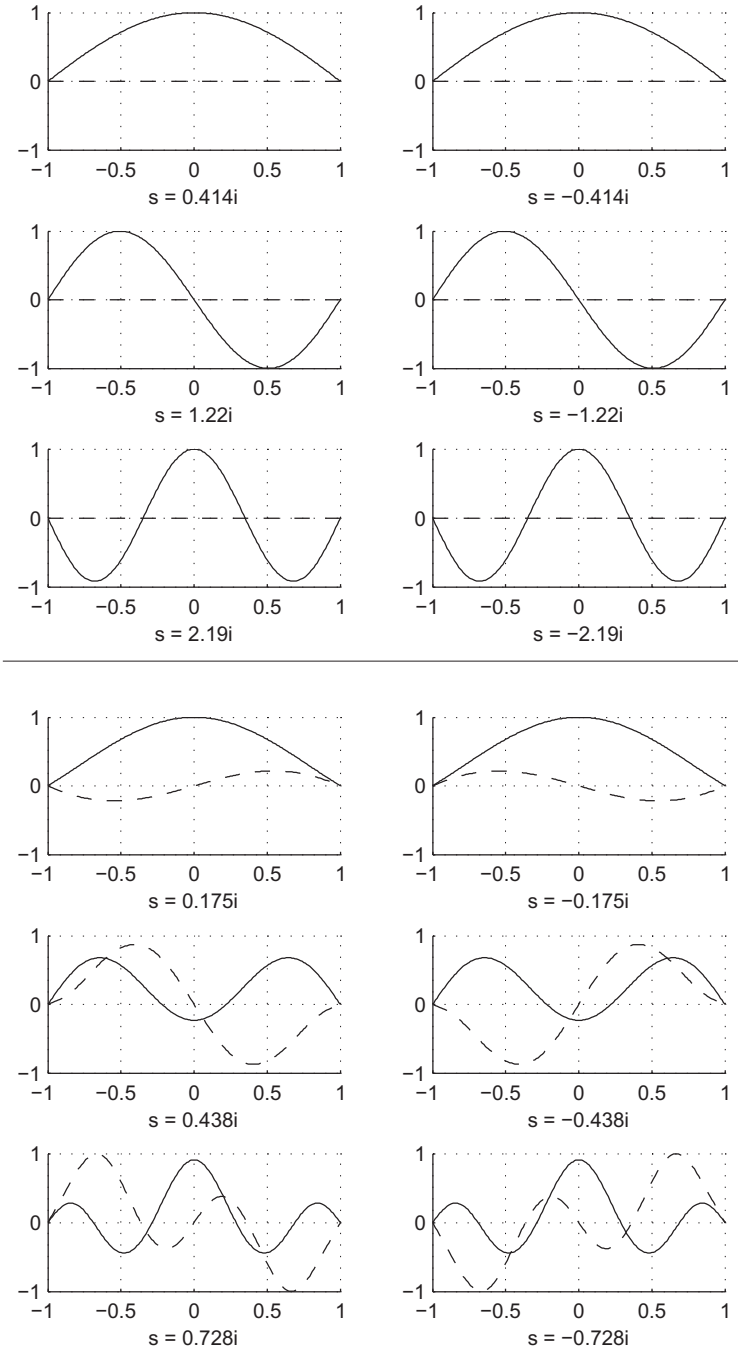

FIGURE 69 Lowest free vibration eigenmodes of an axially moving panel submerged in ideal fluid. Fluid free-stream velocity $v_\infty = 0$ (stationary fluid). Horizontal axis dimensionless x, vertical axis $w(x)$. Solid line is real part, dashed line imaginary part. *Top*: $V_0 = 0$. *Bottom*: $V_0 = 70$ m/s (near critical, $V_{0D} = \sqrt{T/m} = 79.0569$ m/s).

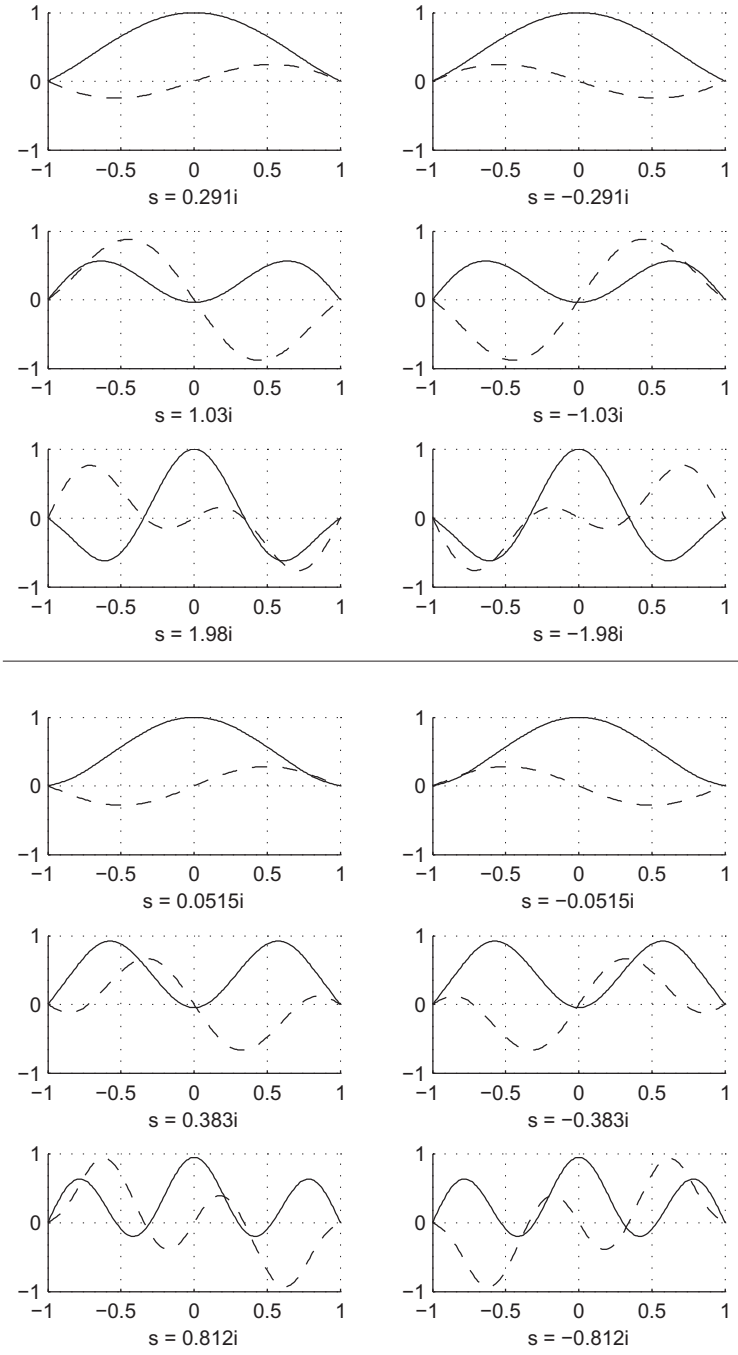

FIGURE 70 Lowest free vibration eigenmodes of an axially moving panel submerged in axially flowing ideal fluid. Fluid free-stream velocity $v_\infty = 20$ m/s. Horizontal axis dimensionless x, vertical axis $w(x)$. Solid line is real part, dashed line imaginary part. *Top*: $V_0 = 0$. *Bottom*: $V_0 = 60$ m/s (near critical; from steady-state problem, $V_0^{\text{crit}} \approx 63.098$ m/s).

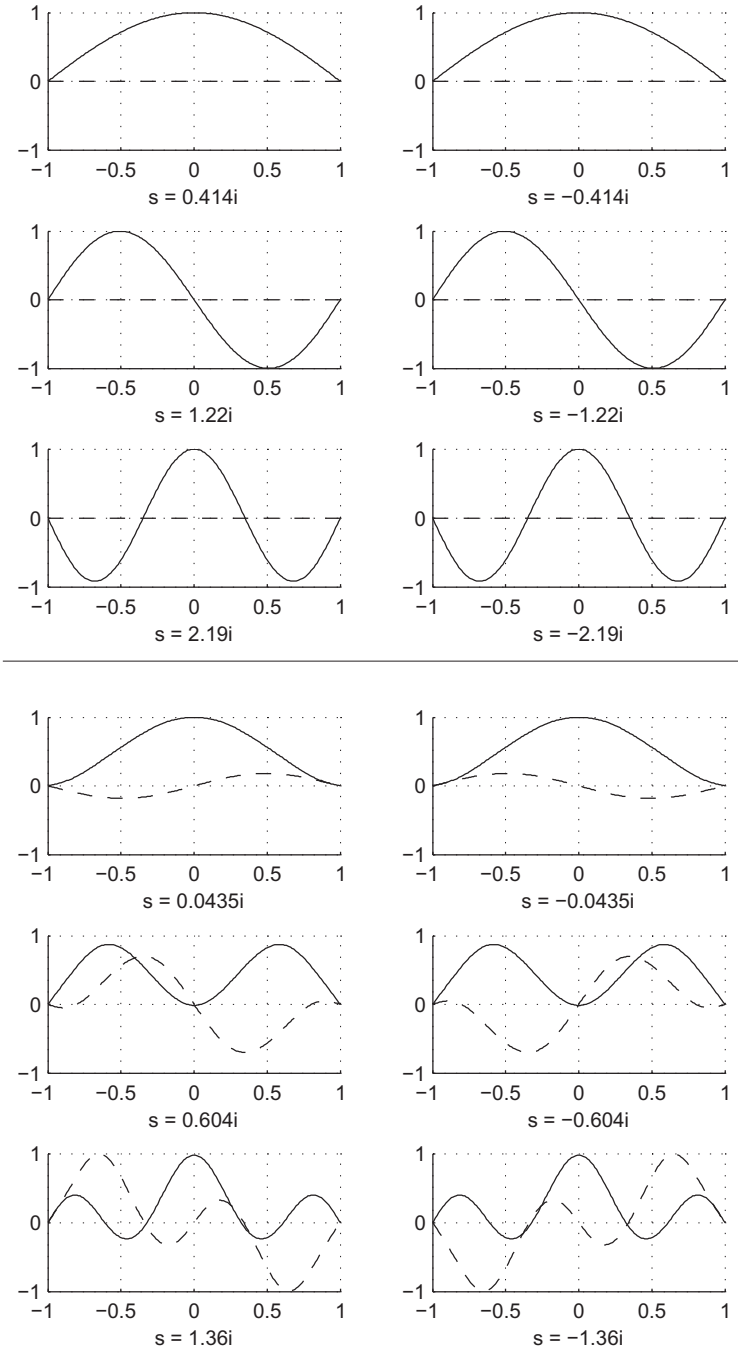

FIGURE 71 Lowest free vibration eigenmodes of an axially moving panel submerged in axially flowing ideal fluid. Fluid free-stream velocity $v_\infty = V_0$, i.e. whole air mass moves axially with the panel. Horizontal axis dimensionless x, vertical axis $w(x)$. Solid line is real part, dashed line imaginary part. *Top*: $V_0 = 0$. *Bottom*: $V_0 = 30$ m/s (near critical, $V_0^{\text{crit}} \approx 30.607$ m/s).

From the present model at the membrane limit ($D = 0$), it was found that if $v_\infty = 0$, there is no instability, but in all other cases a divergence instability is generated at the lowest critical velocity.

In the case where v_∞ has a given nonzero value, it was found that the spectrum becomes asymmetric with respect to reflection of V_0 through the origin. This is due to the asymmetry in the physics of the situation; the velocities v_∞ and V_0 may have either the same or different signs. Near the critical velocity, the spectrum looks completely different for different signs.

For the case $v_\infty = V_0$, very nontrivial eigenvalue interaction (Figure 66) was observed in the postcritical regime. Of course, strictly speaking (see e.g. Païdoussis, 2005) this is outside the region of validity of the linear model, since an instability exists at the lowest critical velocity. However, with both models taken as mathematical objects, it is interesting to compare this more complex case to the more limited kinds of eigenvalue interaction observed for the damped string model in subsection 2.2.5.

Returning to the physics, an important qualitative difference was found between classical added-mass models and the present model. As was noted earlier (Section 3.6), added-mass models with constant coefficients always behave qualitatively exactly like the corresponding vacuum model. Thus, if there is no bending rigidity (membrane limit), there will be no instability at the critical velocity. In contrast, the introduction of the exact analytical aerodynamic reaction, which changes the form of the equation, may change the stability (in the sense of initial postbuckling) predictions, by qualitatively changing the behaviour of the eigenfrequency spectrum of the model. We investigated the eigenfrequency spectra at the membrane limit, and indeed observed the introduction of an instability at the lowest critical panel velocity for nonzero free-stream velocities.

In reality, some of the surrounding air will move with the web due to the boundary layer. Thus, the present model suggests that an instability at the critical velocity is likely to occur in practice.

7 SUMMARY AND CONCLUSION

In this thesis, the dynamical behaviour and stability of a moving panel submerged in ideal fluid was considered, with the application of paper production in mind. In any practical paper machine, mechanical stability of the moving paper web is important in order to avoid web breaks, for both technological and economical reasons. Open draws always exist; hence the motion of the web while it travels between supporting rollers is of interest.

The interaction between the travelling material and the surrounding air is especially important for lightweight materials, such as paper. It is not sufficient to consider only the dynamics of the travelling material, but the behaviour of the surrounding airflow must also be analyzed, and its effects on the material fed back into the dynamical model. The coupling changes the dynamics, which, in turn, affects the surrounding flow.

The presentation started from simplified models, in order to give some context for technical readers from a variety of backgrounds. The analytical free vibration solution was determined for the travelling ideal string, and for the damped, travelling string. The eigenfrequency spectra of both were visualized, to give some insight into the behaviour of problems in the present class; albeit with the important difference that the damped string does not conserve energy, while our main model does.

An analytical solution for the airflow problem was reported in terms of the panel displacement, using the model of potential flow. The solution was used in the fluid-structure interaction model to represent the pressure difference across the web in a mathematically exact manner. This had the further advantage of reducing the fluid-structure interaction model into to a single integro-differential equation, saving computational effort.

The fluid-structure interaction problem was studied with simply supported (pinned) boundary conditions. However, the analytical flow solution is applicable for any boundary conditions for the ends of the moving panel. The presented discretized solution of the moving panel problem can be fairly easily adapted to other Galerkin bases, or to cases with different boundary conditions.

Using Euler's approach for stability analysis and numerical techniques, the

critical velocity of the system was obtained. The critical velocity was analyzed numerically as a function of problem parameters, and validated against some existing studies. These predictions can be used to account for the fundamental, physical stability limit in paper machine design.

Direct temporal simulations of the system dynamics were performed to visualize the time evolution of the system, starting from a given initial condition. The spacetime behaviour was visualized, and briefly studied with respect to the web and air velocities. This was done to give some intuitive understanding of the system behaviour. The cases analyzed were given initial position only, but the approach allows for given initial velocity and given external disturbances (load functions).

The complex eigenfrequencies of the system were determined, and studied parametrically as a function of the web and fluid velocities. By this analysis, it was obtained how the free vibrations of the system behave in different settings. Stability implications were briefly discussed, and it was observed that in the membrane limit, the introduction of the exact analytical aerodynamic reaction qualitatively changes the initial postbuckling behaviour of the model. The results were visualized.

To be able to complete this last item, the two main practical issues in solving and visualizing numerical eigenfrequency spectra were solved. These were the tracking of solution identities in randomly ordered data, and the classification of parts of the solution as correct or as numerical artifact. It was demonstrated that for the simplified problem of the moving string, the discretization introduces spurious flutter modes, which do not exist in the continuum problem.

Two solution tracking algorithms were developed, and their effectiveness was demonstrated on both the moving string and the present problem. The algorithms developed can be applied to a wide variety of eigenvalue problems. The algorithms are useful for visualization, since continuous line plots are easier to read than scatter plots.

The classification problem was solved in a much more limited manner, using a flag-and-track approach (piggybacking on the tracking algorithms). Using this idea requires that the qualitative behaviour of the spectrum of a "nearby" problem is known. For the purposes of the present study, this approach was sufficient.

Returning to the main problem of interest, independent axial motion of the paper web and the free stream were allowed. The model predicted that in all cases, the surrounding air decreases the natural frequencies of the moving panel. Also, if it was assumed that the air mass moves with the web — or if there is a nonzero free-stream velocity — the critical velocities of the web decrease when compared to the corresponding vacuum case. Both results agree with existing literature.

Finally, fast solvers were implemented for the analysis using the MATLAB programming language. The custom solvers developed for this thesis have been open sourced. The thesis serves also as documentation for all the numerical approaches used. It is intended that, if needed, the results are repeatable using only

the information reported here.

Although no formal benchmarking was made, the longest computations for the figures displayed in this thesis were in the order of minutes on a regular desktop computer (of ca. 2010); many figures were computed significantly faster. Especially the steady-state problem was directly solved thousands of times to produce the data for the contour plots of the critical velocity. This demonstrates that the model allows for efficient numerical solution with modest computational resources.

7.1 Accuracy of the results

In the numerical results, we validated our fluid-structure interaction model by comparing against known results in the literature. One question remains: which results are the best?

Purely in the context of potential flow theory, we can confidently state that the results from the present model are more accurate than any added-mass approximation, because the aerodynamic reaction force was determined analytically from the equation of potential flow.

On the flip side of the coin, simple added-mass models (which are classical in this application area) have one advantage: they can be fitted to each experimental situation empirically, by changing the added mass coefficients. This can be viewed as a form of "effect lumping" that may improve the fit, if the qualitative trends predicted by the model are correct.

In contrast, the present model was derived from first principles, and it has no tuning parameters. It either agrees with experimental data, or it does not. The comparisons presented in this study suggest that the degree of accuracy depends mainly on the plate aspect ratio. It was found that the model performs especially well for long, narrow strips.

The discretization issue was discussed earlier (subsection 6.1.2). Although no rigorous verification was made, the validation of the results against known ones suggests that the discretized problem performs correctly.

When we change to a modelling viewpoint, the question changes as well. Which model gives the most accurate predictions? What level of modelling is needed to capture all the relevant physical phenomena in a quantitatively accurate manner?

7.2 Making predictions in the paper production context

To fully answer the modelling question, further studies are needed using the Euler and Navier–Stokes flow models (recall Figure 1, p. 32). The Euler model is needed to account for possible nonlinear convective effects, and the Navier–

Stokes model for the effect of fluid viscosity. One further issue in flow modelling is turbulence; in paper production environments, the airflow is in practice always turbulent. To which extent this affects the paper web dynamics via fluid-structure feedback, is currently an open question.

As for the effects of viscosity, boundary layer theory (as in Frondelius et al., 2006) seems another reasonable approach, since the viscosity of air is relatively small. But as we recall the remark on Chang et al. (1991) (in our literature survey at the very beginning of this work), already the question of how to set up the model is nontrivial. How the boundary layer can be handled, will change depending on whether a leading edge exists in the model chosen.

This brings us to the effect of the problem geometry (and topology!). In the present model, the rollers were ignored. To assess the quality of the predictions via the methods of computational science, models with more realistic problem geometries should be studied numerically. This includes improved 1D web models, e.g. including the rollers as part of the geometry for the panel problem, but also 2D models for the web (recall these, too, from Figure 1, p. 32). In the latter, finite plate width leads to displacement localization toward the free edges; the deformation is no longer cylindrical (see Banichuk et al., 2010a).

A yet further question is the accuracy of the boundary conditions. Is *simply supported* good enough in practice? This could be answered by studying a long web span, with non-reflective (i.e. absorbing) boundary conditions at the ends, placing the rollers inside the domain, and actually modelling the roller contact. Then, the dynamics of the web span between the rollers can be compared to simpler models using various different boundary conditions to represent the rollers, to determine which choice gives the best agreement. As of this writing, preliminary research in this direction has been done by Saksa, but the project is still underway and the results have not yet been published.

Then there is the question of the proper degree of material modelling. What about orthotropicity? (Our study Banichuk et al., 2011a, indicates that there are are no major changes, at least as far as steady-state analysis is concerned.) And is the purely elastic model accurate in the dry end, or should viscoelastic effects be included?

Another viewpoint is model accuracy versus effort expended. In engineering practice, predictions within a few percent are often acceptable. Model implementation always takes time, which translates directly into cost in terms of work hours. A related cost is solver code complexity; shorter programs tend to have fewer bugs and are easier to maintain. There are two approaches to keeping code short: build new tools, bringing the language closer to the problem domain[1] (thus enabling shorter programs), or use the available tools[2] and set a maximum

[1] FreeFEM is an example of this, in the context of solving partial differential equations numerically via the finite element method. See `http://www.freefem.org/` (link referred 14th November 2011).

[2] In this view, MATLAB is basically an extensive numerical linear algebra (and plotting) toolkit; problems must be cast in terms of linear algebra to program a solver in MATLAB. For the most part, the same can be said of Python with NumPy, SciPy and Matplotlib.

acceptable project size.

Thus, it makes sense to ask: what is the simplest model that can get us to within a few percent for a given quantity? This is where the domain of computational science ends; the only way to answer this question is to compare with experimental data.

7.3 Conclusion

The circle is complete. From the motivation on paper production in the Introduction, we have come to moving strings and panels, airflow considerations, fluid-structure interaction, plotting eigenfrequency spectra, numerics and numerical results, and now, back to questions on modelling of paper production. It is of course the hope that the circle is only a projection; that something has been gained along the way (Figure 72).

The main message from this thesis — beside the actual numerical results — is that with careful choice of models, supercomputing is not always needed for investigation of practical problems. Also, on the other hand, with computationally light models it becomes possible to solve the problem thousands of times in a reasonable amount of time. This enables applications such as model parameter optimization, fast direct exploration of the parameter space, or statistical analysis and visualization of the effects of uncertain data.

Many questions still remain; among those, the ones mentioned in the short modelling discussion above. Furthermore, the sensitivity of the physical model to small perturbations in its parameters is an important question, which was not even touched upon in the present work. To include this topic, in a similarly ground-up fashion as the rest, would have doubled the length.

For uncertainty analysis, it may be possible to use deterministic worst-case techniques (as in Neittaanmäki and Repin, 2004; and Banichuk and Neittaanmäki, 2010), but given the computationally light nature of the model, a direct statistical, visual approach is also possible. Preliminary work in this direction, using the statistical approach, has been done by the author, but the project is still underway and the results have yet to be reported.

The aim of investigating ideal models as a solid foundation for more complex multiphysics problems was achieved. The model developed can, with certain limitations, describe the stability limits and dynamic behaviour of a moving paper web interacting with surrounding air.

With these words, this journey has reached the point $(0, 1, 1)$.

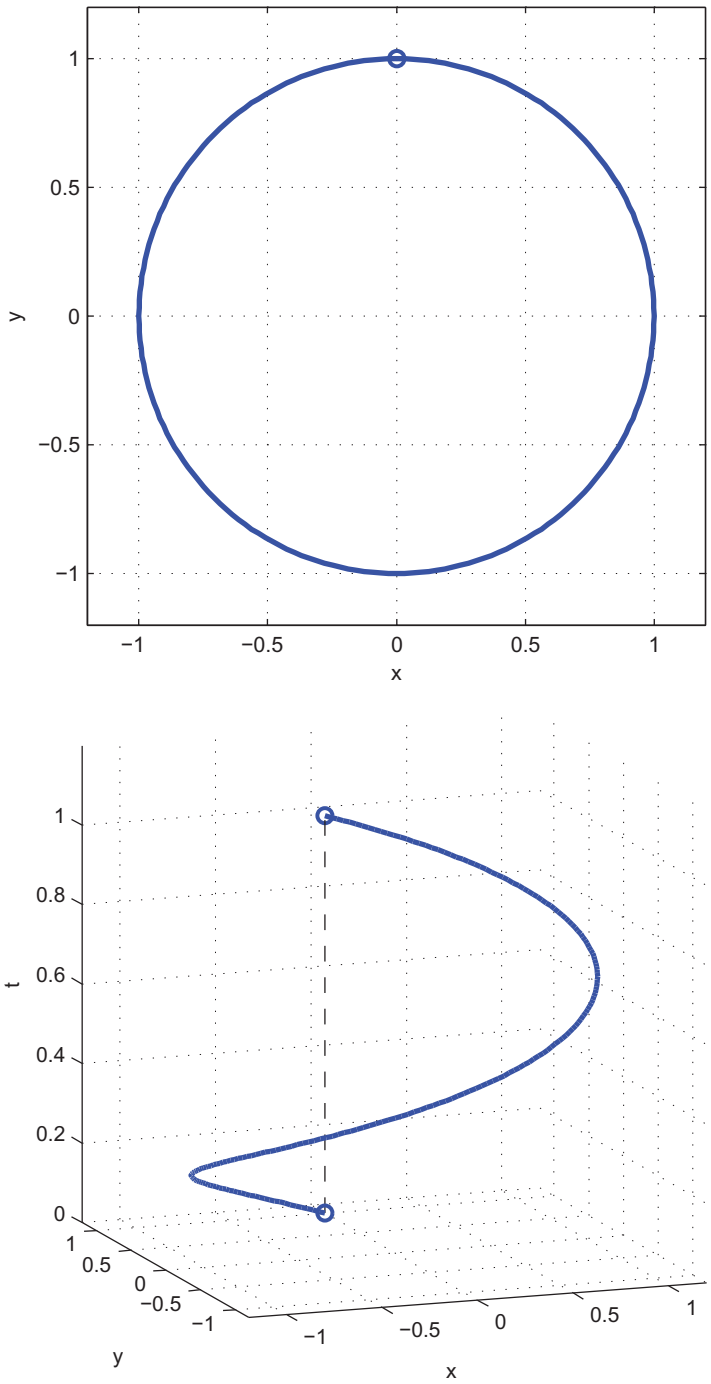

FIGURE 72 The conclusion.

YHTEENVETO (FINNISH SUMMARY)

Työn otsikko: *Ideaalivirtaukseen upotetun, aksiaalisesti liikkuvan paneelin mekaanisesta stabiilisuudesta ja dynamiikasta: tutkimus paperintuotannosta matemaattisin käsittein.*

Tässä laskennallisen mekaniikan alaan kuuluvassa työssä perehdytään *liikkuviin materiaaleihin* paperinvalmistuksen näkökulmasta. Paperinäkökulma valittiin, koska Suomessa paperiteollisuus on teknologisesti ja yhteiskunnallisesti merkittävä ala.

Tuotettava paperi kulkee paperikoneessa ohuena massana, jota nimitetään *rainaksi*. Raina on tyypillisesti hyvin ohut (kopiopaperille n. 0.1 mm, kartongille n. 1 mm; ks. kuva 5, s. 34), ja se koostuu verkosta kuituja (ks. kuva 4). Kuidut ovat kuitenkin hyvin pieniä, halkaisijaltaan tyypillisesti n. 10 μm (eli yhden millimetrin sadasosan). Arkipäivän mittakaavassa katsottuna raina onkin mikroskooppisesta rakenteestaan huolimatta tasa-aineinen, ja paperifysiikan tutkimus perustuu klassiseen *kontinuumimekaniikkaan*.

Kaikissa paperikoneissa esiintyy *vapaita välejä*, joissa raina kulkee ilman mekaanista tukea, tyypillisesti yhdeltä sitä tukevalta rullalta toiselle. Siirto *puristusnipistä* kuivatusosalle on aina tällainen vapaa väli. Perinteisessä *sylinterikuivaimessa* (ks. kuvat 2 ja 3, s. 33) jokaisen sylinteriparin väli on myös tällainen.

Aksiaalisesti liikkuvat materiaalit ovat epävakaita: jos niitä ajetaan riittävän kovaa, ne menettävät stabiilisuutensa. Fysikaalisesti tämä johtuu pystysuuntaisen kiihtyvyyden aiheuttamista nk. inertiaaliefekteistä. Hauraan materiaalin kuten paperin tapauksessa stabiilisuuden menetyksestä tyypillisesti seuraa rainan katkeaminen.

Tällaiset *ratakatkot* paperikoneissa ovat ei-toivottuja sekä teknologisista että taloudellisista syistä. Paperikoneen pitäminen käynnissä vaatii valtavan määrän energiaa riippumatta siitä, kulkeeko koneen läpi paperia vai ei. Toiseksi, mikäli ratakatko sattuu, tehtaan tuotanto keskeytyy, pysyen pysähdyksissä siihen asti kunnes raina saadaan syötettyä uudelleen koneen läpi. Tämä vaatii merkittävästi aikaa.

Jotta ratakatkoilta vältyttäisiin, on ymmärrettävä paperikoneiden teknologisten prosessien takana vaikuttavaa fysikkaa. Tätä ymmärrystä voidaan syventää kontinuumimekaniikan teorioiden kautta.

Paperin tapauksessa pelkän materiaalin liikkeen lisäksi on huomioitava ympäröivän ilman vaikutus, koska paperi on kevyttä ja ilmavirtaukset voivat näin ollen helposti muuttaa sen liikerataa. Päädytään *monifysikaaliseen*[3] malliin, jossa huomioidaan *neste-rakennekytkentä*[4] paperin ja ilman välillä.

---

[3] "Monifysikaalinen" on yleisnimitys malleille, joissa tarvitaan useampaa fysiikan haaraa, kuten tässä elastiikkaa ja virtausmekaniikkaa.

[4] Tavanomaisen englanninkielisen termin *fluid-structure interaction* (FSI) sisältämä "fluid" viittaa sekä nesteisiin että kaasuihin. Näiden virtaukset muistuttavat toisiaan hyvin paljon, ja niitä kuvataan samoilla teorioilla. Suomennoksessa tätä on vaikea huomioida, koska suomen kielessä ei ole yhteisnimitystä näille helposti virtaaville aineille eli "fluideille".

Tämän työn tarkoitus on tutkia tiettyä mallia, jota voidaan käyttää paperikoneen vapaan välin fysiikan kuvaamiseen. Valittu malli koostuu kahdesta osasta. Paperirainaa kuvaa elastinen *paneeli*, joka on malli *sylinterimäisesti* taipuvalle ohuelle levylle. Sylinterimäinen taipuma tarkoittaa, että (esim. paperikoneen) leveyssuunnassa tarkasteltuna levy taipuu joka kohdassa samalla tavalla. Ks. kuva 24 (s. 101).

Mallin virtausmekaniikan komponentti on kaksiulotteinen *ideaalivirtaus* (toiselta nimeltään *potentiaalivirtaus*), jossa ilmahiukkaset voivat siirtyä paikasta toiseen, mutta eivät voi pyöriä. Ilman sisäinen kitka (viskositeetti) sekä äänen nopeuden vaikutus ovat molemmat jätetty huomiotta. Tämä yksinkertaistaa tilanteen matemaattista analyysia huomattavasti verrattuna monimutkaisempiin virtausmalleihin, sekä mahdollistaa tehtävän ratkaisun huomattavasti vaatimattomammilla laskentaresursseilla. Tästä huolimatta malli huomioi ympäröivän ilman vaikutuksen. Yksinkertaisen mallin tutkiminen myös muodostaa vakaan perustan mahdollisille myöhemmille jatkotutkimuksille.

Yhdistetty malli on esitetty kaaviokuvassa 25 (s. 101). Työssä selvitetään tälle mallille paneelin nk. *kriittinen nopeus*, joka on perustavanlaatuisen fysiikan asettama yläraja sille, kuinka nopeasti paperirainaa voidaan mallin mukaan ajaa ennen kuin se muuttuu epästabiiliksi. Kriittinen nopeus selvitetään *dimensiottomien tehtäväparametrien* avulla, jotta se voidaan tarvittaessa helposti laskea mille hyvänsä todelliselle paperimateriaalille. Kriittisen nopeuden lisäksi selvitetään sitä vastaava nk. *ominaismuoto*.

Lisäksi työssä lasketaan suoria simulaatioita rainan dynamiikasta eli aikariippuvasta käyttäytymisestä. Simulaatiotulokset helpottavat käsityksen muodostamista siitä, millä tavalla raina voi värähdellä. Simulaatiot on esitetty kuvissa 46–51 (s. 174 alkaen).

Rainan värähtelyjä tutkitaan myös abstraktimmin, *vapaiden värähtelyjen* matemaattisesta näkökulmasta. Lineaarielastisen järjestelmän värähtelyt noudattavat aina nk. *aikaharmonista* muotoa. Tämä ominaisuus mahdollistaa niiden tutkimisen *kompleksisten ominaistaajuuksien* kautta.

Pääasiallisen tehtävän analyysin lisäksi, työssä on käyty läpi vastaava aikaharmoninen ominaistaajuusanalyysi myös kahdelle yksinkertaisemmalle mallille, joiden tarkoitus on antaa teoreettinen vertailukohta, sekä toimia johdantona työssä käsitellyn tyyppisiin tehtäviin. Liikkuvan ideaalilangan ominaistaajuusspektri on esitetty kuvassa 10 (s. 65), ja vaimennetun liikkuvan langan vastaavat tulokset kuvissa 11–21 (s. 80 alkaen).

Numeerisen ominaistaajuusanalyysin tulosten tulkinnassa ja visualisaatiossa tavattaviin käytännön ongelmiin on kehitetty kaksi ratkaisua, jotka molemmat esitellään työssä. Tämä mahdollistaa selkeiden ominaistaajuuskuvien piirtämisen. Hyödyntäen näitä menetelmiä, ominaistaajuustulokset pääasiallisesta mallista on esitetty kuvissa 55–66 (s. 191 alkaen).

Mallin antamia ennusteita verrataan alan kirjallisuudessa olemassaoleviin. Havaitaan, että malli antaa kaikissa tutkituissa tapauksissa samansuuntaisia tuloksia kuin olemassaolevat, sekä parantaa ennusteita erityisesti pitkille ja kapeille vapaille väleille.

Tutkimuksen laskennallinen osuus toteutettiin numeeriseen ohjelmointiin suunnatulla MATLAB-ohjelmointikielellä. Varsinaisia ajoaikatestejä ei tehty, mutta hitaimmatkin laskenta-ajot työssä esitettyjä kuvia varten valmistuivat minuuteissa tavallisella PC-tietokoneella. Useimmissa kuvissa esitelty data pystyttiin laskemaan huomattavasti nopeammin. Tämä osoittaa, että valittu malli mahdollistaa kuvatun tilanteen tehokkaan laskennallisen analyysin vaatimattomillakin laskentaresursseilla.

Laskennallisesti kevyet mallit ovat tärkeitä, koska niitä voidaan käyttää tehokkaasti esimerkiksi paperikoneen suunnitteluparametrien optimointiin, tehtävän parametriavaruuden suoraan tutkimiseen, sekä parametrien epävarmuuksien aiheuttamien efektien tilastolliseen analyysiin.

Tutkimuksen tulokset ovat, kaksiulotteisen potentiaalivirtausteorian näkökulmasta, tarkempia kuin klassiset *lisämassoihin*[5] perustuvat tulokset. Tämä johtuu siitä, että virtauskenttä on huomioitu tarkemmin.

Peilaten mallinnettuun fysikaaliseen tilanteeseen, tulokset ovat rohkaisevia, mutta lisätutkimuksia tarvitaan, jotta saadaan selville riittääkö nykyinen virtausmalli myös käytännössä, vai pitäisikö tarkkojen tulosten saamiseksi huomioida epälineaariset konvektioefektit (Eulerin malli) tai sen lisäksi vielä ilman viskositeetti (Navier–Stokesin malli).

Joka tapauksessa, työ valottaa yksinkertaistettuja malleja, jotka muodostavat teoreettisen perustan monimutkaisemmalle monifysikaaliselle tutkimukselle. Tulosten mukaan malli on käyttökelpoinen, ja kuten ylempänä todettiin, sen havaittiin toimivan erityisen hyvin pitkille ja kapeille vapaille väleille.

---

5 Englanniksi *added mass*.

REFERENCES

Alava, M., Niskanen, K., 2006. The physics of paper. Reports on Progress in Physics 69 (3), 669–723.

Ames, W., Lee, S., Zaiser, J., 1968. Non-linear vibration of a traveling threadline. International Journal of Non-Linear Mechanics 3, 449–469.

Anderson, Jr., J. D., 1985. Fundamentals of Aerodynamics. McGraw-Hill.

Archibald, F. R., Emslie, A. G., 1958. The vibration of a string having a uniform motion along its length. ASME Journal of Applied Mechanics 25, 347–348.

Archimedes, 3rd century BCE. Works of Archimedes. Dover, ISBN 0-486-42084-1. Reprint (1953) of 1897 translation by T. L. Heath.

Ashley, H., Landahl, M., 1985. Aerodynamics of wings and bodies. Dover.

Banichuk, N., Jeronen, J., Kurki, M., Neittaanmäki, P., Saksa, T., Tuovinen, T., 2011a. On the limit velocity and buckling phenomena of axially moving orthotropic membranes and plates. International Journal of Solids and Structures 48 (13), 2015–2025.
URL http://dx.doi.org/10.1016/j.ijsolstr.2011.03.010

Banichuk, N., Jeronen, J., Neittaanmäki, P., Tuovinen, T., 2010a. On the instability of an axially moving elastic plate. International Journal of Solids and Structures 47 (1), 91–99.
URL http://dx.doi.org/10.1016/j.ijsolstr.2009.09.020

Banichuk, N., Jeronen, J., Neittaanmäki, P., Tuovinen, T., 2010b. Static instability analysis for travelling membranes and plates interacting with axially moving ideal fluid. Journal of Fluids and Structures 26 (2), 274–291.
URL http://dx.doi.org/10.1016/j.jfluidstructs.2009.09.006

Banichuk, N., Jeronen, J., Neittaanmäki, P., Tuovinen, T., 2011b. Dynamic behaviour of an axially moving plate undergoing small cylindrical deformation submerged in axially flowing ideal fluid. Journal of Fluids and Structures 27 (7), 986–1005.
URL http://dx.doi.org/10.1016/j.jfluidstructs.2011.07.004

Banichuk, N., Jeronen, J., Neittaanmäki, P., Tuovinen, T., Saksa, T., 2010c. Theoretical study on travelling web dynamics and instability under a linear tension distribution. Tech. Rep. B1/2010, University of Jyväskylä, Reports of the Department of Mathematical Information Technology. B: Scientific Computing.

Banichuk, N., Jeronen, J., Saksa, T., Tuovinen, T., 2011c. Static instability analysis of an elastic band travelling in the gravitational field. Rakenteiden mekaniikka (Journal of Structural Mechanics) 44 (3), 172–185.

Banichuk, N. V., Neittaanmäki, P. J., 2010. Structural Optimization with Uncertainties. Springer-Verlag, ISBN 978-90-481-2517-3.

Bender, C. M., Orszag, S. A., 1978. Advanced Mathematical Methods for Scientists and Engineers I: Asymptotic Methods and Perturbation Theory. Springer-Verlag, 1999 reprint: ISBN 978-0-387-98931-0.

Bisplinghoff, R. L., Ashley, H., 1962. Principles of Aeroelasticity. Dover Publications, Inc., New York, 2nd edition, 1975.

Bolotin, V. V., 1963. Nonconservative Problems of the Theory of Elastic Stability. Pergamon Press, New York.

Bonnin, A., Huchon, R., Deschamps, M., 2000. Ultrasonic waves propagation in absorbing thin plates: Application to paper characterization. Ultrasonics 37 (8), 555–563.
URL http://dx.doi.org/10.1016/S0041-624X(99)00106-7

Canuto, C., Hussaini, M. Y., Quarteroni, A., Zang, T. A., 1988. Spectral Methods in Fluid Dynamics. Springer-Verlag, New York, ISBN 3-540-17371-4.

Chang, Y. B., Fox, S. J., Lilley, D. G., Moretti, P. M., 1991. Aerodynamics of moving belts, tapes and webs. In: Perkins, N. C., Wang, K. W. (Eds.), ASME DE. Vol. 36. pp. 33–40, presented in ASME Symposium on Dynamics of Axially Moving Continua, Miami, Florida, September 22-25, 1991.

Chang, Y. B., Moretti, P. M., 1991. Interaction of fluttering webs with surrounding air. TAPPI Journal 74 (3), 231–236.

Chang, Y. B., Moretti, P. M., 2002. Flow-induced vibration of free edges of thin films. Journal of Fluids and Structures 16 (7), 989–1008.

Chen, L.-Q., Mar 2005. Analysis and control of transverse vibrations of axially moving strings. ASME Applied Mechanics Reviews 58, 91–116.

Chen, L.-Y., Goldenfeld, N., Oono, Y., 1996. Renormalization group and singular perturbations: Multiple scales, boundary layers, and reductive perturbation theory. Physical Review E 54 (1), 376–394.

Chonan, S., 1986. Steady state response of an axially moving strip subjected to a stationary lateral load. Journal of Sound and Vibration 107, 155–165.

Christou, M. A., Christov, C. I., 2007. Fourier–Galerkin method for 2D solitons of Boussinesq equation. Mathematics and Computers in Simulation 74, 82–92.

Ciarlet, P. G., 1978. The Finite Element Method for Elliptic Problems. Studies in Mathematics and its Applications. North-Holland, Amsterdam.

Darcy, H., 1856. Les fontaines publiques de la ville de Dijon. Paris.

Datko, R., You, Y. C., 1991. Some second-order vibrating systems cannot tolerate small time delays in their damping. Journal of Optimization Theory and Applications 70 (3), 521–537.
URL http://dx.doi.org/10.1007/BF00941300

Doaré, O., 2010. Dissipation effect on local and global stability of fluid-conveying pipes. Journal of Sound and Vibration 329 (1), 72–83.

Dugundji, J., Dowell, E., Perkin, B., 1963. Subsonic flutter of panels on continuous elastic foundations. AIAA Journal 1 (5), 1146–1154.

Eloy, C., Souilliez, C., Schouveiler, L., 2007. Flutter of a rectangular plate. Journal of Fluids and Structures 23 (6), 904–919.

Euler, L., 1766. De motu vibratorio tympanorum. Novi Commentarii academiae scientiarum imperialis Petropolitanae 10, 243–260.
URL http://eulerarchive.maa.org/pages/E302.html

Evans, L. C., 1998. Partial Differential Equations. American Mathematical Society, ISBN 0-8218-0772-2.

Freitas, P., Pais, A. R., Grinfeld, M., Knight, P. A., Du, U. R., 1997. Stability of finite-dimensional systems with indefinite damping. Adv. Math. Sci. Appl. 17, 435–446.

Frondelius, T., Koivurova, H., Pramila, A., 2006. Interaction of an axially moving band and surrounding fluid by boundary layer theory. Journal of Fluids and Structures 22 (8), 1047–1056.

Garziera, R., Amabili, M., 2000. Damping effect of winding on the lateral vibrations of axially moving tapes. ASME Journal of Vibration and Acoustics 122, 49–53.

Golub, G. H., van Loan, C. F., 1996. Matrix Computations, 3rd Edition. Johns Hopkins, ISBN 0-8018-5414-8.

Gorman, D. J., 1982. Free Vibration Analysis of Rectangular Plates. Elsevier North Holland, Inc., ISBN 0-444-00601-X.

Gresho, P. M., Sani, R. L., 1999. Incompressible Flow and the Finite Element Method: Advection–Diffusion and Isothermal Laminar Flow. Wiley, reprinted with corrections. ISBN 0 471 96789 0.

Guo, C. Q., Païdoussis, M. P., 2000. Stability of rectangular plates with free side-edges in two-dimensional inviscid channel flow. ASME Journal of Applied Mechanics 67, 171–176.

Haataja, J., Heikonen, J., Leino, Y., Rahola, J., Ruokolainen, J., Savolainen, V., 2002. Numeeriset menetelmät käytännössä (Numerical methods in practice), 2nd Edition. CSC, Espoo, available on the Internet. http://www.csc.fi/oppaat/num.kayt/.

Hämäläinen, J., Järvinen, J., 2006. Elementtimenetelmä virtauslaskennassa (The finite element method in computational fluid dynamics), 2nd Edition. CSC, Espoo, available on the Internet. ISBN-Internet 952-5520-20-X. http://www.csc.fi/oppaat/.

Hoffman, J., Johnson, C., 2008. Resolution of d'Alembert's paradox. Journal of mathematical fluid mechanics 12 (3), 321–334.
URL http://dx.doi.org/10.1007/s00021-008-0290-1

Hosaka, H., Crandall, S. H., 1992. Self-excited vibrations of a flexible disk rotating on an air film above a flat surface. Acta Mechanica 3, 115–127, supplement.

Huber, M. T., 1914. Die Grundlagen einer rationellen Berechnung der kreuzweise bewehrten Eisenbetonplatten. Zeitschrift der Österreichische Ingeniur- und Architekten-Vereines 30, 557–564.

Huber, M. T., 1923. Die Theorie des kreuzweise bewehrten Eisenbetonplatten. Der Bauingenieur 4, 354–392.

Huber, M. T., Jun. 1926. Einige Andwendungen fer Biegungstheorie orthotroper Platten. Zeitschrift für angewandte Mathematik und Mechanik 6 (3), 228–232.

Hughes, T. J. R., 2000. The Finite Element Method. Linear Static and Dynamic Finite Element Analysis. Dover Publications, Inc., Mineola, N.Y., USA, ISBN 0-486-41181-8.

Huseyin, K., Plaut, R. H., 1974–1975. Transverse vibrations and stability of systems with gyroscopic forces. Journal of Structural Mechanics 3 (2), 163–177.

Johnson, C., 1987. Numerical Solution of Partial Differential Equations by the Finite Element Method. Cambridge University Press, reprint by Dover, 2009.

Karlsson, M. (Ed.), 2000. Papermaking Science and Technology Vol. 9: Papermaking Part 2: Drying. Fapet Oy, Helsinki, Finland, ISBN 952-5216-09-8.

Kim, J., Cho, J., Lee, U., Park, S., 2003. Modal spectral element formulation for axially moving plates subjected to in-plane axial tension. Computers & Structures 81, 2011–2020.
URL http://dx.doi.org/10.1016/S0045-7949(03)00229-3

Kirillov, O. N., Verhulst, F., 2010. Paradoxes of dissipation-induced destabilization or who opened Whitney's umbrella? Zeitschrift für Angewandte Mathematik und Mechanik 90 (6), 462–488.
URL http://dx.doi.org/10.1002/zamm.200900315

Koivurova, H., Pramila, A., 1997. Nonlinear vibrations of axially moving membrane by finite element method. Computational Mechanics 20, 573–581.

Kong, L., Parker, R. G., 2004. Approximate eigensolutions of axially moving beams with small flexural stiffness. Journal of Sound and Vibration 276, 459–469.

Kornecki, A., Dowell, E. H., O'Brien, J., 1976. On the aeroelastic instability of two-dimensional panels in uniform incompressible flow. Journal of Sound and Vibration 47 (2), 163–178.

Kouhia, R., 2009. Computational techniques for the non-linear analysis of structures. Course material: Buckling of Plates, Finnish Graduate School of Engineering Mechanics, Helsinki University of Technology, June 8–12, 2009. Corrected version.

Krechetnikov, R., Marsden, J., 2006. On destabilizing effects of two fundamental non-conservative forces. Physica D 214, 25–32.
URL http://dx.doi.org/10.1016/j.physd.2005.12.003

Kreyszig, E., 1993. Advanced Engineering Mathematics, 7th Edition. John Wiley & Sons, ISBN 0-471-59989-1.

Krizek, M., Neittaanmäki, P., 1990. Finite Element Approximation of Variational Problems and Applications. Longman Scientific & Technical, Harlow, copubl. J. Wiley & Sons, New York.

Kulachenko, A., Gradin, P., Koivurova, H., 2007a. Modelling the dynamical behaviour of a paper web. Part I. Computers & Structures 85, 131–147.

Kulachenko, A., Gradin, P., Koivurova, H., 2007b. Modelling the dynamical behaviour of a paper web. Part II. Computers & Structures 85, 148–157.

Kurki, M., Jeronen, J., Saksa, T., Tuovinen, T., Neittaanmäki, P., 2011. Liikkuvan paperiradan kriittinen rajanopeus ja stabiilisuusanalyysi paperi- ja kartonkikoneen eri osaprosesseissa (The critical velocity and stability analysis of a moving paper web in different subprocesses in paper and cardboard machines). Paperi ja Puu (Paper and wood) 1/2011.

Lagerstrom, P. A., Casten, R. G., 1972. Basic concepts underlying singular perturbation techniques. SIAM Review 14 (1), 63–120.

Launder, B. E., Spalding, D. B., 1972. Lectures in Mathematical Models of Turbulence. Academic Press, London.

Lee, S.-Y., Mote, Jr., C. D., 1996. Vibration control of an axially moving string by boundary control. ASME Journal of Dynamic Systems, Measurement, and Control 118, 66–74.

Lee, U., Oh, H., 2005. Dynamics of an axially moving viscoelastic beam subject to axial tension. International Journal of Solids and Structures 42 (8), 2381 – 2398.
URL http://dx.doi.org/10.1016/j.ijsolstr.2004.09.026

Lighthill, J., 1986. An Informal Introduction to Theoretical Fluid Mechanics. Oxford Science Publications, ISBN 0-19-853630-5.

Lin, C. C., 1997. Stability and vibration characteristics of axially moving plates. International Journal of Solids and Structures 34 (24), 3179–3190.

Lin, C. C., Mote, C. D., 1995. Equilibrium displacement and stress distribution in a two-dimensional, axially moving web under transverse loading. ASME Journal of Applied Mechanics 62, 772–779.

Lin, C. C., Mote, C. D., 1996. Eigenvalue solutions predicting the wrinkling of rectangular webs under non-linearly distributed edge loading. Journal of Sound and Vibration 197 (2), 179–189.

Mann, R. W., Baum, G. A., Habeger, C. C., 1980. Determination of all nine orthotropic elastic constants for machine-made paper. TAPPI Journal 63 (2), 163–166.

Marynowski, K., 2002. Non-linear dynamic analysis of an axially moving viscoelastic beam. Journal of Theoretical and Applied Mechanics 2 (40), 465–482.

Marynowski, K., 2008. Dynamics of the Axially Moving Orthotropic Web. Vol. 38 of Lecture Notes in Applied and Computational Mechanics. Springer–Verlag, Germany.

Miranker, W. L., 1960. The wave equation in a medium in motion. IBM Journal of Research and Development 4, 36–42.

Mote, C. D., 1968a. Divergence buckling of an edge-loaded axially moving band. International Journal of Mechanical Sciences 10, 281–195.

Mote, C. D., May 1968b. Dynamic stability of an axially moving band. Journal of the Franklin Institute 285 (5), 329–346.

Mote, C. D., 1972. Dynamic stability of axially moving materials. Shock and Vibration Digest 4 (4), 2–11.

Mote, C. D., 1975. Stability of systems transporting accelerating axially moving materials. ASME Journal of Dynamic Systems, Measurement, and Control 97, 96–98.

Mote, Jr., C. D., Wickert, J. A., Nov 1991. Response and discretization methods for axially moving materials. Applied Mechanics Review 44 (11), S279–S284.

Mote, Jr., C. D., Wu, W. Z., 1985. Vibration coupling in continuous belt and band systems. Journal of Sound and Vibration 102 (1), 1–9.

Mujumdar, A. S., Douglas, W. J. M., 1976. Analytical modelling of sheet flutter. Svensk Papperstidning 79, 187–192.

Nehari, Z., 1952. Conformal Mapping. Dover, ISBN 0-486-61137-X.

Neittaanmäki, P., Repin, S. I., 2004. Reliable methods for computer simulation: error control and a posteriori estimates. Studies in mathematics and its applications. Elsevier, ISBN 9780444513762.
URL http://books.google.co.uk/books?id=OEX7XWJ1g1EC

Niemi, J., Pramila, A., 1986. Vibration analysis of an axially moving membrane immersed into ideal fluid by FEM. Tech. rep., Tampereen teknillinen korkeakoulu (Tampere University of Technology), Tampere.

Païdoussis, M. P., 1998. Fluid-Structure Interactions: Slender Structures and Axial Flow. Vol. 1. Academic Press, ISBN 0-12-544360-9.

Païdoussis, M. P., 2004. Fluid-Structure Interactions: Slender Structures and Axial Flow. Vol. 2. Elsevier Academic Press, ISBN 0-12-544361-7.

Païdoussis, M. P., 2005. Some unresolved issues in fluid-structure interactions. Journal of Fluids and Structures 20 (6), 871–890.

Païdoussis, M. P., 2008. The canonical problem of the fluid-conveying pipe and radiation of the knowledge gained to other dynamics problems across applied mechanics. Journal of Sound and Vibration 310, 462–492.

Parker, R. G., 1998. On the eigenvalues and critical speed stability of gyroscopic continua. ASME Journal of Applied Mechanics 65, 134–140.

Parker, R. G., 1999. Supercritical speed stability of the trivial equilibrium of an axially-moving string on an elastic foundation. Journal of Sound and Vibration 221 (2), 205–219.

Piskunov, V. G., Rasskazov, A. O., 2002. Evolution of the theory of laminated plates and shells. International Applied Mechanics 38 (2), 135–166.
URL http://dx.doi.org/10.1023/A:1015756726070

Polyanin, A. D., 2004a. Eqworld/exact solutions/first-order partial differential equations/linear equations/section 1.2. Referred 2011-11-13.
URL http://eqworld.ipmnet.ru/en/solutions/fpde/fpde1201.pdf

Polyanin, A. D., 2004b. Eqworld/exact solutions/linear partial differential equations/second-order hyperbolic partial differential equations/telegraph equation. Referred 2010-03-10.
URL http://eqworld.ipmnet.ru/en/solutions/lpde/lpde207.pdf

Polyanin, A. D., Schiesser, W. E., Zhurov, A. I., 2008. Partial differential equation/second-order partial differential equations. Scholarpedia. Revision #121514.
URL http://dx.doi.org/10.4249/scholarpedia.4605

Pramila, A., 1986. Sheet flutter and the interaction between sheet and air. TAPPI Journal 69 (7), 70–74.

Pramila, A., 1987. Natural frequencies of a submerged axially moving band. Journal of Sound and Vibration 113 (1), 198–203.

Pramila, A., Niemi, J., 1987. FEM-analysis of transverse vibrations of an axially moving membrane immersed in ideal fluid. International Journal for Numerical Methods in Engineering 24 (12), 2301–2313, 1-09702-07.
URL http://dx.doi.org/10.1002/nme.1620241205

Prandtl, L., 1928. Motion of fluids with very little viscosity. Tech. Rep. 452, NACA, Technical Memorandums of the National Advisory Committee for Aeronautics.

Qian, J., Lin, W.-W., 2007. A numerical method for quadratic eigenvalue problems of gyroscopic systems. Journal of Sound and Vibration 306 (1-2), 284–296.
URL http://dx.doi.org/10.1016/j.jsv.2007.05.009

Quintard, M., Whitaker, S., 1994a. Transport in ordered and disordered porous media I: The cellular average and the use of weighting functions. Transport in Porous Media 14, 163–177.

Quintard, M., Whitaker, S., 1994b. Transport in ordered and disordered porous media II: Generalized volume averaging. Transport in Porous Media 14, 179–206.

Quintard, M., Whitaker, S., 1994c. Transport in ordered and disordered porous media III: Closure and comparison between theory and experiment. Transport in Porous Media 15, 31–49.

Quintard, M., Whitaker, S., 1994d. Transport in ordered and disordered porous media IV: Computer generated porous media for three-dimensional systems. Transport in Porous Media 15, 51–70.

Quintard, M., Whitaker, S., 1994e. Transport in ordered and disordered porous media V: Geometrical results for two-dimensional systems. Transport in Porous Media 15, 183–196.

Reddy, J. N., 2009. Buckling of laminated composite plates: Theories and analyses. Course material: Buckling of Plates, Finnish Graduate School of Engineering Mechanics, Helsinki University of Technology, June 8–12, 2009.

Renshaw, A. A., Mote, Jr., C. D., Mar 1996. Local stability of gyroscopic systems near vanishing eigenvalues. ASME Journal of Applied Mechanics 63, 116–120.

Rodi, W., 1984. Turbulence Models and Their Application in Hydraulics, 2nd Edition. IAHR state of the art paper, Delft.

Ruggiero, E. J., 2005. Modeling and control of spider satellite components. Ph.D. thesis, Virginia Tech, Department of Mechanical Engineering.
URL http://scholar.lib.vt.edu/theses/available/etd-08022005-145837/

Russo, L., 2004. The Forgotten Revolution: How Science Was Born in 300 BC and Why it Had to Be Reborn. Springer, ISBN 978-3540203964.

Sack, R. A., 1954. Transverse oscillations in traveling strings. British Journal of Applied Physics 5, 224–226.

Sagan, H., 1961. Boundary and Eigenvalue Problems in Mathematical Physics. John Wiley & Sons, Inc., slightly corrected reprint by Dover Publications, Inc., 1989.

Sathe, S., Benney, R., Charles, R., Doucette, E., Miletti, J., Senga, M., Stein, K., Tezduyar, T., 2007. Fluid-structure interaction modeling of complex parachute designs with the space-time finite element techniques. Computers & Fluids 36 (1), 127–135, Challenges and Advances in Flow Simulation and Modeling.
URL http://dx.doi.org/10.1016/j.compfluid.2005.07.010

Schlichting, H., 1960. Boundary Layer Theory, 4th Edition. McGraw-Hill.

Schlichting, H., Gersten, K., 1999. Boundary Layer Theory, 8th Edition. Springer, ISBN 3-540-66270-7.

Sedov, L. I., 1972. A Course in Continuum Mechanics, English Edition. Vol. 3. Wolters-Noordhoff Publishing, Groningen, Netherlands, ISBN 90-0179682-6.

Seo, Y. B., 1999. Determination of in-plane shear properties by an off-axis tension method and laser speckle photography. Journal of Pulp and Paper Sciences 25 (9), 321–325.

Shen, J. Y., Sharpe, L., McGinley, W. M., Jan. 1995. Identification of dynamic properties of plate-like structures by using a continuum model. Mechanics Research Communications 22 (1), 67–78.

Sherman, D. I., 1952. On the stress distribution in partitions, an elastic heavy medium which is weakened by elliptic holes. Izvestiya Akademii Nauk SSSR, Otdelenie Tekhnicheskikh Nauk (OTN) 7, 992–1010.

Shin, C., Chung, J., Kim, W., Sep. 2005. Dynamic characteristics of the out-of-plane vibration for an axially moving membrane. Journal of Sound and Vibration 286 (4-5), 1019–1031.

Silberman, I., Feb. 1954. Planetary waves in the atmosphere. Journal of Meteorology 11, 27–34.

Simpson, A., 1973. Transverse modes and frequencies of beams translating between fixed end supports. Journal of Mechanical Engineering Science 15, 159–164.

Skutch, R., 1897. Uber die Bewegung eines gespannten Fadens, weicher gezwungen ist durch zwei feste Punkte, mit einer constanten Geschwindigkeit zu gehen, und zwischen denselben in Transversal-schwingungen von gerlinger Amplitude versetzt wird. Annalen der Physik und Chemie 61, 190–195.

Stein, K., Benney, R., Kalro, V., Tezduyar, T. E., Leonard, J., Accorsi, M., Oct. 2000. Parachute fluid-structure interactions: 3-D computation. Computer Methods in Applied Mechanics and Engineering 190 (3–4), 373–386.

Stein, K., Benney, R., Tezduyar, T., Potvin, J., Dec. 2001. Fluid-structure interactions of a cross parachute: numerical simulation. Computer Methods in Applied Mechanics and Engineering 191 (6–7), 673–687.

Strang, W. G., Fix, G. J., 1973. An Analysis of the Finite Element Method. Wellesley Cambridge Press, ISBN 978-0961408886.

Sugiyama, Y., Langthjem, M. A., 2007. Physical mechanism of the destabilizing effect of damping in continuous non-conservative dissipative systems. International Journal of Nonlinear Mechanics 42 (1), 132–145.

Swope, R. D., Ames, W. F., 1963. Vibrations of a moving threadline. Journal of the Franklin Institute 275, 36–55.

Sygulski, R., Jan. 2007. Stability of membrane in low subsonic flow. International Journal of Non-Linear Mechanics 42 (1), 196–202.

Tadmor, E., 1987. Stability analysis of finite-difference, pseudospectral and Fourier-Galerkin approximations for time-dependent problems. SIAM Review 29 (4), 525–555.

Thurman, A., Mote, Jr., C., Mar. 1969. Free, periodic, nonlinear oscillation of an axially moving strip. Journal of Applied Mechanics 36 (1), 83–91.
URL http://dx.doi.org/doi:10.1115/1.3564591

Timoshenko, S. P., Woinowsky-Krieger, S., 1959. Theory of plates and shells, 2nd Edition. New York : Tokyo : McGraw-Hill, ISBN 0-07-085820-9.

Tokaty, G. A., 1994. A History and Philosophy of Fluid Mechanics. Dover, republication with corrections. Original by G. T. Foulis & Co., Ltd, 1971.

Tuovinen, T., 2011. Analysis of stability of axially moving orthotropic membranes and plates with linear non-homogeneous tension profile. Ph.D. thesis, Department of Mathematical Information Technology, University of Jyväskylä, Jyväskylä studies in computing 147. ISBN 978-951-39-4577-0.

Ulsoy, A. G., Mote, C. D., 1980. Analysis of bandsaw vibration. Wood Science 13, 1–10.

Ulsoy, A. G., Mote, C. D., 1982. Vibration of wide band saw blades. ASME Journal of Engineering for Industry 104, 71–78.

Ulsoy, A. G., Mote, C. D., Szymni, R., 1978. Principal developments in band saw vibration and stability research. Holz als Roh- und Werkstoff 36 (7), 273–280.

Vaughan, M., Raman, A., 2010. Aeroelastic stability of axially moving webs coupled to incompressible flows. ASME Journal of Applied Mechanics 77, 021001–1 – 021001–17.
URL http://dx.doi.org/10.1115/1.2910902

Ventsel, E., Krauthammer, T., 2001. Thin Plates and Shells: Theory, Analysis, and Applications. Marcel Dekker, Inc., New York.

Wang, X., Jan. 2003. Instability analysis of some fluid-structure interaction problems. Computers & Fluids 32 (1), 121–138.

Wang, Y., Huang, L., Liu, X., 2005. Eigenvalue and stability analysis for transverse vibrations of axially moving strings based on Hamiltonian dynamics. Acta Mechanica Sinica 21, 485–494.

Watanabe, Y., Isogai, K., Suzuki, S., Sugihara, M., 2002. A theoretical study of paper flutter. Journal of Fluids and Structures 16 (4), 543–560.

Weinstock, R., 2008. Calculus of Variations — With Applications to Physics and Engineering. Weinstock Press, ISBN 978-1443728812. Reprint of 1974 edition.

Whitaker, S., Dec. 1969. Advances in theory of fluid motion in porous media. Industrial and Engineering Chemistry 61 (12), 14–28.

Whitaker, S., 1986a. Flow in porous media I: A theoretical derivation of Darcy's law. Transport in Porous Media 1, 3–25.

Whitaker, S., 1986b. Flow in porous media II: The governing equations for immiscible, two-phase flow. Transport in Porous Media 1, 105–125.

White, F. M., 1994. Fluid Mechanics, 3rd Edition. McGraw–Hill.

Wickert, J. A., Mote, C. D., 1988. Current research on the vibration and stability of axially-moving materials. Shock Vib. Dig. 20, 3–13.

Wickert, J. A., Mote, C. D., 1990. Classical vibration analysis of axially moving continua. ASME Journal of Applied Mechanics 57, 738–744.

Wickert, J. A., Mote, Jr., C. D., 1989. On the energetics of axially moving continua. The Journal of the Acoustical Society of America 85 (3), 1365–1368.
URL http://link.aip.org/link/?JAS/85/1365/1

Winkler, E., 1867. Die Lehre Von Elasticität Und Festigkeit, 1st Edition. H. Dominicus, Prague.

Wu, X., Kaneko, S., 2005. Linear and nonlinear analyses of sheet flutter induced by leakage flow. Journal of Fluids and Structures 20, 927–948.

Xing, Y., Liu, B., 2009a. New exact solutions for free vibrations of rectangular thin plates by symplectic dual method. Acta Mechanica Sinica 25, 265–270.

Xing, Y. F., Liu, B., 2009b. New exact solutions for free vibrations of thin orthotropic rectangular plates. Composite Structures 89, 567–574.
URL http://dx.doi.org/10.1016/j.compstruct.2008.11.010

Yang, S. M., Mote, Jr., C. D., 1991. Stability of non-conservative linear discrete gyroscopic systems. Journal of Sound and Vibration 147 (3), 453–464.

Yokoyama, T., Nakai, K., 2007. Evaluation of in-plane orthotropic elastic constants of paper and paperboard. In: 2007 SEM Annual Conference & Exposition on Experimental and Applied Mechanics.

Zhou, Y.-F., Wang, Z.-M., 2007. Transverse vibration characteristics of axially moving viscoelastic plate. Applied Mathematics and Mechanics (English Edition) 28 (2), 209–218.
URL http://dx.doi.org/10.1007/s10483-007-0209-1

APPENDIX 1 CONVERGENCE OF AERODYNAMIC INTEGRALS

This appendix contains the details for the convergence argument of Section 3.5. It is provided for convenience, to save the reader the work of reconstructing the details if they are needed.

Denote the domain of $\Lambda(\xi, x)$ with $D_0 \equiv \{\,(-1,1) \times (-1,1)\,\}$. Let $D_1 \equiv D_0 \cap \{\xi < x\}$. Refer to Figure 73.

Recall relation (128):

$$N(\xi, x) \equiv \frac{1}{\pi} \ln \left| \frac{1+\Lambda}{1-\Lambda} \right| \overset{\text{for } \xi < x}{=} \frac{1}{\pi} \ln \frac{1+\Lambda}{1-\Lambda} < \ln \frac{2}{1-\Lambda} \equiv s(\xi, x) \; .$$

This estimate retains the singularity, but the numerator is now simpler and the absolute value is no longer needed. See Figure 74 for a contour plot of $s(\xi, x)$.

At this point it is useful to define a rotated coordinate system for the (x, ξ) plane, with

$$\eta \equiv x - \xi \tag{215}$$

$$\zeta \equiv x + \xi \; . \tag{216}$$

The coordinate η is the orthogonal distance from $\xi = x$, while ζ is the orthogonal distance from $\xi = -x$. See Figure 75.

As a function to compare with, we will use $r(\eta) \equiv \ln(4/\eta)$. We define $r(\xi, x) \equiv r(\eta) \equiv r(x - \xi)$. Hence, $r(\eta)$ is defined in all of D_1. Note that it is positive everywhere in D_1. The indefinite, improper integral of $r(\eta)$, taken with respect to ξ, is $\int r(x - \xi)\, \mathrm{d}\xi = \ln(4)\xi + (x - \xi)(\ln(x - \xi) - 1) \equiv R(\xi, x)$.

Note that although $r = r(\eta)$, the integral $R = R(\eta, \zeta)$ or equivalently, $R = R(\xi, x)$. The dependence on ζ is needed for the "lonely" ξ, by $\xi = (\zeta - \eta)/2$; it was introduced by the fact that the direction of integration in (127) is not aligned with η.

The function $R(\xi, x)$ is finite for any $(x, \xi) \in D_1$; recall from analysis that $\lim_{x \to 0^+} (x \ln x) = 0$. Hence, it holds that

$$\int_{-1}^{x} r(x - \xi)\, \mathrm{d}\xi = R(\xi, x)|_{\xi = x} - R(\xi, x)|_{\xi = -1} < \infty \; ,$$

i.e. $r(\eta)$ is a valid candidate for the sandwich theorem.

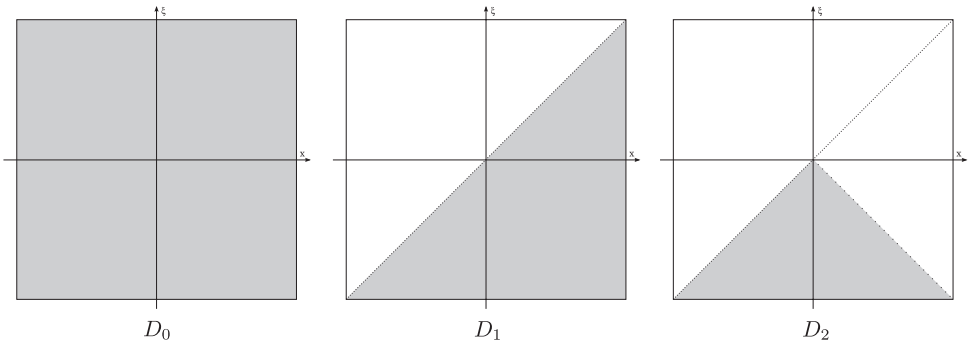

FIGURE 73 The sets D_j for the convergence argument.

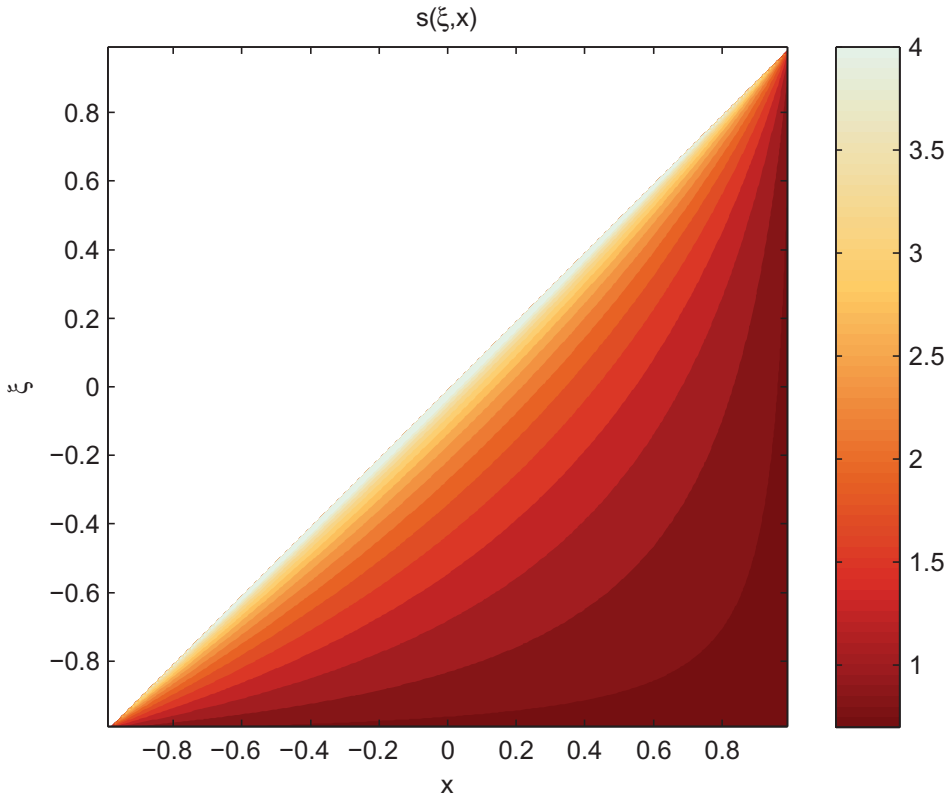

FIGURE 74 Contour plot of the function $s(\xi, x)$. The domain is D_1; in the blank area, the function is not defined. The function is singular on the line $x = \xi$. Compare $N(\xi, x)$ in Figure 31 on p. 116.

We would like to show that $s(\xi, x) < r(\xi, x)$ for all $(x, \xi) \in D_1$. Consider the following question: for which points $(x, \xi) \in D_1$ does the following condition hold?

$$\begin{aligned} s(\xi, x) &< r(\xi, x) \\ \ln \frac{2}{1-\Lambda} &< \ln \frac{4}{x-\xi} \\ \frac{2}{1-\Lambda} &< \frac{4}{x-\xi} \\ 1-\Lambda &> \frac{x-\xi}{2} \\ -\Lambda &> (x-\xi)/2 - 1 \\ \Lambda &< 1 - (x-\xi)/2 \end{aligned} \tag{217}$$

All lines in the algebraic manipulation (217) are equivalent. Note especially that for all $(x, \xi) \in D_1$, the argument in each ln is always ≥ 2 (which > 1); hence the corresponding logarithms are nonnegative, and the exponentiation does not change the sign on either side of the inequality. We have also used the monotonicity of exp and the inverse $(1/x)$. The two-way nature of each operation is important, so that — once we have obtained the admissible (x, ξ) with the help of the last line — we can go back and conclude that $s(\xi, x) < r(\xi, x)$.

We will first investigate the line $\xi = -x$ (i.e. $\zeta = 0$), and then generalize the result. Denote the line segment from the origin $(x, \xi) = (0, 0)$ to the point $(x, \xi) = (1, -1)$ by the symbol S; i.e., let $S \equiv D_1 \cap \{\xi = -x\}$. See Figure 75. Plots giving a general idea of the functions are provided in Figure 76.

Specifically on the line segment S, we have $\xi = -x$. In this case, the last line of the condition (217) becomes

$$\Lambda(-x, x) < 1 - x \, .$$

By the definition of $\Lambda(\xi, x)$, on S we have

$$\Lambda^2|_{\xi=-x} \equiv \Lambda(-x, x)^2 = \frac{(1-x)(1+\xi)}{(1-\xi)(1+x)}\Big|_{\xi=-x} = \frac{(1-x)^2}{(1+x)^2} \, , \tag{218}$$

hence, still on S, we have

$$\Lambda|_{\xi=-x} \equiv \Lambda(-x, x) = \frac{1-x}{1+x} \, .$$

The question becomes: where on S, if anywhere, does the following condition hold?

$$\frac{1-x}{1+x} < 1 - x \, . \tag{219}$$

On S we have $x \in (0, 1)$. It is easily seen that in this particular range, (219) is always true. This is because both sides of (219) are positive, both numerators are the same, and on the right-hand side, the denominator (being just the number 1, omitted from notation as usual) is smaller. Hence, the right-hand side is larger.

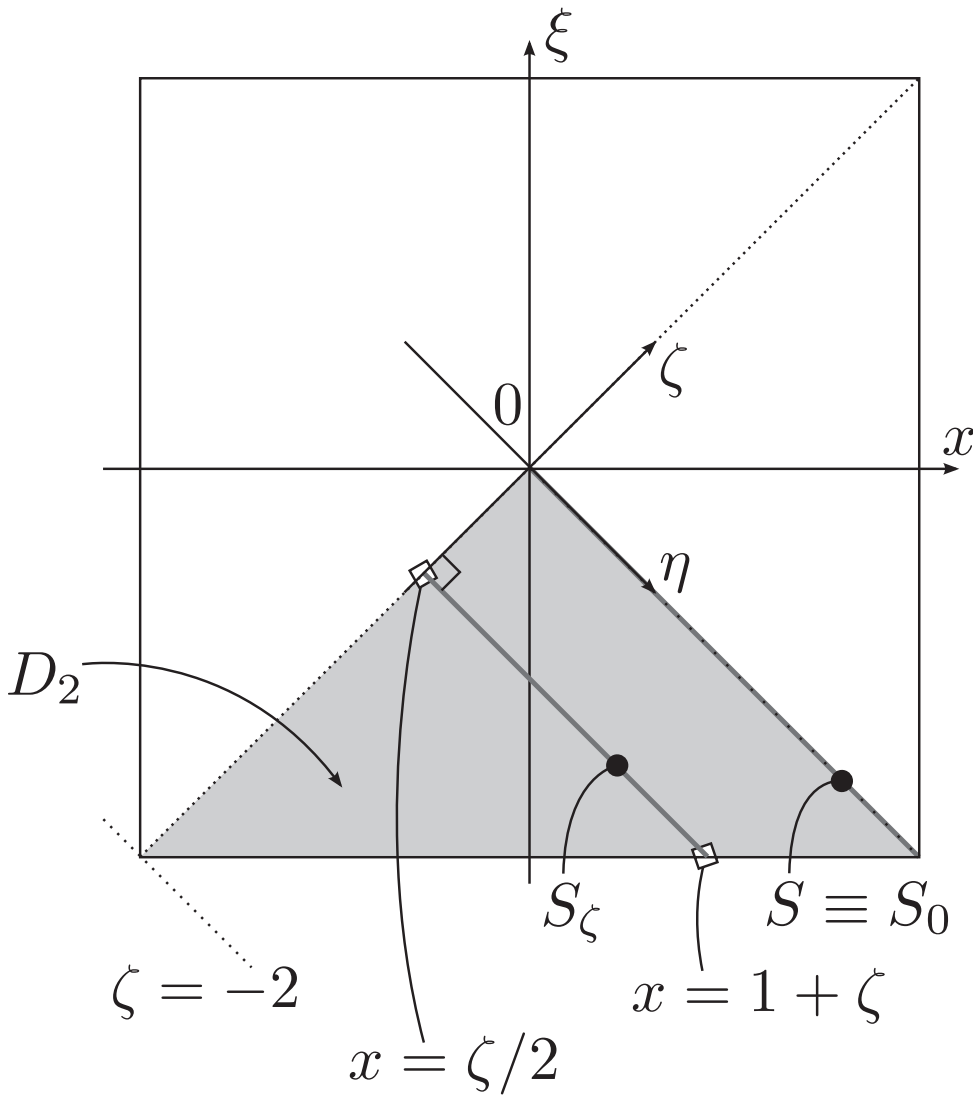

FIGURE 75 The (x, ξ) and (η, ζ) coordinate systems. Line segments S and S_ζ.

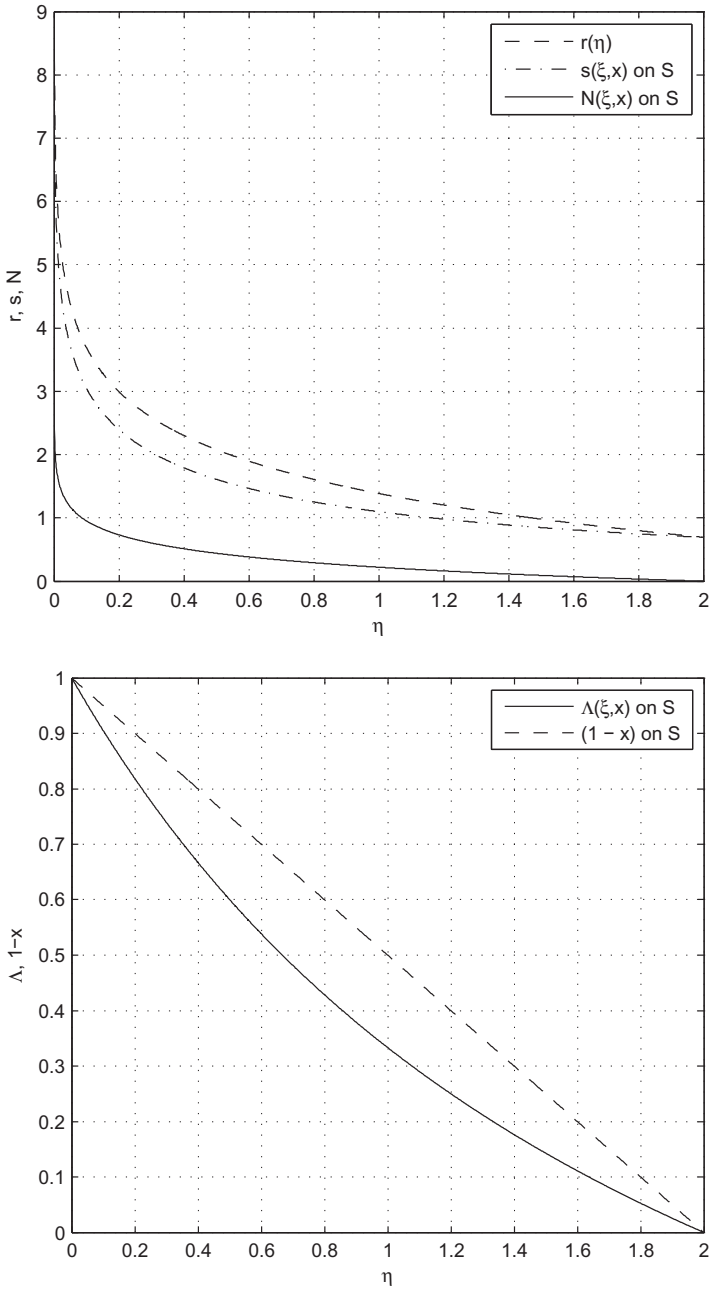

FIGURE 76 *Top*: Plots of the functions $N(\xi, \eta)$, $r(\eta)$ and $s(\xi, x)$ on the line segment S. *Bottom*: Plots of the functions $\Lambda(\xi, x)$ and $1 - x$ on the line segment S.

We have obtained that on the line segment S, the condition (217) always holds, and hence on S, we have $s(\xi, x) < r(\xi, x)$. What remains to be done is to show the same result for the rest of the triangle D_1.

Recall that $\Lambda(\xi, x)$ is symmetric with respect to the line $\xi = -x$. Thus, only one half of the triangle needs to be considered. Define $D_2 \equiv D_1 \cap \{\, \xi < -x \,\}$. This gives us the lower half with corners $(x, \xi) = (0, 0)$, $(-1, -1)$ and $(1, -1)$, while leaving out the line segment S (already handled). Refer to Figure 73.

We can partition D_2 into lines S_ζ parallel with S, where we use the coordinate ζ as a parameter (at $\zeta = 0$, we have $S_0 \equiv S$). Here it will be more convenient to work with Λ^2 than Λ. Because $0 \leq \Lambda \leq 1$ in D_1 and thus also in $D_2 \subset D_1$, no information is lost by squaring.

In the triangle D_2, we have $\zeta \in (-2, 0)$. From the definition (216), we obtain $\xi = \zeta - x$. For a fixed value of ζ, restrict $x \in (\zeta/2,\, 1 + \zeta)$. Call this line segment S_ζ. As ζ varies from 0 to -2, the sets S_ζ cover the triangle D_2 parametrically. See Figure 75.

Now take a fixed value for ζ. On the corresponding line segment S_ζ, we have the expression

$$\Lambda^2|_{\xi=\zeta-x} = \frac{(1-x)(1+\zeta-x)}{(1-\xi)(1-\zeta+x)} \,. \tag{220}$$

As a function of ζ and x, consider the condition

$$\Lambda^2|_{\xi=\zeta-x} - \Lambda^2|_{\xi=-x} \leq 0 \,. \tag{221}$$

We rewrite the condition (221) using the equalities (218) and (220). We obtain the equivalent condition

$$\frac{1-x}{1+x}\left[\frac{(1+x)(1+\zeta-x) - (1-x)(1-\zeta+x)}{(1-\zeta+x)(1-x)}\right] \leq 0 \,.$$

The numerator in the parenthetical term simplifies considerably, leaving just

$$\frac{1-x}{1+x}\left[\frac{2\zeta}{(1-\zeta+x)(1-x)}\right] \leq 0 \,. \tag{222}$$

Now, for all $x \in (-1, 1)$, we have $(1-x)/(1+x) > 0$. Hence, this multiplier does not affect the sign of the left-hand side of (222). When $x \in (\zeta/2,\, 1+\zeta)$, the denominator in the parenthetical term, likewise, is always positive. Hence, the condition (222) holds if and only if $\zeta \leq 0$, with equality only for $\zeta = 0$. Finally, recall that in D_2, we have $\zeta \in (-2, 0)$.

We have obtained the following result: for any fixed ζ, and a given, admissible x, we can estimate $\Lambda|_{\xi=\zeta-x} \equiv \Lambda(\zeta - x, x)$ from above by $\Lambda|_{\xi=x} \equiv \Lambda(-x, x)$. In (η, ζ) coordinates, the result perhaps looks clearer. For all points $(\eta, \zeta) \in D_2$, for the function $\Lambda(\eta, \zeta)$ we have

$$\Lambda(\eta, \zeta) \leq \Lambda(\eta, 0) \,, \tag{223}$$

with equality only if $\zeta = 0$.

Now, the function $r(\xi, x) \equiv r(\eta)$ was chosen precisely so that it is only affected by the value of $\eta = x - \xi$, not $\zeta = x + \xi$. Hence, the shape of $r(\eta)$ at $\zeta = \text{const.}$ is exactly the same regardless of the value of ζ, i.e. which line segment S_ζ it is viewed on. Note that there is no scaling; the shorter line segments will get a shorter portion of this profile (due to the restriction on x in order to stay inside D_2).

The result (223) allows us to eliminate the ζ dependence when estimating Λ from above (for the purposes of (217)). On each S_ζ (with $\zeta = \text{const.}$), the profile of Λ is dominated by the profile at the original S which has $\zeta = 0$. (Similarly to the above, no scaling.)

Note that in (217), we are allowed to make the left-hand side larger (or the right-hand side smaller). If the modified relation holds, then so does the original one.

The direction of estimation is critically important, so that the implication between the two relations will point in the correct direction. Up to this point, we do not yet know whether (217) holds (outside the line segment S); the aim is to show that it does.

Now, to finish this: because the right-hand side in the last line of (217) does not depend on ζ, and on the left-hand side the ζ dependence can be estimated away (making the LHS larger), it follows that (217) holds for any $\zeta \in (-2, 0]$. As before, working backward to the first line, we conclude that $s(\xi, x) < r(\xi, x)$. We obtain that this relation holds in all of D_2.

Symmetry of $\Lambda(\xi, x)$ with respect to $\xi = -x$ immediately obtains $s(\xi, x) < r(\xi, x)$ for the other small triangle, $D_1 \setminus D_2$. Therefore, we have

$$N(\xi, x) < r(\xi, x) \tag{224}$$

everywhere in D_1. Because $\int_{-1}^{x} r(\xi, x)\, \mathrm{d}\xi < \infty$ (as was remarked above), we have by the sandwich theorem that the original integral (127) converges.

APPENDIX 2 COMPUTING THE FLUID-STRUCTURE INTERACTION MATRICES

In this Appendix, we look into practical questions for computing the fluid-structure interaction matrices a_{jn}, b_{jn} and c_{jn}. The observations enable slightly faster computation of these matrices; without any optimizations the computation is very slow.

When the present research was first being prepared in late 2007, on a desktop computer that was current at that time, calculating the required integrals up to $n_0 = 56$ took two weeks of wall time. This was after applying all the analytical optimizations that are documented below. Hence, it makes sense to precalculate them just once, store the results to disk, and then reuse the saved values in all solver codes. This saves time in matrix assembly, and makes it possible to have solvers that start up very fast. The sine basis has the convenient property that more modes can be added without requiring the recalculation of any of the previous ones.

Also, one should beware the singularity of $N(\xi, x)$ at $\xi = x$. We approximate the integrals containing $N(\xi, x)$ as usual,

$$\int_{-1}^{1} f(\xi, x)\, \mathrm{d}\xi \approx \int_{-1}^{x-\varepsilon} f(\xi, x)\, \mathrm{d}\xi + \int_{x+\varepsilon}^{1} f(\xi, x)\, \mathrm{d}\xi \ ,$$

where ε is small.

Also, due to the singularity of $\Lambda(\xi, x)$ at the upper and left edges (see Figure 29 on page 114), evaluating $N(\xi, x)$ directly near these areas should be avoided for numerical accuracy reasons, even though analytically the limits are well-defined. Instead, it is recommended to utilize the symmetries, and always perform the actual evaluation of $N(\xi, x)$ in the half-domain $\{\,(-1, 1) \times (-1, 1)\,\} \cap \{\xi < x\}$.

Finally, in general, each of the basis functions in our sine basis (equation (156), p. 131) is either symmetric or antisymmetric with respect to the origin (which is the midpoint of the domain). This will be used below.

Local inertia

The matrix related to the term that plays a role analogous to local inertia in the vacuum case is a_{jn}. Let us denote the integrand in a_{jn} as $a(\xi, x)$.

We will do the analytical optimizations for a_{jn} in some detail; for the other matrices, the arguments work very much in the same manner.

Consider an antisymmetric basis function $\Psi_j(x) = -\Psi_j(-x)$ (this implies j is even) and a symmetric basis function $\Psi_n(\xi) = \Psi_n(-\xi)$ (this implies n is odd). By equation (164), we have for the integrand

$$\begin{aligned} a(-\xi, -x) &= \Psi_n(-\xi)\, N(-\xi, -x)\, \Psi_j(-x) \\ &= -\Psi_n(\xi)\, N(\xi, x)\, \Psi_j(x) \\ &= -a(\xi, x) \ , \end{aligned}$$

where we have used the symmetries of $N(\xi, x)$. By a similar calculation, we obtain the same result if j is odd and n is even. Hence, if $j+n$ is odd, the sum of the integrand over each pair of points $\{(\xi, x),\ (-\xi, -x)\}$ is zero. We can split the domain of integration as $(-1,1)\times(-1,1) = (-1,1)\times(-1,0) \cup (-1,1)\times(0,1) = D \cup R(D)$, where $R(\cdot)$ denotes reflection through the origin. Hence, the integral vanishes. We conclude that if $j+n$ is odd, $a_{jn} = 0$.

If $j+n$ is even, then we obtain, in a similar manner, $a(-\xi,-x) = a(\xi,x)$. Hence

$$\begin{aligned} a_{jn} &= \int_{-1}^{1}\int_{-1}^{1} \Psi_n(\xi) N(\xi,x)\, \Psi_j(x)\, \mathrm{d}\xi \mathrm{d}x \\ &= 2\int_{0}^{1}\int_{-1}^{1} \Psi_n(\xi) N(\xi,x)\, \Psi_j(x)\, \mathrm{d}\xi \mathrm{d}x\ , \quad \text{if } j+n \text{ is even.} \end{aligned}$$

This must be explicitly evaluated numerically, but requires only half the work compared to the original. Finally, let us show that the matrix a_{jn} is symmetric:

$$\begin{aligned} a_{nj} &\equiv \int_{-1}^{1}\int_{-1}^{1} \Psi_j(\xi) N(\xi,x)\, \Psi_n(x)\, \mathrm{d}\xi \mathrm{d}x \\ &= \int_{-1}^{1}\int_{-1}^{1} \Psi_j(x) N(x,\xi)\, \Psi_n(\xi)\, \mathrm{d}x \mathrm{d}\xi \\ &= \int_{-1}^{1}\int_{-1}^{1} \Psi_j(x) N(\xi,x)\, \Psi_n(\xi)\, \mathrm{d}x \mathrm{d}\xi \\ &= \int_{-1}^{1}\int_{-1}^{1} \Psi_n(\xi) N(\xi,x)\, \Psi_j(x)\, \mathrm{d}x \mathrm{d}\xi \\ &= \int_{-1}^{1}\int_{-1}^{1} \Psi_n(\xi) N(\xi,x)\, \Psi_j(x)\, \mathrm{d}\xi \mathrm{d}x \equiv a_{jn}\ . \end{aligned}$$

The first and last steps come directly from the definition of a_{jn}. For the other steps, the justification is as follows. First, swap the names of the variables x and ξ. In the expression for a_{jn}, both are dummy variables of integration, so this is legal. Next, use the symmetry $N(\xi,x) = N(x,\xi)$. Then, swap the order of multiplication inside the integral. This is legal, since at each point we are multiplying real numbers, and hence the multiplications commute. Finally, use the fact that $\|N\|_{L^1([-1,1]\times[-1,1])} < \infty$, i.e. N is absolutely integrable. This allows us to use Fubini's theorem to swap the order of integration. The conclusion is that $a_{nj} = a_{jn}$; i.e. the matrix a_{jn} is symmetric.

We have reduced the work for computing a_{jn} to roughly $1/8$ of the original. We only need to evaluate the upper triangular part of the matrix, and even that only for every other element (where $j+n$ is even). Furthermore, for each of the integrals we actually need to compute, we can reduce the domain into half and simply multiply the result by two.

Coriolis term

The matrix b_{jn} plays a role somewhat analogous to the Coriolis term of the vacuum case. The matrix is defined as $b_{jn} = \frac{1}{2}\left(I_{jn} - I_{nj}\right)$; recall equation (165).

Therefore, it is antisymmetric (skew-symmetric) with respect to interchange of j and n. That is, $b_{nj} = -b_{jn}$, from which also $b_{jj} = 0$.

It makes sense to only compute I_{jn}, and when finished, use (165) to obtain b_{jn}. Let us look at the definition of I_{jn}, (167):

$$I_{jn} = \int_{-1}^{1} \int_{-1}^{1} \frac{\mathrm{d}\Psi_n}{\mathrm{d}x}(\xi)\, N(\xi, x)\, \Psi_j(x)\ \mathrm{d}\xi \mathrm{d}x\ .$$

It is clear that the derivative of a symmetric Ψ is antisymmetric, and the derivative of an antisymmetric Ψ is symmetric (with respect to the origin). Hence, by an argument similar to what was done with $a(\xi, x)$, we can expect this integral to be nonzero only if $j + n$ is *odd* (note the difference!).

The nonzero values will have no obvious structure, since there is no further symmetry in the integrand for general j and n. Hence, we can save one half of the work (although not 7/8 like for a_{jn}) by only evaluating elements for which $j + n$ is odd. This integral must be evaluated for the whole domain directly.

Once we have I_{jn}, we obtain b_{jn} by equation (165). From the definition we see that b_{jn} will inherit the structure of having nonzeroes only where $j + n$ is odd.

Curiously, it was observed in practice that MATLAB computed entries of I_{jn} about two times faster than either a_{jn} or c_{jn} for j and n of similar magnitude. It is useful that the slowest integrals are the ones that can be optimized the most.

Centrifugal term

The same observations that were made for the matrix a_{jn} can be made for the matrix c_{jn}, which plays a role analogous to the centrifugal term.

Thus, the workload for c_{jn} can be cut to about 1/8 of the original. Evaluate only the upper triangular part, only for those elements for which $j + n$ is even, and for each integral, reduce the domain into half and multiply the result by two.

APPENDIX 3 WIND TUNNEL EXPERIMENT DATA OF CHANG AND MORETTI

The data in the tables originate in the article by Chang and Moretti (1991), and have been included for convenience. The data are used in Section 6.1.1. In the article, imperial units have been used, and the data never appear in textual form; the points are only given as plotted into a figure with log-log axes. Hence, the values of the data points have been visually estimated from Chang and Moretti (1991, Fig. 11). The data are given as both the estimated numerical values in the original imperial units (for verification purposes), and the corresponding values in SI units.

Data estimation and SI conversion courtesy of M. Kurki. Conversion to SI units was performed using the factors 1 lb (force) $=$ 4.44822162 N, 1 in $=$ 0.0254 m and 1 ft $=$ 0.3028 m.

TABLE 3 Wind tunnel experiment data of Chang and Moretti (1991, Fig. 11), case A: $2\ell = 0.508$ m (20 in). Tension per unit width T versus divergence wind speed v_∞^{div}. Values given both in imperial units (used in the referred article) and SI units (used in the present study).

Imperial \ Measurement#	1	2	3	4	5	6
T [lb/in]	0.079	0.141	0.220	0.320	0.405	0.505
v_∞^{div} [ft/s]	40.5	57.0	61.0	70.0	83.0	91.0

SI \ Measurement#	1	2	3	4	5	6
T [N/m]	13.8	24.7	38.5	56.0	70.9	88.4
v_∞^{div} [m/s]	12.3	17.3	18.5	21.2	25.1	27.6

TABLE 4 Wind tunnel experiment data of Chang and Moretti (1991, Fig. 11), case B: $2\ell = 0.254$ m (10 in). Tension per unit width T versus divergence wind speed v_∞^{div}. Values given both in imperial units (used in the referred article) and SI units (used in the present study).

Imperial \ Measurement#	1	2	3	4	5	6
T [lb/in]	0.079	0.141	0.220	0.320	0.505	1.000
v_∞^{div} [ft/s]	49	70	79	80	102	131

SI \ Measurement#	1	2	3	4	5	6
T [N/m]	13.8	24.7	38.5	56.0	88.4	175.1
v_∞^{div} [m/s]	14.8	21.2	23.9	24.2	30.9	39.7

APPENDIX 4 PERFORMING A LEAST-SQUARES FIT USING NORMAL EQUATIONS

Least-squares fitting was used in Section 3.6 to generate a polynomial approximation of the local mean of the aerodynamic kernel, and in subsection 6.3.2 to obtain a continuous relation between Pramila's tabulated β values and plate aspect ratio. This appendix documents the method used, and is included only for convenience and completeness.

Let the measurement points be x_j, $j = 1, \ldots, m$, corresponding to measured values f_j (making up the vector $\mathbf{f}$). Choose a set of linearly independent functions $\phi_k(x)$, $k = 1, \ldots, n$, where $n < m$. Compute the data matrix $\mathbf{B} \in \mathbb{R}^{m \times n}$, where $B_{kj} = \phi_j(x_k)$.

Because the ϕ_k are linearly independent, the matrix $\mathbf{B}$ has full column rank, and the method of normal equations is applicable. This is a standard method, which is given in e.g. Golub and van Loan (1996, pp. 237–239). The details are provided below for convenience.

The normal equations for least-squares optimal coefficients $\mathbf{c}$ are

$$\mathbf{B}^T\mathbf{B}\mathbf{c} = \mathbf{B}^T\mathbf{f}\,. \tag{225}$$

The matrix $\mathbf{B}^T\mathbf{B}$ is symmetric positive definite (see Golub and van Loan, 1996, p. 141). We would like to use the Cholesky decomposition to solve the equation system. To do this without explicitly computing the matrix $\mathbf{B}^T\mathbf{B}$ (which can be numerically unstable), we can use the QR decomposition of $\mathbf{B}$. Using any standard algorithm (refer to Golub and van Loan, 1996 if needed), obtain $\mathbf{B} = \mathbf{Q}\mathbf{R}$. We have $\mathbf{B}^T\mathbf{B} = \mathbf{R}^T\mathbf{Q}^T\mathbf{Q}\mathbf{R} = \mathbf{R}^T\mathbf{R}$ by orthogonality of $\mathbf{Q}$. Hence, equation (225) transforms into

$$\mathbf{R}^T\mathbf{R}\mathbf{c} = \mathbf{B}^T\mathbf{f}\,. \tag{226}$$

The matrix $\mathbf{R} \in \mathbb{R}^{m \times n}$ is upper triangular, $\mathbf{R} = \begin{pmatrix} \mathbf{U} \\ \mathbf{0} \end{pmatrix}$, where $\mathbf{U} \in \mathbb{R}^{n \times n}$ is upper triangular and the $\mathbf{0}$ represents a zero block of size $(m - n) \times n$. Hence, $\mathbf{R}^T = \begin{pmatrix} \mathbf{U}^T & \mathbf{0} \end{pmatrix} = \begin{pmatrix} \mathbf{L} & \mathbf{0} \end{pmatrix}$ is lower triangular, and $\mathbf{R}^T\mathbf{R} = \mathbf{L}\mathbf{U}$. Because on the other hand $\mathbf{R}^T\mathbf{R} = \mathbf{B}^T\mathbf{B}$, we have effectively $\mathbf{L}\mathbf{U}$ decomposed the matrix $\mathbf{B}^T\mathbf{B}$. Furthermore, since $\mathbf{L} = \mathbf{U}^T$, it is a Cholesky decomposition, i.e. $\mathbf{B}^T\mathbf{B} = \mathbf{L}\mathbf{L}^T$. Equation (226) becomes

$$\mathbf{L}\mathbf{L}^T\mathbf{c} = \mathbf{B}^T\mathbf{f}\,. \tag{227}$$

This can be easily solved by the use of forward- and backsubstitutions applied to $\mathbf{L}\mathbf{y} = \mathbf{B}^T\mathbf{f}$ and $\mathbf{L}^T\mathbf{c} = \mathbf{y}$. The least-squares fit to the data is then $f(x) = \sum_k c_k\phi_k(x)$.

The MATLAB documentation for the function `qr()` (version 2009b) suggests, in addition, to use the following iterative correction. Let $\mathbf{c}^{(0)} = \mathbf{c}$ and $M = 3$. Loop M times: at iteration i, compute $\mathbf{r} = \mathbf{f} - \mathbf{B}\mathbf{c}^{(i-1)}$, and solve the linear system $(\mathbf{R}^T\mathbf{R})\mathbf{e} = \mathbf{B}^T\mathbf{r}$ (same LHS as in equation (226)). Set $\mathbf{c}^{(i)} = \mathbf{c}^{(i-1)} + \mathbf{e}$. When finished, set $\mathbf{c} = \mathbf{c}^{(M)}$.

Note that although in all practical cases $\mathbf{r} \neq 0$ (because the data points almost never fall exactly on the fitted curve), with exact arithmetic we would expect

that for the RHS in the correction equation, $\mathbf{B}^T\mathbf{r} = \mathbf{B}^T\mathbf{f} - \mathbf{B}^T\mathbf{B}\mathbf{c} = \mathbf{B}^T\mathbf{f} - \mathbf{L}\mathbf{L}^T\mathbf{c} = 0$. The idea of the iterative correction is to mitigate rounding errors, by solving the normal equations repeatedly. Each iteration finds new least-squares coefficients $\mathbf{e}$ such that the functions ϕ_j approximate the remaining numerical error as well as possible.

Finally, it should be noted that the accuracy of the method of normal equations depends on the condition number of $\mathbf{B}^T\mathbf{B}$ (see Golub and van Loan, 1996, p. 239). Other methods are available to deal with difficult cases; in the present study, this method was sufficient.

JYVÄSKYLÄ STUDIES IN COMPUTING

1 Ropponen, Janne, Software risk management - foundations, principles and empirical findings. 273 p. Yhteenveto 1 p. 1999.
2 Kuzmin, Dmitri, Numerical simulation of reactive bubbly flows. 110 p. Yhteenveto 1 p. 1999.
3 Karsten, Helena, Weaving tapestry: collaborative information technology and organisational change. 266 p. Yhteenveto 3 p. 2000.
4 Koskinen, Jussi, Automated transient hypertext support for software maintenance. 98 p. (250 p.) Yhteenveto 1 p. 2000.
5 Ristaniemi, Tapani, Synchronization and blind signal processing in CDMA systems. - Synkronointi ja sokea signaalinkäsittely CDMA järjestelmässä. 112 p. Yhteenveto 1 p. 2000.
6 Laitinen, Mika, Mathematical modelling of conductive-radiative heat transfer. 20 p. (108 p.) Yhteenveto 1 p. 2000.
7 Koskinen, Minna, Process metamodelling. Conceptual foundations and application. 213 p. Yhteenveto 1 p. 2000.
8 Smolianski, Anton, Numerical modeling of two-fluid interfacial flows. 109 p. Yhteenveto 1 p. 2001.
9 Nahar, Nazmun, Information technology supported technology transfer process. A multi-site case study of high-tech enterprises. 377 p. Yhteenveto 3 p. 2001.
10 Fomin, Vladislav V., The process of standard making. The case of cellular mobile telephony. - Standardin kehittämisen prosessi. Tapaustutkimus solukkoverkkoon perustuvasta matkapuhelintekniikasta. 107 p. (208 p.) Yhteenveto 1 p. 2001.
11 Päivärinta, Tero, A genre-based approach to developing electronic document management in the organization. 190 p. Yhteenveto 1 p. 2001.
12 Häkkinen, Erkki, Design, implementation and evaluation of neural data analysis environment. 229 p. Yhteenveto 1 p. 2001.
13 Hirvonen, Kullervo, Towards better employment using adaptive control of labour costs of an enterprise. 118 p. Yhteenveto 4 p. 2001.
14 Majava, Kirsi, Optimization-based techniques for image restoration. 27 p. (142 p.) Yhteenveto 1 p. 2001.
15 Saarinen, Kari, Near infra-red measurement based control system for thermo-mechanical refiners. 84 p. (186 p.) Yhteenveto 1 p. 2001.
16 Forsell, Marko, Improving component reuse in software development. 169 p. Yhteenveto 1 p. 2002.
17 Virtanen, Pauli, Neuro-fuzzy expert systems in financial and control engineering. 245 p. Yhteenveto 1 p. 2002.
18 Kovalainen, Mikko, Computer mediated organizational memory for process control. Moving CSCW research from an idea to a product. 57 p. (146 p.) Yhteenveto 4 p. 2002.
19 Hämäläinen, Timo, Broadband network quality of service and pricing. 140 p. Yhteenveto 1 p. 2002.
20 Martikainen, Janne, Efficient solvers for discretized elliptic vector-valued problems. 25 p. (109 p.) Yhteenveto 1 p. 2002.
21 Mursu, Anja, Information systems development in developing countries. Risk management and sustainability analysis in Nigerian software companies. 296 p. Yhteenveto 3 p. 2002.
22 Seleznyov, Alexandr, An anomaly intrusion detection system based on intelligent user recognition. 186 p. Yhteenveto 3 p. 2002.
23 Lensu, Anssi, Computationally intelligent methods for qualitative data analysis. 57 p. (180 p.) Yhteenveto 1 p. 2002.
24 Ryabov, Vladimir, Handling imperfect temporal relations. 75 p. (145 p.) Yhteenveto 2 p. 2002.
25 Tsymbal, Alexey, Dynamic integration of data mining methods in knowledge discovery systems. 69 p. (170 p.) Yhteenveto 2 p. 2002.
26 Akimov, Vladimir, Domain decomposition methods for the problems with boundary layers. 30 p. (84 p.). Yhteenveto 1 p. 2002.
27 Seyukova-Rivkind, Ludmila, Mathematical and numerical analysis of boundary value problems for fluid flow. 30 p. (126 p.) Yhteenveto 1 p. 2002.
28 Hämäläinen, Seppo, WCDMA Radio network performance. 235 p. Yhteenveto 2 p. 2003.
29 Pekkola, Samuli, Multiple media in group work. Emphasising individual users in distributed and real-time CSCW systems. 210 p. Yhteenveto 2 p. 2003.
30 Markkula, Jouni, Geographic personal data, its privacy protection and prospects in a location-based service environment. 109 p. Yhteenveto 2 p. 2003.
31 Honkaranta, Anne, From genres to content analysis. Experiences from four case organizations. 90 p. (154 p.) Yhteenveto 1 p. 2003.
32 Raitamäki, Jouni, An approach to linguistic pattern recognition using fuzzy systems. 169 p. Yhteenveto 1 p. 2003.
33 Saalasti, Sami, Neural networks for heart rate time series analysis. 192 p. Yhteenveto 5 p. 2003.
34 Niemelä, Marketta, Visual search in graphical interfaces: a user psychological approach. 61 p. (148 p.) Yhteenveto 1 p. 2003.
35 You, Yu, Situation Awareness on the world wide web. 171 p. Yhteenveto 2 p. 2004.
36 Taatila, Vesa, The concept of organizational competence – A foundational analysis. - Perusteanalyysi organisaation kompetenssin käsitteestä. 111 p. Yhteenveto 2 p. 2004.

37 LYYTIKÄINEN, VIRPI, Contextual and structural metadata in enterprise document management. - Konteksti- ja rakennemetatieto organisaation dokumenttien hallinnassa. 73 p. (143 p.) Yhteenveto 1 p. 2004.
38 KAARIO, KIMMO, Resource allocation and load balancing mechanisms for providing quality of service in the Internet. 171 p. Yhteenveto 1 p. 2004.
39 ZHANG, ZHEYING, Model component reuse. Conceptual foundations and application in the metamodeling-based systems analysis and design environment. 76 p. (214 p.) Yhteenveto 1 p. 2004.
40 HAARALA, MARJO, Large-scale nonsmooth optimization variable metric bundle method with limited memory. 107 p. Yhteenveto 1 p. 2004.
41 KALVINE, VIKTOR, Scattering and point spectra for elliptic systems in domains with cylindrical ends. 82 p. 2004.
42 DEMENTIEVA, MARIA, Regularization in multistage cooperative games. 78 p. 2004.
43 MAARANEN, HEIKKI, On heuristic hybrid methods and structured point sets in global continuous optimization. 42 p. (168 p.) Yhteenveto 1 p. 2004.
44 FROLOV, MAXIM, Reliable control over approximation errors by functional type a posteriori estimates. 39 p. (112 p.) 2004.
45 ZHANG, JIAN, Qos- and revenue-aware resource allocation mechanisms in multiclass IP networks. 85 p. (224 p.) 2004.
46 KUJALA, JANNE, On computation in statistical models with a psychophysical application. 40 p. (104 p.) 2004.,
47 SOLBAKOV, VIATCHESLAV, Application of mathematical modeling for water environment problems. 66 p. (118 p.) 2004.
48 HIRVONEN, ARI P., Enterprise architecture planning in practice. The Perspectives of information and communication technology service provider and end-user. 44 p. (135 p.) Yhteenveto 2 p. 2005.
49 VARTIAINEN, TERO, Moral conflicts in a project course in information systems education. 320 p. Yhteenveto 1p. 2005.
50 HUOTARI, JOUNI, Integrating graphical information system models with visualization techniques. - Graafisten tietojärjestelmäkuvausten integrointi visualisointitekniikoilla. 56 p. (157 p.) Yhteenveto 1p. 2005.
51 WALLENIUS, EERO R., Control and management of multi-access wireless networks. 91 p. (192 p.) Yhteenveto 3 p. 2005.
52 LEPPÄNEN, MAURI, An ontological framework and a methodical skeleton for method engineering – A contextual approach. 702 p. Yhteenveto 2 p. 2005.
53 MATYUKEVICH, SERGEY, The nonstationary Maxwell system in domains with edges and conical points. 131 p. Yhteenveto 1 p. 2005.
54 SAYENKO, ALEXANDER, Adaptive scheduling for the QoS supported networks. 120 p. (217 p.) 2005.
55 KURJENNIEMI, JANNE, A study of TD-CDMA and WCDMA radio network enhancements. 144 p. (230 p.) Yhteenveto 1 p. 2005.
56 PECHENIZKIY, MYKOLA, Feature extraction for supervised learning in knowledge discovery systems. 86 p. (174 p.) Yhteenveto 2 p. 2005.
57 IKONEN, SAMULI, Efficient numerical methods for pricing American options. 43 p. (155 p.) Yhteenveto 1 p. 2005.
58 KÄRKKÄINEN, KARI, Shape sensitivity analysis for numerical solution of free boundary problems. 83 p. (119 p.) Yhteenveto 1 p. 2005.
59 HELFENSTEIN, SACHA, Transfer. Review, reconstruction, and resolution. 114 p. (206 p.) Yhteenveto 2 p. 2005.
60 NEVALA, KALEVI, Content-based design engineering thinking. In the search for approach. 64 p. (126 p.) Yhteenveto 1 p. 2005.
61 KATASONOV, ARTEM, Dependability aspects in the development and provision of location-based services. 157 p. Yhteenveto 1 p. 2006.
62 SARKKINEN, JARMO, Design as discourse: Representation, representational practice, and social practice. 86 p. (189 p.) Yhteenveto 1 p. 2006.
63 ÄYRÄMÖ, SAMI, Knowledge mining using robust clustering. 296 p. Yhteenveto 1 p. 2006.
64 IFINEDO, PRINCELY EMILI, Enterprise resource planning systems success assessment: An integrative framework. 133 p. (366 p.) Yhteenveto 3 p. 2006.
65 VIINIKAINEN, ARI, Quality of service and pricingin future multiple service class networks. 61 p. (196 p.) Yhteenveto 1 p. 2006.
66 WU, RUI, Methods for space-time parameter estimation in DS-CDMA arrays. 73 p. (121 p.) 2006.
67 PARKKOLA, HANNA, Designing ICT for mothers. User psychological approach. – Tieto- ja viestintätekniikoiden suunnittelu äideille. Käyttäjäpsykologinen näkökulma. 77 p. (173 p.) Yhteenveto 3 p. 2006.
68 HAKANEN, JUSSI, On potential of interactive multiobjective optimization in chemical process design. 75 p. (160 p.) Yhteenveto 2 p. 2006.
69 PUTTONEN, JANI, Mobility management in wireless networks. 112 p. (215 p.) Yhteenveto 1 p. 2006.
70 LUOSTARINEN, KARI, Resource , management methods for QoS supported networks. 60 p. (131 p.) 2006.
71 TURCHYN, PAVLO, Adaptive meshes in computer graphics and model-based simulation. 27 p. (79 p.) Yhteenveto 1 p.
72 ZHOVTOBRYUKH, DMYTRO, Context-aware web service composition. 290 p. Yhteenveto 2 p. 2006.

73 KOHVAKKO, NATALIYA, Context modeling and utilization in heterogeneous networks. 154 p. Yhteenveto 1 p. 2006.
74 MAZHELIS, OLEKSIY, Masquerader detection in mobile context based on behaviour and environment monitoring. 74 p. (179 p). Yhteenveto 1 p. 2007.
75 SILTANEN, JARMO, Quality of service and dynamic scheduling for traffic engineering in next generation networks. 88 p. (155 p.) 2007.
76 KUUVA, SARI, Content-based approach to experiencing visual art. - Sisältöperustainen lähestymistapa visuaalisen taiteen kokemiseen. 203 p. Yhteenveto 3 p. 2007.
77 RUOHONEN, TONI, Improving the operation of an emergency department by using a simulation model. 164 p. 2007.
78 NAUMENKO, ANTON, Semantics-based access control in business networks. 72 p. (215 p.) Yhteenveto 1 p. 2007.
79 WAHLSTEDT, ARI, Stakeholders' conceptions of learning in learning management systems development. - Osallistujien käsitykset oppimisesta oppimisympäristöjen kehittämisessä. 83 p. (130 p.) Yhteenveto 1 p. 2007.
80 ALANEN, OLLI, Quality of service for triple play services in heterogeneous networks. 88 p. (180 p.) Yhteenveto 1 p. 2007.
81 NERI, FERRANTE, Fitness diversity adaptation in memetic algorithms. 80 p. (185 p.) Yhteenveto 1 p. 2007.
82 KURHINEN, JANI, Information delivery in mobile peer-to-peer networks. 46 p. (106 p.) Yhteenveto 1 p. 2007.
83 KILPELÄINEN, TURO, Genre and ontology based business information architecture framework (GOBIAF). 74 p. (153 p.) Yhteenveto 1 p. 2007.
84 YEVSEYEVA, IRYNA, Solving classification problems with multicriteria decision aiding approaches. 182 p. Yhteenveto 1 p. 2007.
85 KANNISTO, ISTO, Optimized pricing, QoS and segmentation of managed ICT services. 45 p. (111 p.) Yhteenveto 1 p. 2007.
86 GORSHKOVA, ELENA, A posteriori error estimates and adaptive methods for incompressible viscous flow problems. 72 p. (129 p.) Yhteenveto 1 p. 2007.
87 LEGRAND, STEVE, Use of background real-world knowledge in ontologies for word sense disambiguation in the semantic web. 73 p. (144 p.) Yhteenveto 1 p. 2008.
88 HÄMÄLÄINEN, NIINA, Evaluation and measurement in enterprise and software architecture management. - Arviointi ja mittaaminen kokonais- ja ohjelmistoarkkitehtuurien hallinnassa. 91 p. (175 p.) Yhteenveto 1 p. 2008.
89 OJALA, ARTO, Internationalization of software firms: Finnish small and medium-sized software firms in Japan. 57 p. (180 p.) Yhteenveto 2 p. 2008.
90 LAITILA, ERKKI, Symbolic Analysis and Atomistic Model as a Basis for a Program Comprehension Methodology. 321 p. Yhteenveto 3 p. 2008.
91 NIHTILÄ, TIMO, Performance of Advanced Transmission and Reception Algorithms for High Speed Downlink Packet Access. 93 p. (186 p.) Yhteenveto 1 p. 2008.
92 SETÄMAA-KÄRKKÄINEN, ANNE, Network connection selection-solving a new multiobjective optimization problem. 52 p. (111p.) Yhteenveto 1 p. 2008.
93 PULKKINEN, MIRJA, Enterprise architecture as a collaboration tool. Discursive process for enterprise architecture management, planning and development. 130 p. (215 p.) Yhteenveto 2 p. 2008.
94 PAVLOVA, YULIA, Multistage coalition formation game of a self-enforcing international environmental agreement. 127 p. Yhteenveto 1 p. 2008.
95 NOUSIAINEN, TUULA, Children's involvement in the design of game-based learning environments. 297 p. Yhteenveto 2 p. 2008.
96 KUZNETSOV, NIKOLAY V., Stability and oscillations of dynamical systems. Theory and applications. 116 p. Yhteenveto 1 p. 2008.
97 KHRIYENKO, OLEKSIY, Adaptive semantic Web based environment for web resources. 193 p. Yhteenveto 1 p. 2008.
98 TIRRONEN, VILLE, Global optimization using memetic differential evolution with applications to low level machine vision. 98 p. (248 p.) Yhteenveto 1 p. 2008.
99 VALKONEN, TUOMO, Diff-convex combinations of Euclidean distances: A search for optima. 148 p. Yhteenveto 1 p. 2008.
100 SARAFANOV, OLEG, Asymptotic theory of resonant tunneling in quantum waveguides of variable cross-section. 69 p. Yhteenveto 1 p. 2008.
101 POZHARSKIY, ALEXEY, On the electron and phonon transport in locally periodical waveguides. 81 p. Yhteenveto 1 p. 2008.
102 AITTOKOSKI, TIMO, On challenges of simulation-based globaland multiobjective optimization. 80 p. (204 p.) Yhteenveto 1 p. 2009.
103 YALAHO, ANICET, Managing offshore outsourcing of software development using the ICT-supported unified process model: A cross-case analysis. 91 p. (307 p.) Yhteenveto 4 p. 2009.
104 KOLLANUS, SAMI, Tarkastuskäytänteiden kehittäminen ohjelmistoja tuottavissa organisaatioissa. - Improvement of inspection practices in software organizations. 179 p. Summary 4 p. 2009.
105 LEIKAS, JAANA, Life-Based Design. 'Form of life' as a foundation for ICT design for older adults. - Elämälähtöinen suunnittelu. Elämänmuoto ikääntyville tarkoitettujen ICT tuotteiden ja palvelujen suunnittelun lähtökohtana. 218 p. (318 p.) Yhteenveto 4 p. 2009.

106 VASILYEVA, EKATERINA, Tailoring of feedback in web-based learning systems: Certitude-based assessment with online multiple choice questions. 124 p. (184 p.) Yhteenveto 2 p. 2009.

107 KUDRYASHOVA, ELENAV., Cycles in continuous and discrete dynamical systems. Computations, computer assisted proofs, and computer experiments. 79 p. (152 p.) Yhteenveto 1 p. 2009.

108 BLACKLEDGE, JONATHAN, Electromagnetic scattering and inverse scattering solutions for the analysis and processing of digital signals and images. 297 p. Yhteenveto 1 p. 2009.

109 IVANNIKOV, ANDRIY, Extraction of event-related potentials from electroencephalography data. - Herätepotentiaalien laskennallinen eristäminen EEG-havaintoaineistosta. 108 p. (150 p.) Yhteenveto 1 p. 2009.

110 KALYAKIN, IGOR, Extraction of mismatch negativity from electroencephalography data. - Poikkeavuusnegatiivisuuden erottaminen EEG-signaalista. 47 p. (156 p.) Yhteenveto 1 p. 2010.

111 HEIKKILÄ, MARIKKA, Coordination of complex operations over organisational boundaries. 265 p. Yhteenveto 3 p. 2010.

112 FEKETE, GÁBOR, Network interface management in mobile and multihomed nodes. 94 p. (175 p.) Yhteenveto 1 p. 2010.

113 KUJALA, TUOMO, Capacity, workload and mental contents - Exploring the foundations of driver distraction. 146 p. (253 p.) Yhteenveto 2 p. 2010.

114 LUGANO, GIUSEPPE, Digital community design - Exploring the role of mobile social software in the process of digital convergence. 253 p. (316 p.) Yhteenveto 4 p. 2010.

115 KAMPYLIS, PANAGIOTIS, Fostering creative thinking. The role of primary teachers. - Luovaa ajattelua kehittämässä. Alakoulun opettajien rooli. 136 p. (268 p.) Yhteenveto 2 p. 2010.

116 TOIVANEN, JUKKA, Shape optimization utilizing consistent sensitivities. - Muodon optimointi käyttäen konsistentteja herkkyyksiä. 55 p. (130p.) Yhteenveto 1 p. 2010.

117 MATTILA, KEIJO, Implementation techniques for the lattice Boltzmann method. - Virtausdynamiikan tietokonesimulaatioita Hila-Boltzmann -menetelmällä: implementointi ja reunaehdot. 177 p. (233 p.) Yhteenveto 1 p. 2010.

118 CONG, FENGYU, Evaluation and extraction of mismatch negativity through exploiting temporal, spectral, time-frequency, and spatial features. - Poikkeavuusnegatiivisuuden (MMN) erottaminen aivosähkönauhoituksista käyttäen ajallisia, spektraalisia, aikataajuus - ja tilapiirteitä. 57 p. (173 p.) Yhteenveto 1 p. 2010.

119 LIU, SHENGHUA, Interacting with intelligent agents. Key issues in agent-based decision support system design. 90 p. (143 p.) Yhteenveto 2 p. 2010.

120 AIRAKSINEN, TUOMAS, Numerical methods for acoustics and noise control. - Laskennallisia menetelmiä akustisiin ongelmiin ja melunvaimennukseen. 58 p. (133 p.) Yhteenveto 2 p. 2010.

121 WEBER, MATTHIEU, Parallel global optimization Structuring populations in differential evolution. - Rinnakkainen globaalioptimointi. Populaation rakenteen määrittäminen differentiaalievoluutiossa. 70 p. (185 p.) Yhteenveto 2 p. 2010.

122 VÄÄRÄMÄKI, TAPIO, Next generation networks, mobility management and appliances in intelligent transport systems. - Seuraavan sukupolven tietoverkot, liikkuvuuden hallinta ja sovellutukset älykkäässä liikenteessä. 50 p. (111 p.) Yhteenveto 1 p. 2010.

123 VIUKARI, LEENA, Tieto- ja viestintätekniikka-välitteisen palvelun kehittämisen kolme diskurssia. - Three discourses for an ICT-service development . 304 p. Summary 5 p. 2010.

124 PUURTINEN, TUOMAS, Numerical simulation of low temperature thermal conductance of corrugated nanofibers. - Poimutettujen nanokuitujen lämmönjohtavuuden numeerinen simulointi matalissa lämpötiloissa . 114 p. Yhteenveto 1 p. 2010.

125 HILTUNEN, LEENA, Enhancing web course design using action research . - Verkko-opetuksen suunnittelun kehittäminen toimintatutkimuksen keinoin . 192 p. Yhteenveto 2 p. 2010.

126 AHO, KARI, Enhancing system level performance of third generation cellular networks through VoIP and MBMS services. 121 p. (221 p.). Yhteenveto 2 p. 2010.

127 HÄKKINEN, MARKKU, Why alarms fail. A cognitive explanatory model. 102 p. (210 p.). Yhteenveto 1 p. 2010.

128 PENNANEN, ANSSI, A graph-based multigrid with applications. - Graafipohjainen monihilamenetelmä sovelluksineen. 52 p. (128 p.). Yhteenveto 2 p. 2010.

129 AHLGREN, RIIKKA, Software patterns, organizational learning and software process improvement. 70 p. (137 p.). Yhteenveto 1 p. 2011.

130 NIKITIN, SERGIY, Dynamic aspects of industrial middleware architectures 52 p. (114 p.). Yhteenveto 1 p. 2011.

131 SINDHYA, KARTHIK, Hybrid Evolutionary Multi-Objective Optimization with Enhanced Convergence and Diversity. 64 p. (160 p.). Yhteenveto 1 p. 2011.

132 Mali, Olli, Analysis of errors caused by incomplete knowledge of material data in mathematical models of elastic media. 111 p. Yhteenveto 2 p. 2011.
133 Mönkölä, Sanna, Numerical Simulation of Fluid-Structure Interaction Between Acoustic and Elastic Waves. 136 p. Yhteenveto 2 p. 2011.
134 Puranen, Tuukka, Metaheuristics Meet Metamodels. A Modeling Language and a Product Line Architecture for Route Optimization Systems. 270 p. Yhteenveto 1 p. 2011.
135 Mäkelä, Jukka, Mobility Management in Heterogeneous IP-networks. 86 p. (145 p.) Yhteenveto 1 p. 2011.
136 Savolainen, Paula, Why do software development projects fail? Emphasising the supplier's perspective and the project start-up. 81 p. (167 p.) Yhteenveto 2 p. 2011.
137 Kuznetsova, Olga, Lyapunov quantities and limit cycles in two-dimensional dynamical systems: analytical methods, symbolic computation and visualization. 80 p. (121 p.) Yhteenveto 1 p. 2011.
138 Kozlov, Denis, The quality of open source software and its relation to the maintenance process. 125 p. (202 p.) Yhteenveto 1 p. 2011.
139 Iacca, Giovanni, Memory-saving optimization algorithms for systems with limited hardware. 100 p. (236 p.) Yhteenveto 1 p. 2011.
140 Isomöttönen, Ville, Theorizing a one-semester real customer student software project course. 189 p. Yhteenveto 1 p. 2011.
141 Hartikainen, Markus, Approximation through interpolation in nonconvex multiobjective optimization. 74 p. (164 p.) Yhteenveto 1 p. 2011.
142 Mininno, Ernesto, Advanced optimization algorithms for applications in control engineering. 72 p. (149 p.) Yhteenveto 1 p. 2011.
143 Tykhomyrov, Vitaliy, Mitigating the amount of overhead arising from the control signaling of the IEEE 802.16 OFDMa System. 52 p. (138 p.) Yhteenveto 1 p. 2011.
144 Maksimainen, Johanna, Aspects of values in human-technology interaction design—a content-based view to values. - Ihmisen ja teknologian vuorovaikutussuunnittelun arvoulottuvuudet—sisältöperustainen lähestymistapa arvoihin. 111 p. (197 p.) Yhteenveto 2 p. 2011.
145 Juutinen, Sanna, Emotional obstacles of e-learning. 97 p. (181 p.) Yhteenveto 3 p. 2011.
146 Tuovinen, Tero, Analysis of stability of axially moving orthotropic membranes and plates with a linear non-homogeneous tension profile. 104 p. Yhteenveto 1 p. 2011.
147 Hilgarth, Bernd, The systemic cognition of e-Learning success in internationally operating organizations. - Kokonaisvaltainen käsitys e-oppimisen menestyksestä kansainvälisissä organisaatioisssa. 100 p. (181 p.) Yhteenveto 1 p. 2011.
148 Jeronen, Juha, On the mechanical stability and out-of-plane dynamics of a travelling panel sub-merged in axially flowing ideal fluid. A study into paper production in mathematical terms. - Ideaali virtaukseen upotetun, aksiaalisesti liikkuvan paneelin mekaanisesta stabiilisuudesta ja dynamiikasta. Tutkimus paperintuotannosta matemaattisin käsittein. 243 p. Yhteenveto 3 p. 2011.